Stabilized finite element methods for natural and forced convection-radiation heat transfer

JAAFAR NABEEL JAAFAR ALBADR

Stabilized finite element methods for natural and forced convection-radiation heat transfer

A dissertation submitted for the degree of
Doctor of Philosophy

Jaafar Albadr

Supervised by
DR. MOHAMMED SEAID

Department of Engineering, Durham University
UK
October 21, 2020

Dedication

To my extending roots in the soil of my gracious homeland Iraq…..

To the spirit of my father who lies in peace, who taught me patriotism and selfless…..

To my mother who sustained the empty cup to hold me a drop of love, who harvested the thorns from my path to guide me through knowledge…..

To my precious sisters, Noor and Nessreen…..

To each one who sacrificed his youth, blood and life for the dignity of Iraq and its pride…..

الى جذوري الممتده في تربة بلدي العراق المعطاء.....

الى من علمني حب الوطن ونكران الذات، الى روح والدي التي ترقد بسلام.....

الى من جرع الكأس فارغاً ليسقيني قطرة حُب، الى من حصد الاشواك عن دربي ليمهد لي طريق العلم، الى امي الغاليه.....

الى اخواتي الحبيبات نور ونسرين.....

الى كل من ضحى بشبابه ودمه وحياته من اجل كرامة العراق وعزته.....

Declaration

I hereby confirm that all of the results described in this thesis are the original work of mine. Any published ideas or techniques from the others are fully acknowledged in accordance with the standard referencing practices.

Acknowledgements

In the name of God, most Gracious, most Merciful. I wish to express my sincere appreciation to those who have contributed to this thesis and supported me in one way or another during this amazing journey.

First and foremost I want to thank my advisor Dr. Mohammed Seaid. It has been an honour to be his Ph.D student. I appreciate all his contributions of time, challenging ideas, critical remarks, constant guidance and support to make my Ph.D experience productive and stimulating. My special thanks to you for providing me all the theoretical insight for many problems and especially for allowing me knocking your door without appointments. I would like also to convey my deepest gratitude to my second advisor Prof. Jon Trevelyan for his support, constructive suggestions and kind help that paved a joyful and enthusiastic way in accomplishing this thesis.

I am highly indebted and grateful to Prof. Mofdi El-Amrani, for his generous help, encouragements and his particular peeping in my manuscripts that helped me enormously in reaching my goals.

I am very grateful to Dr. Konstantinos Krestenitis, Dr. Meshal Alharbi, Mrs. Alia Al-Ghosoun for their advices, motivation, inspiration and immense knowledge in life and managements that, taken together, make them my best second family.

I would like to express my sincere thanks to Miss Yuhe Tian for being my amazing source of spirited support and encouragement. You have been of great help to me throughout the relentless endurance test of my Ph.D.

I must thank Miss Binhui Lyu for showing me what it means to be a dedicated, in her own unique way. You have given of your time, energy, and expertise. Thank you for always being there, cheering me up and stood by me in the good times and bad.

To Miss Yeeting Wong, thank you for being an amazing source of inspiration. I really appreciate you taking the time to polish my thesis, to spread your good energy everywhere and for your patience and understanding.

To Miss Zhiyu Li, thank you for listening, offering me advice, and supporting me through this entire process. Thank you for sharing our life stories with each other!!!

I am deeply grateful for Miss Xiaowei Wang for being so generous with her time in encouraging, helping and supporting me.

I am also grateful to all of my well-wishers for their invaluable advice and support that has helped me greatly to make it this far.

To my friends scattered around my country, thank you for your thoughts, well-wishes/prayers, phone calls, emails, texts, visits, editing advice, and being there whenever I needed a friend.

Finally, I would like to acknowledge the most important persons in my life: my late father who made me the person who I am now, my beloved mom, sisters, aunt Raja, aunt Naema, aunt Hanna, aunt Najlaa, the rest of family members and Mr. Imad Assfoor. I owe you all much more than I can possibly express. This Ph.D journey would not have been possible without your support. Much appreciated for encouraging me in all of my pursuits and inspiring me to follow my dreams. I am especially grateful to you, who supported me emotionally and financially. You have been the constance source of strength, inspiration, determinations and prayers that ultimate made it possible for me to see this project to the end. Thank you for teaching me that my job in life was to learn, to be happy, and to know and understand myself; only then could I know and understand others. Thank you to my mother, Najat Ibrahim, for guiding me as a person and teacher and for offering her editing expertise throughout this process.

List of publications

Below are the published studies done during my Ph.D time as a main author.

Conference papers:

1 - **J. Albadr**, M. El-Amrani, M. Seaid, J. Trevelyan. Stabilized finite element simulation of heat transfer inside industrial furnaces, 15^{th} UK Heat Transfer Conference, Brunel University, 4^{th}-5^{th} September, 2017. Paper ID: 91.

2 - **J. Albadr**, M. El-Amrani, M. Seaid, J. Trevelyan. Stabilized mixed finite element analysis for heat flow inside industrial furnaces with horizontal burners, Proceedings of 91^{st} The IRES International Conference, Chicago, USA, 24^{th} -25^{th} November, 2017. Pages: 55-60.

Journal papers:

1 - **J. Albadr**, M. El-Amrani, M. Seaid, J. Trevelyan. Stabilized mixed finite element analysis for heat flow inside industrial furnaces with horizontal burners, International Journal of Advanced Computational Engineering and Networking, ISSN(p): 2320-2106, ISSN(e): 2321-2063, Volume-6, Issue-1, Jan. 2018.

2 - **J. Albadr**. Effect of Al_2O_3 nanofluid at difference concentrations on solar parabolic trough. Submitted to Athens Journal of Technology & Engineering.

3 - **J. Albadr**, M. El-Amrani, M. Seaid. Simplified P_N finite element approximations for coupled natural convection and radiation heat transfer. Submitted to Numerical Heat Transfer, Part A.

4 - **J. Albadr**, M. El-Amrani, M. Seaid. A second-order mixed finite element method for convection-radiation flows in furnaces with burners. Submitted to International Journal of Numerical Methods for Heat & Fluid Flow.

Chapter in a book:

1 - **J. Albadr**. Thermal performance of shell and tube heat exchanger using PG/water and

Al_2O_3 Nanofluid. DIO: 10.5772/intechopen.80082.

Abstract

Thermal radiation in forced and natural convection can be an important mode of heat transfer in high temperature chambers, such as industrial furnaces and boilers, even under non-soot conditions. Growing concern with high temperature processes has emphasized the need for an evaluation of the effect of radiative heat transfer. Nevertheless, the modelling of radiation is often neglected in combustion analysis, mainly because it involves tedious mathematics, which increase the computation time, and also because of the lack of detailed information on the optical properties of the participating media and surfaces. Ignoring radiative transfer may introduce significant errors in the overall predictions. The most accurate procedures available for computing radiation transfer in furnaces are the Zonal and Monte Carlo methods. However, these methods are not widely applied in comprehensive combustion calculations due to their large computational time and storage requirements. Also, the equations of the radiation transfer are in non-differential form, a significant inconvenience when solved in conjunction with the differential equations of flow and combustion. For this reason, numerous investigations are currently being carried out worldwide to assess computationally efficient methods. In addition efficient modelling of forced and natural convection-radiation would help to simulate and understand heat transfer appearing in various engineering applications, especially in the case of the heat treatment of high-alloy steel or glass by a continuously heating process inside industrial furnaces, ovens or even smaller applications like microwaves. This thesis deals with the design of such methods and shows that a class of simplified approximations provides advantages that should be utilized in treating radiative transfer problems with or without flow convection. Much of the current work on modelling energy transport in high-temperature gas furnaces or chemically reacting flows, uses computational fluid dynamics (CFD) codes. Therefore, the models for solving the radiative transfer equations must be compatible with the numerical methods employed to solve the transport equations. The Zonal and Monte Carlo methods for solving the radiative transfer problem are incompatible with the mathematical formulations used in CFD codes, and require prohibitive computational times for spatial resolution desired. The main objectives of this thesis is then to understand and better model the heat treatment at the same time in the furnace/oven chamber and within the workpieces under specified furnace geometry, thermal schedule, parts loading design, initial operation conditions, and performance requirements. Nowadays, there is a strong need either for appropriate fast and accurate algorithms for the mixed and natural convection-radiation or for reduced models which still incorporate its main radiative transfer physics. During the last decade, a lot of research was focused on the derivation of approximate models allowing for an accurate description of the important physical phenomena at reasonable numerical costs. Hence, a whole hierarchy of approximative equations is available, ranging from half-space moment approximations over full-space moment systems to the diffusion-type simplified P_N approximations. The latter were developed and extensively tested for various radiative transfer problems, where they proved to be sufficiently accurate. Although they were derived in the asymptotic regime

for a large optical thickness of the material, these approximations yield encouraging even results in the optically thin regime. The main advantage of considering simplified P_N approximations is the fact that the integro-differential radiative transfer equation is transformed into a set of elliptic equations independent of the angular direction which are easy to solve. The simplified P_N models are proposed in this thesis for modelling radiative heat transfer for both forced and natural convection-radiation applications. There exists a variety of computational methods available in the literature for solving coupled convection-radiation problems. For instance, applied to convection-dominated flows, Eulerian methods incorporate some upstream weighting in their formulations to stabilize the numerical procedure. The most popular Eulerian methods, in finite element framework, are the streamline upwind Petrov-Galerkin, Galerkin/least-squares and Taylor-Galerkin methods. All these Eulerian methods are easy to formulate and implement. However, time truncation errors dominate their solutions and are subjected to Courant-Friedrichs-Lewy (CFL) stability conditions, which put a restriction on the size of time steps taken in numerical simulations. Galerkin-characteristic methods (also known by semi-Lagrangian methods in meteorological community) on the other hand, make use of the transport nature of the governing equations. The idea in these methods is to rewrite the governing equations in term of Lagrangian co-ordinates as defined by the particle trajectories (or characteristics) associated with the problem. Then, the Lagrangian total derivative is approximated, thanks to a divided difference operator. The Lagrangian treatment in these methods greatly reduces the time truncation errors in the Eulerian methods. In addition, these methods are known to be unconditionally stable, independent of the diffusion coefficient, and optimally accurate at least when the inner products in the Galerkin procedure are calculated exactly. In Galerkin-characteristic methods, the time derivative and the advection term are combined as a directional derivative along the characteristics, leading to a characteristic time-stepping procedure. Consequently, the Galerkin-characteristic methods symmetrize and stabilize the governing equations, allow for large time steps in a simulation without loss of accuracy, and eliminate the excessive numerical dispersion and grid orientation effects present in many upwind methods. This class of numerical methods have been implemented in this thesis to solve the developed models for mixed and natural convection-radiation applications. Extensive validations for the numerical simulations have been carried out and full comparisons with other published numerical results (obtained using commercial softwares) and experimental results are illustrated for natural and forced radiative heat transfer. The obtained convection-radiation results have been studied under the effect of different heat transfer characteristics to improve the existing applications and to help in the furnace designs.

Contents

List of Figures

List of Tables

Acronyms

CFD	Computational fluid dynamics
RTE	Radiative transfer equation
DOM	Discrete ordinates method
FVM	Finite volume method
SP_N	Simplified P_N approximations
FDM	Finite difference method
FEM	Finite element method
X-FEM	Extended finite element method
BICGSTAB	Bi conjugate gradient stabilized method
GMRES	Generalized minimal residual
DSA	Diffusion Synthetic Acceleration
ILU	Incomplete LU
SI	Source iteration
PDE	Partial differential equations
CGM	Convective glass melting

Nomenclature

Symbols	Description
$\mathcal{D}$	Space domain
f	Centred valued function
I	Angular flux
t	Time
T	Final value of time
c	Speed of light
q	External source
$\mathbf{n}$	Unit normal
E	Energy variable
n	Number of direction cosines
$\mathbf{Q}$	Vector in radiative equation
I	Identity matrix
$\mathcal{A}$	Schur matrix
d	Values on the nodes
A	SP_3 boundary conditions variable
C	SP_3 boundary conditions variable
D	SP_3 boundary conditions variable
$\mathcal{B}$	Vector in Schur equation
$\mathbf{P}$	Preconditioner
$\mathcal{T}$	Nonsymetric positive definite matrix
$\mathcal{R}$	Vector of the external source
B	Blank function
k	Iteration number
Cp	Specific heat at constant pressure
Pl	Plank number
M	Mach number
Pr	Prandtle number
Ra	Rayleigh number
Re	Reynolds number
Pe	Peclet number
S	Unit sphere
h	Mesh size
V	Volume
P	Penetration radiation
$\mathcal{O}$	Expansion order
mi	Counting number
p	Pressure
u	Velocity
j	General parameter
$\mathbf{e}$	Unit vector
w	General variable
Ne	Number of element

Greek symbols

$\Im$	Thermal conductivity
Θ	Temperature
τ	Optical thickness
γ	Domain or element side
ϱ	Coefficient of thermal expansion
$\wp$	Kinematic viscosity
$\Im$	Thermal conductivity
$\hbar$	Convective heat transfer coefficient
α	Emissivity
$\aleph$	Relaxation parameter
ϵ	Diffusivity
ρ	Density
λ	CFL condition
ψ	Value on node
ι	Counting number
υ	Neutron speed
ν	Frequency
γ	Scattering ratio
ϑ	Optical coefficient
ϕ	Scalar flux
ω	Weights
φ	Direction angle
θ	Inclination angle
Φ	Scalar flux
σ	Scattering cross section
κ	Absorption
Ω	Domain
δ	Tolerance
$\mathbf{\Theta}$	Diagonal
ϖ	General parameter

Subscripts

a	Initial value
r	Residual
$refl$	Reflection radiation
ref	Reference value
r	Integral
H	Hot
C	Cold

Chapter 1

Introduction

Heat transfer takes place when high temperature exists within a system or between a system and its surroundings. In thermodynamics, heat is defined as energy of a system and with a growing concern on environment and energy crisis; the investigation of heat transfer has been an important part of engineering research over the past years [54]. The applications cover a wide range of areas from the aspects of environmental, atmospheric and geophysical problems to manufacturing systems, space research and heat injection/rejection. The three modes of heat transfer are conduction, radiation and convection, these usually occur in most practical systems where every mode of heat transfer can be investigated separately and the results of heat transfer is then combined to give a total heat transfer rate within systems. However, in some cases heat transfer from a system may involve a combination of two or three modes which interact with each other. For the conduction and radiation, heat transfer processes, the former occurs when temperature differences exist in the material of a system and also due to the motion of particles which may comprise materials as well as microscopic particles. Diffusion of energy occurs due to the difference in the local temperature and fluid motion. The energy transfer in the radiation however occurs in the form of electromagnetic waves where the energy is emitted from a material due to the high temperature in mediums, and is transferred to other layers through the superseding space.

A lot of studies are considered to understand radiation heat transfer by solving the full radiative transfer equation. For instance, authors in [157] developed a new study based on P_3 approximations to decompose the radiative transfer equation. Results were carried out for one dimensional and two dimensional problems of scattering, absorbing and emitting media using variable and constant properties. Their proposed approach however suffers from false scattering. This is because of the intensity expansion into a smoother series of spherical harmonic. Likewise, author in [102] developed 2D P_1, P_3 and P_5 approximations. Results validated against Monte Carlo approach while Marshak boundary condition are reformulated in the light of the elliptic formulation. The study on the other hand requires more calculations and more investigation is needed for the calculation of the flux divergence and the incident radiation. Furthermore, authors in [105] investigated a conduction-radiation in diffusive grey materials based on the simplified P_1 approximation. However, only simple tests were carried out and the method is still not proven to be accurate for more complicated problems. Additionally, authors in [97] derived the SP_N approximations to the order of SP_1, SP_3 and SP_5. However, no examples were conducted nor derivations of boundary conditions. The study was more about a comparison with the P_N approximations rather than investigating the SP_N approximations in details. Furthermore, a partitioned of unity method for the numerical resolution of thermal boundary layers is investigated by [107] for conduction-radiation problems using finite element

method. The study however struggled with the steep gradient in the boundary layers and no strong validations were carried out. Likewise, an efficient partition of unity finite element method for three-dimensional transient diffusion problem is developed by [93]. Remeshing is not needed as the solution is refined by adapting the enrichment functions. However, the study is not suitable for moving heat sources and results were not validated properly. Likewise, authors in [104] developed a new methodology on spherical harmonic P_N. The advantage of this methodology is that it employed successive elimination of the spherical harmonic tensors. This leads to a reduction in the number of first order partial differential equations required for solving P_N approximations. The challenge in this study is that for a low order technique, it is difficult to describe in intensity with sharp directional gradients. The solution of nonlinear problems is studied by [95] using the partition of unity method to enriched finite element technique. No remeshing is needed in this study. However, extensive validations are still required. Additionally, authors in [94] investigated the nonlinear transient heat transfer in functionally graded materials. The advantage of this study is the ability to approximate complicated local features of the solution utilizing coarse mesh. However, refine mesh is needed for an accurate results. Also, a non-uniform rational B-splines is needed to mesh the domain.
Moreover, authors in [92] used the Rosseland model for approximating thermal radiation to study the transfer of heat on optically thick non-gray medium. The advantage of this study is that it reduced the computational cost. However, the approach is not suitable to study heat flow as full radiative transfer can not be coupled with Navier-Stokes equation. Furthermore, a high order enriched partition of unity finite element approach is proposed by [5] for nonlinear and linear time dependent diffusion problems. The main advantage of this study is that it does not need to remesh as it is able to refine the solution by adapting the enrichment without generating new mesh. However, the accuracy of this study is needed to be investigated for higher orders of finite element. Likewise, authors in [106] used the generalized finite element solution of time-dependent boundary-value problems for testing the performance of iterative solver based on Krylov subspaces. The study solved the linear system using generalized minimum residual. However, more validations are needed as the study was not applied on an engineering application. Convection occurs when there is a relative motion between a surface and a fluid over the surface and there is a temperature difference between the surface and flow. The mechanism of flow on a heated surface is divided into three distinct groups: natural convection, forced convection and mixed convection. The movement of mass in natural convection depends on the density gradient which is driven by the buoyancy force of the flow, while the flow in forced convection is driven by other external forces such as flow speed and pressure gradient. On the other hand, mixed convection is driven by both free and forced convections. Over recent years, more attention has been given to natural convection as it occurs naturally in environmental systems. Moreover, most practical and economical methods for developing heating and cooling systems use natural convection induced by buoyancy forces. This chapter proceeds as follows. Section 1.1 gives an overview of the convection-radiation heat transfer that occurs naturally inside different computational domains. Section 1.2 shows different studies of forced convection-radiation heat transfer that take place inside various industrial furnaces. The evolution of modeling process for heat transfer is explained in section 1.3. Challenges and novelties are explained in section 1.4. Objectives of the thesis are presented in section 1.5. Finally, thesis layout is outlined in section 1.6.

(a) Car paint drying process[1]

(b) Food heating inside a domestic microwave[2]

Figure 1.1: An illustration of natural convection-radiation transfer of heat.

1.1 Natural convection-radiation heat transfer

Coupling of natural-convection and radiation heat transfer occurs in various engineering problems. One of the common examples of natural convection and radiation coupling is the cooling of electronic components such as laptops, CD players, and cell phones. These listed devices put a premium on power conservation to reduce the drain on the battery power. Other examples of applications for coupled natural convection and radiation heat transfer include water quality management, environmental planning in coastal regions [85], furnaces [158], solar energy [35], crystal growth [69] and room fires [65]. Figure 1.1 shows two widely used applications on natural heat convection-radiation transfer. Many of these systems can be evaluated through experiments. However, experiments can be costly, time consuming, and limiting on the variation that may be investigated. Modern computers and simulation softwares are used to augment experiments in evaluating and designing engineering systems. Because the simulation programs are benchmarked against experiments, sometimes only simulations are performed and experiments are avoided entirely. The problem with the numerical simulations is the calculations can become complicated and computationally intensive for simulations where natural convection and radiation heat transfer are included. If one of the heat transfer modes (natural convection, conduction, or radiation) can be neglected, the calculations may be simplified: reducing computation times and resources. A heat transfer mode may be neglected when its contribution is small compared to other heat transfer modes.

1.1.1 Literature review on natural convection-radiation heat

Natural convection-radiation heat transfer problems can be found in many industrial and realistic applications such as building insulations, double glazed windows and solar collectors. The effects and contributions of natural convection and radiation have been studied in many forms over the years ranging from pure natural convection to natural convection with participating media. The importance of radiation heat transfer interacting with natural convection is generally well recognized [128]. Radiation typically has a larger impact on natural convection than for forced convection [71]. This is due to forced convection having higher heat transfer fluxes than the relatively low values of natural convection. In [125, 151], authors found that radiative heat transfer was substantial at minimum temperature of 273 K in systems coupled with

[1] www.carrozzeriaautorizzata.com/news/623/impianti-di-essiccazione-irt-power-cure-by-covea
[2] www.panasonic.com/uk/consumer/home-appliances/microwaves.html

natural convection. Researchers propose to study pure natural convection have had to be very careful to avoid any effects from radiation. In [26], liquid Nitrogen (temperature of 77 K) was utilized in experiments to determine the natural convection around a heated cylinder made of Bronze. Thermo-resistive properties of bronze were used to determine the temperature of the cylinder. In [52], researchers conducted a time-dependent natural convection experiment in a $150 \times 50 \times 60$ mm cuboid enclosure. Two isothermal baths were used to set the temperatures on two opposing surfaces while the top and bottom surfaces were insulated. The front and rear surfaces were Plexiglas to allow for flow visualization of the silicon oil in the system. In the worst-case scenario, the system was placed under a temperature difference of 333 K with the ambient temperature at 298 K. Under these conditions, radiation from the hot surface to the cold surface was around two percent. Their results indicated that radiation contributed at relatively low temperatures even when precautions were taken to minimize radiation heat transfer.

Radiative heat transfer is categorized into two broad classifications: participating and non-participating media. Optical thickness (defined as the product of the characteristic length and the absorption coefficient) is often cited as the criteria for whether the medium is radiatively participating or not. If a medium has a relatively large optical thickness, participating media calculations should be performed. Participating media reduces heat transfer at the boundaries because the medium has a more uniform temperature than without participating media [158]. In [10], authors looked at heat transfer between two concentric cylinders for different values of optical thickness. Conditions for the simulations were emissivity of the inner cylinder was 0.9, and the outer cylinder emissivity was 0.4. Increasing the optical thickness reduced the radiation heat transfer in a decreasing exponential manner.

Fluids such as air, Nitrogen, and the inert gasses are essentially non-emitting and non-absorbing. These two characteristics make these fluids effectively non-participating. This criteria holds as long as temperatures are not high enough for either ionization or electronic excitation to occur, such as in the bow shock wave of a spacecraft in re-entry [100] or a nuclear explosion [41]. More studies appear to be available for enclosures filled with participating media than non-participating media. In [125], researchers had similar findings in their literature review. The majority of the research coupling natural convection and radiation heat transfer was for steady state conditions [47, 151, 158, 160] where one surface was set as the 'hot' surface while the other surface was set as the 'cold' surface. Some researchers investigated thoroughly the transient natural convection and radiation interaction [85, 88]. In [88], investigators found in their numerical simulations that retaining time derivative terms improved the rate of convergence of their simulations. Time derivative terms are differentials in the equations defined by a quantity change over a time change. Authors also found that after a certain mesh and time step size, the benefits of refining the mesh or decreasing time step sizes were offset by round off errors in the computer.

A typical system for simulating and conducting experiments for combined natural convection and radiation is a simple rectangular enclosure. In [151], authors performed two-dimensional steady state simulations in a simple rectangular enclosure with a non-participating media. The enclosure was described as a rectangle with width and height. The top and bottom surfaces were insulated while the left surface was set as the 'cold' surface and the right surface was set as the 'hot' surface. The Rayleigh numbers ranged from 10^9 to 10^{12}, emissivity was between 0 to 0.9, initial temperature was between 223 to 423 K, temperature difference between the hot and cold surface was ranged from 10 to 250 K and the aspect ratio (enclosure height divided by length) varied from 1 to 200. In all of the simulations, air was the working medium. Results showed the surface-to-surface radiation modified the temperature on the top and bottom

surfaces, which in turn affected the natural convection heat transfer in the enclosure. The top surface served to cool the fluid and then to re-emit the heat flux to other surfaces as radiation. The bottom surface absorbed radiation and heated the fluid by convection. Heating of the fluid along the bottom surface reduced the temperature difference between the hot surface and the boundary layer. Velocity and turbulence levels were enhanced by surface radiation resulting in higher convective heat transfer. In [35, 36], researchers took the simple two-dimensional rectangular enclosure and extended it to three-dimensions. Length and width were the original edges that formed a square, while depth represented the expansion into three dimensions forming the cube. In the simulations, the cold temperature was 278 K, and the hot temperature was 833 K. Fluid properties were taken at the reference temperature of 555 K. The height for the cube enclosure varied from 2.57×10^{-2} m to 4.66×10^{-1} m. Carbon dioxide was the working medium with a Prandlt number of 0.68. Under these conditions, carbon dioxide was treated as a participating media. To account for the participating media, the P_1 radiation model was selected. This model uses spherical harmonic approximations for radiation intensity to predict both temperature and heat transfer [127]. A limitation to the model is the need for optically thick media: materials with appreciable optical depth values. Several heat transfer models were considered by [35, 36] for carrying simulations. One option was to neglect radiation. Results showed that the temperature field varied only slightly in the z direction, while the velocity field had weak secondary flows in the corners. Steady state solutions were not reached in the natural convection mode. With radiation included, steady state solutions could be acquired. The presence of the end surfaces and radiation had a large effect on the formation of three-dimensional flow fields. Secondary flows reached a higher intensity and the secondary vortex corners moved towards the symmetry plane. Surface radiation was attributed to causing variations in the temperature field near the back surface mainly due to an increase in the surface temperature [36].

Comparing the results obtained in two-dimensional simulations performed by [33, 36] and three-dimensional work, heat transfer was approximately 15 to 20 percent less than for the two dimensional counterpart. End surface temperatures in the three-dimensional model reached a maximum value relative to all temperatures the surfaces will reach which reduced the total radiative flux from the isothermal surfaces and cause the difference in heat transfer. As for the flow fields [84], it was found that two-dimensional simulations were able to capture the major features of the flow development. For full understanding of the flow field and instabilities, three-dimensional simulations are needed. Simulations and experiments available for simple enclosures provide large amounts of information, especially for systems that are simple enclosures such as windows, but do not adequately capture more complicated systems where there are partitions and obstacles. Room fire phenomena as discussed by [158] and the experimental model for the research being presented have blocking features and more complicated heat transfer interactions.

Among the past work, numerical calculations were carried out in in [76] for obtaining results for a squared cavity at Rayleigh numbers between 10^3-10^6 as a benchmark solution. Finite Volume Method (FVM) was adopted to solve the Navier-Stokes equations and Disctrete Ordinates Method (DOM) were accounted for the Radiative Transfer Equations (RTE). Results showed that different values of Rayleigh number and optical thickness affect on the transfer of heat across the cavity. However, the study was limited to a fixed Planck coefficient of 0.1 without considering the effect of the inclined angle. In [139], natural convection-radiation interaction was studied inside a squared enclosure at different values of Planck coefficient, optical depth and Rayleigh number. The RTE was solved utilizing five different approaches, DOM, FVM, P_1, SP_3 and P_3. Nevertheless, the study was limited as the effect of the inclined angle was

not considered. Furthermore, numerical investigation was conducted in [7] for natural thermal flow under laminar and turbulent conditions inside a squared cavity using the control volume method with Rayleigh number up to 10^{10}. Nonetheless, only convection heat was investigated to solve the conservation equations. Likewise, a combined heat transfer of radiation and natural convection study was investigated in [34] in a squared cavity containing participating gases. The effect of Rayleigh number of values between 10^3-10^6 with optical thickness values from 0-100 on temperature, velocity distribution and Nusselt numbers were studied. The study on the other hand was limited to convection heat transfer and can not be used for complex geometries as Finite Difference Method (FDM) was used.
Moreover, P_1 approximation for representing the radiative heat transfer was utilized in [82, 83] in narrow vertical cavities. The effect of radiation on the transition, conduction and boundary condition was dealt with. However, the study was limited to P_1 approximation without the effect of the inclined angle. Additionally, authors investigated the interaction between natural convection and radiation with and without participating media for an undivided cavity with wide range of Rayleigh and Planck coefficient [24, 91]. However, the FDM was considered in [24] which can not be used for complex geometries and in [91], the effect of optical depth and the inclined angle was not presented. In [11], radiation-natural convection heat transfer was investigated in an inclined rectangular enclosure at different Rayleigh numbers and inclined angles using FVM for solving the governing equations. It was found a reduction in the effect of heat transfer when the increase in the inclined angle was considered. The study however did not consider the effect of Planck coefficient or optical thickness. In [141], an absorbing, emitting and isotropically scattering medium at three different values of Rayleigh number and a wide range of radiation-conduction parameters was studied inside a squared enclose using non-linear successive-over-relaxation method for combining radiation and convection-conduction heat transfer. Yet, the effect of the inclined angle, Planck coefficient and optical depth were not taken into account.
In [154], interaction effect between convection and radiation was taken into account in a squared cavity with inclined angle. The FDM was the method chosen which is limited to simple geometries. Results showed the heat transfer were affected by the inclined angle, emissivity and Rayleigh number. The result was limited to a constant optical depth of unity and Planck coefficient of 0.1. Furthermore, a numerical study was considered in [74] for the effect of radiation-convection heat transfer in a slanted cavity with two different angles of 45° and 60°. The FVM was considered with different ranges of τ. The study was limited to one value of Rayleigh number at a fixed Planck coefficient. Moreover, convection-radiation heat transfer was investigated experimentally and numerically in [86]. The numerical investigation was done using ANSYS Fluent software. The study considered variety values of Rayleigh and inclined angle. Results showed that the maximum heat rate was at an inclined angle of 0°. The limitations in this study were regulating the effect of radiation as the commercial softwares can not deal with radiation transfer equations properly. In addition, in [156], a numerical study was performed based on thermosolutal buoyancies with Dufour and Soret effects for double-diffusive convection. The model was desicritized using FVM and solved utilizing SIMPLE algorithm with QUICK scheme in non-uniform staggered mesh. Heat transfer characteristics were investigated with different values of Rayleigh, Soret and Dufour coefficients, aspect ratios and buoyancy ratios. The average Sherwood as well as Nusselt numbers were kept constant without considering the radiation effect or the inclined angle. Likewise, a numerical analysis of combined double diffusion radiation convection transfer of heat in a squared cavity were conducted using FDM and DOM for the RTE in [110]. Results showed that heat transfer was affected by the optical thickness. However, the study used FDM which can only be performed

on simple geometries and the effect of Planck coefficient and the inclined angle were not investigated. Furthermore, a convection-radiation transfer of heat was accounted for a rotating cavity of a squared shape with a local heater in [99]. The non-dimensional mathematical formulation was solved by FDM. The influence of Rayleigh number, Nusselt number, Taylor number, emissivity and Ostrogradsky number on the natural heat flow was studied. The results showed that the increase in the emissivity as well as the rotation reduce the temperature inside the heating element. Additionally, the study can not be applied on complex geometries due to the limitations of FDM. Likewise, a double-diffusive natural convection study in [63] for Soret and Dufour effects as well as viscosity dissipation in a squared cavity filled with Bingham fluid was simulated by Fictitious Domain (FD) Lattice Boltzmann technique. Various values of Rayleigh number, Lewis number, Bingham number, Eckert number, Dufour and Soret parameters, Buoyancy ratio and inclined angle were carried out. Results showed that mass transfer increases with the increase in Soret parameter while the heat transfer increases with the increase in Dufour parameter for different values of Rayleigh and Bingham numbers. The rise in both Dufour and Soret parameters enhances the raises of the fluid friction and enhances the generation of entropy. Results also showed that the growing in the buoyancy ratio boosts heat and mass transfer. The augmentation of Eckert number decreases the transfer of heat while the increase in Rayleigh number decreases the average Bejan number. From another point of view, the study can not be used for considering complex geometries and it misses the effect of radiation heat transfer.
A thorough investigation of the numerical performance of the Simplified approximations (SP_N) hierarchy in the context of coupled radiation, convection and diffusion problems are given in the current study. We examine the accuracy and efficiency of the SP_N approximations of radiative transfer for natural convection problems in a squared enclosure with the effect of the inclined angle. The vertical walls of the enclosure are heated with uniform different temperatures and the horizontal walls are adiabatic. A Boussinesq approximation of the Navier-Stokes equations is employed for the fluid subject to combined natural convection and radiation. Coupled with the SP_N models, the system of equations results into a set of partial differential equations independent of the angle variable and easy to be numerically solved using standard computational fluid dynamics methods. We believe that this is the first investigation on the effect of convection-radiation heat transfer using the Taylor-Hood finite element method with SP_3 approximations. Previous studies failed to show a noticeable difference between radiation and pure convection. This is due to the fact that previous researchers focused on considering the P_1 radiative equations that are discussed in this thesis. Furthermore, to the best of our knowledge, another novelty lies in the complex geometry heater that is added to the square cavity with two different inclined angles.

1.1.2 Computational tool

The studies in this section create a basis regarding heat transfer in a system with natural convection and radiation. In addition to the investigation of the interaction of natural convection and radiation, the current work expands on the baffled enclosure work to examine combined natural convection and radiation for a geometry with an inclined angles as well as the inclusion of a complex heater inside the inclined squared cavity. The method has been implemented using FORTRAN code and the obtained results have been validated against those published in the literature, commercial available Computational Fluid Dynamics software (CFD) and experimental data. A thorough investigation of the numerical performance of the SP_N hierarchy in

the context of coupled radiation, convection and diffusion problems are given. We examine the accuracy and efficiency of the SP_N approximations of radiative transfer for natural convection problems in a squared cavity. The vertical walls of the domain are heated with uniform different temperatures and the horizontal walls are adiabatic. A Boussinesq approximation of the Navier-Stokes equations is carried out subject to combined natural convection and radiation. Coupled with the SP_N models, the system of equations results into a set of partial differential equations independent of the angle variable and easy to be numerically solved using standard computational fluid dynamics methods.

1.2 Mixed convection-radiation models

Due to the growing demands for reducing energy consumption and emissions of pollutants, the simulation of heat transfer features of the structure in an industrial furnace, is the topic of significant amount of research investigations [56, 111]. It is important to note that the process of heating of furnaces signifies an important step which will help achieve the appropriate thermal characteristics of the treated structure. The following factors tend to perform an important part in such processes to maintain uniform temperature gradients minimization, avoid as many surface defect (skid marks) as possible and to increase the capacity of the furnace. Likewise, increase the structure product quality in particular in terms of resistance and hardness. Essentially, control the hot fire flows inside the furnace. Thereafter, the heat (radiation and convection) transfer through conduction in the structure with time [135]. Nevertheless, the problem can be challenging to analyse precisely owing to the unsteady heat, the location of the treated inclusion, the given geometry and the orientation of the burners along the sophisticated structure of the furnace which includes the thermal coupling of the structures and fluids. Thus, the design of a CFD tool is so crucial for the successful investigation of these physical phenomena and also for predicting the global behaviour of the furnace.
The main purpose of this study is to introduce a technique which can predict this phenomena that takes place in a complex two dimensional configuration under the operation of several burners. In particular, the main focus of this study is to represent thoroughly heat flow, physical domain and consider both heat convection and radiation. To perform such a study, we propose a mixed finite element method [27]. Over the recent years, the focus of many scientific studies was on the diverse engineering applications, involving thermal coupling of structures and fluids [51, 29]. In [96], a simplified method for on-line model for controlling a rotating reheat furnace was developed to study the process of reheating and annealing processes of the metals. The idea was to examine the radiative exchanges in a pusher furnace. However, the study was limited to monitor the evolution of temperature with time without coupling convection-radiation heat transfer and without studying the effect of the optical depth and Planck coefficient on the radiative equation. Likewise, in [8], a simplified method for on-line temperature control of a pusher kind of furnace was developed to improve the operation practice and propose a better furnace design. However, the study focused on the radiative combustion gases rather than studying the number and location of the burners for a better new design. On one hand, authors in [126] developed a model of an indirect firing furnace that is capable of predicting the fuel consumption. On the other hand, the study focused on thermal chemistry without considering thermal physics. Similarly, in [4], models for analysing heat radiation in furnaces were developed for reheating slabs rotating and rolling hearth furnaces. Nevertheless, the study was limited to measure the temperature on the slab without considering convection transfer of heat, heat flow behaviour and controlling the operation and location of the burners.

Furthermore, in [48], a computational model was used for predicting heat transfer in direct-fire pusher type reheat furnace was developed using FVM for computing the gas radiation heat transfer. The research was bounded to study the radiative transfer without the effect of the turbulence of the heat flow inside the furnace. Moreover, a mathematical model was developed in [67] using FVM to predict radiation heat transfer on slab surface and temperature distribution inside the slab. However, the study was limited to solve the RTE of heat transferred from the burners without solving the heat propagation (the Navier-Stokes equations). Moreover, the SP_N approximations have been modelled to study the radiative heat transfer in glass by [68]. The study was focusing only on the cooling process of glass sheet. The results showed that simplified approximations were efficient and sufficiently accurate. Furthermore, the SP_N approximations of radiative transfer were investigated in [40] considering a high-order discontinuous Galerkin method. The results showed that for optically thick media, the SP_N approximations produced results which were close to those computed by the full radiative transfer problem. Yet the method was applied to simple problems and more study and error estimator are required.
As far as dealing with a diverse range of physical characteristics, dimensions and shapes of structures to heat are concerned, such experimental identifications become increasingly time consuming, limited, as well as costly. We believe that this is the first investigation on the effect of mixed convection-radiation heat transfer using the Taylor-Hood finite element method with the SP_3 approximations. Furthermore, to the best of our knowledge, another novelty lies in the complex geometry furnace that is considered inspired from the glass manufacturing and glass melting industrial furnaces. Moreover, different operation of burners are considered. This is important to understand the behaviour of heat inside the furnace, predict the furnace life time and being able to redesign the furnace geometry which can help the realistic industrial furnaces in obtaining the required results and minimising the manufacturing and operating costs. In this investigation, the radiation heat transfer is included into the thermal incompressible Navier-Stokes equations through the SP_1 and SP_3 problems. We propose a Galerkin-characteristic procedure where the time derivative and the convection term are combined as a direct derivative along the characteristics, which leads to a characteristic time stepping procedure.

1.2.1 Introduction to heat treatment furnaces

Heat transfer is involved in several physical processes, and in actual fact it can be the limiting factor for many processes. The modelling of heat transfer effects inside industrial furnaces has started drawing attention to many more investigators as a result of the demand for energy conservation through efficiency improvement and for reduction of pollutant emissions. It has also become even more important in the design of the products itself in many areas such as the electronics, automotive, machinery and equipment manufacturing industries. Research in both experimental and numerical areas and through mathematical models has proven to be effective in accelerating the understanding of complex problems as well as helping decrease the development costs for new processes. In the past, the optimizations and savings in large productions were made by only large companies that could support and afford the cost of sophisticated heat transfer modelling tools, specialized engineers and computer software. Nowadays, modelling has turned out to be an important element of research and development for several industrial and realistic models of complex structure of the furnace that can be feasible on a personal computer. A direct fire flow furnace is a manufacturing process to control the physical and mechanical properties of the product components. It involves conduction within the load, un-

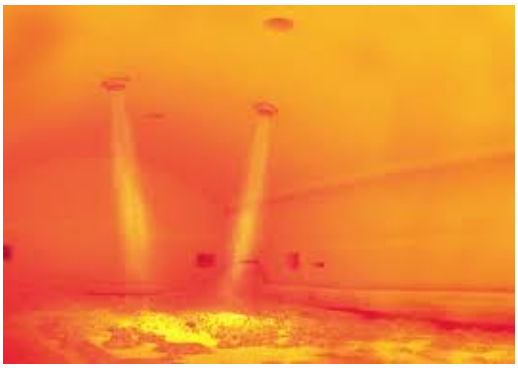

(a) Direct fired furnace [62]

(b) Furnace with regenerative burners[3]

Figure 1.2: An illustration of mixed convection-radiation transfer of heat.

steady flows, furnace control, convection and thermal radiation simultaneously. The thermal history of each part and the temperature distribution in the whole load are critical for the final microstructure and the mechanical properties of structure and can directly determined the final quality of parts in terms of hardness, toughness and resistance. Figure 1.2 illustrates two types of industrial fire furnaces. To achieve higher treatment efficiency, the major influencing factors such as the design of the furnace, the location of the workpieces, thermal schedule and position of the burners should be understood thoroughly. The damage to the global environment and the prospective depletion of essential resources caused by growing human activity constitute a dual challenge that calls for coordinated measures by multilateral organizations. Since simulation of the heat flow for treating the structure inside the furnace is of great importance for the control and prediction of the ultimate microstructure of the structure but specially the reduction of both pollutant emissions and energy consumption.

1.2.2 Role of computational modelling in heat furnace design

As mentioned previously, the major factor to be considered in the working of a furnace is the heat transfer by all the modes, which occur simultaneously. To either study a new furnace or to optimize the heating process in existing ones, the heat transfer in the furnace has to be modelled in the same way of a real situation as closely as possible. Given the geometry of the furnace, different boundary conditions along the furnace length, gas composition and properties and other complexities, an analytical solution is not feasible and computational modelling has to be carried out. Over the last 20 years, the CFD has gained its reputation of being an efficient tool in identifying and solving such problems. Modelling the heating process involves solving coupled heat transfer equations. By solving them computationally, the technique should be able to do so in a precise mode and within a reasonable computational time. Heat transfer and treatment that take place inside the furnace are conduction, convection, radiation, furnace control and turbulent flow. Conduction mainly exists in structure materials. Unsteady convection occurs between the solid materials and heat flow surrounds them and the surface furnace walls that are in direct contact to the heat flow. Radiation exists when the heat flow that transfers inside the geometry of the furnace.

[3] www.linde-gas.com/en/industries/glass/glass_melting/glass_melting.html

1.3 Modelling heat transfer

We give a review on modelling process for transient heating in heat furnaces, a brief review will be presented here. Different methods and models have been used and each model can be characterized upon the assumptions made. Numerous practical methods and models for the prediction of thermal heating process have been developed and applied to various different furnace geometries. For a complete description about computational modelling of heat transfer in reheat furnaces, we refer to [48]. In [115], authors modelled combustions chambers and furnaces using the composite-flux radiation model. The heat transfer was modelled by [72] using some empirical relations in both the pusher-type and walking beam furnaces. Only radiation was considered and convection was neglected. In [101], authors showed by studying walking beam furnaces that the convective heat transfer coefficient changes very little along the furnace. In [149], researchers investigated the effects of non-gray combustion products using the zone method proposed by [50]. This method was used for absorbing, emitting and non-scattering homogeneous gas to predict radiative heat transfer in a reheating furnace. The zonal energy balance method was used to compute the gas temperature. However, it was stated that the coupling of the temperature distribution in the load and refractories with heat transfer from the combustion gases was not accurate. In the work of [39], passive experiments were conducted as an addition to a statistical mathematical model, monitoring the dimensions of the load, speed of movement and thermocouple readings. Authors found out that by considering only a uniform continuous entry of inclusion into the furnace and by assuming that the temperature of the furnace atmosphere was constant in a zone, good results can be obtained. In [16], Researchers developed a simplified model capable of determining detailed temperatures profiles in the load for a continuous reheating furnace. This model consists in computing the gas temperature as a function of the distance through the furnace. The mean-beam length technique was used to compute the radiation effects using the gray model assumption for gases. In [89], investigators developed a mathematical model for predicting steadystate heat transfer. The radiation effects were computed using the zone method while transient 2D conduction equation was solved to compute the temperature profiles in the slab. Researchers pointed out that the computing cost of the zone-method is too expensive and should be replaced.
In [126], Authors developed a model of an indirectly fired continuous furnace capable of predicting the fuel consumption. The radiation heat transfer was calculated using the radiosity method assuming that the gases are a non-participating medium. A 1D model was used for the conduction in the solid. A mathematical system model for modelling direct fired continuous reheat furnaces was developed in [16]. The convective heat-transfer rate to the refractory and load surfaces was calculated utilizing existing correlations from the literature. The zone approach was applied to compute the radiation heat exchange between the combustion gases, the refractory and the load. A parametric research was also obtained to study the effects of refractory emissivities, the load and the height of the combustion area on the thermal performance of the continuous reheating furnace. In [8], testers developed an interesting simplified approach for on-line temperature control of a pusher type furnace. The temperature was computed in the longitudinal section of each bloom inside a long-furnace type. An implicit FDM was used to solve the convection heat transfer and a zonal method was applied to calculate the radiation effects. In [96], analysts developed a simplified on-line model for controlling a rotating reheat furnace. The radiation effects between individual load segments and between the burners and the load as well as the convection were neglected. In [4], scientists developed both off-line and on-line models of the pusher-type and walking beam furnaces. The problem was divided into the load problem and the radiation problem for the purpose of analysis. The

zonal method was used to calculate the radiation heat transfer and a finite volume approach was used to calculate the conduction heat transfer in the load. In [49], a computational model was developed for predicting the heat transfer in a direct-fired pusher type reheat furnace. The FVM was used to compute the gas radiative heat transfer. Recently, a mathematical model was developed in [67] for predicting the temperature distribution inside the slab and the radiative heat flux impinging on its surface. The furnace is modelled as radiating medium with constant absorption coefficient and spatially varying temperature.

1.4 Challenges and novelty

Developing a method gives rise to a class of computational challenges related to the heat flow problems/subproblems. The behaviour of the flow depends very much on the geometry of the application and location of the inclusion. Non-uniform temperature distribution is the result of the fluid mechanics forces applying on the structure. From the mathematical point of view, heat flow problem may be characterized as follows. The system of differential equations and boundary conditions related to the medium. Main challenges that can be addressed in this field of study are: (1) difficulty to handle vast rotations or/and translations which results in very distorted elements and consequently inaccurate outcomes, (2) difficulty in using Lagrangian multipliers to put in weak form which results in a force distribution which leads to inaccurate computational results when computing the pressure and velocity gradient, (3) the partial integrated elements can be very small which leads to inaccuracies, (4) difficulty to set onto the Cartesian grid on the boundary conditions that are required to solve the flow equations. Not to mention, it is difficult to enforce the effect of the physical boundary conditions on the solution of the flow which is computed on the Cartesian grid, (5) an increase in computational costs as well as inaccurate results. For instance due to velocity interpolation, (6) the sparsity patterns are very unstructured in 2D. Hard to deal with a dominant convection term in the governing equations, (7) the approximation of the functions that approximate the solution can not be easily made of higher order. Also, it is challenging sometimes when dealing with incompressible fluids.
We propose a research on developing a technique based on mixed FEM that can deal with and solve the mentioned research challenges while acquiring the research novelties. Mixed FEM is considered as it has been proven to produce the most desirable results [137, 138]. Two main advantages of mixed models are the relaxation of continuity requirements on the interpolation functions. Linear triangular elements (three nodes) are taken into consideration for the pressure and quadratic triangular elements (six nodes) are taken into account for the temperature and velocity. This technique allows us to solve the Navier-Stokes equations instead of interpolating lower degrees functions. Another requirement is for dealing with the instabilities associated with Galerkin formulation of the challenge. This is due to the fact that the presence of the advection terms in the governing equations can result in node-to-node oscillations mainly in the velocity field. This kind of oscillations become more apparent for advection-dominant (e.g. at high Reynolds number). To predominant this challenge, split method is considered which is done by solving the convection term first then the diffusion term. This allows large time steps to be utilized in the numerical simulations without loosing in accuracy and lead to a great improvement in efficiency. The method provides a consistent framework for conserving mass and general boundary conditions. Motivated by this method in its applications to the Navier-Stokes equations [117], we carried out our research on using characteristics technique and the Taylor-Hood finite element. Another consideration is that the incompressible fluid. This is

due to the fact that the change in density with pressure is very small as to be negligible. This is because of the fluid flows in large volume domains that makes the pressure variation very small as compared with the absolute pressure (low Mach number). Furthermore, Boussinesq approximation is required to restrict the analysis of our system whose background density and temperature do not vary much over their mean values. Likewise, the Crank-Nicolson method time discretization is considered as it is unconditionally stable and has higher order of accuracy. Due to the high temperature that takes place, radiation is the dominant mode inside the investigated domains. The SP_N approximations are considered as they offer the possibility of improved accuracy relative to diffusion by capturing some transport effects while still preserving many of the features that make diffusion solvers attractive. The SP_N models approximate the full radiative transfer equation with less computational cost and give results which are more accurate than those obtained by the classical Rosseland approach traditionally used by physicists [103].
In this work, a developed approach to design a model for simulating the heat flow is carried out. A new high level programming interface which leads to improve and increase flexibility with respect to the functionality are investigated and applied. It provides all necessary implementations in a clear and dynamical configurable way. A complete set of algorithms for the heat flow governing equations are integrated and applied on different applications for the first time. Finally, a set of validation scenarios are computed to validate the chosen approach and implemented features, ranging from academic benchmarking scenarios to two-dimensional realistic application scenarios with engineering relevance.

1.5 Objectives of the thesis

The main objectives of this research are: (1) to determine the relative importance of radiation and natural convection in a small enclosure with inclined angles and with/without heating element inside the enclosure, and (2) to estimate the natural convection-radiation heat transfer characteristics. Interaction between natural convection and radiation is carried out using temperatures and heat transfer relations (e.g. Nusselt and Rayleigh numbers) in order to predict the heat flux contribution. Fully developed model is used to perform the numerical calculations used to estimate the bulk natural convection and radiation heat transfer as well as to estimate the convective-radiative heat transfer behaviour. The resulting data and analyses are used to determine the effect of heat transfer mode and adjusting certain heat transfer characteristics.
As explained previously, heat treatment represents a critical step within the steel/glass making process. It can be defined as a combination of heating and cooling operations applied to a structure in solid state which controls its mechanical properties, therefore contributes to the product quality in terms of hardness, resistance and toughness. Therefore, the objective of the proposed project is to develop a computational methodology able to predict the furnace atmosphere as well as the transient heat transfer to the load in a continuous heat treatment process. This can help to: (1) improve the structure quality, (2) increase furnace lifetime, (3) possibility to select desired number of burners (not limited by breast wall space) and (4) cost reduction of the structure annealing/bending or manufacturing processes.
Due to the complexities of the physics that may occur for such applications, many mathematical models have been proposed over the past years. Of course this complexity has decreased with the available computing power but most of the time, the general idea of these models was to solve only for heat convection and radiation within the load and employ different assumption and simplification about the surrounding gas temperature within the furnace using

different heat transfer characteristics inspired from known furnaces or previous experimental works [31, 17, 152]. Additionally, in recent years, different environmental constrained pushed the industrials to change their previous regulations. Consequently, many experimental tests must be made to deduce such transfer characteristics that ensure both the convective and radiative effects on and from the treated solid. However, when dealing with a large diversity of shapes, dimensions and physical properties of these structures to heat or to quench, such operations can become rapidly very costly and time consuming.
The development of efficient methods to understand and simulate heat flow for multi-components systems (fluid-solid) is then highly demanded. In recent years, there has been increasing interest in studying numerically a variety of engineering applications that involve such coupling (fluids-solids) [51, 29, 123]. Typically, the general idea of these techniques consists in dividing the global domain and solving on each subdomain the corresponding equation independently. The global solution can then be constructed by suitably constructing local solutions from individually modelled subdomains. However, during the assembly, the coordination between the meshes can become complicated or even sometimes not feasible. Other alternative approaches have been applied for multi-phase flows problems and are available in the literature, such as the ghost fluid method introduced by [28], the immersed boundary method [116], the domain decomposition [129], the Extended Finite Element Method (X-FEM) [136]. They introduced and improved enrichment functions for material interfaces and voids by means of the level set representations of surfaces. Nevertheless, in general when using all these techniques, one still needs to know the value of the heat transfer coefficients between the two domains which ensures, as a Neumann/Dirichlet boundary conditions, the heat exchange at the air/solid interface. The main objective of this work aims to overcome this drawback and to present a multidomain approach to solve the heat flow for which the two modes, convective and radiative heat transfer interfere simultaneously and in the fluid part in order to maintain the required temperature distribution over the entire structure surface. The proposed numerical method for modelling such multimaterial flows is referred as the Taylor-Hood FEM. When dealing with this kind of study, this method was proven to be the best and the closest to the experimental results [137, 138]. A full description and details about this method is given in this thesis.
To complete, the two-dimensional FEM needed for solving the transient heat transfer and heat flow inside the furnaces must be capable of taking into account also the proposed thermal coupling. Therefore, the first part of the thesis consists in developing different numerical methods for modelling the heat transfer and heat flow. At the burners level and inside the domain, it is well known that for convection-dominated problems, spurious oscillations may appear in the standard finite element resolution of the advection-diffusion equations. In order to overcome this numerical difficulty, stabilized finite element methods are presented, such as mixed Galerkin-characteristics finite element methods. A new approach is presented to obtain stabilized finite element formulation that ensures an oscillation-free solution and treats the thermal shocks. The velocity and the pressure fields are computed by solving the Navier-Stokes equations coupled to heat equations. An extension of this solver is studied, analyzed and added to take into account the convection/radiation terms for simulating heat flow at the chosen Reynolds numbers. The work mainly involves the implementation studying heat flow inside the direct fired furnace under the operation of different burners. Two furnaces are examined in this study, direct fired as well as furnaces with regenerative burners. All the numerical results obtained for benchmark problems are compared with other numerical models and analytical solutions for validation purposes [37]. This will be the subject of the last part where also several industrial applications will be presented. To summarize, the originality of this work is that

the combination of stabilization methods, unstructured meshes, transient flows, heat transfer and radiation models in a multidomain approach. All the mentioned elements represent the features dedicated to industrial abilities of the method. The main tasks within this thesis are:

- The establishment of physics-mathematical models for temperature and heat transfer analysis during a continuous heating inside the furnace. This is mainly include a heat flow model, and heat radiation/convection model in a multi-domain approach.
- The development of a numerical calculation method for estimating the temperature distributions in the furnace and workpieces by using stabilized finite element methods, under a specified furnace geometry, thermal schedule, performance requirements and initial operation conditions.
- Finally, the development of a model, which will provide an interface for the information input of the furnace, workpieces, thermal and physical properties, and initial operation conditions that are used in the simulation.

Another encouraging point for serving the industry is the establishment of such user friendly interface. The thesis is built not only on the idea of offering accurate results for the heat furnace treatment but also in answering all the industry needs in a fully novel and developed study. Here is a list of some industrial demands.

- Accurate prediction of temperature profiles in the furnace chamber.
  - Temperature capturing at different positions (walls, corners...).
  - Temperature capturing at the surface of the inclusion.
  - Capable of handling multiple parts in two-dimensional simulations.
- Ability to simulate various configurations.
  - Ability to arrange or randomly distribute loaded parts.
  - Simulating different thermal timing.
  - Ability to insert or remove ingots at any time during the simulation.
- Facility to calculate important terms such as:
  - The heat losses from the furnace.
  - The heat and energy required for the load under different conditions.
  - The heat stored in the furnace or in the load as a function of time.
- Ability to adjust the heat flow.
  - Turning on or cutting off some burners during the simulation.

1.6 Layout of the thesis

This thesis is divided into six chapters. Chapter 1 introduces problems and challenges related to forced and natural convection-radiation heat transfer and provides some realistic applications related to the topic considered. A literature review is given thoroughly to provide ideas and information on the models and computational tools related along with the methods used

in the previous simulation experiments. Inspired from the literature review, goals, challenges and novelties are formally stated to overcome and cover the difficulties explained. Chapter 2 summarizes the strategy required to choose the governing equations of the radiative transfer. Certain methods and algorithms are adopted and a full comparison is considered in order to examine the efficiency and the accuracy of the methods chosen. The obtained results inspired us to choose the considered simplified P_N approximations instead of solving the full radiative transfer that can be computationally expensive and costly. Chapter 3 gives a detailed description of the formulations of the method of simplified P_N approximations that lead to the chosen simplified radiative governing equations. A detailed SP_1 and the novel SP_3 derivations are given with the required boundary conditions for the first time in this study to deal with natural as well as forced convection-radiation heat transfer. Chapter 4 shows the model geometries, dimensional and non-dimensional governing equations, the SP_N formulations, time stepping, finite element and the computational procedure needed to solve the natural convection-radiation problems for the first time with different computational arrangements. The obtained novel results are validated with various results from the literature and with several experimental and computational comparisons. Natural convection-radiation heat behaviour is studied and adjusted by adjusting the related heat transfer characteristics inside various geometry conditions. Chapter 5 is devoted to the forced convection-radiation heat flow that takes place inside a direct fired furnaces and its conducted results from this novel study along with the validations of the obtained results with the available results from the literature. Different furnace operations and types are examined with different heat transfer arrangements in order to predict and investigate the unsteady heat flow at different locations inside the furnaces. Convection versus radiation effects are investigated in details under various heat transfer scenarios that are inspired from the realistic operations of industrial furnaces. The conclusions and the future extension for future directions of the present work that might take place inside the same chosen applications and/or different engineering applications are included in chapter 6.

Chapter 2

Numerical methods for radiative transfer

In this chapter, we present thorough numerical techniques for solving the two-dimensional RTE. Diamond differencing is used for space discretization. For angle collocation, discrete ordinates approach is accounted for angle collocation. The result is producing a system of sparse matrices in which the RTE is turned into. The source iteration, Biconjugate Gradient Stabilized (BICGSTAB) and Generalized Minimal Residual (GMRES) algorithms are formulated in order to solve the final system. Two numerical examples are utilized for showing the robustness, convergence rates and efficiency of the chosen methods.

The problem of non-energetic Neutron transport in a certain material surrounded on all sides by vacuum can be formulation by the following integro-differential equation

$$\begin{aligned} \frac{1}{c}\frac{\partial I}{\partial t} + \Omega \cdot \nabla I + (\sigma + \kappa) I &= \frac{\sigma}{4\pi}\int_{S^2} I(t, \mathbf{x}, \Omega') d\Omega' + q(t, \mathbf{x}, \Omega), \quad \text{in} \quad [0, T) \times \mathcal{D} \times S^2, \\ I(t, \mathbf{x}, \Omega) &= g(t, \mathbf{x}, \Omega), \qquad \text{on} \quad [0, T) \times \partial\mathcal{D}^- \times S^2, \\ I(0, \mathbf{x}, \Omega) &= I_0(\mathbf{x}, \Omega), \qquad \text{in} \quad \mathcal{D} \times S^2. \end{aligned} \tag{2.1}$$

Here, $\mathcal{D}$ is a space domain with smooth boundary $\partial\mathcal{D}$, $[0, T)$ is a time interval and the unit sphere is S^2. Here, $I(t, \mathbf{x}, \Omega)$ is the angular flux at time t and the location of point $\mathbf{x} := (x, y, z)^T$ in the orientation $\Omega := (\mu, \xi, \eta)^T$ with fixed speed c, $\sigma := \sigma(t, \mathbf{x})$ is the scattering cross-section, $\kappa := \kappa(t, \mathbf{x})$ is the absorption cross-section, and $q(t, \mathbf{x}, \Omega)$ is an external source. In (2.1), $g(t, \mathbf{x}, \Omega)$ and $I_0(\mathbf{x}, \Omega)$ are known boundary and initial functions, respectively. σ and κ are assumed to be non-negative functions. We define the boundary region $\partial\mathcal{D}^-$ as

$$\partial\mathcal{D}^- := \big\{\mathbf{x} \in \partial\mathcal{D} | \quad \mathbf{n}(\mathbf{x}) \cdot \Omega < 0\big\}, \tag{2.2}$$

where $\mathbf{n}(\mathbf{x})$ is the outward normal at the point $\mathbf{x}$ on $\partial\mathcal{D}$. Despite the linear equation (2.1), computing its numerical solution is inconsiderable because of:

1. The vast number of dependent unknowns. The solution I in (2.1) in general is a function of eight independent variables, three variables (μ, ξ, η) for the angle, three space variables (x, y, z), and one variable for time t. The computational cost and the memory requirements become drastically immense after discretization of these variables. Due to these challenges, severe restrictions on computational approaches for solving (2.1) are imposed.

2. In the RTE (2.1), the solution is not a smooth function of the dependent variables $(t, \mathbf{x}, \Omega)$. Shock discontinuities as well as steep fronts can arise. This needs to be resolved accurately in engineering applications and often can cause severe numerical challenges.

3. In equation (2.1), it is clearly known that the behaviour changes from a certain physical situation to another. For instance, the equation (2.1) behaves like elliptic for steady-state case in optically dense region, a parabolic for time-dependent case and a hyperbolic in void-like regions. It is extremely difficult to construct an unified computational algorithm that can be able to resolve accurately all the mentioned behaviour cases.

For physical interest, we define an optical coefficient ϑ and a scattering ratio γ associated to the equation (2.1) as

$$\gamma := \max_{\mathbf{x}\in\mathcal{D}}\left(\frac{\sigma(\mathbf{x})}{\sigma(\mathbf{x})+\kappa(\mathbf{x})}\right), \qquad \text{and} \qquad \vartheta := \min_{\mathbf{x}\in\mathcal{D}}\Big(\sigma(\mathbf{x})+\kappa(\mathbf{x})\Big)\mathrm{diam}(\mathcal{D}), \tag{2.3}$$

respectively. In (2.3), $\mathrm{diam}(\mathcal{D})$ is the space domain diameter $\mathcal{D}$. Two extreme situations in computational RT remain active field of research

1. $\gamma = 1$, pure scattering, no absorption ($\kappa = 0$),

2. $\vartheta \gg 1$, optically thick, dense absorption ($\kappa \gg 1$),

and the conventional methods suffer some difficulties to solve accurately these two cases as mentioned in [2, 3, 87]. The two-dimensional version of (2.1) is considered for simplicity in this chapter. Thus, $\mathcal{D} \subset \mathbb{R}^2$, $\mathbf{x} := (x, y)^T$ and $\Omega := (\mu, \eta)^T$. By introducing the scalar flux ϕ

$$\phi(\mathbf{x}) := \frac{1}{4\pi}\int_{S^2} I(\mathbf{x}, \Omega')d\Omega', \tag{2.4}$$

the two-dimensional time-independent RTE reads

$$\begin{aligned} \mu\frac{\partial I}{\partial x} + \eta\frac{\partial I}{\partial y} + (\sigma+\kappa)I &= \sigma\phi(x,y) + q(x,y,\mu,\eta), \quad \text{in} \quad \mathcal{D}\times S^2, \\ I(x,y,\mu,\eta) &= g(x,y,\mu,\eta), \qquad\qquad \text{on} \quad \partial\mathcal{D}^-\times S^2. \end{aligned} \tag{2.5}$$

The aim of this chapter is to give a detailed overview on the quality and efficiency of classical and modern algorithms in computational radiative transfer. At first we will show the way of discretizing the equation (2.5) in space and angle. By the example of discrete ordinates and Diamond difference methods, we will demonstrate how to develop iterative solvers for the fully discrete system. Many studies of these solvers have been done in variety of references [2, 3, 87, 119, 118, 13, 6]. This chapter contains several approaches to the construction of a suitable algorithm which can serve as solver for the general RTE (2.1). The easiest possibility is the use of Richardson iteration known by astrophysicists as γ-iteration. This strategy has been theoretically analysed in details in [2, 87]. Another basic solver is the P_1/Diffusion approach, which means the equation (2.1) is replaced by a scaled diffusion problem such that at the limit tends to approximate the solution of (2.1). Generalized P_1/Diffusion and other simplified P_N approximations have been introduced in [79, 81, 146]. Iterative solvers for linear systems based on Krylov subspace methods like the BICGSTAB [150] or GMRES [131] are also implemented in this chapter. Generalizing the idea of constructing preconditioner for an accelerated γ-iteration we show how to use the P_1/Diffusion approach as an optimal preconditioner for a

given γ-iteration. The resulting solver known as diffusion synthetic acceleration was introduced in [3] and studied from a linear algebra point of view in [13, 6]. Finally we apply these solvers to various test cases from RT problem. Dependent on the scattering ratio γ and the optical coefficient ϑ of the problem under consideration, the most suitable solver in terms of accuracy and computing cost can be identified.
This chapter is organized as follows. In section 2.1, a full description to the approach of discrete ordinates is introduced. In section 2.2, a space discretization based on volume controls and cell averaging is proposed. Section 2.3 describes the numerical techniques for solving the linear system. Diffusion synthetic acceleration method is formulated in section 2.4. Finally, numerical examples are discussed in section 2.5. Conclusions are clarified in section 2.6.

2.1 Discrete ordinates method

In order to solve a variety of basic problems accurately in the field of heat radiation, discrete ordinates approach was introduced and used in [15]. This is done by the replacement of some of the integral terms in the Boltzmann equation by numerical quadrature approximations of those terms. The resulting set of ordinary differential equations is then solved. In much of the literature [15, 119, 118, 87] the discrete ordinate method is detailed only for the one-dimensional slab geometry case and the theoretical results remain valid for the multi-dimensional cases. In the current section we formulate this technique for the two-dimensional model (2.5). A standard approach for the integral expression over the unit sphere S^2 in (2.12) is the quadrature rule of the form

$$\int_{S^2} I(\mathbf{x}, \Omega')d\Omega' \simeq \sum_{l=1}^{\bar{N}} \omega_l I(\mathbf{x}, \Omega'_l), \tag{2.6}$$

in which $\Omega'_l := (\mu_l, \xi_l, \eta_l)^T$, for $l = 1, 2, \ldots, \bar{N}$, with $\bar{N} = n(n+2)$, and n is the number of directions cosines. Because $\Omega'_l \in S^2$, we have

$$\mu_l^2 + \xi_l^2 + \eta_l^2 = 1, \qquad \text{for all} \quad l = 1, 2, \ldots, \bar{N}.$$

n is assumed to be an even number of quadrature points. For this assumption, the points (μ_l, ξ_l, η_l) are nonzeros, symmetric about the origin, and

$$\mu_l^2 = \mu_1^2 + 2\frac{l-1}{n-2}(2 - 3\mu_1^2). \tag{2.7}$$

For the weights ω_l we assume all are positive which satisfy

$$\sum_{l=1}^{\bar{N}} \omega_l = 4\pi, \quad \sum_{l=1}^{\bar{N}} \omega_l \mu_l = 0, \quad \sum_{l=1}^{\bar{N}} \omega_l \xi_l = 0, \quad \text{and} \quad \sum_{l=1}^{\bar{N}} \omega_l \eta_l = 0. \tag{2.8}$$

A simple way to guaranty the conditions (2.8) is to set all weights positive and equal to $\frac{4\pi}{\bar{N}}$. Note that the approximation (2.6) can be derived using the spherical coordinates. If the direction vector $\Omega := (\sin\varphi\cos\theta, \sin\varphi\sin\theta, \cos\varphi)^T$, then

$$\int_{S^2} I(\mathbf{x}, \Omega')d\Omega' = \int_0^{\pi}\int_0^{2\pi} I(\mathbf{x}, \theta', \varphi')d\theta' \sin\varphi' d\varphi'.$$

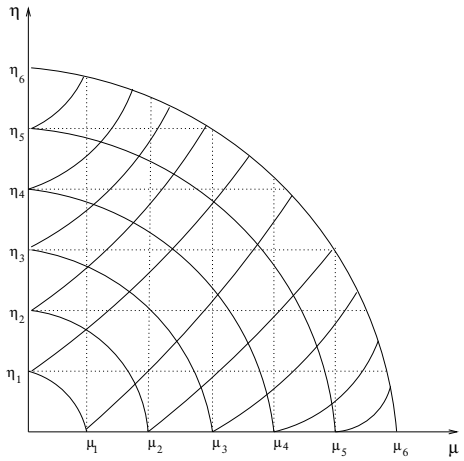

Figure 2.1: The S_{12}-direction set for the two-dimensional problems of a quarter of sphere.

The trapezoidal rule for each one-dimensional integral separately yields

$$\int_0^{\pi}\int_0^{2\pi} I(\mathbf{x},\theta',\varphi')d\theta'\sin\varphi' d\varphi' \simeq \sum_{l=1}^{L}\sum_{k=1}^{K} w_{lk} I(\mathbf{x},\theta_l,\varphi_k), \tag{2.9}$$

where the quadrature weights

$$w_{lk} = \frac{\pi}{2LK}\sin\varphi_l.$$

By taking the sum over k in w_{lk}, the expression (2.9) is equivalent to the quadrature rule (2.6) with

$$\omega_l = \sum_{k=1}^{K} w_{lk}, \quad \text{and} \quad \bar{N} = LK.$$

Other methods to discretize the unit sphere S^2 are the so-called S_n-direction sets. A review dealing with the S_n sets can be found in [32], and a comparison between different S_n sets for radiative transfer has been done in [43]. These S_n sets satisfy the conditions (2.7) and (2.8). Furthermore, they are arranged on $n/2$ levels, invariant under 90° rotations, and they have equal positive weights, see Figure 2.1 for an illustration of S_{12} set in two-dimensional case. Here, the direction ξ is omitted. Let $S_{\bar{N}}$ be a chosen set of discrete directions in the unit sphere S^2, then the two-dimensional direction set is just the simplification of one direction in $S_{\bar{N}}$ such that the simplified set is symmetric, has nonzero direction, and with positive weights. Hence a semi-discrete formulation of the RTE (2.5) is given by

$$\begin{aligned} \mu_l\frac{\partial I_l}{\partial x} + \eta_l\frac{\partial I_l}{\partial y} + (\sigma+\kappa)I_l &= \sigma\phi(x,y) + q_l(x,y), \quad \text{in} \quad \mathcal{D}\times S_{\bar{N}}, \\ I_l(x,y) &= g_l(x,y), \qquad\qquad \text{on} \quad \partial\mathcal{D}^-\times S_{\bar{N}}, \end{aligned} \tag{2.10}$$

where $I_l(x,y)$, $q_l(x,y)$ and $g_l(x,y)$ are discrete approximations to $I(x,y,\mu_l,\eta_l)$, $q(x,y,\mu_l,\eta_l)$ and $g(x,y,\mu_l,\eta_l)$, respectively. Note that the angular discretization (2.10) transforms the original integro-differential equation (2.5) into a system of $\bar{N}$ coupled differential equations.

Remark 1 One of our favourite S_n-direction set is the C-60 known as buckyball in [18]. the set contains 60 equal weighted directions with high symmetry configuration. The C-60 set is reproduced in Table 2.1. In our numerical examples we used others S_n sets but the C-60

yields the best results. However, the main disadvantage using these sets is we can not refine the ordinates within the same set as we can do using the usual trapezoidal or Gauss quadrature rules.

2.2 Space discretization

In general, applying discrete ordinates method is done by combining it with spectral methods, finite elements or finite differences. In [13], the author combines the Petrov-Galerkin method with the discrete ordinates collocation for the RTE (2.1). Since it is easier to combine the upwinding with finite volume discretization than other methods, we consider in these notes a space discretization based on volume control and cell averaging. The space domain is assumed to be a rectangle for simplicity, $\mathcal{D} := [a, b] \times [c, d]$. Thus the numerical grid is determine by

$$\mathcal{D}_h := \Big\{ \mathbf{x}_{ij} = (x_i, y_j)^T, x_i = i(\Delta x)_i, y_j = j(\Delta y)_j, i = 1, 2 \ldots, N, j = 1, 2 \ldots, M \Big\},$$

$x_0 = a, x_N = b$, $y_0 = c, y_M = d$, and h is the maximum cell size $h := \max_{ij}\big((\Delta x)_i, (\Delta y)_j\big)$. We define the averaged grid points as

$$(\Delta x)_{i+\frac{1}{2}} := x_{i+1} - x_i, \quad (\Delta y)_{j+\frac{1}{2}} := y_{j+1} - y_j, \quad x_{i+\frac{1}{2}} := \frac{x_{i+1} + x_i}{2}, \quad y_{j+\frac{1}{2}} := \frac{y_{j+1} + y_j}{2}.$$

The notation f_{ij} is used for denoting the estimated value of the function f which is located at the grid point (x_i, y_j). Utilizing the semi-discrete formulation (2.10), a fully discrete approximation for the equation (2.5) can be directly written as

$$\begin{aligned} \mu_l \frac{I_{l,i+1j} - I_{l,ij}}{(\Delta x)_{i+\frac{1}{2}}} + \eta_l \frac{I_{l,ij+1} - I_{l,ij}}{(\Delta y)_{j+\frac{1}{2}}} \quad + \quad & \big(\sigma_{i+\frac{1}{2}j+\frac{1}{2}} + \kappa_{i+\frac{1}{2}j+\frac{1}{2}}\big) I_{l,i+\frac{1}{2}j+\frac{1}{2}} = \\ & \sigma_{i+\frac{1}{2}j+\frac{1}{2}} \phi_{i+\frac{1}{2}j+\frac{1}{2}} + q_{l,i+\frac{1}{2}j+\frac{1}{2}}, \end{aligned} \tag{2.11}$$

where the cell averages of I are given by

$$\begin{aligned} I_{l,i+1j} &= \frac{1}{(\Delta x)_{i+\frac{1}{2}}} \int_{y_j}^{y_{j+1}} I_l(x_i, y) dy, \\ I_{l,ij+1} &= \frac{1}{(\Delta y)_{j+\frac{1}{2}}} \int_{x_i}^{x_{i+1}} I_l(x, y_j) dx, \\ I_{l,ij} &= \frac{1}{(\Delta x)_{i+\frac{1}{2}} (\Delta y)_{j+\frac{1}{2}}} \int_{x_i}^{x_{i+1}} \int_{y_j}^{y_{j+1}} I_l(x, y) dx dy. \end{aligned} \tag{2.12}$$

To approximate the fluxes (2.12), we employ the well known Diamond difference approach which consist on centred differences and the approximation of the function values at the cell centers by the average of their values at the neighbouring nodes. See Figure 2.2 for an illustration of the grids used in these notes. Bilinear interpolation is accounted for the approximation of the function value of $f_{i+\frac{1}{2}j+\frac{1}{2}}$ at the cell center

$$f_{i+\frac{1}{2}j+\frac{1}{2}} = \frac{f_{ij} + f_{i+ij} + f_{ij+1} + f_{i+1j+1}}{4}. \tag{2.13}$$

Hence, the scalar flux $\phi_{i+\frac{1}{2}j+\frac{1}{2}}$ in (2.11) is given by

$$\phi_{i+\frac{1}{2}j+\frac{1}{2}} = \sum_{l=1}^{\bar{N}} \omega_l \frac{I_{ij} + I_{i+ij} + I_{ij+1} + I_{i+1j+1}}{4}.$$

Table 2.1: The C-60 directions set used in our numerical test problems.

l	μ_l	η_l	ω_l
1	-0.9642754578	-0.1716393065	0.2094395102
2	-0.9642754578	-0.1716393065	0.2094395102
3	-0.8987150765	0.1716393065	0.2094395102
4	-0.8987150765	0.1716393065	0.2094395102
5	-0.8331546952	0.5149179195	0.2094395102
6	-0.8331546952	0.5149179195	0.2094395102
7	-0.7926361513	-0.5149179195	0.2094395102
8	-0.7926361513	-0.5149179195	0.2094395102
9	-0.6865572261	-0.7270757700	0.2094395102
10	-0.6615153887	0.1716393065	0.2094395102
11	-0.6615153887	0.1716393065	0.2094395102
12	-0.5554364635	-0.5149179195	0.2094395102
13	-0.5554364635	0.7270757700	0.2094395102
14	-0.5554364635	0.7270757700	0.2094395102
15	-0.5554364635	-0.5149179195	0.2094395102
16	-0.4898760822	-0.1716393065	0.2094395102
17	-0.4898760822	-0.1716393065	0.2094395102
18	-0.4493575383	0.5149179195	0.2094395102
19	-0.4493575383	0.5149179195	0.2094395102
20	-0.3432786130	-0.9392336205	0.2094395102
21	-0.2777182317	0.9392336205	0.2094395102
22	-0.2777182317	0.9392336205	0.2094395102
23	-0.2121578505	-0.7270757700	0.2094395102
25	-0.1060789252	-0.1716393065	0.2094395102
26	-0.1060789252	-0.9392336205	0.2094395102
27	-0.1060789252	-0.9392336205	0.2094395102
28	-0.1060789252	-0.1716393065	0.2094395102
29	-0.0655603813	0.5149179195	0.2094395102
30	-0.0655603813	0.5149179195	0.2094395102
31	0.0655603813	-0.5149179195	0.2094395102
32	0.0655603813	-0.5149179195	0.2094395102
33	0.1060789252	0.1716393065	0.2094395102
34	0.1060789252	0.9392336205	0.2094395102
35	0.1060789252	0.9392336205	0.2094395102
36	0.1060789252	0.1716393065	0.2094395102
37	0.2121578505	0.7270757700	0.2094395102
38	0.2121578505	0.7270757700	0.2094395102
39	0.2777182317	-0.9392336205	0.2094395102
40	0.2777182317	-0.9392336205	0.2094395102
41	0.3432786130	0.9392336205	0.2094395102
42	0.4493575383	-0.5149179195	0.2094395102
43	0.4493575383	-0.5149179195	0.2094395102
44	0.4898760822	0.1716393065	0.2094395102
45	0.4898760822	0.1716393065	0.2094395102
46	0.5554364635	0.5149179195	0.2094395102
47	0.5554364635	-0.7270757700	0.2094395102
48	0.5554364635	-0.7270757700	0.2094395102
49	0.5554364635	0.5149179195	0.2094395102
50	0.6615153887	-0.1716393065	0.2094395102
51	0.6615153887	-0.1716393065	0.2094395102
52	0.6865572261	0.7270757700	0.2094395102
53	0.7926361513	0.5149179195	0.2094395102
54	0.7926361513	0.5149179195	0.2094395102
55	0.8331546952	-0.5149179195	0.2094395102
56	0.8331546952	-0.5149179195	0.2094395102
57	0.8987150765	-0.1716393065	0.2094395102
58	0.8987150765	-0.1716393065	0.2094395102
59	0.9642754578	0.1716393065	0.2094395102
60	0.9642754578	0.1716393065	0.2094395102

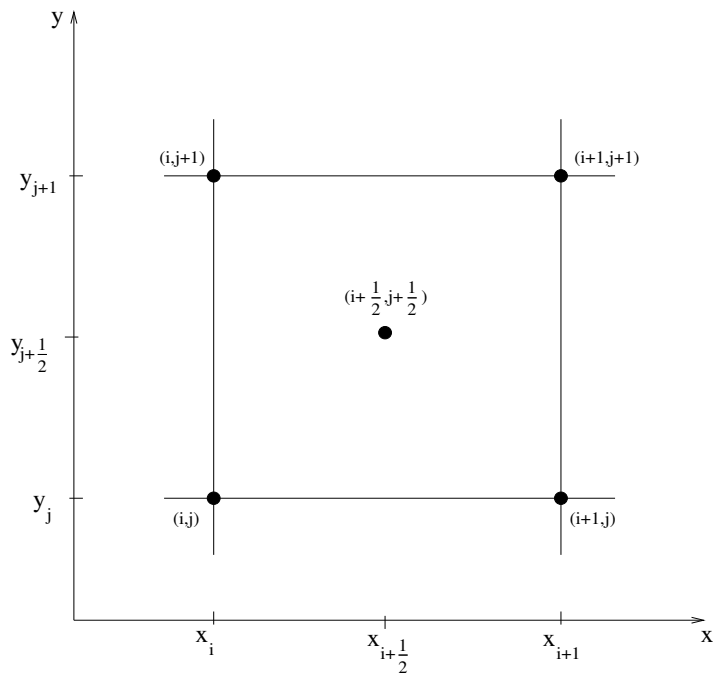

Figure 2.2: The staggered grid chosen for the space discretization.

We can proceed for the boundary conditions in (2.10) as follows:

- when $x = a$, the normal $\mathbf{n} = (-1, 0)^T$, then $\mathbf{n} \cdot \Omega_l = -\mu_l$, and for $\mu_l > 0$ we have $I_{l,0j} = g_{l,0j}$,
- when $x = b$, the normal $\mathbf{n} = (1, 0)^T$, then $\mathbf{n} \cdot \Omega_l = \mu_l$, and for $\mu_l < 0$ we have $I_{l,Nj} = g_{l,Nj}$,
- when $y = c$, the normal $\mathbf{n} = (0, -1)^T$, then $\mathbf{n} \cdot \Omega_l = -\eta_l$, and for $\eta_l > 0$ we have $I_{l,i0} = g_{l,i0}$,
- when $y = d$, the normal $\mathbf{n} = (0, 1)^T$, then $\mathbf{n} \cdot \Omega_l = \eta_l$, and for $\eta_l < 0$ we have $I_{l,iM} = g_{l,iM}$,

Remark 2 If the space domain $\mathcal{D}$ presents some points on the boundary $\partial\mathcal{D}^-$ where the normal is not unique (corners for example in the case of a rectangular domain) then, it is possible to define a new normal on those points with multiple components. For instance, at the left lower corner point $\mathbf{x} = (a, c)^T$ in the rectangle a new normal can be define as $\tilde{\mathbf{n}} = (-\frac{\sqrt{2}}{2}, -\frac{\sqrt{2}}{2})^T$, and for $\tilde{\mathbf{n}} \cdot \Omega_l = -\frac{\sqrt{2}}{2}\mu_l - \frac{\sqrt{2}}{2}\eta_l < 0$, we have $I_{l,00} = g_{l,00}$. Similar work can be done for other three remaining corners. The matrix entries are first defined for allowing us to get accurate linear algebra formulation as well as simplify the notation of (2.11) as:

$$
\begin{aligned}
d_{l,i+\frac{1}{2}j+\frac{1}{2}} &:= \frac{|\mu_l|}{2(\Delta x)_{i+\frac{1}{2}}} + \frac{|\eta_l|}{2(\Delta y)_{j+\frac{1}{2}}} + \frac{\sigma_{i+\frac{1}{2}j+\frac{1}{2}} + \kappa_{i+\frac{1}{2}j+\frac{1}{2}}}{4}, \\
\bar{e}_{l,i+\frac{1}{2}j+\frac{1}{2}} &:= \frac{|\mu_l|}{2(\Delta x)_{i+\frac{1}{2}}} + \frac{-|\eta_l|}{2(\Delta y)_{j+\frac{1}{2}}} + \frac{\sigma_{i+\frac{1}{2}j+\frac{1}{2}} + \kappa_{i+\frac{1}{2}j+\frac{1}{2}}}{4}, \\
\underline{e}_{l,i+\frac{1}{2}j+\frac{1}{2}} &:= \frac{-|\mu_l|}{2(\Delta x)_{i+\frac{1}{2}}} + \frac{|\eta_l|}{2(\Delta y)_{j+\frac{1}{2}}} + \frac{\sigma_{i+\frac{1}{2}j+\frac{1}{2}} + \kappa_{i+\frac{1}{2}j+\frac{1}{2}}}{4}, \\
e_{l,i+\frac{1}{2}j+\frac{1}{2}} &:= \frac{-|\mu_l|}{2(\Delta x)_{i+\frac{1}{2}}} + \frac{-|\eta_l|}{2(\Delta y)_{j+\frac{1}{2}}} + \frac{\sigma_{i+\frac{1}{2}j+\frac{1}{2}} + \kappa_{i+\frac{1}{2}j+\frac{1}{2}}}{4}.
\end{aligned}
$$

Define the vectors

$$\mathbf{I}_l \equiv \begin{pmatrix} I_{l,0} \\ \vdots \\ I_{l,M} \end{pmatrix} \in \mathbb{R}^{(N+1)(M+1)}, \quad \text{with} \quad I_{l,j} \equiv \begin{pmatrix} I_{l,0j} \\ \vdots \\ I_{l,Nj} \end{pmatrix} \in \mathbb{R}^{N+1},$$

$$\mathbf{\Phi} \equiv \begin{pmatrix} \Phi_{\frac{1}{2}} \\ \vdots \\ \Phi_{M-\frac{1}{2}} \end{pmatrix} \in \mathbb{R}^{NM}, \quad \text{with} \quad \Phi_{j-\frac{1}{2}} \equiv \begin{pmatrix} \phi_{\frac{1}{2}j-\frac{1}{2}} \\ \vdots \\ \phi_{N-\frac{1}{2}j-\frac{1}{2}} \end{pmatrix} \in \mathbb{R}^{N};$$

$$\text{and} \qquad \mathbf{Q}_l \equiv \begin{pmatrix} Q_{l,\frac{1}{2}} \\ \vdots \\ Q_{l,M-\frac{1}{2}} \end{pmatrix} \in \mathbb{R}^{NM}, \quad \text{with} \quad Q_{l,j-\frac{1}{2}} \equiv \begin{pmatrix} q_{l,\frac{1}{2}j-\frac{1}{2}} \\ \vdots \\ q_{l,N-\frac{1}{2}j-\frac{1}{2}} \end{pmatrix} \in \mathbb{R}^{N}.$$

Recall that the $S_{\bar{N}}$-direction set used for the discrete ordinates formulation (2.10) avoids the zero component in a given direction $\Omega_l = (\mu_l, \eta_l)$. So, only one of the four cases; $\mu_l < 0$ and $\eta_l < 0$, $\mu_l < 0$ and $\eta_l > 0$, $\mu_l > 0$ and $\eta_l < 0$, or $\mu_l > 0$ and $\eta_l > 0$ can hold. Here, we define the matrices $\mathbf{H}_l$ and $\mathbf{\Sigma}_l$ for the case $\mu_l < 0$ and $\eta_l < 0$, similarly, the other three cases can be derived,

$$\mathbf{H}_l \equiv \begin{pmatrix} D_l & \underline{\mathrm{E}}_l & & & \\ & \ddots & \ddots & & \\ & & D_l & \underline{\mathrm{E}}_l & \\ & & & D_l & S \\ & & & & S \end{pmatrix} \in \mathbb{R}^{(N+1)(M+1)\times(N+1)(M+1)}, \qquad \text{with}$$

$$D_l \equiv \begin{pmatrix} d & \bar{e} & & \\ & \ddots & \ddots & \\ & & d & \bar{e} \\ & & & 1 \end{pmatrix} \in \mathbb{R}^{(N+1)\times(M+1)}, \quad \underline{\mathrm{E}}_l \equiv \begin{pmatrix} \underline{\mathrm{e}} & e & & \\ & \ddots & \ddots & \\ & & \underline{\mathrm{e}} & e \\ & & & 1 \end{pmatrix} \in \mathbb{R}^{(N+1)\times(M+1)},$$

$$\text{and} \qquad \mathbf{S} \equiv \begin{pmatrix} 1 & 1 & & \\ & \ddots & \ddots & \\ & & 1 & 1 \\ & & & 1 \end{pmatrix} \in \mathbb{R}^{(N+1)\times(M+1)}.$$

$$\mathbf{\Sigma}_l \equiv \begin{pmatrix} \Sigma_{l,\frac{1}{2}} & & & \\ & \ddots & & \\ & & \Sigma_{l,M-\frac{1}{2}} & \\ & & & \mathbf{0} \end{pmatrix} \in \mathbb{R}^{(N+1)(M+1)\times NM}, \qquad \text{with}$$

$$\Sigma_{l,j} \equiv \begin{pmatrix} \frac{\sigma_{i+\frac{1}{2}j+\frac{1}{2}}+\kappa_{i+\frac{1}{2}j+\frac{1}{2}}}{4} & & \\ & \ddots & \\ & & \frac{\sigma_{i+\frac{1}{2}j+\frac{1}{2}}+\kappa_{i+\frac{1}{2}j+\frac{1}{2}}}{4} \\ & & 0 \end{pmatrix} \in \mathbb{R}^{(N+1)\times M}.$$

With these definitions, the equation (2.11) can be written in the unknowns I and $\mathbf{\Phi}$ as

$$\left(\begin{array}{ccc|c} \mathbf{H}_1 & & & -\Sigma_1 \\ & \ddots & & \vdots \\ & & \mathbf{H}_{\bar{N}} & -\Sigma_{\bar{N}} \\ \hline -\omega_1\mathbf{S} & \dots & -\omega_{\bar{N}}\mathbf{S} & \mathrm{I}_{NM} \end{array}\right)\left(\begin{array}{c} \mathrm{I}_1 \\ \vdots \\ \mathrm{I}_{\bar{N}} \\ \hline \mathbf{\Phi} \end{array}\right) = \left(\begin{array}{c} \mathbf{Q}_1 \\ \vdots \\ \mathbf{Q}_{\bar{N}} \\ \hline \mathbf{0} \end{array}\right), \tag{2.14}$$

where I_{NM} is the $N \times M$ identity matrix and $\mathbf{0}$ is the N null vector. The usual technique to solve the equation (2.14), is to eliminate the angular flux $\mathrm{I}_1, \dots, \mathrm{I}_{\bar{N}}$ using the Gaussian elimination. Therefore, the storage requirements is reduced and the resulting equation

$$\left(\mathrm{I}_{NM} - \frac{1}{4\pi}\sum_{l=1}^{\bar{N}} \omega_l \mathbf{S}\mathbf{H}_l^{-1}\mathbf{\Sigma}_l\right)\mathbf{\Phi} = \frac{1}{4\pi}\sum_{l=1}^{\bar{N}} \omega_l \mathbf{S}\mathbf{H}_l^{-1}\mathbf{Q}_l, \tag{2.15}$$

is solved for the scalar flux $\mathbf{\Phi}$, which does not depend on direction variables. Furthermore, solving (2.15) does not need to store the dense $NM \times NM$ schur matrix,

$$\mathcal{A} \equiv \mathrm{I}_{NM} - \frac{1}{4\pi}\sum_{l=1}^{\bar{N}} \omega_l \mathbf{S}\mathbf{H}_l^{-1}\mathbf{\Sigma}_l. \tag{2.16}$$

For instance, to apply this matrix to a given NM vector $\mathbf{U}$, only three NM vectors are needed. The first is used to store the product $\mathbf{U}$ by $\mathbf{\Sigma}_l$, in the second the solution of the linear system is stored with the matrix $\mathbf{H}_l$. Multiplying by $\mathbf{S}$ and subtracting the weighted resulting vector from $\mathbf{U}$ is stored in the third vector.
Since the key idea in all the incoming numerical methods dealing with the equation (2.15) is inverting the matrix $\mathbf{H}_l$ for $l = 1, \dots, \bar{N}$, we work out the following Algorithm 1 performing this step. Note that Algorithm 1 is based on the Gaussian elimination recognized in computational RT as sweeping procedures that are illustrated in Figure 2.3. Furthermore, only one sweep is needed for every direction in $S_{\bar{N}}$.

Remark 3 When reflective boundaries arise on no more than one vertical and one horizontal boundary, Algorithm 1 starts first sweeping at the boundaries with known incoming flux then, reflected flux from the boundary is used for back sweeping. If both horizontal and/or vertical boundaries are reflective, an iterative process must be done on the boundaries. Suppose for example, both vertical boundaries are reflective *i.e.*,

$$I_{0j}(\mu_l, \eta_l) = I_{0j}(-\mu_l, \eta_l), \quad \text{for} \quad \mu_l > 0 \quad \text{and} \quad I_{N+1j}(\mu_l, \eta_l) = I_{N+1j}(-\mu_l, \eta_l), \quad \text{for} \quad \mu_l < 0.$$

Then, the angular fluxes at the vertical boundaries which were calculated in one step are used as inflow boundary for the next step of iteration. The iterations are stopped as soon as, the inequality

$$\|I^{old} - I^{new}\|_{L^\infty} \leq \delta_r \|I^{old}\|_{L^\infty} + \delta_a$$

is satisfied. Here, δ_a, δ_r are given tolerances and $\|.\|_{L^\infty}$ is the L^∞-norm.

Algorithm 1 Sweeping(N,M,$\bar{N}$,Δx,Δy,σ,κ,μ,η,$\mathbf{Q}$,I,$\mathbf{U}$)

for $l = 1, \ldots, \bar{N}$ **do**
  for $i = 1, \ldots, N$ **do**
    for $j = 1, \ldots, M$ **do**

$$d_{l,i+\frac{1}{2}j+\frac{1}{2}} = \frac{|\mu_l|}{2(\Delta x)_{i+\frac{1}{2}}} + \frac{|\eta_l|}{2(\Delta y)_{j+\frac{1}{2}}} + \frac{\sigma_{i+\frac{1}{2}j+\frac{1}{2}} + \kappa_{i+\frac{1}{2}j+\frac{1}{2}}}{4}$$

$$\bar{e}_{l,i+\frac{1}{2}j+\frac{1}{2}} = \frac{|\mu_l|}{2(\Delta x)_{i+\frac{1}{2}}} + \frac{-|\eta_l|}{2(\Delta y)_{j+\frac{1}{2}}} + \frac{\sigma_{i+\frac{1}{2}j+\frac{1}{2}} + \kappa_{i+\frac{1}{2}j+\frac{1}{2}}}{4}$$

$$\underline{\mathrm{e}}_{l,i+\frac{1}{2}j+\frac{1}{2}} = \frac{-|\mu_l|}{2(\Delta x)_{i+\frac{1}{2}}} + \frac{|\eta_l|}{2(\Delta y)_{j+\frac{1}{2}}} + \frac{\sigma_{i+\frac{1}{2}j+\frac{1}{2}} + \kappa_{i+\frac{1}{2}j+\frac{1}{2}}}{4}$$

$$e_{l,i+\frac{1}{2}j+\frac{1}{2}} = \frac{-|\mu_l|}{2(\Delta x)_{i+\frac{1}{2}}} + \frac{-|\eta_l|}{2(\Delta y)_{j+\frac{1}{2}}} + \frac{\sigma_{i+\frac{1}{2}j+\frac{1}{2}} + \kappa_{i+\frac{1}{2}j+\frac{1}{2}}}{4}$$

    end for
  end for
  if ($\mu_l < 0$ and $\eta < 0$) **then**
    for $i = 1 \ldots, N+1$ **do**
      $I_{l,iM+1} = q_{l,iM+1}$
    end for
    for $j = 1, \ldots, M+1$ **do**
      $I_{l,N+1j} = q_{l,N+1j}$
    end for
    for $i = N, \ldots, 1$ **do**
      for $j = M, \ldots, 1$ **do**

$$I_{l,ij} = \frac{u_{i+\frac{1}{2}j+\frac{1}{2}} - \underline{\mathrm{e}}_{l,i+\frac{1}{2}j+\frac{1}{2}} I_{l,i+1j} - e_{l,i+\frac{1}{2}j+\frac{1}{2}} I_{l,i+1j+1} - \bar{e}_{l,i+\frac{1}{2}j+\frac{1}{2}} I_{l,ij+1}}{d_{l,i+\frac{1}{2}j+\frac{1}{2}}}$$

      end for
    end for
  end if
  if ($\mu_l < 0$ and $\eta > 0$) **then**
    for $i = 1, \ldots, N+1$ **do**
      $I_{l,i1} = q_{l,i1}$
    end for
    for $J = 1, \ldots, M+1$ **do**
      $I_{l,N+1j} = q_{l,N+1j}$
    end for
    for $i = N, \ldots, 1$ **do**
      for $j = 1, \ldots, M$ **do**

$$I_{l,ij+1} = \frac{u_{i+\frac{1}{2}j+\frac{1}{2}} - e_{l,i+\frac{1}{2}j+\frac{1}{2}} I_{l,i+1j} - \bar{e}_{l,i+\frac{1}{2}j+\frac{1}{2}} I_{l,ij} - \underline{\mathrm{e}}_{l,i+\frac{1}{2}j+\frac{1}{2}} I_{l,i+1j+1}}{d_{l,i+\frac{1}{2}j+\frac{1}{2}}}$$

      end for
    end for
  end if
  if ($\mu_l > 0$ and $\eta < 0$) **then**
    for $i = 1, \ldots, N+1$ **do**
      $I_{l,iM+1} = q_{l,iM+1}$
    end for
    for $j = 1, \ldots, M+1$ **do**
      $I_{l,1j} = q_{l,1j}$
    end for
    for $i = 1, \ldots, N$ **do**
      for $j = M, \ldots, 1$ **do**

$$I_{l,i+1j} = \frac{u_{i+\frac{1}{2}j+\frac{1}{2}} - \underline{\mathrm{e}}_{l,i+\frac{1}{2}j+\frac{1}{2}} I_{l,ij} - \bar{e}_{l,i+\frac{1}{2}j+\frac{1}{2}} I_{l,i+1j+1} - e_{l,i+\frac{1}{2}j+\frac{1}{2}} I_{l,ij+1}}{d_{l,i+\frac{1}{2}j+\frac{1}{2}}}$$

      end for
    end for
  end if
  if ($\mu_l > 0$ and $\eta > 0$) **then**
    for $i = 1, \ldots, N+1$ **do**
      $I_{l,i1} = q_{l,i1}$
    end for
    for $J = 1, \ldots, M+1$ **do**
      $I_{l,1j} = q_{l,1j}$
    end for
    for $i = 1, \ldots, N$ **do**
      for $j = 1, \ldots, M$ **do**

$$I_{l,i+1j+1} = \frac{u_{i+\frac{1}{2}j+\frac{1}{2}} - \bar{e}_{l,i+\frac{1}{2}j+\frac{1}{2}} I_{l,i+1j} - e_{l,i+\frac{1}{2}j+\frac{1}{2}} I_{l,ij} - \underline{\mathrm{e}}_{l,i+\frac{1}{2}j+\frac{1}{2}} I_{l,ij+1}}{d_{l,i+\frac{1}{2}j+\frac{1}{2}}}$$

      end for
    end for
  end if
end for

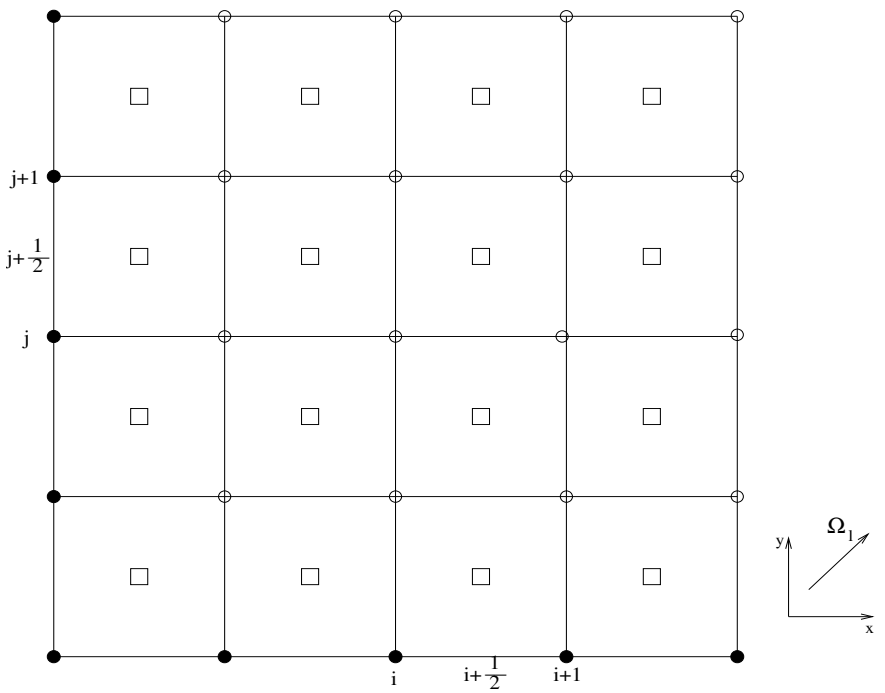

Figure 2.3: Illustration of a sweep for $\mu_l > 0$ and $\eta_l > 0$. Here, $\bullet$ known boundary flux ϕ, $\circ$ computed flux ϕ at cell interfaces, and $\square$ computed flux ϕ at cell centre.

2.3 Iterative methods

In the currrent section, some numerical techniques used in the literature are introduced for solving the linear system (2.14), which can be rewritten in common linear algebra notation as

$$\mathbf{AX} = \mathbf{b}, \tag{2.17}$$

with

$$\mathbf{A} \equiv \left(\begin{array}{ccc|c} \mathbf{H}_1 & & & -\Sigma_1 \\ & \ddots & & \vdots \\ & & \mathbf{H}_{\bar{N}} & -\Sigma_{\bar{N}} \\ \hline -\omega_1\mathbf{S} & \dots & -\omega_{\bar{N}}\mathbf{S} & \mathrm{I}_{NM} \end{array}\right), \qquad \mathbf{X} \equiv \left(\begin{array}{c} \mathrm{I}_1 \\ \vdots \\ \mathrm{I}_{\bar{N}} \\ \hline \mathrm{I} \end{array}\right), \quad \text{and} \quad \mathbf{b} \equiv \left(\begin{array}{c} \mathbf{Q}_1 \\ \vdots \\ \mathbf{Q}_{\bar{N}} \\ \hline \mathbf{0} \end{array}\right).$$

In the same spirit we can rewrite the system (2.15) as

$$\mathcal{A}\mathbf{\Phi} = \mathcal{B}, \tag{2.18}$$

where $\mathcal{A}$ is the Schur matrix given in (2.16) and the right hand side $\mathcal{B} = \dfrac{1}{4\pi}\displaystyle\sum_{l=1}^{\bar{N}} \omega_l \mathbf{S}\mathbf{H}_l^{-1}\mathbf{Q}_l$.

Recall that the matrices $\mathbf{A}$ and $\mathcal{A}$ are sparse and nonsymmetric. In large scale problems, iterative methods are computationally more efficient than direct methods; however, most iterative methods for nonsysmmetric systems, with the possible exception of multigrid methods, are less efficient than their symmetric counterparts.

The most popular and easiest iterative approach for solving (2.18) is the Source Iteration (SI) method also known in the computational RT as Richardson iteration. Given an initial guess

Algorithm 2 The SI algorithm

Require: $Kmax$, $\bar{N}$, ω, tol

Given the initial guess $\mathbf{I}^{(0)}$ compute $\mathbf{\Phi}^{(0)} = \frac{1}{4\pi}\sum_{l=1}^{\bar{N}} \omega_l \mathbf{SI}^{(0)}$
for $k = 0, \ldots, Kmax$ **do**
  for $l = 1, \ldots, \bar{N}$ **do**
    compute $\mathbf{W} = \mathbf{Q}_l + \mathbf{\Sigma}_l \mathbf{\Phi}^{(k)}$
  end for
  call **sweeping**$(N, M, \bar{N}, \Delta x, \Delta y, \sigma, \kappa, \mu, \eta, \mathbf{Q}, \mathbf{I}^{(k+1)}, \mathbf{W})$
  compute $\mathbf{\Phi}^{(k+1)} = \frac{1}{4\pi}\sum_{l=1}^{\bar{N}} \omega_l \mathbf{SI}_l^{(k+1)}$
  compute $\mathbf{Res}^{(k+1)} = \|\mathbf{\Phi}^{(k+1)} - \mathbf{\Phi}^{(k)}\|_{L^2}$
  if $\Big(\frac{\mathbf{Res}^{(k+1)}}{\mathbf{Res}^{(0)}} \leq tol\Big)$ **then**
    stop
  end if
end for

$\mathbf{\Phi}^{(0)}$, the $(k+1)$-iterate solution is obtained by

$$\mathbf{\Phi}^{(k+1)} = \mathbf{\Phi}^{(k)} + \frac{1}{4\pi}\sum_{l=1}^{\bar{N}} \omega_l \mathbf{SH}_l^{-1}\mathbf{Q}_l - \mathcal{A}\mathbf{\Phi}^{(k)},$$

or simply

$$\mathbf{\Phi}^{(k+1)} = \frac{1}{4\pi}\sum_{l=1}^{\bar{N}} \omega_l \mathbf{SH}_l^{-1}\Big(\mathbf{Q}_l + \Sigma_l \mathbf{\Phi}^{(k)}\Big). \tag{2.19}$$

In what follows, Algorithm 2 is presented.
Here, $Kmax$ is the highest value of the iterations, the given tolerance is tol, $\|.\|_{L^2}$ is the discrete L^2-norm, and $\mathbf{Res}^{(k)}$ denotes the residual vector at iteration k.
Note that iteration (2.19) is equivalent to a preconditioned block Gauss-Seidel technique applied to (2.17), where the preconditioner is the block lower triangle of the matrix $\mathbf{A}$. Thus, if $\mathbf{M}$ is the block lower triangle of $\mathbf{A}$, then

$$\mathbf{MX}^{(k+1)} = (\mathbf{M} - \mathbf{A})\mathbf{X}^{(k)} + \mathbf{b},$$

and

$$\mathbf{X}^{(k+1)} = \Big(\mathbf{I_{NM}} - \mathbf{M}^{-1}\mathbf{A}\Big)\mathbf{X}^{(k)} + \mathbf{M}^{-1}\mathbf{b}. \tag{2.20}$$

Therefore, the $(k+1)$-iterate scalar flux satisfy

$$\begin{aligned}\mathbf{\Phi}^{(k+1)} &= \frac{1}{4\pi}\sum_{l=1}^{\bar{N}} \omega_l \mathbf{SH}_l^{-1}\mathbf{I}_l^{(k+1)},\\ &= \frac{1}{4\pi}\sum_{l=1}^{\bar{N}} \omega_l \mathbf{SH}_l^{-1}\Big(\mathbf{Q}_l + \Sigma_l \mathbf{\Phi}^{(k)}\Big),\end{aligned}$$

which is identical to (2.19). Regarding to the matrix formulations (2.17) and (2.18), we have the following properties:

Algorithm 3 The matrix-vector multiplication

1: Given a vector $\mathbf{U}$, to apply the matrix $\mathcal{A}$ to $\mathbf{U}$ we proceed as:
2: **for** $l = 1, \ldots, \bar{N}$ **do**
3: compute $\mathbf{V} = \mathbf{\Sigma}_l \mathbf{U}$
4: **end for**
5: call **sweeping**$(N, M, \bar{N}, \Delta x, \Delta y, \sigma, \kappa, \mu, \eta, \mathbf{Q}, \mathbf{V}, \mathbf{W})$
6: **for** $l = 1, \ldots, \bar{N}$ **do**
7: compute $\mathbf{V} = \mathbf{S}_l \mathbf{W}$
8: **end for**
9: set $\mathbf{U} = \mathbf{U} - \dfrac{1}{4\pi} \displaystyle\sum_{l=1}^{\bar{N}} \omega_l \mathbf{V}$

1. The matrices $\mathbf{A}$ and $\mathcal{A}$ are nonsymmetric. In general they are not diagonally dominant.

2. When $\bar{e}_{l,i+\frac{1}{2}j+\frac{1}{2}} \leq 0$ and $\underline{e}_{l,i+\frac{1}{2}j+\frac{1}{2}} \leq 0$, for all l, i, j, the matrix $\mathbf{A}$ is weakly diagonally dominant.

3. Since $S_{\bar{N}}$ has nonzero directions and σ and κ are nonnegative functions, the matrix $\mathbf{A}$ has nonpositive off-diagonal elements and positive diagonal elements.

The fact that $\bar{e}_{l,i+\frac{1}{2}j+\frac{1}{2}} \leq 0$ and $\underline{e}_{l,i+\frac{1}{2}j+\frac{1}{2}} \leq 0$ is equivalent to

$$h := \max_{ij}\big((\Delta x)_i, (\Delta y)_j\big) \leq \max_{ij}\left(\frac{2|\mu_l|}{\sigma_{i+\frac{1}{2}j+\frac{1}{2}} + \kappa_{i+\frac{1}{2}j+\frac{1}{2}}}, \frac{2|\eta_l|}{\sigma_{i+\frac{1}{2}j+\frac{1}{2}} + \kappa_{i+\frac{1}{2}j+\frac{1}{2}}}\right), \quad \forall\, l, \tag{2.21}$$

physically this means physically that the cell size is no more than two mean free paths of the particles being simulated. Needless to say that the condition (2.21) gives the bound of the coarser mesh should be utilized in the computations. In order to overcome the disadvantage of SI method to efficiently solve the problem (2.15) when $\gamma \approx 1$, two Krylov subspace-based techniques are proposed, especially the BICGSTAB [150] and the GMRES [131]. The main idea behind these methods is that the Krylov subspace techniques can be interpreted as the weighted Richardson iteration

$$\mathbf{X}^{(k+1)} = \aleph\Big(\mathbf{I}_{NM} - \mathbf{P}^{-1}\mathbf{A}\Big)\mathbf{X}^{(k)} + \mathbf{P}^{-1}\mathbf{b}, \qquad 0 < \aleph < 2, \tag{2.22}$$

where the preconditioner $\mathbf{P}$ and the relaxation parameters $\aleph$ are variables within each iteration step. Note that, when $\mathbf{P} = \mathbf{M}$ and $\aleph = 1$, the iteration (2.22) is reduced to the SI technique. The GMRES and BICSTAB algorithms for solving the linear system (2.18) can be implemented in the conventional way as in [42, 44, 64, 131, 150]. The only difference is that the sparse matrix $\mathcal{A}$ can not be explicitly stored. All what is required, on the other hand, is a subroutine that performs a matrix-vector multiplication as illustrated in Algorithm 3.
Note that we need only three vectors ($\mathbf{W}$, $\mathbf{V}$ and $\mathbf{U}$) for performing the multiplication of the matrix $\mathcal{A}$ to the vector $\mathbf{U}$. Likewise, we require only three calls for Algorithm 3 from the GMRES or BICGSTAB subroutines.

Remark 4 Preconditioned GMRES or BICGSTAB techniques can also be utilized. For example, in the case when the matrix $\mathcal{A}$ in (2.16) is diagonally dominant, the GMRES or BICGSTAB approaches can be accelerated by utilizing the diagonal as a preconditioner. This method can be easily implemented. However, it requires additional computational work. It goes without

saying that since, the matrix $\mathcal{A}$ does not have an explicit representation, ILU type preconditioners can not be accounted for solving (2.15).
It is worth mentioning that direct solvers are not suitable to work as the matrices are big in the order of hundreds of thousands or more. When the matrices are very big in the order of m, then m $\times$ m operations are required in order to solve the system utilizing Gaussian elimination. Furthermore, when dealing with sparse matrices, it would be meaningless as the operation (for instance, multiplication zero by zero) will be waste of computing resources. Likewise, direct solvers do not have the direct access to the overall matrix at the same time. Iterative solvers on the other hand starts the operation by assuming an approximate solution for the computed unknown. Then the solution is iterated upon till it reaches the exact solution [61].

2.4 Diffusion synthetic acceleration method

It has been shown in [79, 80, 81], under the physical assumptions that the scattering of medium is dominate and it is optically thick, the RTE (2.5) can be approximated by the diffusion problem

$$\begin{aligned} -\nabla\cdot\Big(\frac{1}{3(\sigma+\kappa)}\nabla\varphi\Big)+\kappa\varphi &= q \qquad \text{in} \quad \mathcal{D},\\ \varphi+\frac{2}{3(\sigma+\kappa)}\mathbf{n}\cdot\nabla\varphi &= 4\pi g, \quad \text{on} \quad \partial\mathcal{D}. \end{aligned} \tag{2.23}$$

The authors in [79, 80, 81] used asymptotic analysis to prove that, in the diffusive limit, the solution to the equation (2.23) approaches asymptotically solution of the full RTE (2.5). Further analysis and other asymptotic approximations to the transport problem in radiative heat transfer context can be found in [150]. The main advantages to consider the diffusion approach lie on the fact that it is linear elliptic equation, equation (2.23) does not depend on the angle variable Ω, easy to solve numerically with less memory requirement and computational cost, and when κ is positive (2.23) has a unique solution. In order to build a discretization for the diffusion problem (2.23) which is consistent to the one used for the RTE (2.5) and converges asymptotically to the same solution as the mesh size h tends to zero, we consider in this section the same grid structure as Figure 2.2 and the same notations as those used in section 2.2. Hence, for the equation (2.23), a space discretization reads as

$$-\mathcal{D}_h^2\Big(\frac{1}{3(\sigma+\kappa)}\varphi\Big)_{ij}+\kappa\varphi_{i+\frac{1}{2}j+\frac{1}{2}} = q_{i+\frac{1}{2}j+\frac{1}{2}}, \tag{2.24}$$

where the difference operator $\mathcal{D}_h^2$ is given by $\mathcal{D}_h^2 := \mathcal{D}_x^2+\mathcal{D}_y^2$, with

$$\begin{aligned} \mathcal{D}_x^2(\varpi\omega)_{ij} &:= \frac{\varpi_{ij}+\varpi_{i+1j}}{2}\frac{\omega_{i+1j}-\omega_{ij}}{(\Delta x)^2_{i+\frac{1}{2}}}-\frac{\varpi_{i-1j}+\varpi_{ij}}{2}\frac{\omega_{ij}-\omega_{i-1j}}{(\Delta x)^2_{i+\frac{1}{2}}},\\ \mathcal{D}_y^2(\varpi\omega)_{ij} &:= \frac{\varpi_{ij}+\varpi_{ij+1}}{2}\frac{\omega_{ij+1}-\omega_{ij}}{(\Delta y)^2_{j+\frac{1}{2}}}-\frac{\varpi_{ij-1}+\varpi_{ij}}{2}\frac{\omega_{ij}-\omega_{ij-1}}{(\Delta y)^2_{j+\frac{1}{2}}}, \end{aligned}$$

and the functions $\varphi_{i+\frac{1}{2}j+\frac{1}{2}}$ and $q_{i+\frac{1}{2}j+\frac{1}{2}}$ appeared in (2.24) are given by the formula (2.13). Without using ghost points, the gradient in the boundary conditions is approximated by upwinding. For instance, the boundary discretization on the left boundary of the domain ($x = x_0$) is

$$\varphi_{\frac{1}{2}j+\frac{1}{2}}-\frac{2}{3(\sigma_{\frac{1}{2}j+\frac{1}{2}}+\kappa_{\frac{1}{2}j+\frac{1}{2}})}\frac{\varphi_{\frac{3}{2}j+\frac{1}{2}}-\varphi_{\frac{1}{2}j+\frac{1}{2}}}{(\Delta x)_{\frac{1}{2}}} = 4\pi g_{\frac{1}{2}j+\frac{1}{2}},$$

Algorithm 4 The DSA algorithm

1: Given the initial guess $\mathbf{I}^{(0)}$ compute $\mathbf{\Phi}^{(0)} = \dfrac{1}{4\pi}\displaystyle\sum_{l=1}^{\bar{N}} \omega_l \mathbf{SI}^{(0)}$
2: **for** $k = 0, \ldots, Kmax$ **do**
3: **for** $l = 1, \ldots, \bar{N}$ **do**
4: compute $\mathbf{W} = \mathbf{Q}_l + \mathbf{\Sigma}_l \mathbf{\Phi}^{(k)}$
5: **end for**
6: call **sweeping**$(N, M, \bar{N}, \Delta x, \Delta y, \sigma, \kappa, \mu, \eta, \mathbf{Q}, \mathbf{I}^{(k+1)}, \mathbf{W})$
7: compute $\mathbf{\Phi}^{(k+\frac{1}{2})} = \dfrac{1}{4\pi}\displaystyle\sum_{l=1}^{\bar{N}} \omega_l \mathbf{SI}_l^{(k+1)}$
8: compute φ by solving the diffusion problem

$$\begin{aligned} -\nabla \cdot \left(\frac{1}{3(\sigma+\kappa)} \nabla \varphi \right) + \kappa \varphi &= \sigma \Big(\mathbf{\Phi}^{(k+\frac{1}{2})} - \mathbf{\Phi}^{(k)} \Big), \\ \varphi + \frac{2}{3(\sigma+\kappa)} \mathbf{n} \cdot \nabla \varphi &= 0. \end{aligned}$$

9: set $\mathbf{\Phi}^{(k+1)} = \mathbf{\Phi}^{(k+\frac{1}{2})} + \varphi$
10: compute $\mathbf{Res}^{(k+1)} = \|\mathbf{\Phi}^{(k+1)} - \mathbf{\Phi}^{(k)}\|_{L^2}$
11: if $\left(\dfrac{\mathbf{Res}^{(k+1)}}{\mathbf{Res}^{(0)}} \leq tol \right)$ stop
12: **end for**

and similar work has to be done for the other boundaries. All together, the above discretization leads to a linear system of form

$$\mathcal{T}\varphi = \mathcal{R}, \tag{2.25}$$

where $\mathcal{T}$ is $N \times M$ nonsymmetric positive definite matrix obtained from the difference diffusion operator (2.24) with boundary conditions included, and $\mathcal{R}$ is NM vector containing the right hand q and boundary function g. The system (2.25) can be solved using one of the iterative methods BICGSTAB or GMRES already discussed in section 2.3. In our numerical examples presented in this chapter, we used the preconditioned BICGSTAB with the diagonal as preconditioner.

As mentioned early the diffusion approach (2.23) is a good approximation to the full RTE (2.5) only when the transport field is optically thick ($\vartheta \gg 1$) or with dense absorption ($\kappa \gg 1$). In medium with small absorption or pure scattering ($\kappa = 0$), the diffusion approach (2.23) becomes unable to approximate accurately the correct solution of the full transport problem. Nevertheless, this approach can be used for accelerating the source iteration algorithm in all the regimes. The resulting accelerated algorithm, widely known in computational RT as Diffusion Synthetic Acceleration (DSA) method, was first introduced in [3] and studied in various papers, see for instance [6, 13]. The implementation of DSA technique for approximating the solution of the RTE (2.5) is achieved in Algorithm 4.

Recall that in the matrix notation of section 2.3 the SI iteration is given by the Richardson iteration applied to the system (2.17) as

$$\mathbf{X}^{(k+1)} = \Big(\mathbf{I}_{NM} - \mathbf{M}^{-1}\mathbf{A} \Big) \mathbf{X}^{(k)} + \mathbf{M}^{-1}\mathbf{b},$$

where $\mathbf{M}$ is the block lower triangle of $\mathbf{A}$. Roughly speaking, the DSA approach can be viewed

Table 2.2: The values of σ, κ and boundary function g used for different test problems.

	$\sigma(x,y)$	$\kappa(x,y)$	$g_{\Gamma_l}(y)$	$g_{\Gamma_r}(y)$	$g_{\Gamma_b}(x)$	$g_{\Gamma_t}(x)$
Test 1	0.99	0.01	0	1	x	x
Test 2	99	1	0	1	x	x
Test 3	1	10	y	$1-y$	x	$1-x$
Test 4	10	0	y	$1-y$	x	$1-x$

as preconditioned Richardson iteration with the diffusion matrix $\mathcal{T}$ like preconditioner,

$$\mathbf{X}^{(k+1)} = \Big(\mathbf{I}_{NM} - \mathcal{T}^{-1}\mathbf{A}\Big)\mathbf{X}^{(k)} + \mathcal{T}^{-1}\mathbf{b},$$

and $\mathcal{T}^{-1}$ is obtained by solving the diffusion linear system (2.25).
It is worth noting that Algorithm 4 and Algorithm 2 share the first lines. However, the source iteration algorithm gives only the intermediate solution $\mathbf{\Phi}^{(k+\frac{1}{2})}$ which has to be corrected by adding the solution φ obtained by the diffusion method.

2.5 Numerical examples

To assess the performance of the methods introduced in the previous sections, some numerical experiments of two examples are run for the RTE (2.5).

$$\text{Relative Residual} := \frac{Res^{(k)}}{Res^{(0)}} \leq 10^{-6}, \tag{2.26}$$

Here $Res^{(0)}$ and $Res^{(k)}$ denote the initial residual and the residual at the iteration k in the iterative algorithm, respectively. We used the discrete L^2-norm for the computation of these residuals. The convergence rates along with cross-section plots of the results give an acceptable percentage of accuracy of the algorithms. The CPU time context is monitored to compare how efficient the solvers are. All the calculations reported in this section have been carried out in FORTRAN implementation with double precision.
The first example is the equations (2.5) in the unit square $\mathcal{D} = [0,1]\times[0,1]$ covered by 100×100 grid points and augmented with the following boundary function g

$$\begin{aligned} g(0,y,\Omega) &= g_{\Gamma_l}(y), \qquad g(1,y,\Omega) = g_{\Gamma_r}(y), \qquad \text{for} \quad 0 \leq y \leq 1; \\ g(x,0,\Omega) &= g_{\Gamma_b}(x), \qquad g(x,1,\Omega) = g_{\Gamma_t}(x), \qquad \text{for} \quad 0 \leq x \leq 1. \end{aligned}$$

We set $q(x,y,\Omega) = 0$. The coefficients σ, κ; the functions g_{Γ_l}, g_{Γ_r}, g_{Γ_b} and g_{Γ_t}, are selected for four different test problems according to Table 2.2. The main issues we wish to address in these test problems are concerned with the comparison on convergence and efficiency of all the methods presented in these notes using different values of σ, κ and g to show the advantages of a method over the others. To this end, we first plot in Figure 2.4 the convergence rates for the four test problems. A log-scale on the y-axis is used. A first remark concerning these plots is that the SI method converges slowly when $\gamma \approx 1$. For example, in **Test 2** ($\gamma = 0.99$) SI needs 866 iterations to converge and in **Test 4** ($\gamma = 1$) needs 262 iterations. However, in both

Table 2.3: The number of iterations (# Iter) and the CPU time (in seconds) for SI, GMRES, BICGSTAB, DSA and Diffusion techniques for the four test examples.

	Test 1		**Test 2**		**Test 3**		**Test 4**	
	# Iter	CPU	# Iter	CPU	# Iter	CPU	# Iter	CPU
SI	17	7.65	866	317.29	6	3.10	262	107.98
GMRES	4	5.51	50	51.14	2	3.68	16	17.43
BICGSTAB	4	3.61	52	28.12	3	3.12	14	8.68
DSA	7	19.97	21	14.84	4	4.01	8	14.27
Diffusion	224	3.48	58	0.94	60	0.9	154	2.33

tests, DSA approach shows fast convergence over all the others methods. On the other hand, when $\gamma \ll 1$ the BICGSTAB method can be competed with DSA. In **Test 1** and **Test 3**, a few iterations are enough for the convergence of all methods, but still SI method is the slowest.
In Table 2.3 the number of iterations needed are displayed by each method for the four tests together with the consumed CPU time. It is clear that the BICGSTAB method uses less CPU time in all tests except in **Test 2** ($\vartheta = 100$). The diffusion results are also included in Table 2.3. These results are less CPU time consuming. However, the diffusion results should not be compared to other methods since the problem they solve has a different structure than those solved by SI, BICGSTAB, GMRES, or DSA methods.
In Figure 2.5 we plot the scalar flux ϕ obtained by DSA method for the four test problems. Similar results are plotted in Figure 2.6 but using the diffusion procedure. The SI, BISCATAB and GMRES results are not presented here, because they overlap those obtained by DSA method. In order to compare these results, we show in Figure 2.7 a cross-section at the main diagonal ($y = x$) of the scalar flux obtained by all techniques. As can be slightly seen, the diffusion failed to approach accurately the DSA results when $\gamma = 0.99$; $\vartheta = 1$ (**Test 1**), and $\gamma = 0.09$; $\vartheta = 11$ (**Test 3**). In other two tests (**Test 2** and **Test4**), diffusion approach resolves the RTE correctly as the DSA technique does, but with less computational time in Table 2.3.

Our second example consists of tests arising in radiative transfer problems. Usually the transport equation (2.5) is coupled to the heat equation to model radiative heat transfer phenomena, compare [98, 15, 43, 146] for detailed studies on radiative transfer. Since our goal is concerned with numerical tools for simulating the transport equation, we fix the temperature profile in the RTE and we try to solve the transport equation coupled to this temperature profile. Thus, the problem statements we consider here are:
The frequency-independent problem

$$\Omega \cdot \nabla I + (\sigma + \kappa) I \;=\; \frac{\sigma}{4\pi} \int_{S^2} I(\mathbf{x}, \Omega') d\Omega' + \kappa B(\Theta). \tag{2.27}$$

The frequency-dependent problem

$$\Omega \cdot \nabla I_\nu + \big(\sigma_\nu + \kappa_\nu\big) I_\nu \;=\; \frac{\sigma_\nu}{4\pi} \int_{S^2} I_\nu(\mathbf{x}, \Omega', \nu) d\Omega' + \kappa_\nu B(\Theta, \nu). \tag{2.28}$$

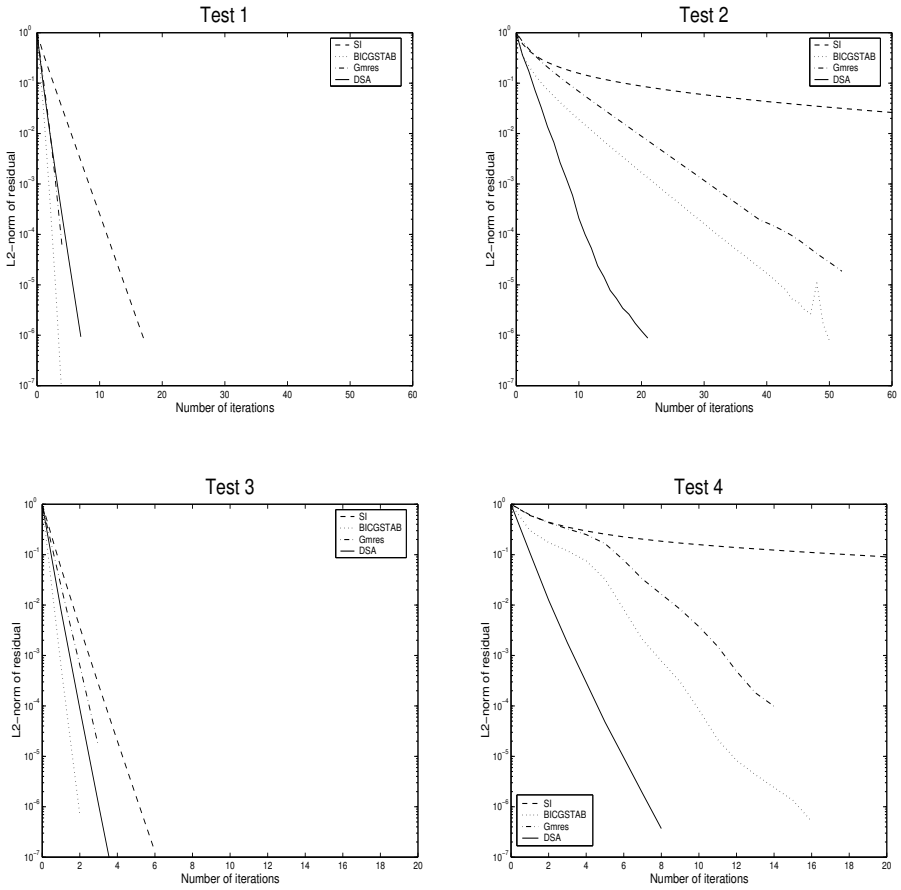

Figure 2.4: The convergence plots for the four test examples from Table 2.2.

Here, $\Theta = \Theta(\mathbf{x})$, $I_\nu = I(\mathbf{x}, \Omega, \nu)$, $\kappa_\nu = \kappa(\mathbf{x}, \nu)$ and $\sigma_\nu = \sigma(\mathbf{x}, \nu)$ denote respectively, the temperature, the radiation intensity, the opacity and the scattering within the frequency $\nu > 0$. In (2.27), B is the Planck function given by

$$B(\Theta, \nu) = \frac{2\hbar\nu^3}{c^2}\left(e^{\hbar\nu/k_B\Theta} - 1\right)^{-1}, \tag{2.29}$$

where k_B, $\hbar$ and c Boltzmann constant, Planck coefficient and the speed of light, respectively. Notice that, in the frequency-independent problem (2.27), the function $B = B(\Theta) = a_R\Theta^4$, with a_R is a radiation constant ($a_R = 1.8067.10^{-8}\ J/K$). The computational domain is a square of 1×1 discretized into 100×100 grid cells. The temperature we used in our computations is a linear profile between 800 K and 1800 K in the unit square *i.e.*,

$$\Theta(x, y) = 800x + 1000, \qquad (x, y) \in [0, 1] \times [0, 1].$$

Using this temperature profile we set the boundary conditions for the intensity according to the radiative equilibrium

$$I(\hat{\mathbf{x}}) = B(\Theta(\hat{\mathbf{x}})), \qquad \hat{\mathbf{x}} \in \partial\mathcal{D}^-, \tag{2.30}$$

for the frequency-independent problem (2.27), and

$$I_\nu(\hat{\mathbf{x}}) = B(\Theta(\hat{\mathbf{x}}), \nu), \qquad \hat{\mathbf{x}} \in \partial\mathcal{D}^-, \tag{2.31}$$

for the frequency-dependent problem (2.28). First, we solve the grey problem (2.27)-(2.30) using the methods studied in the previous sections. In Figure 2.8, we report the convergence

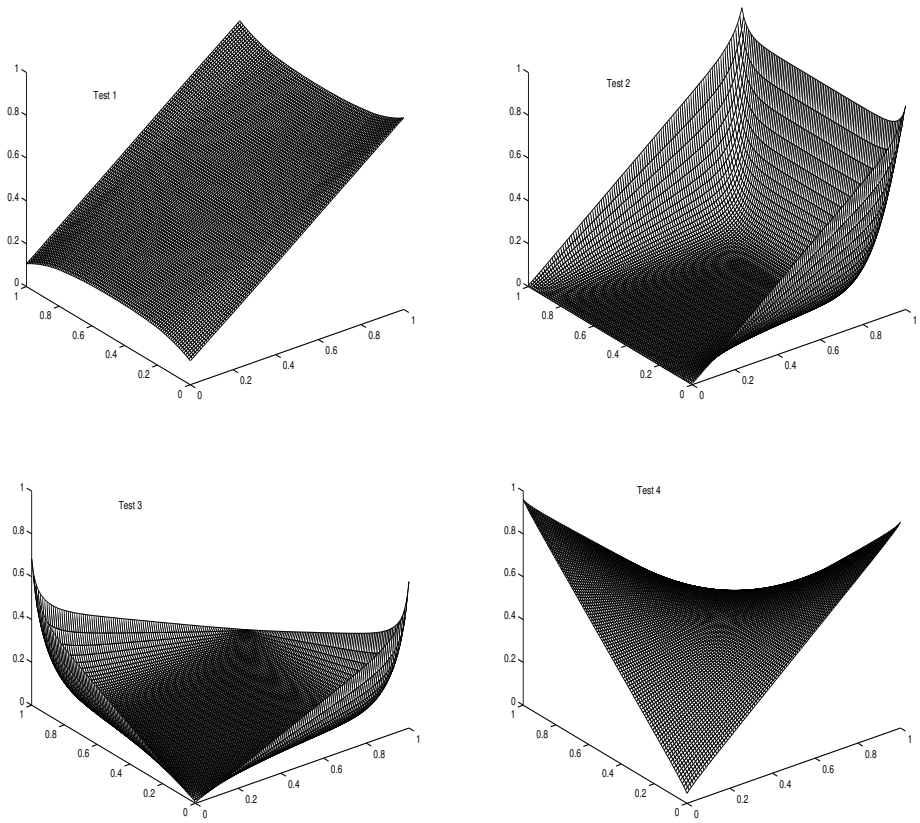

Figure 2.5: The scalar flux ϕ obtained by DSA method for the four test problems from Table 2.2.

plots for two different values of the absorption κ while the scattering is fixed to $\sigma = 1\ cm^{-1}$ in both tests. It is apparent that the convergence of SI method becomes slow when the scattering ratio γ changes from 0.09 ($\kappa = 10\ cm^{-1}$) to 1 ($\kappa = 0\ cm^{-1}$). The accuracy plots given in Figure 2.9 represent a cross-section at $y = 0.5$ of the scalar flux obtained by all the techniques with the diffusion approach included. As the opacity κ decreases, the diffusion results become slightly far from the results obtained for the full transport problem. We now turn our attention to the frequency-dependent problem (2.28)-(2.31). In order to discretize the equations (2.28)-(2.31) with respect to the frequency variable ν, we assume $\tilde{N}$ frequency bands $[\nu_\iota, \nu_{\iota+1}]$, $\iota = 1, \ldots, \tilde{N}$ with piecewise constant absorptions given by

$$\kappa_\nu = \kappa_\iota, \qquad \forall\ \nu \in [\nu_\iota, \nu_{\iota+1}] \quad \iota = 1, \ldots, \tilde{N}.$$

The frequency-averaged intensity in the band $[\nu_\iota, \nu_{\iota+1}]$ is defined by

$$I_\iota = \int_{\nu_\iota}^{\nu_{\iota+1}} I_{\nu'}(\mathbf{x}, \Omega, \nu') d\nu'. \tag{2.32}$$

Then, the equations (2.28)-(2.31) are transformed to a system of $\tilde{N}$ transport equations of the form

$$\begin{aligned} \Omega \cdot \nabla I_\iota + \big(\sigma_\iota + \kappa_\iota\big) I_\iota &= \frac{\sigma_\iota}{4\pi} \int_{S^2} I_\iota(\mathbf{x}, \Omega', \nu_\iota) d\Omega' + \kappa_\iota \int_{\nu_\iota}^{\nu_{\iota+1}} B(\Theta, \nu') d\nu', \\ I_\iota(\hat{\mathbf{x}}) &= \int_{\nu_\iota}^{\nu_{\iota+1}} B(\Theta, \nu') d\nu', \qquad \hat{\mathbf{x}} \in \partial\mathcal{D}^-. \end{aligned} \tag{2.33}$$

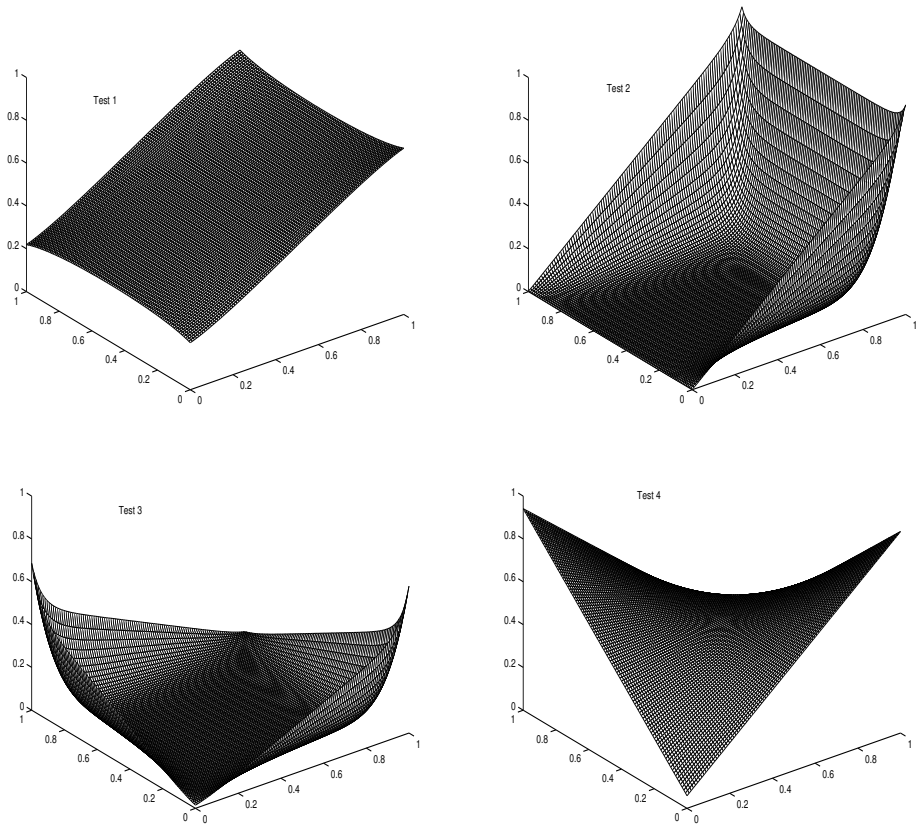

Figure 2.6: The scalar flux ϕ in the Diffusion approach for the four test problems from Table 2.2.

Note that after the discretization of ordinates in $\bar{N}$ directions and the space in $N \times M$ gridpoints, one has to deal with systems with $\tilde{N} \times \bar{N} \times N \times M$ unknowns and, finding solutions to such systems requires a big memory storage and high computational cost. Eight frequency bands $[\nu_\iota, \nu_{\iota+1}]$, $\iota = 1, \ldots, 8$ given in Table 2.4 are used in out numerical simulations. These values are frequently used in the glass manufacturing, we refer to [146] for more physical details.
Using two different values for the scattering ($\sigma = 1\ cm^{-1}$ and $\sigma = 100\ cm^{-1}$), we summarize in Table 2.5 the CPU time and the number of iterations used by all methods except the BICSTAB method, because its results are identical to the GMRES ones. It is important to mention two points with respect to the results in Table 2.5. First, we observe that by decreasing the scattering ratio γ and keeping σ fixed to 100 cm^{-1} or 1 cm^{-1}, the number of iterations reduce asymptoticly in all the methods with the advantage of the GMRES method over the others. Second, when $\sigma = 100\ cm^{-1}$, the SI method required unreasonable number of iterations for the first frequency bands, consequently the CPU time used is very large. In contrast, the Diffusion approach uses only 0.012% of the CPU time used by SI method for this case, and the results obtained by both approaches are similar, see Figure 2.10.
In order to quantify the solution of (2.33) we define the frequency-mean scalar flux φ as

$$\begin{aligned} \varphi(\mathbf{x}) &= \frac{1}{4\pi} \int_{S^2} \int_0^\infty I(x, \Omega', \nu') d\Omega' d\nu', \\ &= \frac{1}{4\pi} \sum_{l=1}^{\bar{M}} \sum_{\iota=1}^{\tilde{N}} I_{\iota,l}(\mathbf{x}). \end{aligned}$$

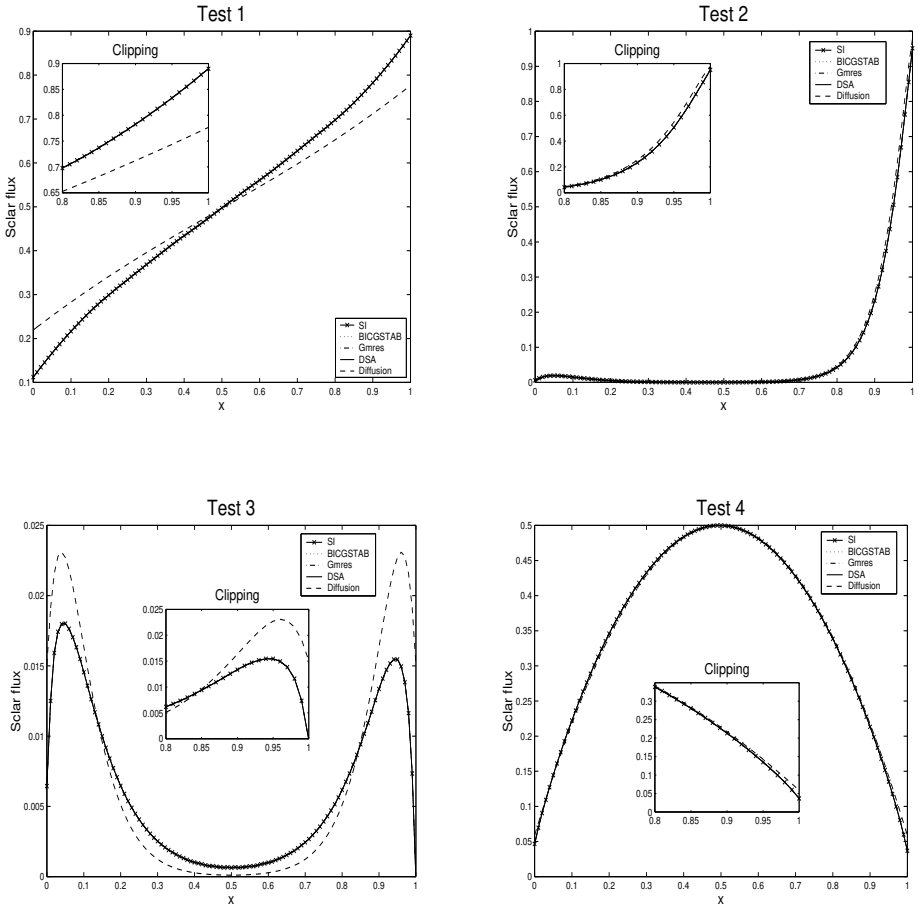

Figure 2.7: The cross section at $y = x$ of the scalar flux ϕ for the four test problems from Table 2.2.

Table 2.4: The bands used in the numerical simulation of the frequency-dependent problem.

Band ι	ν_ι (μm)	$\nu_{\iota+1}$ (μm)	κ_ι (m^{-1})
1	∞	5	0.4
2	5	0.333	0.5
3	0.333	0.285	7.7
4	0.285	0.250	15.4
5	0.250	0.222	27.9
6	0.222	0.181	267.9
7	0.181	0.166	567.3
8	0.166	0.142	7136
	0.142	0	opaque

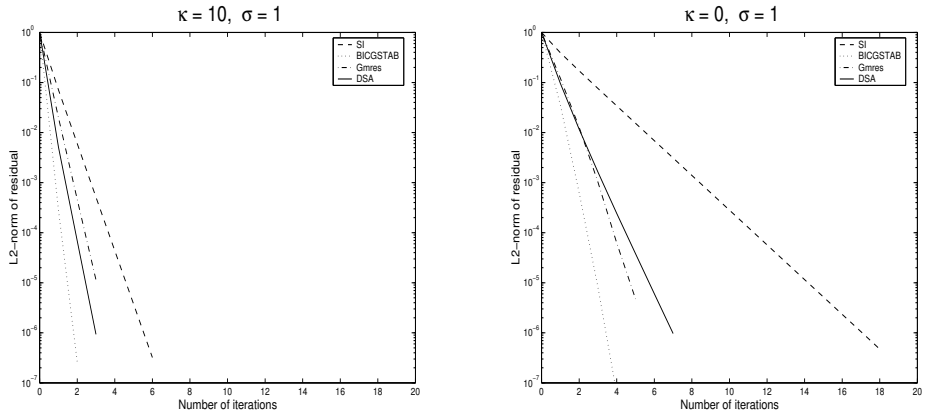

Figure 2.8: The convergence plots for the grey problem (2.27)-(2.30) with $\sigma = 1$ and two different values of opacity.

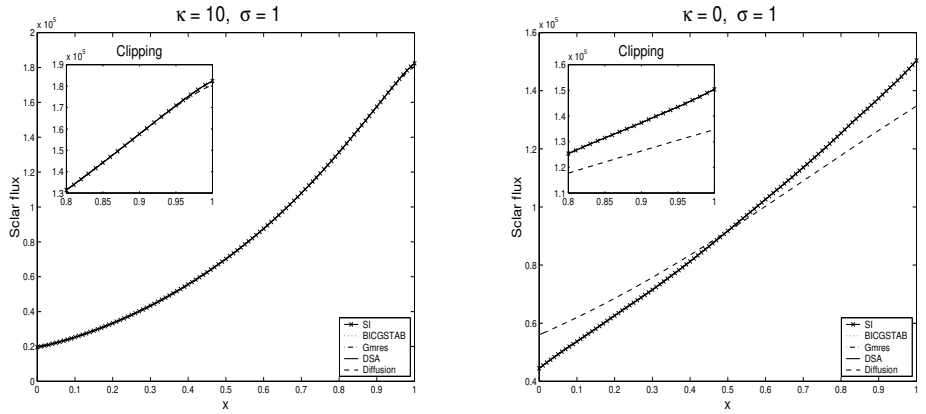

Figure 2.9: The cross section at $y = 0.5$ of the scalar flux ϕ for the grey problem (2.27)-(2.30) with $\sigma = 1$ and two different values of opacity.

Figure 2.10 shows a cross-section of φ at $y = 0.5$ for the two values of σ. The main message taken from this figure is that, the diffusion results coincides with the transport results only when the scattering is large ($\sigma = 100\ cm^{-1}$) and for this case the SI scheme is unreasonably slow (compare the CPU time in Table 2.5). Therefore, it is worth using the diffusion approach because, at least for this test problem, it gives results that are as accurate as those obtained for the full transport equation but with less computational cost.

2.6 Concluding remarks

We have combined the discrete ordinates collocation and the Diamond differencing to reconstruct numerical techniques for the two-dimensional radiative transfer equation. These techniques include the source iteration scheme, GMRES and full BICGSTAB algorithms, and the diffusion synthetic acceleration method. We have compared the results obtained by these methods on several test problems. The principal conclusions achieved through this comparison are the following:

1. For radiative transfer equation with small scattering ratio ($\gamma \ll 1$) and moderate optical coefficient ϑ, the SI method can be a reasonable solver, but still not efficient enough as BICGSTAB, GMRES or DSA methods.

Table 2.5: The number of iterations and the CPU time (in minutes) for SI, GMRES, DSA and Diffusion techniques for the eight frequency-band examples along with two different values of σ.

	Band ι	Scattering ratio γ	SI	GMRES	DSA	Diffusion
$\sigma = 1\ cm^{-1}$	1	0.71428	16	6	7	217
	2	0.66666	15	6	7	212
	3	0.11494	8	4	4	91
	4	0.06077	6	4	4	46
	5	0.03450	6	4	3	25
	6	0.00371	4	2	3	4
	7	0.00175	4	2	3	3
	8	0.00014	3	1	2	2
	CPU	———	25.63	3.94	14.69	0.21
$\sigma = 100\ cm^{-1}$	1	0.99601	1700	92	32	87
	2	0.99502	1321	89	30	82
	3	0.92850	178	26	29	25
	4	0.86617	95	18	29	17
	5	0.78137	57	14	27	11
	6	0.27175	12	5	9	3
	7	0.14985	9	4	6	3
	8	0.01381	5	2	3	2
	CPU	———	981.16	6.43	69.72	0.12

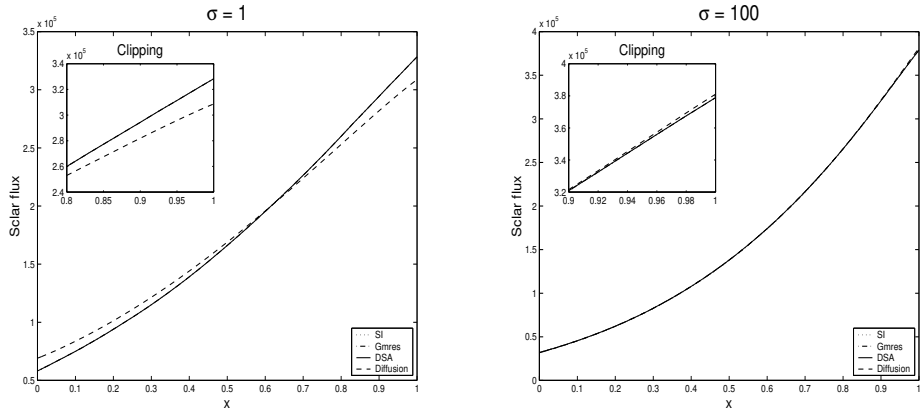

Figure 2.10: The cross section at $y = 0.5$ of the mean scalar flux φ for the problem (2.28)-(2.31) with the eight frequency-bands given in Table 2.5 and two different values of σ.

2. For radiative transfer equation with large or pure scattering ($\gamma \approx 1$), the SI method become very slow and loses efficiency. In parallel, the DSA method is the best and presents fast convergence rate over all other methods.

3. For radiative transfer equation in optically thick regime ($\vartheta \gg 1$), the diffusion approach may be a valid alternative for the iterative methods since it gives results that are as accurate as those obtained by DSA method, but with less computational cost, and diffusion

approach does not need extra discretization for the angular directions.

Nevertheless, comparing the simplified P_N approximations to the transport equation and following the argument of section 2.4, it is convenient to devise generalized preconditioners to the SI method with high accelerated convergence. Such methods can be used in radiative heat transfer and radiation hydrodynamic couplings rather than the transport equation (2.1).
We want to point out that general time-dependent radiative transfer problem (2.1) can also numerically solved in a similar manner. By utilizing the discrete ordinates and the Diamond differencing methods, and by using the same notations as in section 2.2, the equations (2.1) are transformed to the system of ordinary differential equations below

$$\begin{aligned}\frac{1}{c}\frac{d}{dt}\psi_{l,i+\frac{1}{2}j+\frac{1}{2}}+\mu_l\frac{\psi_{l,i+1j}-\psi_{l,ij}}{(\Delta x)_{i+\frac{1}{2}}}+\eta_l\frac{\psi_{l,ij+1}-\psi_{l,ij}}{(\Delta y)_{j+\frac{1}{2}}} &+ \big(\sigma_{i+\frac{1}{2}j+\frac{1}{2}}+\kappa_{i+\frac{1}{2}j+\frac{1}{2}}\big)\psi_{l,i+\frac{1}{2}j+\frac{1}{2}} = \\ &\sigma_{l,i+\frac{1}{2}j+\frac{1}{2}}\phi_{i+\frac{1}{2}j+\frac{1}{2}}+q_{l,i+\frac{1}{2}j+\frac{1}{2}},\\ \psi_{l,ij}(t) &= g_{l,ij}(t),\\ \psi_{l,ij}(0) &= \psi^0_{l,ij},\end{aligned} \tag{2.34}$$

where each centered valued function $f_{l,i+\frac{1}{2}j+\frac{1}{2}}$ appeared in (2.34) is given by

$$f_{l,i+\frac{1}{2}j+\frac{1}{2}}=\frac{f_{l,ij}+f_{l,i+ij}+f_{ij+1}+f_{l,i+1j+1}}{4}.$$

For the time integration of (2.34), one can use any ordinary differential equation solver. However, the presence of the term $1/c$ in the front of the time-derivative operator, makes the use of explicit schemes inefficient, because these explicit schemes are subject to a CFL condition of the form

$$\lambda := c\frac{\Delta t}{h}\leq 1, \tag{2.35}$$

where Δt is the time stepsize, $h := \max_{ij}\big((\Delta x)_i,(\Delta y)_j\big)$ is the mesh size and c is the speed of light (extremely large, order of speed of light). Therefore, implicit schemes which alleviate the stability restriction (2.35), should be used. For simplicity, the implicit Euler method is considered here to integrate the equations (2.34).
Let the time interval $[0,T]$ be divided into NM subintervals $[t_n,t_{n+1}]$ of length Δt such that $t_n=n\Delta t$ and $T=NM\Delta t$. The notation $W^n_{l,ij}$ is used to denote the value of the function W at $(t_n,\mu_l,\eta_l,x_i,y_j)$. Then, the fully discrete formulation of the equation (2.1) can be written as

$$\begin{aligned}\mu_l\frac{\psi^{n+1}_{l,i+1j}-\psi^{n+1}_{l,ij}}{(\Delta x)_{i+\frac{1}{2}}}+\eta_l\frac{\psi^{n+1}_{l,ij+1}-\psi^{n+1}_{l,ij}}{(\Delta y)_{j+\frac{1}{2}}} &+ \left(\sigma^{n+1}_{i+\frac{1}{2}j+\frac{1}{2}}+\kappa^{n+1}_{i+\frac{1}{2}j+\frac{1}{2}}+\frac{1}{c\Delta t}\right)\psi^{n+1}_{l,i+\frac{1}{2}j+\frac{1}{2}} = \\ &\sigma^{n+1}_{l,i+\frac{1}{2}j+\frac{1}{2}}\phi^{n+1}_{i+\frac{1}{2}j+\frac{1}{2}}+q^{n+1}_{l,i+\frac{1}{2}j+\frac{1}{2}}+\frac{1}{c\Delta t}\psi^{n}_{l,i+\frac{1}{2}j+\frac{1}{2}}.\end{aligned} \tag{2.36}$$

Once again, the discrete equation (2.36) can be reformulated in matrices as in (2.14) by using the following new matrix entries

$$\begin{aligned}
d_{l,i+\frac{1}{2}j+\frac{1}{2}} &:= \frac{|\mu_l|}{2(\Delta x)_{i+\frac{1}{2}}} + \frac{|\eta_l|}{2(\Delta y)_{j+\frac{1}{2}}} + \frac{\sigma_{i+\frac{1}{2}j+\frac{1}{2}} + \kappa_{i+\frac{1}{2}j+\frac{1}{2}} + \frac{1}{c\Delta t}}{4},\\
\bar{e}_{l,i+\frac{1}{2}j+\frac{1}{2}} &:= \frac{|\mu_l|}{2(\Delta x)_{i+\frac{1}{2}}} + \frac{-|\eta_l|}{2(\Delta y)_{j+\frac{1}{2}}} + \frac{\sigma_{i+\frac{1}{2}j+\frac{1}{2}} + \kappa_{i+\frac{1}{2}j+\frac{1}{2}} + \frac{1}{c\Delta t}}{4},\\
\underline{e}_{l,i+\frac{1}{2}j+\frac{1}{2}} &:= \frac{-|\mu_l|}{2(\Delta x)_{i+\frac{1}{2}}} + \frac{|\eta_l|}{2(\Delta y)_{j+\frac{1}{2}}} + \frac{\sigma_{i+\frac{1}{2}j+\frac{1}{2}} + \kappa_{i+\frac{1}{2}j+\frac{1}{2}} + \frac{1}{c\Delta t}}{4},\\
e_{l,i+\frac{1}{2}j+\frac{1}{2}} &:= \frac{-|\mu_l|}{2(\Delta x)_{i+\frac{1}{2}}} + \frac{-|\eta_l|}{2(\Delta y)_{j+\frac{1}{2}}} + \frac{\sigma_{i+\frac{1}{2}j+\frac{1}{2}} + \kappa_{i+\frac{1}{2}j+\frac{1}{2}} + \frac{1}{c\Delta t}}{4}.
\end{aligned}$$

The SI, BICGSTAB, GMRES, DSA methods and the Diffusion approach studied in the previous sections remain valid to solve the problem (2.36) in the same way that are done for the time-independent problem (2.11) with the only difference that another loop must be added for the time integration. Furthermore, the convergence rate of the source iteration is governed, at each time step, by the new scattering ratio

$$\gamma(t_n) := \max_{\mathbf{x}\in\mathcal{D}}\left(\frac{\sigma(t_n,\mathbf{x})}{\sigma(t_n,\mathbf{x}) + \kappa(t_n,\mathbf{x}) + \frac{1}{c\Delta t}}\right).$$

We would like to mention that, the space discretization used is second order. Therefore, to be consistent that the fully dicrestized scheme maintains the same order of accuracy, a second-order time integration scheme should be used. For example, Crank-Nicolson method can be a good candidate, since it can be formulated easily as (2.36) and the resulting linear systems have the same structures as those obtained by Euler method.

Chapter 3

Simplified $\mathrm{P_N}$ approximations for radiative heat transfer

Radiative heat transfer equations can be found in various engineering applications, for instance, heat from a stove burner [53], microwave oven [53], electromagnetic radiation from cell phones [155], laser beam [22], etc. Since a major part of this heat is transferred by photons, the numerical solution of the radiative equations can be computationally expensive and complicated because of the dependence of frequency, time and the directional variables. This is due to the involvement of the direct-dependent thermal radiation field. Approximations of the full radiative transfer model are required as they need less computational time, yet with a great solution accuracy [79]. The most common approximations used in dealing with radiative transfer equations are the spherical harmonic $\mathrm{P_N}$ approximations. The major drawback however is that the approximations become complicated specially with high order dimensions.
In this chapter, we propose the simplified $\mathrm{P_N}$ approximations as alternative approximations to the $\mathrm{P_N}$ equations. The simplified $\mathrm{P_N}$ approximations provide an extension to the approximate solution of arbitrary high order, by transforming the equation of transfer into a set of partial differential equations (PDEs). The approach was first proposed by [58] in his work on radiative transfer in stars. Further description of the method may be found in the books by [70, 19, 109] in which they dealt with the Neutron transport theory. The great advantage of these approximations is the conversion of the governing equation to relatively simple partial differential equations. This chapter focuses on the the simplified $\mathrm{P_N}$ approximations and a full description is given. The reason behind considering the $\mathrm{SP_N}$ approximations is that they offer the possibility to improve the accuracy of the solution by capturing the transport effects while still preserving the features that makes the diffusion solver attractive. Gelbard [38] introduced the simplified $\mathrm{P_N}$ approximations as an intuitive three-dimensional extension to the one-dimensional slab $\mathrm{P_N}$ formulation [103]. For any location $\mathbf{x}$ in the domain $V \subset \mathbb{R}^2$, we have the balanced equation of energy

$$C_p \rho \frac{\partial \Theta}{\partial t} - \nabla \cdot \left(\Im \nabla \Theta \right) = - \int_{\nu_1}^{\infty} \int_{s^2} \kappa (B - I) \, d\Omega \, d\nu, \tag{3.1}$$

and the transfer equation

$$\forall \nu > \nu_1, \Omega \in S^2 : \qquad \frac{1}{c} \frac{\partial I}{\partial t} + \Omega \cdot \nabla I = \kappa (B - I). \tag{3.2}$$

On the boundary, $\mathbf{x} \in \partial V$, the radiation incident is described by the semi-transparent boundary condition

$$\rho(\mathbf{n}\cdot\Omega)I(\mathbf{x},\Omega',\nu) + \Big(1-\rho(\mathbf{n}\cdot\Omega)\Big)B(\nu,\Theta_b) = I(\mathbf{x},\Omega,\nu), \qquad \forall \mathbf{n}\cdot\Omega < 0, \tag{3.3}$$

where

$$\Omega - 2(\mathbf{n}\cdot\Omega)\mathbf{n} = \Omega'$$

is the specular reflection of Ω on the surface ∂V, and the temperature satisfies

$$\hbar(\Theta_b - \Theta) + \alpha\pi\left(\frac{n_2}{n_1}\right)^2 \int_0^{\nu_1} \Big(B(\nu,\Theta_b) - B(\nu,\Theta)\Big)d\nu = \Im\nabla\Theta\cdot\mathbf{n}, \tag{3.4}$$

the temperature at initial time t = 0 is prescribed by

$$\Theta(\mathbf{x},0) = \Theta_0(\mathbf{x}), \quad \mathbf{x} \in V. \tag{3.5}$$

In the above equations, $\hbar$ denotes convective heat transfer coefficient, $\Im$ the thermal conductivity, $I(\mathbf{x},\Omega,\nu)$ the specific intensity of radiation at the point $\mathbf{x} \in V$, travelling with frequency $\nu > \nu_1$ in the direction $\Omega \in S^2$. The Temperature Θ(**x**,t) the material temperature at time ($t \geq 0$) and a direction $\mathbf{x} \in V$. As for the exterior boundary ∂V which is between the surrounding and the domain, with refractive indices $n_2 < n_1$, respectively, the light rays are refracted and reflected. Semi-transparent boundary condition in (3.3) is considered, the physics that is described next.

For all directions **x** exterior to V and for the direction Ω pointing towards V, radiation of the photon propagates in a Planckian distribution $B(\nu,\Theta_b)$ at a certain temperature Θ_b. Thus, this Planckian radiation is observed by the location **x** just outside of V for all directions of Ω satisfying $\Omega\cdot\mathbf{n} < 0$, where **n** is the outer unit normal. On ∂V of the above incident radiation, a specific fraction $[\rho(\mathbf{n}\cdot\Omega)]$ is specularly reflected back into the exterior of V, while the remaining fraction, $1-\rho(\mathbf{n}\cdot\Omega)$, penetrates through ∂V into V. The photons inside V that attempt to leak out through ∂V are applied to the same physics. Thus, for incident directions Ω of the location **x** inside of ∂V, the penetrating radiation described above is:

$$I_p(\mathbf{x},\Omega,\nu) \equiv \Big(1-\rho(\mathbf{n}\cdot\Omega)\Big)B(\nu,\Theta_b).$$

Also, the radiation which in the process of attempting to leak out through ∂V, is reflected back to V:

$$I_{refl}(\mathbf{x},\Omega,\nu) \equiv \rho(\mathbf{n}\cdot\Omega)I(\mathbf{x},\Omega',\nu).$$

The sum $I_{refl} + I_p$ constitutes the left side of equation (3.3). This boundary condition holds for location **x** just inside of ∂V. The boundary condition is given by (3.4) and the initial temperature is prescribed by (3.5). Radiation is completely absorbed in this considered work. Thus, the integration in the second term of this equation is performed on the opaque interval of the spectrum $[0,\nu_1]$. Note that, equations (3.1)-(3.5) contain the opacity $\kappa(\nu)$, the speed of light in the vacuum c, the heat conductivity $\Im$, the density ρ, the specific heat C_p, the Planck function

$$B(\nu,\Theta) = n_1^2\,\frac{2\;Pl\;\nu^3}{c^2}\left(e^{\frac{Pl\;\nu}{k_B\;\Theta}} - 1\right)^{-1},$$

where Pl is the Planck coefficient and k_B Boltzmann's constant. For industrial purposes as well as for our considerations in this study, the term $\frac{1}{c}$ in (3.2) is neclected. This is due to

the fact that the value is almost zero. The reflected proportion of radiation is the reflectivity $\rho \in [0,1]$. If the total reflection occures then it is equal to unity, i.e., if $\theta_1 > \theta_c$, where θ_c is the critical angle which is given by $\sin\theta_c = \frac{n_2}{n_1}$. Otherwise, the calculation of ρ is carried out according to Fresnel's equation

$$\rho(\mu) = \frac{1}{2}\left[\frac{\tan^2(\theta_1-\theta_2)}{\tan^2(\theta_1+\theta_2)} + \frac{\sin^2(\theta_1-\theta_2)}{\sin^2(\theta_1+\theta_2)}\right],$$

where the fraction angles θ_1 and θ_2 are given by $\cos\theta_1 = |\mathbf{n}\cdot\Omega| = \mu$ and the Snell's law of refraction

$$n_1 \sin\theta_1 = n_2 \sin\theta_2.$$

Finally, the boundary surface of (3.4) of the hemispheric emissivity α is related to the reflectivity ρ by

$$\alpha = 2n_1 \int_0^1 \Big(1-\rho(\mu)\Big)d\mu.$$

We will focus here on optically thick problems. This means that the opacity κ is large and the radiation propagates mainly in a diffused-like manner. We rewrite the above equations in dimensionless form in order to introduce a proper scaling. We introduce reference values that corresponds to typical values of the physical quantities.

$$t_{ref} = c\ \rho\ \kappa_{ref}\ \mathbf{x}_{ref}^2\ \frac{\Theta_{ref}}{I_{ref}} \quad \text{and} \quad \Im_{ref} = \frac{I_{ref}}{\kappa_{ref}\Theta_{ref}}.$$

Here, we define the dimensionless parameters:

$$\varepsilon = \frac{1}{\kappa_{ref} x_{ref}},$$

which satisfies $0 < \varepsilon << 1$ in the diffusive, optically thick regime. The non-dimensional equations read

$$\varepsilon^2 \nabla\cdot\Big(\Im\nabla\Theta\Big) - \varepsilon^2\frac{\partial\Theta}{\partial t} = -\int_{\nu_1}^{\infty}\int_{S^2}\kappa(B-I)d\Omega\ d\nu, \tag{3.6a}$$

$$\forall \nu > \nu_1, \Omega\in S^2: \qquad \varepsilon\ \Omega\cdot\nabla I = \kappa(B-I). \tag{3.6b}$$

The boundary condition for the temperature becomes

$$\varepsilon\Big(\Im\ \nabla\Theta\Big)\cdot\mathbf{n} - \hbar(\Theta_b-\Theta) = \alpha\pi\left(\frac{n_2}{n_1}\right)^2\int_0^{\nu_1}\Big(B(\nu,\Theta_b)-B(\nu,\Theta)\Big)d\nu. \tag{3.7}$$

It is worth mentioning that the initial condition for the temperature in (3.4) will not be affected by this conversion to dimensionless variables. It is well known that an asymptotic expansion of (3.6a) and (3.6b) leads to the Rosseland approximation or the equilibrium diffusion

$$\frac{\partial\Theta}{\partial t} - \nabla\cdot\Big(\Im + \Im_r(\Theta)\Big)\nabla\Theta = 0, \qquad \text{with } \Im_r(\Theta) = \frac{4\pi}{3}\int_{\nu_1}^{\infty}\frac{1}{\kappa}\frac{\partial B}{\partial\Theta}\ d\nu, \tag{3.8}$$

which is expected to be valid in the interior of V [78, 121, 122]. However, boundary layers can not be described by this simple diffusion approximation in the regions in which the temperature gradients are very large. Thus, the need arises for more sophisticated diffusion approximations

that can model the boundary layers at internal interfaces and the outer boundary of the system. For the Neutron transport, simplified P_N approximations are used for high-order asymptotic corrections to the diffusion theory, see for instance [12, 38, 77, 147]. The simplified P_N approximations can accurately describe the boundary layers and the diffusion of Neutrons. This chapter proceeds as follows. In section 3.1, asymptotic expansions to (3.6a) and (3.6b) are derived. We couple the frequency-dependent diffusion equations to each other as well as to the frequency-independent heat transfer equation (3.6a). Boundary conditions for the SP_N equations are formulated in section 3.2. A summary of the SP_N approximations is outlined in section 3.3. Finally, concluding remarks are discussed in section 3.5.

3.1 Asymptotic derivations of SP_N equations

In order to derive (3.6b) in the domain V, the equation can be formulated as

$$\left(1+\frac{\varepsilon}{\kappa}\Omega\cdot\nabla\right)I(\mathbf{x},\Omega,\nu)=B(\nu,\Theta).$$

By applying the Neumann series, we obtain

$$\begin{aligned} I &= \left(1+\frac{\varepsilon}{\kappa}\Omega\cdot\nabla\right)^{-1}B(\nu,\Theta)\\ &\cong \left(1-\frac{\varepsilon}{\kappa}\Omega\cdot\nabla+\frac{\varepsilon^2}{\kappa^2}(\Omega\cdot\nabla)^2-\frac{\varepsilon^3}{\kappa^3}(\Omega\cdot\nabla)^3+\frac{\varepsilon^4}{\kappa^4}(\Omega\cdot\nabla)^4\cdots\right)B(\nu,\Theta). \end{aligned} \tag{3.9}$$

By integrating with respect to Ω where $\nabla^2=\nabla\cdot\nabla$, and using [103]:

$$\int_{S^2}(\Omega\cdot\nabla)^n d\Omega=\left(1+(-1)^n\right)\frac{2\pi}{n+1}\nabla^n,$$

we obtain

$$\varphi(\mathbf{x})=\int_{S2}I d\Omega=4\pi\left(1+\frac{\varepsilon^2}{3\kappa^2}\nabla^2+\frac{\varepsilon^4}{5\kappa^4}\nabla^4+\frac{\varepsilon^6}{7\kappa^6}\nabla^6\cdots\right)B(\nu,\Theta)+\mathcal{O}(\varepsilon^8). \tag{3.10}$$

Hence,

$$\begin{aligned} 4\pi B(\nu,\Theta) &= \left(1+\frac{\varepsilon^2}{3\kappa^2}\nabla^2+\frac{\varepsilon^4}{5\kappa^4}\nabla^4+\frac{\varepsilon^6}{7\kappa^6}\nabla^6\right)^{-1}\varphi+\mathcal{O}(\varepsilon^8)\\ &= \left(1-\left(\frac{\varepsilon^2}{3\kappa^2}\nabla^2+\frac{\varepsilon^4}{5\kappa^4}\nabla^4+\frac{\varepsilon^6}{7\kappa^6}\nabla^6\right)+\left(\frac{\varepsilon^2}{3\kappa^2}\nabla^2+\frac{\varepsilon^4}{5\kappa^4}\nabla^4+\frac{\varepsilon^6}{7\kappa^6}\nabla^6\right)^2\right.\\ &- \left.\left(\frac{\varepsilon^2}{3\kappa^2}\nabla^2+\frac{\varepsilon^4}{5\kappa^4}\nabla^4+\frac{\varepsilon^6}{7\kappa^6}\nabla^6\right)^3\cdots\right)\varphi+\mathcal{O}(\varepsilon^8). \end{aligned}$$

The formal asymptotic equation for φ yields:

$$\forall\nu>\nu_1: 4\pi B(\nu,\Theta)=\left(1-\frac{\varepsilon^2}{3\kappa^2}\nabla^2-\frac{4\varepsilon^4}{45\kappa^4}\nabla^4-\frac{44\varepsilon^6}{945\kappa^6}\nabla^6\right)\varphi+\mathcal{O}(\varepsilon^8). \tag{3.12}$$

Taking the terms of $\mathcal{O}(\varepsilon^4)$ and $\mathcal{O}(\epsilon^6)$ into consideration, the approximations are independent of Ω and angle variation.

3.1.1 Formulation of the Rosseland and SP_1 approximations

In this following subsection, we truncate (3.12) up to $\mathcal{O}(\varepsilon^4)$:

$$4\pi B(\nu,\Theta) = \varphi - \frac{\varepsilon^2}{3\kappa^2}\nabla^2\varphi + \mathcal{O}(\varepsilon^4),$$

we obtain:

$$\forall \nu > \nu_1 : \qquad -\frac{\varepsilon^2}{3\kappa}\nabla^2\varphi + \kappa\varphi = \kappa(4\pi B(\nu,\Theta)). \tag{3.13}$$

The derivation of (3.12), we have written κ as independent of space although it is dependent of space. It remains correct from the asympotical point of view. Thus, we can consider the energy equation (3.6a) up to $\mathcal{O}(\varepsilon^2)$,

$$\frac{\partial\Theta}{\partial t} - \nabla\cdot\left(\Im\nabla\Theta\right) = \int_{\nu_1}^{\infty}\frac{1}{3\kappa}\nabla^2\varphi\ d\nu. \tag{3.14}$$

Equations (3.13) and (3.14) are the SP_1 approximation to (3.6a) and (3.6b). Due to the $\mathcal{O}(\varepsilon^2)$ error in (3.14), the SP_1 error is $\mathcal{O}(\varepsilon^2)$. With the use of $\varphi = 4\pi B(\nu,\Theta) + \mathcal{O}(\varepsilon^2)$ in (3.14), we can truncate to $\mathcal{O}(\varepsilon^2)$ equation

$$\begin{aligned}
\frac{\partial\Theta}{\partial t} - \nabla\cdot\left(\Im\nabla\Theta\right) &= \int_{\nu_1}^{\infty}\nabla\cdot\frac{1}{3\kappa}\nabla(4\pi B)\ d\nu,\\
\frac{\partial\Theta}{\partial t} - \nabla\cdot\left(\Im\nabla\Theta\right) &= \nabla\cdot\left(\frac{4\pi}{3}\int_{\nu_1}^{\infty}\frac{1}{\kappa}\frac{\partial B}{\partial\Theta}\ d\nu\right)\nabla\Theta.
\end{aligned} \tag{3.15a}$$

Due to the presence of the frequency variable ν, equations (3.13) and (3.14) are easier to solve compared to (3.15a) because of the existence of non-linearity in (3.15a).

3.1.2 Formulation of the SP_3 approximation

By ignoring the terms of $\mathcal{O}(\varepsilon^8)$ in (3.12), we obtain

$$\begin{aligned}
4\pi B(\nu,\Theta) &= \varphi - \frac{\varepsilon^2}{3\kappa^2}\nabla^2\left(\varphi + \frac{4\varepsilon^2}{15\kappa^2}\nabla^2\varphi + \frac{44\varepsilon^4}{315\kappa^4}\nabla^4\varphi\right) + \mathcal{O}(\varepsilon^8)\\
&= \varphi - \frac{\varepsilon^2}{3\kappa^2}\nabla^2\left(\varphi + \left(1 + \frac{11\varepsilon^2}{21\kappa^2}\nabla^2\right)\left(\frac{4\varepsilon^2}{15\kappa^2}\nabla^2\varphi\right)\right) + \mathcal{O}(\varepsilon^8)\\
&= \varphi - \frac{\varepsilon^2}{3\kappa^2}\nabla^2\left(\varphi + \left(1 - \frac{11\varepsilon^2}{21\kappa^2}\nabla^2\right)^{-1}\left(\frac{4\varepsilon^2}{15\kappa^2}\nabla^2\varphi\right)\right) + \mathcal{O}(\varepsilon^8).
\end{aligned} \tag{3.16}$$

Hence, by defining

$$\varphi_2 \equiv \left(1 - \frac{11}{21}\frac{\varepsilon^2}{\kappa^2}\nabla^2\right)^{-1}\left(\frac{2\varepsilon^2}{15\kappa^2}\nabla^2\varphi\right), \tag{3.17}$$

then, in (3.16) up to $\mathcal{O}(\varepsilon^8)$, it becomes

$$4\pi B(\nu,\Theta) = \varphi - \frac{\varepsilon^2}{3\kappa^2}\nabla^2(\varphi + 2\varphi_2),$$

or

$$\forall \nu > \nu_1 : \qquad -\varepsilon^2\nabla\cdot\frac{1}{3\kappa}\nabla(\varphi + 2\varphi_2) + \kappa\varphi = \kappa(4\pi B(\nu,\Theta)). \tag{3.18}$$

Hence, equation (3.17) can be written as:

$$\begin{aligned} -\frac{11}{21}\frac{\varepsilon^2}{\kappa^2}\nabla^2\varphi^2+\varphi_2 &= \frac{2}{15}\frac{\varepsilon^2}{\kappa^2}\nabla^2\varphi=\frac{2}{5}\bigg(\frac{\varepsilon^2}{3\kappa^2}\nabla^2\varphi\bigg),\\ &= \frac{2}{5}\bigg[-4\pi B(\nu,\Theta)+\varphi-\frac{2\varepsilon^2}{3\kappa^2}\nabla^2\varphi_2\bigg], \end{aligned}$$

or

$$\frac{2}{5}(\varphi-4\pi B(\nu,\Theta))=\bigg(\frac{4}{15}-\frac{11}{21}\bigg)\frac{\varepsilon^2}{\kappa^2}\varphi_2+\varphi_2,$$

or eventually:

$$\forall\nu>\nu_1: \qquad -\varepsilon^2\nabla\cdot\frac{9}{35\kappa}\nabla\varphi_2+\kappa\varphi_2-\frac{2}{5}\kappa\varphi=\frac{2}{5}\kappa(4\pi B(\nu,\Theta)). \tag{3.20}$$

By (3.18), we get up to $\mathcal{O}(\varepsilon^6)$

$$-\varepsilon^2\int_{\nu_1}^{\infty}\nabla\cdot\frac{1}{3\kappa}\nabla(\varphi+2\varphi_2)\;d\nu=\int_{\nu_1}^{\infty}\int_{S^2}\kappa(B(\nu,\Theta)-I)\;d\Omega\;d\nu.$$

Thus, the energy equation (3.6b) becomes:

$$\frac{\partial\Theta}{\partial t}-\nabla\cdot\bigg(\Im\nabla\Theta\bigg)=\int_{\nu_1}^{\infty}\nabla\cdot\frac{1}{3\kappa}\nabla(\varphi+2\varphi_2)\;d\nu. \tag{3.21}$$

Equation (3.21) and the two approximate equations (3.18) and (3.20) form the SP_3 approximation to (3.6a) and (3.6b). The SP_3 equations can be expressed in an algebraically simpler way. First, we multiply $\theta\times|(3.18)|+(3.20)$:

$$\kappa\bigg(\theta-\frac{2}{5}\bigg)(4\pi B)=-\varepsilon^2\nabla\cdot\frac{1}{\kappa}\nabla\bigg(\frac{\theta}{3}(\varphi+2\varphi_2)+\frac{9}{35}\varphi_2\bigg)+\kappa\bigg(\theta\varphi+\varphi_2-\frac{2}{5}\varphi\bigg).$$

Value of θ is required so that two functions in the braces on the right are scalars multiplies by each other. The required values of θ are needed such that

$$\mu^2\bigg(\theta\varphi+\varphi_2-\frac{2}{5}\varphi\bigg)=\frac{\theta}{3}(\varphi+2\varphi_2)+\frac{9}{35}\varphi_2, \tag{3.22}$$

where $\mu^2>0$ is a constant needed to be calculated. The challenge in equation (3.22) is that it has two unknowns φ and φ_2. To overcome this difficulty, we reformulate equation (3.22) in this form:

$$\frac{\theta}{3}=\mu^2\bigg(\theta-\frac{2}{5}\bigg) \quad\text{and}\quad \mu^2=\frac{2\theta}{3}+\frac{9}{35}.$$

By eliminating θ, we get a quadratic equation in μ^2,

$$\mu^2\bigg(\frac{2}{3}\mu^2-\frac{11}{14}\bigg)=\frac{1}{2}\mu^2-\frac{9}{70},$$

which has two positive solutions,

$$\mu_1^2=\frac{3}{7}-\frac{2}{7}\sqrt{\frac{6}{5}} \qquad\text{and}\qquad \mu_2^2=\frac{3}{7}+\frac{2}{7}\sqrt{\frac{6}{5}}.$$

The corresponding values of θ are

$$\theta_1 = \frac{9}{35} - \frac{3}{7}\sqrt{\frac{6}{5}} \qquad \text{and} \qquad \theta_2 = \frac{9}{35} + \frac{3}{7}\sqrt{\frac{6}{5}}.$$

Relation (3.22) implies, for n = 1, 2,

$$\left(\theta_n - \frac{2}{5}\right)\kappa(4\pi B(\nu,\Theta)) = \left(-\nabla\cdot\left(\frac{\varepsilon^2\mu_n^2}{\kappa}\nabla\right) + \kappa\right)\left(\theta_n\varphi + \varphi_2 - \frac{2}{5}\varphi\right). \tag{3.23}$$

This suggests that two new independent variables are needed to be defined for $n = 1, 2$,

$$\psi_n = \frac{\theta_n\varphi + \varphi_2 - 2/5\varphi}{\theta_n - 2/5} = \varphi + \frac{\varphi_2}{\theta_n - 2/5} = \varphi + \gamma_n\theta_2, \tag{3.24}$$

where

$$\gamma_n = \frac{1}{\theta_n - 2/5} = \frac{5}{7}\left(1 + (-1)^n 3\sqrt{\frac{6}{5}}\right).$$

The two equations in (3.23) become

$$\kappa(4\pi B(\nu,\Theta)) = -\nabla\cdot\left(\frac{\varepsilon^2\mu_1^2}{\kappa}\nabla\psi_1\right) + \kappa\psi_1, \tag{3.25a}$$

$$\kappa(4\pi B(\nu,\Theta)) = -\nabla\cdot\left(\frac{\varepsilon^2\mu_2^2}{\kappa}\nabla\psi_2\right) + \kappa\psi_2. \tag{3.25b}$$

The diffusion equations are uncoupled in this form the of SP_3 equations. However, a weak coupling is still a drawback and it is shown in subsection 3.2. We used the linear transformation of variables above according to the formula,

$$\varphi = \frac{\gamma_2\psi_1 - \gamma_1\psi_2}{\gamma_2 - \gamma_1} \qquad \text{and} \qquad \varphi_2 = \frac{\psi_2 - \psi_1}{\gamma_2 - \gamma_1}. \tag{3.26}$$

The three constants can be defined as [79]:

$$\omega_0 = \frac{1}{\gamma_2 - \gamma_1} \;=\; \frac{7}{30}\sqrt{\frac{5}{6}} = \frac{7}{36}\sqrt{\frac{6}{5}}, \tag{3.27a}$$

$$\omega_1 = \frac{\gamma_2}{\gamma_2 - \gamma_1} = \frac{1}{6}\left(3 + \sqrt{\frac{5}{6}}\right) \quad , \qquad \omega_2 = \frac{-\gamma_1}{\gamma_2 - \gamma_1} = \frac{1}{6}\left(3 - \sqrt{\frac{5}{6}}\right), \tag{3.27b}$$

φ and φ_2 can be written as $\varphi = \omega_1\psi_1 + \omega_2\psi_2$ and $\varphi_2 = \omega_0(\psi_2 - \psi_1)$ respectively. This can lead to:

$$\frac{1}{3}(\varphi + 2\varphi_2) = \frac{1}{3}(\omega_1 - 2\omega_0)\psi_1 + \frac{1}{3}(\omega_2 + 2\omega_0)\psi_2 = a_1\psi_1 + a_2\psi_2.$$

Two constants are introduced here, which are equal to:

$$a_1 = \frac{\omega_1 - 2\omega_0}{3} = \frac{1}{30}\left(5 - 3\sqrt{\frac{5}{6}}\right), \quad a_2 = \frac{\omega_2 + 2\omega_0}{3} = \frac{1}{30}\left(5 + 3\sqrt{\frac{5}{6}}\right). \tag{3.28}$$

The SP_3 equations (3.21) becomes:

$$\nabla\cdot\left(\Im\nabla\Theta\right) + \int_{\nu_1}^{\infty}\nabla\cdot\frac{1}{\kappa}\nabla(a_1\psi_1 + a_2\psi_2)\,d\nu = \frac{\partial\Theta}{\partial t}. \tag{3.29}$$

The SP_3 equations (3.25) and (3.29) are asymptotic when either κ is independent of space or the problem has a planar-geometry space dependence.

3.2 Derivation of the simplified P_N boundary conditions

Developed boundary conditions for the SP_1 and SP_3 approximations, the transport problem in (3.6b) with the boundary condition in (3.3) are taken into account. The transport equation (3.6b) is considered

$$\forall \nu > \nu_1 : \qquad \varepsilon\ \Omega \cdot \nabla I(\mathbf{x}, \Omega) + \kappa I(\mathbf{x}, \Omega) = \kappa B(\nu, \Theta), \quad \mathbf{x} \in V,$$

with semi-transparent boundary conditions on ∂V

$$I(\mathbf{x}, \Omega) = \rho(n \cdot \Omega) I(\mathbf{x}, \Omega') + \Big(1 - \rho(\mathbf{n} \cdot \Omega)\Big) B(\nu, \Theta_b), \quad \mathbf{n} \cdot \Omega < 0.$$

Same like what has been defined earlier, the mean radiative intensity:

$$\varphi(\mathbf{x}) = \int_{S^2} I(\mathbf{x}, \Omega)\ d\Omega.$$

The two integrals of the penetration radiation are also defined from $mi = 1$ and 3,

$$\begin{aligned} I_{mi}(\mathbf{x}, \nu) &= \int_{\mathbf{n}.\Omega<0} P_{mi}(|\Omega \cdot \mathbf{n}|) I_p(\Omega, \nu)\ d\Omega \\ &= \left(\int_{\mathbf{n}.\Omega<0} P_{mi}(|\Omega \cdot \mathbf{n}|)[1 - \rho(\mathbf{n} \cdot \Omega)]\ d\Omega \right) B(\nu, \Theta_b) \\ &= \left(2\pi \int_0^1 P_{mi}(\mu)[1 - \rho(-\mu)] d\mu \right) B(\nu, \Theta_b) \\ &= \rho_{mi} B(\nu, \Theta_b), \end{aligned} \tag{3.30}$$

where

$$\rho_{mi} = \begin{cases} (1 - 2r_1)\pi, & mi = 1, \\ -(\frac{1}{4} + 2r_5)\pi, & mi = 3. \end{cases} \tag{3.31}$$

Here, the Legendre polynomials of order 1 and 3 are used,

$$P_1(\mu) = \mu \quad \text{and} \quad P_3(\mu) = \frac{5}{2}\mu^3 - \frac{3}{2}\mu,$$

and the integrals are defined as:

$$\begin{aligned} r_1 &= \int_0^1 \mu\rho(-\mu)\ d\mu, & r_5 &= \int_0^1 P_3(\mu)\rho(-\mu)\ d\mu, \\ r_2 &= \int_0^1 \mu^2\rho(-\mu)\ d\mu, & r_6 &= \int_0^1 P_2(\mu)P_3(\mu)\rho(-\mu)\ d\mu, \\ r_3 &= \int_0^1 \mu^3\rho(-\mu)\ d\mu, & r_7 &= \int_0^1 P_3(\mu)P_3(\mu)\rho(-\mu)\ d\mu, \\ r_4 &= \int_0^1 \mu P_3(\mu)\rho(-\mu)\ d\mu. \end{aligned}$$

The boundary condition for φ in the SP_1 approximation (3.13) is

$$\forall \nu > \nu_1 : \qquad \varphi(\mathbf{x}) + \left(\frac{1 + 3r_2}{1 - 2r_1} \frac{2\varepsilon}{3\kappa} \right) \mathbf{n} \cdot \nabla\varphi(\mathbf{x}) = 4\pi B_b(\nu, \Theta_b), \tag{3.33}$$

where $B(\nu,\Theta_b) = B(\nu,\Theta_b(\mathbf{x}))$. For all frequencies $\nu > \nu_1$ and $\mathbf{x} \in \partial V$, the SP_3 boundary conditions for φ and φ_2 in (3.18) and (3.20) are [12]:

$$\begin{aligned}(1-2r_1)\frac{1}{4}\varphi(\mathbf{x}) + (1-8r_3)\frac{5}{16}\varphi_2(\mathbf{x}) + (1+3r_2)\frac{\varepsilon}{6\kappa}\mathbf{n}\cdot\nabla\varphi(\mathbf{x})\\ +\left(\frac{1+3r_2}{3}+\frac{3r_4}{2}\right)\frac{2\varepsilon}{3\kappa}\mathbf{n}\cdot\nabla\varphi_2(\mathbf{x}) = \rho_1 B(\nu,\Theta_b), \qquad (3.34a)\\ -(1+8r_5)\frac{1}{16}\varphi(\mathbf{x}) + (1-8r_6)\frac{5}{16}\varphi_2(\mathbf{x}) + 3r_4\frac{\varepsilon}{6\kappa}\mathbf{n}\cdot\nabla\varphi(\mathbf{x})\\ +\left(r_4+\frac{3}{14}(1+7r_7)\right)\frac{\varepsilon}{\kappa}\mathbf{n}\cdot\nabla\varphi_2(\mathbf{x}) = \rho_3 B(\nu,\Theta_b), \qquad (3.34b)\end{aligned}$$

or in a formal style:

$$\begin{aligned}A_1\varphi(\mathbf{x}) + A_2\varphi_2(\mathbf{x}) + A_3\frac{\varepsilon}{\kappa}\mathbf{n}\cdot\nabla\varphi(\mathbf{x}) + A_4\frac{\varepsilon}{\kappa}n\cdot\varphi_2(\mathbf{x}) = \rho_1 B(\nu,\Theta_b),\\ B_1\varphi(\mathbf{x}) + B_2\varphi_2(\mathbf{x}) + B_3\frac{\varepsilon}{\kappa}\mathbf{n}\cdot\nabla\varphi(\mathbf{x}) + B_4\frac{\varepsilon}{\kappa}\mathbf{n}\cdot\nabla\varphi_2(\nu,\Theta_b) = \rho_3 B(\nu,\Theta_b).\end{aligned}$$

By using the formula in (3.26), the above boundary conditions can be transformed for φ and φ_2 into boundary conditions for ψ_1 and ψ_2. We obtain

$$\begin{aligned}\omega_0(\gamma_2A_1 - A_2)\psi_1 + \omega_0(A_2-\gamma_1A_1)\psi_2 + \omega_0(\gamma_2A_3-A_4)\frac{\varepsilon}{\kappa}\mathbf{n}\cdot\nabla\psi_1\\ +\omega_0(A_4-\gamma_1A_3)\frac{\varepsilon}{\kappa}\mathbf{n}\cdot\nabla\psi_2 = \rho_1 B(\nu,\Theta_b),\\ \omega_0(\gamma_2B_1 - B_2)\psi_1 + \omega_0(B_2-\gamma_1B_1)\psi_2 + \omega_0(\gamma_2B_3-B_4)\frac{\varepsilon}{\kappa}\mathbf{n}\cdot\nabla\psi_1\\ +\omega_0(B_4-\gamma_1B_3)\frac{\varepsilon}{\kappa}\mathbf{n}\cdot\nabla\psi_2 = \rho_3 B(\nu,\Theta_b),\end{aligned}$$

or, we can formally rewrite for convenience,

$$\begin{aligned}\rho_1 B = C_1\psi_1 + C_2\psi_2 + C_3\frac{\varepsilon}{\kappa}\mathbf{n}\cdot\nabla\psi_1 + C_4\frac{\varepsilon}{\kappa}\mathbf{n}\cdot\nabla\psi_2,\\ \rho_3 B = D_1\psi + D_2\psi_2 + D_3\frac{\varepsilon}{\kappa}\mathbf{n}\cdot\nabla\psi_1 + D_4\frac{\varepsilon}{\kappa}\mathbf{n}\cdot\nabla\psi_2.\end{aligned}$$

The gradient terms $\mathbf{n}\cdot\nabla\psi_2$ in the first equation and $\mathbf{n}\cdot\nabla\psi_1$ in the second equation are eliminated to get the boundary conditions for both ψ_1 and ψ_2 equations. This becomes:

$$\begin{aligned}(C_1D_4 - D_1C_4)\psi_1 + (C_3D_4-D_3C_4)\frac{\varepsilon}{\kappa}\mathbf{n}\cdot\nabla\psi_1 = -(C_2D_4-D_2C_4)\psi_2 + (D_4\rho_1 - C_4\rho_3)B,\\ -(C_2D_3 - D_2C_3)\psi_2 + (C_3D_4-D_3C_4)\frac{\varepsilon}{\kappa}\mathbf{n}\cdot\nabla\psi_2 = (C_1D_3-D_1C_3)\psi_1 - (D_3\rho_1 - C_3\rho_3)B.\end{aligned}$$

Thus, by setting $D = C_3D_4 - D_3C_4$ and defining constants

$$\begin{aligned}\alpha_1 &= \frac{C_1D_4 - D_1C_4}{D}, \qquad \alpha_2 = \frac{C_3D_2 - C_2D_3}{D},\\ \beta_1 &= \frac{C_3D_1 - D_3C_1}{D}, \qquad \beta_2 = \frac{C_2D_4 - C_4D_2}{D},\\ \eta_1 &= \frac{D_4\rho_1 - C_4\rho_3}{D}, \qquad \eta_2 = \frac{C_3\rho_3 - D_3\rho_1}{D},\end{aligned}$$

we get the following boundary conditions for the SP_3:

$$-\beta_2\psi_2(\mathbf{x}) + \eta_1 B(\nu,\Theta_b) = \alpha_1\psi_1(\mathbf{x}) + \frac{\varepsilon}{\kappa}\mathbf{n}\cdot\nabla\psi_1(\mathbf{x}), \tag{3.40a}$$

$$-\beta_1\psi_1(\mathbf{x}) + \eta_2 B(\nu,\Theta_b) = \alpha_2\psi_2(\mathbf{x}) + \frac{\varepsilon}{\kappa}\mathbf{n}\cdot\nabla\psi_2(\mathbf{x}). \tag{3.40b}$$

Equations (3.40a) and (3.40b) are compatible with the diffusion equations (3.25a) and (3.25b), respectively with a weak coupling of ψ_1 and ψ_2. If we consider that no reflection is occurring ($\rho = 0$), then all the constants from r_1 to r_7 will be zero. The value of $D = \frac{1}{144}\sqrt{6/5}$ and all the constants in (3.40a) and (3.40b) are:

$$\alpha_1 = \frac{5}{96}\Big(34 + 11\sqrt{\frac{5}{6}}\Big), \qquad \alpha_2 = \frac{5}{96}\Big(34 - 11\sqrt{\frac{5}{6}}\Big),$$
$$\beta_1 = \frac{5}{96}\Big(2 - \sqrt{\frac{5}{6}}\Big), \qquad \beta_2 = \frac{5}{96}\Big(2 + \sqrt{\frac{5}{6}}\Big),$$
$$\eta_1 = \frac{5\pi}{2}\Big(3 + \sqrt{\frac{5}{6}}\Big), \qquad \eta_2 = \frac{5\pi}{2}\Big(3 - \sqrt{\frac{5}{6}}\Big).$$

The above equations can be performed for any other boundary conditions.

3.3 Summary of the SP_N approximations

In this section we summarize the governing equation for SP_1 and SP_3 approximations for radiative heat transfer in both gray and nongray media.

3.3.1 SP_N equations for nongray media

For the SP_1 approximation:

$$\begin{aligned} \varepsilon^2\frac{\partial\Theta}{\partial t} - \varepsilon^2\nabla\cdot\Big(\Im\nabla\Theta\Big) &= -\int_{\nu_1}^{\infty}\kappa(4\pi B(\nu,\Theta)-\varphi)d\Omega\, d\nu, \\ -\nabla\cdot\Big(\frac{\varepsilon^2}{3\kappa}\nabla\varphi\Big) + \kappa\varphi &= 4\pi\kappa B(\nu,\Theta), \end{aligned} \tag{3.41}$$

equipped with the following boundary conditions

$$\begin{aligned} \varepsilon\Big(\Im\,\nabla\Theta\Big)\cdot\mathbf{n} - \hbar(\Theta_b-\Theta) &= \alpha\pi\Big(\frac{n_2}{n_1}\Big)^2\int_0^{\nu_1}\Big(B(\nu,\Theta_b)-B(\nu,\Theta)\Big)d\nu, \\ \varphi + \left(\frac{1+3r_2}{1-2r_1}\frac{2\varepsilon}{3\,(\kappa+\sigma)}\right)\mathbf{n}(\hat{\mathbf{x}})\cdot\nabla\varphi &= 4\pi B(\nu,\Theta_b), \end{aligned} \tag{3.42}$$

and initial condition

$$\Theta(\mathbf{x},0) = \Theta_0(\mathbf{x}). \tag{3.43}$$

In (3.41)-(3.42), the Planck function $B(\nu,\Theta)$ is defined as

$$B(\nu,\Theta) = n_1^2\,\frac{2\;Pl\;\nu^3}{c^2}\left(e^{\frac{Pl\;\nu}{k_B\;\Theta}}-1\right)^{-1},$$

and the variables r_1 and r_2 appeared in the boundary conditions are defined above.

For the SP_3 approximation:

$$\begin{aligned}
\varepsilon^2\frac{\partial\Theta}{\partial t}-\varepsilon^2\nabla\cdot\Big(\Im\nabla\Theta\Big) &= -\int_{\nu_1}^{\infty}\kappa(4\pi B(\nu,\Theta)-\varphi)d\Omega\ d\nu,\\
-\nabla\cdot\Big(\frac{\varepsilon^2\mu_1^2}{\kappa}\nabla\psi_1\Big)+\kappa\psi_1 &= 4\pi\kappa B(\nu,\Theta),\\
-\nabla\cdot\Big(\frac{\varepsilon^2\mu_2^2}{\kappa}\nabla\psi_2\Big)+\kappa\psi_2 &= 4\pi\kappa B(\nu,\Theta),
\end{aligned}\tag{3.44}$$

equipped with the following boundary conditions

$$\begin{aligned}
\varepsilon\Big(\Im\ \nabla\Theta\Big)\cdot\mathbf{n}-\hbar(\Theta_b-\Theta) &= \alpha\pi\Big(\frac{n_2}{n_1}\Big)^2\int_0^{\nu_1}\Big(B(\nu,\Theta_b)-B(\nu,\Theta)\Big)d\nu,\\
\alpha_1\psi_1+\frac{\varepsilon}{\kappa}\mathbf{n}(\hat{\mathbf{x}})\cdot\nabla\psi_1 &= -\beta_2\psi_2+\eta_1 B(\nu,\Theta_b),\\
\alpha_2\psi_2+\frac{\varepsilon}{\kappa}\mathbf{n}(\hat{\mathbf{x}})\cdot\nabla\psi_2 &= -\beta_1\psi_1+\eta_2 B(\nu,\Theta_b),
\end{aligned}\tag{3.45}$$

and initial condition

$$\Theta(\mathbf{x},0)=\Theta_0(\mathbf{x}).\tag{3.46}$$

3.3.2 SP_N equations for gray media

For the SP_1 approximation:

$$\begin{aligned}
\varepsilon^2\frac{\partial\Theta}{\partial t}-\varepsilon^2\nabla\cdot\Big(\Im\nabla\Theta\Big) &= -\kappa\big(4\pi B(\Theta)-\varphi\big),\\
-\nabla\cdot\Big(\frac{\varepsilon^2}{3\kappa}\nabla\varphi\Big)+\kappa\varphi &= 4\pi\kappa B(\Theta),
\end{aligned}\tag{3.47}$$

equipped with the following boundary conditions

$$\begin{aligned}
\varepsilon\Big(\Im\ \nabla\Theta\Big)\cdot\mathbf{n}-\hbar(\Theta_b-\Theta) &= \alpha\pi\Big(\frac{n_2}{n_1}\Big)^2\Big(B(\Theta_b)-B(\Theta)\Big)d\nu,\\
\varphi+\frac{2\varepsilon}{3\kappa+}\mathbf{n}(\hat{\mathbf{x}})\cdot\nabla\varphi &= 4\pi B(\Theta_b),
\end{aligned}\tag{3.48}$$

and initial condition

$$\Theta(\mathbf{x},0)=\Theta_0(\mathbf{x}).\tag{3.49}$$

In (3.47)-(3.48), the Planck function $B(\Theta)$ is defined as

$$B(\Theta)=\sigma_B\Theta^4,$$

where σ_B is the Boltzmann coefficient.

For the SP_3 approximation:

$$\begin{aligned}
\varepsilon^2\frac{\partial\Theta}{\partial t}-\varepsilon^2\nabla\cdot\Big(\Im\nabla\Theta\Big) &= -\kappa\left(4\pi B(\Theta)-\frac{\gamma_2\psi_1-\gamma_1\psi_2}{\gamma_2-\gamma_1}\right),\\
-\nabla\cdot\Big(\frac{\varepsilon^2\mu_1^2}{\kappa}\nabla\psi_1\Big)+\kappa\psi_1 &= 4\pi\kappa B(\Theta),\\
-\nabla\cdot\Big(\frac{\varepsilon^2\mu_2^2}{\kappa}\nabla\psi_2\Big)+\kappa\psi_2 &= 4\pi\kappa B(\Theta),
\end{aligned}\tag{3.50}$$

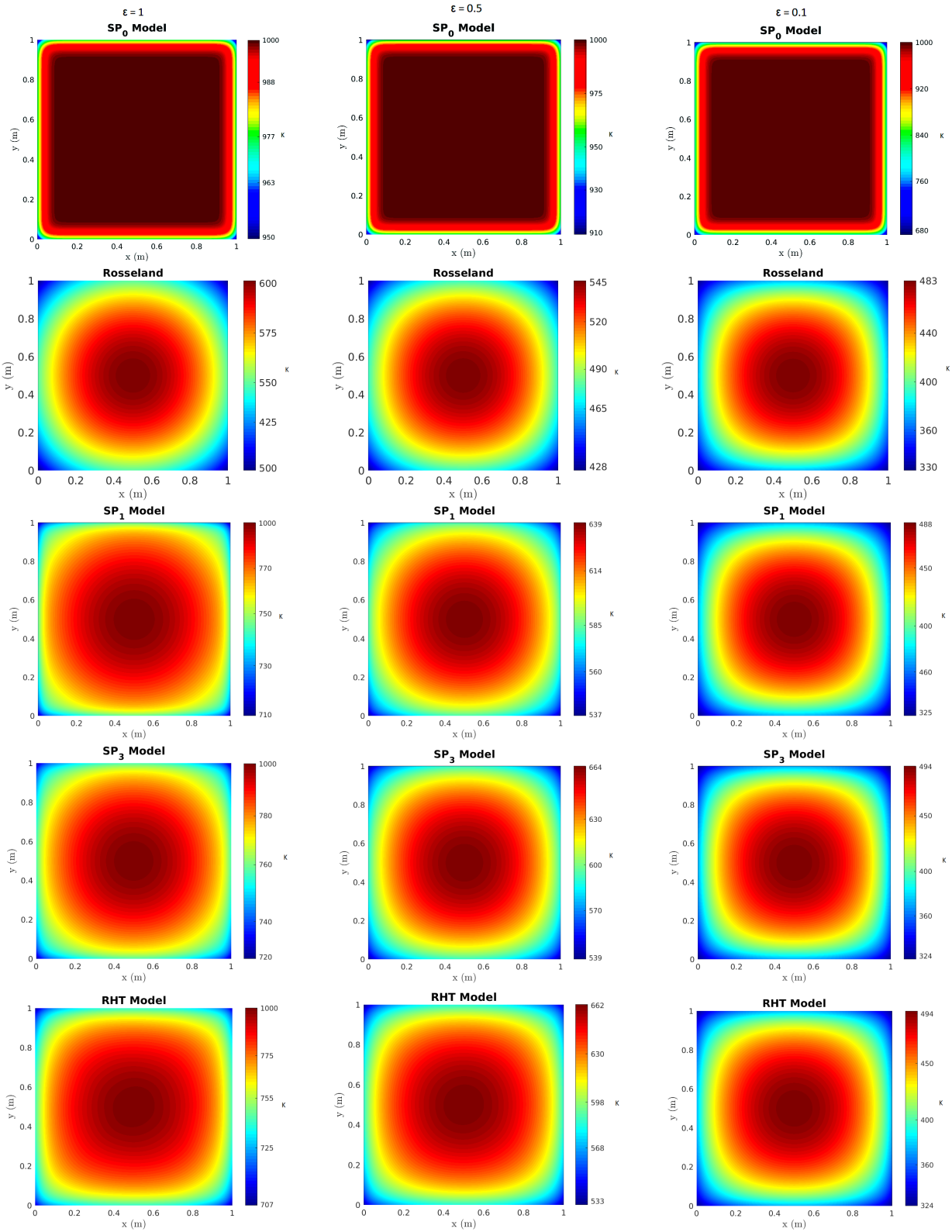

Figure 3.1: Temperature distribution obtained for the cooling example at time t = 4 minutes using the full RHT model and the considered SP_N approximations.

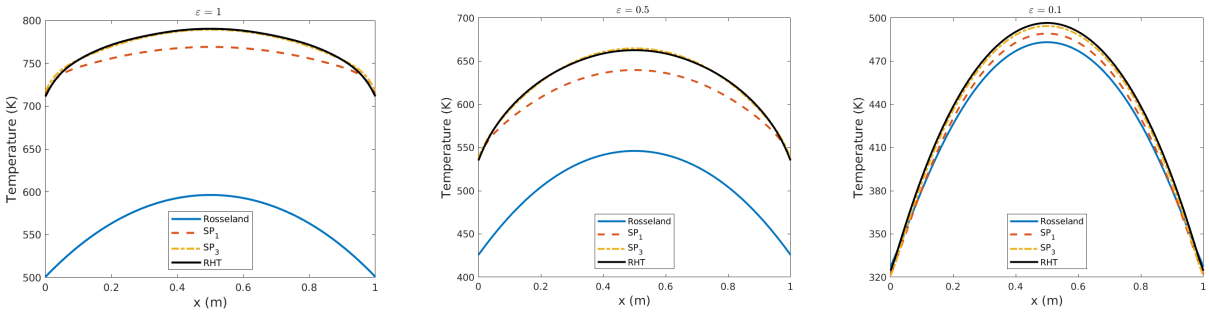

Figure 3.2: Cross-sections of the temperature shown in Figure 3.1 at the main diagonal for the considered values of the optical parameter ε.

equipped with the following boundary conditions

$$\begin{aligned} \varepsilon\Big(\Im\,\nabla\Theta\Big)\cdot\mathbf{n} - \hbar(\Theta_b-\Theta) &= \alpha\pi\left(\frac{n_2}{n_1}\right)^2\Big(B(\Theta_b)-B(\Theta)\Big)d\nu, \\ \alpha_1\psi_1 + \frac{\varepsilon}{\kappa}\mathbf{n}(\hat{\mathbf{x}})\cdot\nabla\psi_1 &= -\beta_2\psi_2 + \eta_1 B(\Theta_b), \\ \alpha_2\psi_2 + \frac{\varepsilon}{\kappa}\mathbf{n}(\hat{\mathbf{x}})\cdot\nabla\psi_2 &= -\beta_1\psi_1 + \eta_2 B(\Theta_b), \end{aligned} \tag{3.51}$$

and initial condition

$$\Theta(\mathbf{x},0) = \Theta_0(\mathbf{x}). \tag{3.52}$$

3.4 Numerical validations

An example is carried out in this section to validate the simplified P_N approximations against the RHT and to show the effect of different values of medium thickness on the heat distribution. An unit squared cavity is considered for this study with Robin boundary conditions (3.48) for the temperature on its sides. The surrounding temperature Θ_b is 300 K and the initial temperature Θ_0 is 1000 K at time t = 0. Figure 3.1 shows the temperature behaviour of Rosseland, the SP_1 and the SP_3 approximations against the obtained results from the full radiative transfer equation at different values of the medium thickness of $\varepsilon = 1$, 0.5 and 0.1 while the absorption coefficient $\kappa = 1$, convective heat transfer coefficient $\hbar = 1$, thermal conductivity $\Im = 1$, the Boltzman constant is 5.67×10^{-8} and the scattering coefficient $\sigma = 0$. The size of the timestep is fixed to $\Delta t = 10^{-4}$. It can be seen that results obtained from the SP_0 are inaccurate. The temperature evolution obtained from the SP_3 approximation is closer to the full radiative transfer results at the three chosen values of ε. The second part is to consider the accuracy of the results by taking the cross-sectional results at the main diagonal. Figure 3.2 shows the effect of medium thickness on the transfer of heat. Results show that the simplified approximations are in a good agreement with the full radiative transfer. It can be seen that with different radiation scenarios, the SP_3 approximation is accurate and it can be reliable for the radiative heat transfer applications. It is also more accurate than results obtained by the Rosseland approximation. With smaller values of ε, the photons tend to keep the energy inside them. For more details about the validations procedure, we refer to [133, 132, 143]. Following facts are obtained from the validation results. First, radiation can not be neglected. Results from the SP_0 are overestimated the real value of the temperature in this cooling process example. Second, results from Rosseland approximations failed to produce

the accurate rise in the boundary conditions specially with higher values of ε. Solving one single equation (diffusion) is not accurate in radiation heat transfer. Third, the simplified P_1 and P_3 gave the closest results to the full radiative transfer equation under different optical regimes. Fourth, with lower value of ε, the SP_3 gave us a full convergence which is required as an evidence of a successful solver. The last fact worth mentioning is that considering a higher order of SP approximations (more than SP_3) is not needed specially with low values of ε.

3.5 Concluding remarks

The asymptotic name was chosen as the approximation represents the transport solution in asymptotic regions that are far away from the boundary layers and sources in which the behaviour of the scalar is exponentially. Approximation for the full radiative transfer are needed in order to reduce the computational time while maintaining the accuracy of the solution. The main focus of this chapter was then to develop qualitative and asymptotic approximations able to capture the complex features of the radiation heat transfer. Asymptotic approximations are introduced, the so called simplified P_N approximations for the radiative transfer equation. The simplified P_N approximations help us to obtain an extension to the approximate solution of the arbitrary high order. This is accomplished by transforming the equation of transfer into a set of partial differential equations. The best element these approximations can offer is that the conversion of the governing equation to relatively simple partial differential equations. The reason behind adopting the SP_N approximations is that they offer the possibility to improve the accuracy of the solution by capturing the transport effects while still preserving the features that makes the diffusion solver attractive. Two higher-order of N approximations are considered for this thesis that are SP_1 and SP_3. Since most of the studies done by authors from the literature are based on SP_1 approximation as it is the simplest approximation. Higher order of SP_3 approximation is considered here in order to compare in the next chapters between SP_1 and SP_3 in terms of accuracy. These approximations allow us to do further investigation as they are less complicated compared with the standard spherical harmonic P_N equations. These approximations are applied in the next chapters to help us in studying the effect of natural and forced convection-radiation while considering the accuracy with the lowest possible computational requirements. The SP_2 is not considered in this study as the solutions of all even-order SP_N equations are discontinuous at the interface with different cross sections [147]. The even-order SP_N are not employed because the transport scalar flux is spatially continuous. However, the SP_3 approximation reserve the advantages that the SP_2 is unable to keep. As far as the efficiency is concerned, it has been proven in this chapter that the simplified P_N approximations can be chosen to deal with engineering applications related to radiative transfer and heat flow for optically thick media. It became an evident that further approximations are not needed as the SP_3 gave us the required results with acceptable computational time. Higher approximations can results in slightly more accurate results. However, the increase in the accuracy is negligible as it is very small while causing a dramatic increase in the numerical effort. The algorithms used and the approaches adopted are approved to be accurate and can easily be integrated and used in an existing library or CFD codes for heat flow applications.

Chapter 4

Simplified P_N models for natural convection-radiation heat transfer

In this chapter, the SP_N models are performed to study effects of natural convection-radiation in enclosures with different heat transfer characteristics and inclined angles. Inclusion of complex geometry heating source inside the cavity is considered and investigated as well. Radiation heat transfer between two or more surfaces depends very much on the radiation properties of the surfaces. One of these properties is the orientation of two surfaces relative to each other. The effects of the orientation of the surfaces relative to each other on the radiation heat transfer between the hot and cold sides are known from a parameter called the view factor [45]. The view factor is defined as the fraction of the radiation leaving a certain surface that strikes a second surface. In particular, the aim is to investigate the behaviour of heat transfer (radiation and natural convection) inside a cavity. The left vertical wall of the enclosure is heated while maintaining the vertical right wall at room temperature with both adiabatic upper and lower walls. The governing equations are the Navier-Stokes equations subjected to the Boussinesq approximation to account for the change in the density. The natural convection-radiation equations are solved continuously to obtain the temperature, velocity and pressure. The Galerkin-characteristics and the Taylor-Hood finite element methods have been adopted to solve the equations using triangular mesh. Effects of the Rayleigh number, the Planck coefficient and optical thickness on the results are considered, presented and analyzed. Results show that the adiabatic walls, the Planck coefficient as well as the inclined angle play an important role in the distribution of heat transfer inside the cavity. The chapter is organized as follows. In section 4.1, geometric set up and an introduction to the coupled system consisting of the Boussinesq approximation and the radiative transfer equation are presented. Dimensionless derivations are produced in section 4.2. The SP_N approximations are formulated in section 4.3 where we especially introduce the SP_1 and SP_3 systems. The numerical methods for the solution of the SP_N coupled systems are based on the Galerkin-characteristics method which is presented in sections 4.4 and 4.5. In section 4.6, results are presented. Subsection 4.6.1 shows the validation for the obtained results. Finally, numerical results are discussed in subsection 4.6.4, where we compare the different models for different flow and radiation regimes. Especially, we present numerical comparisons for wide range of physical parameters, e.g. the optical depth, the Prandtl number, the Planck coefficient and the Rayleigh number. Conclusions are summarized in section 4.7.

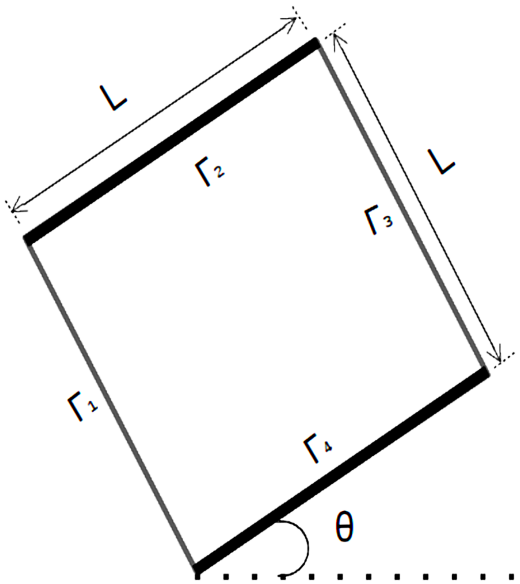

Figure 4.1: The geometry of the squared cavity with inclination angle used in the current study.

4.1 Governing equations for natural convection-radiation

The radiation heat transfer between two surfaces forming an enclosure that can be solved using a set of equations. The dimensions of any physical quantities can be manipulated algebraically and the results can be utilized for providing useful information for the physical processes consideration. Authors defined dimensional analyses as a process for eliminating irrelevant information from a relation between different physical quantities [142]. In [113], it was defined as a way that can be used to represent and clarify relationships between physical quantities. There are two basic approaches to establish the dimensionless relations that characterize the behaviour of a system [55]. The first approach is to study the equations that control the behaviour of the system. The second approach is to find the suitable physical quantities that can lead to the desirable dimensionless set of equations.
For any equation to meaningfully express properties of a physical system, this equation must have numerical equality and dimensional homogeneity between its right and left hand sides [140]. Dimensional analysis is concerned only with the nature of the properties involved in the situation and not on their numerical values, particularly where the numerical value of the dimensional quantity is a dependent on the system of units used for its measurement [21]. This study focuses on choosing the accurate dimensional equations for solving the natural convection-radiation heat that flows inside the squared enclosure shown in Figure 4.1. The current system contains a squared domain with all sides of length L and inclination angle θ' subject to a temperature difference $(\Theta'_H - \Theta'_C)$, with Θ'_H and Θ'_C are the hot and cold temperatures of the vertical walls. Primed variables in the current study refer to dimensional quantities. The enclosure consists of a gray, emitting, absorbing and non-scattering fluid surrounded by rigid walls. The fluid is considered to be Newtonian and all the thermo-physical properties are treated to be constant with an exception for density in the buoyancy term that can be adequately modelled by the Boussinesq approximation [57]. The governing equations for these assumptions are:

Conservation of mass:

$$\frac{\partial u'}{\partial x} + \frac{\partial v'}{\partial y} = 0. \tag{4.1}$$

Conservation of x-momentum:

$$\frac{\partial u'}{\partial t} + u'\frac{\partial u'}{\partial x} + v'\frac{\partial u'}{\partial y} + \frac{1}{\rho}\frac{\partial p'}{\partial x} = \wp\left(\frac{\partial^2 u'}{\partial x^2} + \frac{\partial^2 u'}{\partial y^2}\right) + g\varrho\left(\Theta' - \Theta_{ref}\right)\sin\theta'. \tag{4.2}$$

Conservation of y-momentum:

$$\frac{\partial v'}{\partial t} + u'\frac{\partial v'}{\partial x} + v'\frac{\partial v'}{\partial y} + \frac{1}{\rho}\frac{\partial p'}{\partial y} = \wp\left(\frac{\partial^2 v'}{\partial x^2} + \frac{\partial^2 v'}{\partial y^2}\right) + g\varrho\left(\Theta' - \Theta_{ref}\right)\cos\theta'. \tag{4.3}$$

Conservation of energy:

$$\rho_{ref} Cp\left(\frac{\partial \Theta'}{\partial t} + u'\frac{\partial \Theta'}{\partial x} + v'\frac{\partial \Theta'}{\partial y}\right) = \Im\left(\frac{\partial^2 \Theta'}{\partial x^2} + \frac{\partial^2 \Theta'}{\partial y^2}\right) - \nabla \cdot q'_R. \tag{4.4}$$

Here, ρ_{ref} is the fluid density, Θ_{ref} the reference temperature, p' the dimensional pressure, $\mathbf{u}' = (u', v')^T$ the velocity field, Cp the specific heat at constant pressure, Θ' the temperature, $\wp$ the kinematic viscosity, g the gravity force, $\Im$ the thermal conductivity and ϱ the coefficient of thermal expansion. The radiation effect is taken into account in the equation of energy as the divergence of radiative heat flux, $\nabla \cdot q'_R$. This term is given by

$$\nabla \cdot q'_R = \int_{\mathbb{S}^2} \kappa\Big(B'(\Theta') - I'\Big)\, d\Omega, \tag{4.5}$$

where $I' = I'(\omega, \mathbf{x})$ is the spectral intensity at position $\mathbf{x} = (x, y)^T$ and propagating along the angular direction ω in the unit sphere $\mathbb{S}^2$. The intensity I' of a non-scattering medium is obtained from the radiative transfer equation

$$\omega \cdot \nabla I' + \kappa I' = \kappa B'(\Theta'), \tag{4.6}$$

where κ is the absorption coefficient and $B'(\Theta)$ is the spectral intensity of the black-body radiation given by the Planck function

$$B'(\Theta) = \sigma_B \Theta^4, \tag{4.7}$$

with σ_B is the Boltzmann constant.

4.2 Dimensionless equations for natural convection-radiation

The governing equations for the mass, momentum and energy conservations within the enclosure. We define the following nondimensional variables for obtaining dimensionless formulation

$$\mathbf{x} = \frac{\mathbf{x}'}{L}, \qquad t = \frac{\epsilon t'}{L^2}, \qquad \mathbf{u} = \frac{L\mathbf{u}'}{\epsilon}, \qquad p = \frac{p' L^2}{\rho_{ref}\epsilon^2}, \qquad \Theta = \frac{\Theta' - \Theta'_C}{\Theta'_H - \Theta'_C},$$

$$\kappa = \frac{\kappa'}{\kappa_{ref}}, \qquad I = \frac{I'}{\sigma_B \Theta^4_{ref}}, \qquad q_R = \frac{q'_R}{\sigma_B \Theta^4_{ref}}, \qquad \theta = \frac{\theta'}{\theta_{ref}}, \qquad j = \frac{\Theta'_H - \Theta'_C}{\Theta_{ref}},$$

where ϵ is thermal diffusivity, j a general parameter used in the calculation of the non-dimensional radiation energy, L length parameter. The optical depth τ, the Prandtl number Pr, the Rayleigh number Ra, and the Planck coefficient Pl are defined as

$$\tau = \kappa_{\text{ref}} L, \qquad Pr = \frac{\wp}{\epsilon}, \qquad Ra = \frac{\beta g(\Theta'_H - \Theta'_C)L^3}{\wp\epsilon}, \qquad Pl = \frac{j\Im}{\sigma_B \Theta^2_{ref} L}. \tag{4.8}$$

Hence, the equations (4.1)-(4.4) can be rewritten in non-dimensional form as

$$\begin{aligned} \nabla \cdot \mathbf{u} &= 0, \\ \frac{D\mathbf{u}}{Dt} + \nabla p - Pr\nabla^2 \mathbf{u} &= RaPr\Theta \mathbf{e}, \\ \frac{D\Theta}{Dt} - \nabla^2 \Theta &= -\frac{1}{Pl}\nabla \cdot q_R, \end{aligned} \tag{4.9}$$

where $\mathbf{e} = (\sin\theta, \cos\theta)^T$ is the unit vector associated with the inclination angle and $\frac{Dw}{Dt}$ is the total derivative of any physical variable w defined by

$$\frac{Dw}{Dt} = \frac{\partial w}{\partial t} + \mathbf{u} \cdot \nabla w. \tag{4.10}$$

The non-dimensional radiative heat flux is given by

$$\nabla \cdot q_R = \frac{1}{\tau}\big(\varphi - B(\Theta)\big), \tag{4.11}$$

where φ is the total incident radiation defined as

$$\varphi(\mathbf{x}) = \int_{\mathbb{S}^2} I(\omega, \mathbf{x})\, d\omega. \tag{4.12}$$

The dimensionless of Planck function is given by

$$B(\Theta) = 4\Theta^4.$$

The radiation heat transfer equation (4.6) can be rewritten in non-dimensional as

$$\tau\omega \cdot \nabla I + \kappa I = \kappa B(\Theta). \tag{4.13}$$

For the formulation of a well-posed problem, equations (4.9) and (4.13) have to be solved in a bounded domain Ω with smooth boundary $\partial\Omega$ and subject to chosen initial and boundary conditions. As shown in Figure 4.1,

$$\partial\Omega = \Gamma_1 \cup \Gamma_2 \cup \Gamma_3 \cup \Gamma_4, \tag{4.14}$$

where Γ_1 and Γ_3 are the hot and cold walls, respectively, whereas Γ_2 and Γ_4 are adiabatic walls. Hence, the boundary conditions are

$$\mathbf{u}(t, \hat{\mathbf{x}}) = 0, \qquad \forall\, \hat{\mathbf{x}} \in \partial\Omega, \tag{4.15}$$

for the flow, and

$$\begin{aligned} \Theta(t, \hat{\mathbf{x}}) &= \Theta_H, && \forall\, \hat{\mathbf{x}} \in \Gamma_1, \\ \Theta(t, \hat{\mathbf{x}}) &= \Theta_C, && \forall\, \hat{\mathbf{x}} \in \Gamma_3, \\ \mathbf{n}(\hat{\mathbf{x}}) \cdot \nabla\Theta(t, \hat{\mathbf{x}}) &= 0, && \forall\, \hat{\mathbf{x}} \in \Gamma_2 \cup \Gamma_4, \end{aligned} \tag{4.16}$$

for the temperature. In (4.16), $\mathbf{n}(\hat{\mathbf{x}})$ represents the outward unit normal in $\hat{\mathbf{x}}$ with respect to $\partial\Omega$. The boundary conditions for the transfer of heat radiation are for diffuse black walls

$$\begin{aligned} I(\hat{\mathbf{x}},\omega) &= B(\Theta_H), && \forall\, \hat{\mathbf{x}} \in \Gamma_1^-, \\ I(\hat{\mathbf{x}},\omega) &= B(\Theta_C), && \forall\, \hat{\mathbf{x}} \in \Gamma_3^-, \\ \mathbf{n}(\hat{\mathbf{x}}) \cdot \nabla I(t,\hat{\mathbf{x}}) &= 0, && \forall\, \hat{\mathbf{x}} \in \Gamma_2^- \cup \Gamma_4^-, \end{aligned} \tag{4.17}$$

where the boundary regions Γ_i^- are defined as

$$\Gamma_i^- = \{\hat{\mathbf{x}} \in \Gamma_i : \quad \mathbf{n}(\hat{\mathbf{x}}) \cdot \omega < 0\}, \qquad i = 1, \ldots, 4.$$

It should be noted that other boundary conditions for flow, temperature and radiative intensity can also be incorporated in the chosen formulation without major conceptual alteration.

4.3 The simplified $\mathrm{P_N}$ equations

Clearly, the coupled problem presented in Section 4.2 is numerically coupled due to the directional dependence of the radiative intensity. Main reduction of the discrete space can be accomplished when replacing the equation of the radiative transfer with a new model that can involve physical quantities which are independent of the direction of the angle. To do that, the simplified $\mathrm{P_N}$ approximations are needed. For the purpose of completeness, we summarize how the $\mathrm{SP_N}$ approximations are derived from an asymptotic analysis applied to the radiation heat equation [78, 79]. The first step is to rewrite the equation (4.13) as

$$\left(1 + \frac{\tau}{\kappa}\omega \cdot \nabla\right) I = B(\Theta).$$

Then, a Neumann series are applied for the inversion of the transport operator

$$\begin{aligned} I &= \left(1 + \frac{\tau}{\kappa}\omega \cdot \nabla\right)^{-1} B(\Theta), \\ &\approx \left(1 - \frac{\tau}{\kappa}\omega \cdot \nabla + \frac{\tau^2}{\kappa^2}(\omega \cdot \nabla)^2 - \frac{\tau^3}{\kappa^3}(\omega \cdot \nabla)^3 + \cdots\right) B(\Theta). \end{aligned}$$

Integrating with respect to ω is considered over all directions in the unit sphere $\mathbb{S}^2$, and using

$$\int_{\mathbb{S}^2} (\omega \cdot \nabla)^n d\omega = \left(1 + (-1)^n\right) \frac{2\pi}{n+1} \nabla^n,$$

The formal asymptotic equation is obtained for φ

$$4\pi B(\Theta) = \left(1 - \frac{\tau^2}{3\kappa^2}\nabla^2 - \frac{4\tau^4}{45\kappa^4}\nabla^4 - \frac{44\tau^6}{945\kappa^6}\nabla^6\right)\varphi + \mathcal{O}(\tau^8). \tag{4.18}$$

The $\mathrm{SP_0}$, $\mathrm{SP_1}$ and $\mathrm{SP_3}$ approximations are obtained by neglecting terms of $\mathcal{O}(\tau^2)$, $\mathcal{O}(\tau^4)$ and $\mathcal{O}(\tau^8)$. In a similar manner, higher order approximations can be derived. The $\mathrm{SP_0}$ approximation reduces (4.18) to

$$4\pi B(\Theta) = \varphi. \tag{4.19}$$

This corresponds to the thermodynamic equilibrium for which the radiation effects are dropped out from the energy equation in (4.9). In the present work, the $\mathrm{SP_1}$ and $\mathrm{SP_3}$ approximations are

considered and our methods can be extended straightforwardly to other $\mathrm{SP_N}$ approximations. Thus, the $\mathrm{SP_1}$ approximation:

$$4\pi B(\Theta) = \varphi - \frac{\tau^2}{3\kappa^2}\nabla^2\varphi + \mathcal{O}(\tau^4),$$

which is equivalent to

$$-\frac{\tau^2}{3\kappa}\nabla^2\varphi + \kappa\varphi = \kappa B(\Theta). \tag{4.20}$$

The $\mathrm{SP_3}$ approximation:

$$4\pi B(\Theta) = \left(1 - \frac{\tau^2}{3\kappa}\nabla^2 - \frac{4\tau^4}{45\kappa^4}\nabla^4 - \frac{44\tau^6}{945\kappa^6}\nabla^6\right)\varphi + \mathcal{O}(\tau^8),$$

and its associated equations are given by

$$\begin{aligned} -\frac{\tau^2}{\kappa}\mu_1^2\nabla^2\varphi_1 + \kappa\varphi_1 &= \kappa 4\pi B(\Theta), \\ -\frac{\tau^2}{\kappa}\mu_2^2\nabla^2\varphi_2 + \kappa_k\varphi_2 &= \kappa 4\pi B(\Theta). \end{aligned} \tag{4.21}$$

The new variables φ_1 and φ_2 in (4.25) are related to the total incident intensity (4.12) by

$$\varphi = \frac{\gamma_2\varphi_1 - \gamma_1\varphi_2}{\gamma_2 - \gamma_1}. \tag{4.22}$$

The radiative heat flux can easily be formulated as in (4.11), once the mean intensity φ is obtained from the above $\mathrm{SP_N}$ approximations. The boundary conditions for the $\mathrm{SP_N}$ approximations are strongly connected to the $\mathrm{P_N}$ approximations Marshak's conditions and are derived from variational principles. Here, boundary conditions which are consistent with the temperature boundary conditions (4.16) are formulated for the $\mathrm{SP_N}$ approximations. Hence, for the $\mathrm{SP_1}$ equation (4.20), boundary conditions are

$$\begin{aligned} \frac{\tau}{3\kappa}\mathbf{n}(\hat{\mathbf{x}})\cdot\nabla\varphi(t,\hat{\mathbf{x}}) + \varphi(t,\hat{\mathbf{x}}) &= B\left(\Theta_H\right), && \forall\,\hat{\mathbf{x}}\in\Gamma_1, \\ \frac{\tau}{3\kappa}\mathbf{n}(\hat{\mathbf{x}})\cdot\nabla\varphi(t,\hat{\mathbf{x}}) + \varphi(t,\hat{\mathbf{x}}) &= B\left(\Theta_C\right), && \forall\,\hat{\mathbf{x}}\in\Gamma_3, \\ \mathbf{n}(\hat{\mathbf{x}})\cdot\nabla\varphi(t,\hat{\mathbf{x}}) &= 0, && \forall\,\hat{\mathbf{x}}\in\Gamma_2\cup\Gamma_4. \end{aligned} \tag{4.23}$$

For the $\mathrm{SP_3}$ equations (4.25), boundary conditions are given by

$$\begin{aligned} \frac{\tau}{\kappa}\mathbf{n}(\hat{\mathbf{x}})\cdot\nabla\varphi_1(t,\hat{\mathbf{x}}) + \alpha_1\varphi_1(t,\hat{\mathbf{x}}) &= \eta_1 B\left(\Theta_H\right) + \beta_2\varphi_2(t,\hat{\mathbf{x}}), && \forall\,\hat{\mathbf{x}}\in\Gamma_1, \\ \frac{\tau}{\kappa}\mathbf{n}(\hat{\mathbf{x}})\cdot\nabla\varphi_1(t,\hat{\mathbf{x}}) + \alpha_1\varphi_1(t,\hat{\mathbf{x}}) &= \eta_1 B\left(\Theta_C\right) + \beta_2\varphi_2(t,\hat{\mathbf{x}}), && \forall\,\hat{\mathbf{x}}\in\Gamma_3, \\ \frac{\tau}{\kappa}\mathbf{n}(\hat{\mathbf{x}})\cdot\nabla\varphi_2(t,\hat{\mathbf{x}}) + \alpha_2\varphi_2(t,\hat{\mathbf{x}}) &= \eta_2 B\left(\Theta_H\right) + \beta_1\varphi_1(t,\hat{\mathbf{x}}), && \forall\,\hat{\mathbf{x}}\in\Gamma_1, \\ \frac{\tau}{\kappa}\mathbf{n}(\hat{\mathbf{x}})\cdot\nabla\varphi_2(t,\hat{\mathbf{x}}) + \alpha_2\varphi_2(t,\hat{\mathbf{x}}) &= \eta_2 B\left(\Theta_C\right) + \beta_1\varphi_1(t,\hat{\mathbf{x}}), && \forall\,\hat{\mathbf{x}}\in\Gamma_3, \\ \mathbf{n}(\hat{\mathbf{x}})\cdot\nabla\varphi_1(t,\hat{\mathbf{x}}) = \mathbf{n}(\hat{\mathbf{x}})\cdot\nabla\varphi_2(t,\hat{\mathbf{x}}) &= 0, && \forall\,\hat{\mathbf{x}}\in\Gamma_2\cup\Gamma_4. \end{aligned} \tag{4.24}$$

where

$$\alpha_1 = \frac{5}{96}\Big(34 + 11\sqrt{\frac{5}{6}}\Big), \qquad \alpha_2 = \frac{5}{96}\Big(34 - 11\sqrt{\frac{5}{6}}\Big),$$
$$\beta_1 = \frac{5}{96}\Big(2 - \sqrt{\frac{5}{6}}\Big), \qquad \beta_2 = \frac{5}{96}\Big(2 + \sqrt{\frac{5}{6}}\Big),$$
$$\eta_1 = \frac{5\pi}{2}\Big(3 + \sqrt{\frac{5}{6}}\Big), \qquad \eta_2 = \frac{5\pi}{2}\Big(3 - \sqrt{\frac{5}{6}}\Big).$$

It is worth noting that the current parameters are valid only when the radiative transfer equation (4.13) is supplied with non-reflective boundary conditions. In summary, the SP_0 approximation is:

$$4\pi B(\Theta) = \varphi,$$

the SP_1 approximation:

$$\kappa B(\Theta) = -\frac{\tau^2}{3\kappa}\nabla^2\varphi + \kappa\varphi,$$

and the SP_3 approximation is:

$$\begin{aligned} -\frac{\tau^2}{\kappa}\mu_1^2\nabla^2\varphi_1 + \kappa\varphi_1 &= \kappa 4\pi B(\Theta), \\ -\frac{\tau^2}{\kappa}\mu_2^2\nabla^2\varphi_2 + \kappa_k\varphi_2 &= \kappa 4\pi B(\Theta). \end{aligned}$$

4.4 Finite element solution procedures

Solving the governing equations presented in section 4.3 can be interpreted as a fractional step approach where the convection part is decoupled from the Stokes/Boussinesq part in the temporal discretization. Thus, at each time step, the temperature and the velocity are updated by solving the convection equations

$$\begin{aligned} \frac{\partial \mathbf{u}}{\partial t} + \mathbf{u}\cdot\nabla\mathbf{u} &= 0, \\ \frac{\partial \Theta}{\partial t} + \mathbf{u}\cdot\nabla\Theta &= 0, \end{aligned} \tag{4.25}$$

then, the Stokes/Boussinesq equations in (4.9). The equations are solved inside the squared enclosure. Notice that the equation of energy in (4.9) has been decoupled from the equation of momentum, which can be solved separately once the convection step (4.25) is approximated.

4.4.1 The Lagrangian stage

The finite element Galerkin approximations to the convection equations usually suffer from instability problems. This is due to the fact that the traditional finite element Galerkin discretization leads to the central difference approximation of differential operators. The characteristic-Galerkin schemes are considered for improving stability, streamline upwind finite element Petrov-Galerkin. The characteristic-Galerkin scheme is carried out by discretizing the original equation in time along the characteristic curves before applying the spatial discretization. It can be implemented in the framework of the typical Galerkin finite element formulation. We describe the ingredients of the numerical scheme used in this section. We

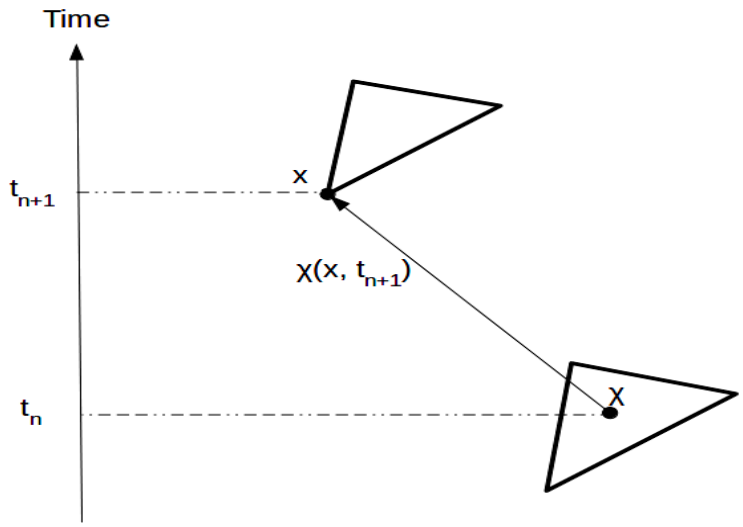

Figure 4.2: Schematic diagram illustrates the characteristics.

chose a time step Δt to discretize the time domain into subintervals $[t_n, t_{n+1}]$ with $t_n = n\Delta t$ and $n = 0, 1, \ldots$ We use the following notation $\omega^n(\mathbf{x}) = \omega(\mathbf{x}, t_n)$. Furthermore, the characteristic curves associated with the material derivative (4.10) are denoted by $\mathbf{X}(\mathbf{x}, t_{n+1}; t)$ which solve the following initial-value problem

$$\begin{aligned} \frac{d\mathbf{X}(\mathbf{x}, t_{n+1}; t)}{dt} &= \mathbf{u}\left(\mathbf{X}(\mathbf{x}, t_{n+1}; t), t\right), \quad \forall\ (\mathbf{x}, t) \in \bar{\Omega} \times [t_n, t_{n+1}], \\ \mathbf{X}(\mathbf{x}, t_{n+1}; t_{n+1}) &= \mathbf{x}. \end{aligned} \tag{4.26}$$

Notice that $\mathbf{X}(\mathbf{x}, t_{n+1}; t) = (X(\mathbf{x}, t_{n+1}; t), Y(\mathbf{x}, t_{n+1}; t))^T$ is the departure point and represents the location at time t of a particle that arrives at time t_{n+1} to the point $\mathbf{x} = (x, y)^T$. Figure 4.2 shows the characteristics. Hence, for all $\mathbf{x} \in \bar{\Omega} = \Omega \cup \partial\Omega$ and $t \in [t_n, t_{n+1}]$ the solution of (4.26) can be written as

$$\mathbf{X}(\mathbf{x}, t_{n+1}; t_n) = \mathbf{x} - \int_{t_n}^{t_{n+1}} \mathbf{u}\left(\mathbf{X}(\mathbf{x}, t_{n+1}; t), t\right)\ dt. \tag{4.27}$$

It is important to obtain an accurate estimation of the characteristic curves $\mathbf{X}(\mathbf{x}, t_{n+1}; t_n)$ as it affects the overall accuracy of the characteristic-Galerkin approach. In the current study, a technique is utilized which is first proposed in [144] in the context of semi-Lagrangian schemes for integrating the equations of the weather prediction. To approximate the integral in (4.27), a second-order extrapolation based on the mid-point rule scheme is used. Here, we use C to denote the displacement between a mesh point on the new level $\mathbf{x}_h$ and the departure point of the trajectory to this point on the previous time level $\mathbf{X}_h(\mathbf{x}, t_{n+1}; t_n)$, e.g.

$$\mathsf{C} = \mathbf{x} - \mathbf{X}(\mathbf{x}, t_{n+1}; t)$$

Applying the mid-point rule to approximate the integral in (4.27) yields

$$\mathsf{C} = \Delta t \mathbf{u}(\mathbf{X}(\mathbf{x}, t_n; t_{n+(1/2)}), t_{n+(1/2)}), \tag{4.28}$$

utilizing the second-order extrapolation

$$\mathbf{u}(\mathbf{x}, t_{n+(1/2)}) = \frac{3}{2}\mathbf{u}(\mathbf{x}, t_n) - \frac{1}{2}\mathbf{u}(\mathbf{x}, t_{n-1}), \tag{4.29}$$

and the second-order approximation is:

$$\mathbf{X}(\mathbf{x}, t_n; t_{n+(1/2)}) = \mathbf{x} - \frac{1}{2}\mathsf{C}.$$

The following implicit formula is obtained for C:

$$\mathsf{C} = \Delta t\left(\frac{3}{2}\mathbf{u}(\mathbf{x} - \frac{1}{2}\mathsf{C}, t_n) - \frac{1}{2}\mathbf{u}(\mathbf{x} - \frac{1}{2}\mathsf{C}, t_{n-1})\right).$$

The following iterative procedure is considered in order to compute C:

$$\begin{aligned}
\mathsf{C}^{(0)} &= \Delta t\left(\frac{3}{2}\mathbf{u}(\mathbf{x}, t_n) - \frac{1}{2}\mathbf{u}(\mathbf{x}, t_{n-1})\right) \\
\mathsf{C}^{(k)} &= \Delta t\left(\frac{3}{2}\mathbf{u}(\mathbf{x} - \frac{1}{2}\mathsf{C}^{(k-1)}, t_n) - \frac{1}{2}\mathbf{u}(\mathbf{x} - \frac{1}{2}\mathsf{C}^{(k-1)}, t_{n-1})\right), \qquad k = 1, 2, \ldots
\end{aligned} \tag{4.30}$$

The iterations in (4.30) are terminated when the following criteria

$$\frac{||\mathsf{C}^{(k)} - \mathsf{C}^{(k-1)}||}{||\mathsf{C}^{(k-1)}||} < tol$$

is fulfilled for the Euclidean norm $||\cdot||$ and a given tolerance tol. It is known that [124]:

$$||\mathsf{C} - \mathsf{C}^{(k)}|| \leq \frac{1}{4}||\mathsf{C} - \mathsf{C}^{(k-1)}||||\nabla\mathbf{u}||\Delta t, \qquad k = 1, 2 \ldots$$

Hence, an important condition for the convergence of iteration (4.30) is that the velocity gradient satisfies

$$||\nabla\mathbf{u}||\Delta t < 1. \tag{4.31}$$

Since the Courant-Friedrichs-Lewy condition associated with the advection term is relaxed to the condition (4.31). The main advantage of this condition is that it allows for large time steps to be used in the simulations. Likewise, the condition (4.31) guarantees that the characteristics' curves will not intersect during the Δt time size. We set the iteration until the trajectory changes by 10^{-6}. The discretization of the space domain $\bar{\Omega}$ is proceed as follows. Given h_0, $0 < h_0 < 1$, let h be a spatial discretization parameter such that $0 < h < h_0$. A quasi-uniform partition $\Omega_h \subset \bar{\Omega}$ of small elements $\mathcal{T}_j$ is generated that satisfy the following conditions:

(i) $\bar{\Omega} = \bigcup_{j=1}^{Ne} \mathcal{T}_j$, where Ne is the number of elements of Ω_h.

(ii) If $\mathcal{T}_i$ and $\mathcal{T}_j$ are two different elements of Ω_h, then

$$\mathcal{T}_i \cap \mathcal{T}_j = \begin{cases} P_{ij}, & \text{a certain point in the mesh, or} \\ \Gamma_{ij}, & \text{a common element side, or} \\ \emptyset, & \text{far away from each other.} \end{cases}$$

(iii) There exists a positive constant k such that for all $j \in \{1, \cdots, Ne\}$, $\frac{d_j}{h_j} > k$ $(h_j \leq h)$, where d_j is the diameter of the circle inscribed in $\mathcal{T}_j$ and h_j is the largest side of $\mathcal{T}_j$.

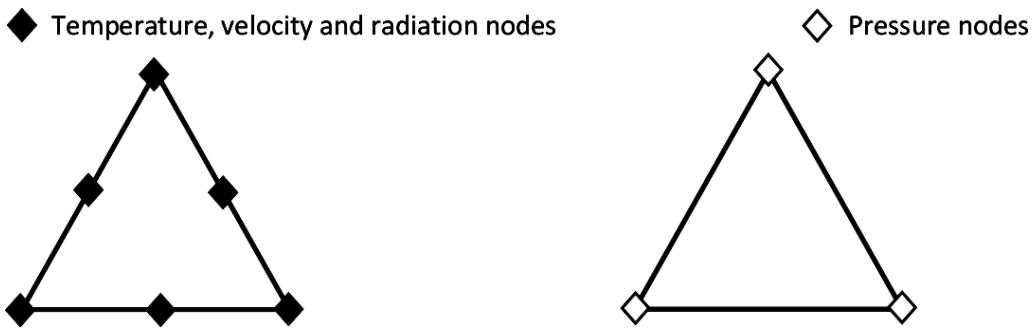

Figure 4.3: Definition of the Taylor-Hood finite elements.

The conforming finite element spaces used in this research for velocity-temperature-radiation and pressure are the Taylor-Hood finite elements P_m/P_{m-1} *i.e.*, polynomial of degree $m \geq 2$ for $\{u, v, \Theta, \varphi\}$ and polynomial of degree $m-1$ for the finite element $\{P\}$ on simplices, respectively. A depicted illustration can be seen in Figure 4.3 for triangular mesh. For such elements, the discrete velocity-temperature-radiation and pressure fields must satisfy the inf-sup condition. This property guarantees the convergence and stability of the approximate solutions, compare [9, 153]. These elements can be defined as

$$\begin{aligned} V_h &= \Big\{ v_h \in C^0(\bar{\Omega}) : \quad v_h\big|_{\mathcal{T}_j} \in S(\mathcal{T}_j), \quad \forall\, \mathcal{T}_j \in \Omega_h \Big\}, \\ \mathcal{Q}_h &= \Big\{ q_h \in C^0(\bar{\Omega}) : \quad q_h\big|_{\mathcal{T}_j} \in R(\mathcal{T}_j), \quad \forall\, \mathcal{T}_j \in \Omega_h \Big\}, \end{aligned}$$

where $C^0(\bar{\Omega})$ represents the space of bounded and continuous functions in $\bar{\Omega}$, $S(\mathcal{T}_j)$ and $R(\mathcal{T}_j)$ are polynomial spaces defined in $\mathcal{T}_j$ as $S(\mathcal{K}_j) = P_m(\mathcal{T}_j)$ for simplices, $S(\mathcal{T}_j) = Q_m(\mathcal{T}_j)$ for quadrilaterals, $R(\mathcal{T}_j) = P_{m-1}(\mathcal{T}_j)$ for simplices and $R(\mathcal{T}_j) = Q_{m-1}(\mathcal{T}_j)$ for quadrilaterals. Hence, the finite element solutions to $u^n(\mathbf{x})$, $v^n(\mathbf{x})$, $T^n(\mathbf{x})$, $\varphi^n(\mathbf{x})$ and $p^n(\mathbf{x})$ are formulated as

$$\begin{gathered} u_h^n = \sum_{j=1}^{M} U_j^n \phi_j, \qquad v_h^n = \sum_{j=1}^{M} V_j^n \phi_j, \qquad \Theta_h^n = \sum_{j=1}^{M} \Lambda_j^n \phi_j, \\ \varphi_h^n = \sum_{j=1}^{M} \xi_j^n \phi_j, \qquad p_h^n = \sum_{j=1}^{N} P_j^n \psi_j, \end{gathered} \tag{4.32}$$

where M and N are representing the number of velocity-temperature-radiation and pressure mesh points in the partition Ω_h. The functions U_j^n, V_j^n, Λ_j^n and P_j^n are the corresponding nodal values of $u_h^n(\mathbf{x})$, $v_h^n(\mathbf{x})$, $\Theta_h^n(\mathbf{x})$ and $p_h^n(\mathbf{x})$, respectively. They are defined as $U_j^n = u_h^n(\mathbf{x}_j)$, $V_j^n = v_h^n(\mathbf{x}_j)$, $\Lambda_j^n = \Theta_h^n(\mathbf{x}_j)$ and $P_j^n = p_h^n(\mathbf{y}_j)$ where $\{\mathbf{x}_j\}_{j=1}^M$ and $\{\mathbf{y}_j\}_{j=1}^N$ are the set of velocity-temperature-radiation and pressure mesh points in the partition Ω_h, respectively, so that $N < M$ and $\{\mathbf{y}_1, \ldots, \mathbf{y}_N\} \subset \{\mathbf{x}_1, \ldots, \mathbf{x}_M\}$. In (4.32), $\{\phi_j\}_{j=1}^M$ and $\{\psi_j\}_{j=1}^N$ are the set of global nodal basis functions of $\mathbf{V}_h$ and S_h, respectively, characterized by the property $\phi_i(\mathbf{x}_j) = \delta_{ij}$ and $\psi_i(\mathbf{y}_j) = \delta_{ij}$ with δ_{ij} denoting the Kronecker symbol.
Taking the assumption that for all $j = 1, \ldots, M$, the pairs $(\mathbf{X}_{hj}^n, \hat{\mathcal{T}}_j)$ and the mesh point values

$\{U_j^n, V_j^n, \Lambda_j^n\}$ are known, the values $\{\hat{U}_j^n, \hat{V}_j^n, \hat{\Lambda}_j^n\}$ are computed as

$$\begin{aligned} \hat{U}_j^n := u_h^n(\mathbf{X}_{hj}^n) = \sum_{k=1}^{M} U_k \phi_k(\mathbf{X}_{hj}^n), \qquad \hat{V}_j^n := v_h^n(\mathbf{X}_{hj}^n) = \sum_{k=1}^{M} V_k \phi_k(\mathbf{X}_{hj}^n), \\ \hat{\Lambda}_j^n := \Theta_h^n(\mathbf{X}_{hj}^n) = \sum_{k=1}^{M} \Lambda_k \phi_k(\mathbf{X}_{hj}^n). \end{aligned} \tag{4.33}$$

Then, the solution $\{\hat{u}_h^n(\mathbf{x}), \hat{v}_h^n(\mathbf{x}), \hat{\Theta}_h^n(\mathbf{x})\}$ at the characteristic feet is obtained by

$$\hat{u}_h^n(\mathbf{x}) = \sum_{j=1}^{M} \hat{U}_j^n \phi_j(\mathbf{x}), \qquad \hat{v}_h^n(\mathbf{x}) = \sum_{j=1}^{M} \hat{V}_j^n \phi_j(\mathbf{x}), \qquad \hat{\Theta}_h^n(\mathbf{x}) = \sum_{j=1}^{M} \hat{\Lambda}_j^n \phi_j(\mathbf{x}). \tag{4.34}$$

It is worth mentioning that the traditional characteristic-Galerkin techniques in [23, 117] evaluate $\hat{u}_h^n$, $\hat{v}_h^n$ and $\hat{\Theta}_h^n$ using an L^2-projection on the space of the velocity-temperature-radiation V_h. The evaluation of integrals in the L^2-projection is computationally very demanding in several applications.

4.4.2 The Eulerian stage

We compute the characteristics and we interpolate, $\hat{u}_h^n$, $\hat{v}_h^n$ and $\hat{\Theta}_h^n$ are known at the characteristic feet. The procedure to advance the solution of (4.9) and (4.20) or (4.9) and (4.25) from a time t_n to the next time t_{n+1} is achieved using the following steps:

1. Solve for φ^{n+1}

$$-\frac{\tau^2}{3\kappa}\nabla^2\varphi^{n+1} + \kappa\varphi^{n+1} = \kappa B(\hat{\Theta}^n), \tag{4.35}$$

subject to the boundary conditions (4.23) in case of the SP_1 approximation or

$$\begin{aligned} -\frac{\tau^2}{\kappa}\mu_1^2\nabla^2\varphi_1^{n+1} + \kappa\varphi_1^{n+1} &= \kappa B(\hat{\Theta}^n), \\ -\frac{\tau^2}{\kappa}\mu_2^2\nabla^2\varphi_2^{n+1} + \kappa\varphi_2^{n+1} &= \kappa B(\hat{\Theta}^n), \end{aligned} \tag{4.36}$$

$$\varphi^{n+1} = \frac{\gamma_2\varphi_1^{n+1} - \gamma_1\varphi_2^{n+1}}{\gamma_2 - \gamma_1}. \tag{4.37}$$

subject to the boundary conditions (4.24) in case of the SP_3 approximation.

2. Solve for Θ^{n+1}

$$\frac{\Theta^{n+1} - \hat{\Theta}^n}{\Delta t} - \nabla^2\Theta^{n+1/2} = -\frac{1}{Pl}\nabla\cdot q_R^{n+1}, \tag{4.38}$$

subject to the boundary conditions (4.16).

3. Solve for $\bar{\mathbf{u}}^{n+1}$

$$\begin{aligned} \frac{\bar{\mathbf{u}}^{n+1} - \hat{\mathbf{u}}^n}{\Delta t} + \gamma\nabla p^n - Pr\nabla^2\bar{\mathbf{u}}^{n+1/2} &= RaPr\Theta^{n+1/2}\mathbf{e}, \qquad \text{in} \quad \Omega, \\ \bar{\mathbf{u}}^{n+1} &= \mathbf{0}, \qquad \text{on} \quad \Gamma. \end{aligned} \tag{4.39}$$

4. Solve for $\bar{p}$ and $\mathbf{u}^{n+1}$

$$\begin{aligned} \frac{\mathbf{u}^{n+1}-\bar{\mathbf{u}}^{n+1}}{\Delta t}+\nabla\bar{p} &= \mathbf{0}, && \text{in} \quad \Omega, \\ \nabla\cdot\mathbf{u}^{n+1} &= 0, && \text{in} \quad \Omega, \\ \mathbf{n}\cdot\nabla\mathbf{u}^{n+1} &= 0, && \text{on} \quad \Gamma. \end{aligned} \tag{4.40}$$

5. Update p^{n+1}

$$p^{n+1}=p^n+2\bar{p}.$$

In (4.38) and (4.39), $\Theta^{n+1/2}$ and $\bar{\mathbf{u}}^{n+1/2}$ are defined as

$$\Theta^{n+1/2}=\frac{1}{2}\Theta^{n+1}+\frac{1}{2}\hat{\Theta}^n, \qquad \bar{\mathbf{u}}^{n+1/2}=\frac{1}{2}\bar{\mathbf{u}}^{n+1}+\frac{1}{2}\hat{\mathbf{u}}^n,$$

The current solution of (4.40) leads to a pressure-Poisson problem for $\bar{p}$ of the form

$$\begin{aligned} \nabla^2\bar{p} &= \frac{1}{\Delta t}\nabla\cdot\bar{\mathbf{u}}^{n+1}, && \text{in} \quad \Omega, \\ \mathbf{n}\cdot\nabla\bar{p} &= 0, && \text{on} \quad \Gamma. \end{aligned} \tag{4.41}$$

Furthermore, in the solution procedure, only linear systems have to be computed at every time step to update the solution $\{p^{n+1}, u^{n+1}, v^{n+1}, \Theta^{n+1}, \varphi^{n+1}\}$ from (4.35)-(4.41). To solve the current linear systems in our approach, a BiCGSTAB algorithm is implemented.

4.5 Approximation of Stokes/Boussinesq system

In order to solve the Stokes/Boussinesq problem in (4.9) at each time step, a procedure is required. This is done by applying the conjugate gradient approach [20]. The Stokes/Boussinesq solution is solved in the following way:

Step 1. Solve for $\Theta_h^{n+1} \in \mathbf{V_h}$ such that for all $v_h \in V_h^0$

$$\frac{1}{\Delta t}\int \Theta_h^{n+1}v_h d\Omega+\int\nabla\Theta_h^{n+1}\cdot\nabla v_h d\Omega=\frac{1}{\Delta t}\int\hat{\Theta}_h^n v_h d\Omega. \tag{4.42}$$

Step 2. Given $P_h=P_h^n$, solve for $\mathbf{u}_h \in V_h\times V_h$ such that for all $\mathbf{v}_h \in V_h\times V_h$

$$\begin{aligned} \frac{1}{\Delta t}\int \mathbf{u}_h\mathbf{v}_h d\Omega+Pr\int\nabla\mathbf{u}_h\cdot\nabla\mathbf{v}_h d\Omega &= \frac{1}{\Delta}\int\hat{\mathbf{u}}_h^n\mathbf{v}_h d\Omega-Pr\int\nabla\hat{\mathbf{u}}_h^n\cdot\nabla\mathbf{v}_h d\Omega \\ &+\int P_h^{(0)}\nabla\cdot\mathbf{v}_h d\Omega+PrRa\int\Theta_h^{n+1}\mathbf{v}_h\mathbf{e}d\Omega. \end{aligned} \tag{4.43}$$

Afterwards, calculate

$$r_h=\nabla\cdot\mathbf{u}_h.$$

Step 3. Solve for $\psi_h \in Q_h$ such that for all $\phi_h \in Q_h$

$$\int_\Omega \nabla\psi_h \cdot \nabla\phi_h d\Omega = \int_\Omega r_h\phi_h d\Omega, \tag{4.44}$$

and set

$$g_h = \frac{1}{\Delta t}\psi_h + r_h, \qquad \omega_h = g_h.$$

From $m \geq 0$, based on the assumption that we know $P_h^{(m)}, \mathbf{u}_h^{(m)}, r_h^{(m)}, g_h^{(m)}, \omega_h^{(m)}$, $P_h^{(m+1)}, \mathbf{u}_h^{(m+1)}, r_h^{m+1}, g_h^{(m+1)}, \omega_h^{(m+1)}$ is calculated:

a. Solve for $\bar{\mathbf{u}}_h \in V_h \times V_h$ such that for all $\mathbf{v}_h \in V_h \times V_h$

$$\frac{1}{\Delta t}\int \bar{\mathbf{u}}_h^{(m)}\mathbf{v}_h d\Omega + \int \nabla\bar{\mathbf{u}}_h^{(m)} \cdot \nabla\mathbf{v}_h d\Omega = \int \omega_h^{(m)}\nabla \cdot \mathbf{v}_h d\Omega, \tag{4.45}$$

and set

$$\bar{r}_h^{(m)} = \nabla \cdot \bar{\mathbf{u}}_h^{(m)}.$$

b. Compute

$$\rho_m = \frac{\int r_h^{(m)} g_h^{(m)} d\Omega}{\int \bar{r}_h^{(m)}\omega_h^{(m)} d\Omega}.$$

c. Set

$$\begin{aligned} P^{(m+1)} &= P_h^{(m)} - \rho_m\omega_h^{(m)}, \\ \mathbf{u}_h^{(m+1)} &= \mathbf{u}_h^{(m)} - \rho_m\bar{\mathbf{u}}_h^{(m)}, \\ r_h^{(m+1)} &= r_h^{(m)} - \rho_m\bar{r}_h^{(m)}. \end{aligned}$$

d. Solve for $\bar{\psi}_h^{(k)} \in S_h$ such that for all $\phi_h \in S_h$

$$\int \nabla\bar{\psi}_h^{(m)} \cdot \nabla\phi_h d\Omega = \int \bar{r}_h^{(m)}\phi_h d\Omega,$$

and set

$$g_h^{(m+1)} = g_h^{(m)} - \rho_m\left(\frac{1}{\Delta t}\psi_h^{(m)} + \frac{1}{2}Pr\ r_h^{(m+1)}\right).$$

i. If $\dfrac{\int r_h^{(m+1)} g_h^{(m+1)} d\Omega}{\int r_h^{(0)} g_h^{(0)} d\Omega} \leq \epsilon$, then

$$P_h^{n+1} = P_h^{m+1}, \qquad \mathbf{u}_h^{n+1} = \mathbf{u}_h^{m+1},$$

stop.

ii. Otherwise, compute

$$\eta = \frac{\int r_h^{(m+1)} g_h^{(m+1)} d\Omega}{\int r_h^{(m)} g_h^{(m)} d\Omega}, \quad \omega_h^{(m+1)} = g_h^{(m+1)} + \eta_m\omega_h^{(m)},$$

change $m \leftarrow m+1$, go to step a. and repeat the process.
iii. End if

Notice that, the integration of equations (4.35)-(4.41) for triangular elements is easy and described in many text books, compare [60] among others.

4.6 Numerical results

This section can be divided into two main subsections. First, complete validations and comparisons has been carried out to compare the obtained results with the results conducted by several authors from the literature. Second, we carried out with our novel strategies and plans after validating our methods and algorithms to create and understand different thermal scenarios that can serve the industry. Our novel simplified P_3 approximation has been applied for the first time to study the natural convection-radiation. For the first time, we have considered a squared cavity with different inclination angles and with the inclusion of complex heat source inside it. We believe that this is the first attempt to apply the Taylor-Hood finite element method with the adoption of Galerkin-characteristics method to study the natural convection-radiation under turbulent conditions.

4.6.1 Validation of convection-radiation heat transfer without inclination angles

The results have been extensively checked on benchmark problems to check the accuracy. For verification of the numerical results, we have compared our results with different published scenarios. The first validation that has been considered is comparing the accuracy of our results with the experimental results obtained by Bajorek and Lloyd [130] for the pure heat convection inside air-filled vertical squared cavity with all surfaces coated in black. The right and left sides were the hot and cold walls, while the bottom and top are maintained adiabatic. The results have been validated with the simulation results obtained by Vivek et al. [154] for the convection heat transfer for the temperature values at the mid-height of the domain. Figure 4.4 shows an excellent agreement to the horizontal cross-sectional study for the dimensionless temperature at the middle of the squared cavity along with the values of the Nusselt number on the hot wall with [154] at $Ra = 3.557 \times 10^5$, $\Theta_H = 312.1$ K, $\Theta_C = 296.6$ K. The next validation that has been considered is comparing our results with the results obtained by [76] for pure convection. The upper and lower sides of the cavity remained adiabatic, while heat transferred from the hot wall located on the left to the cold wall which is on the right. Figure 4.5 shows a very good agreement with our results obtained for the temperature contour at $Ra = 10^6$. The third validation has been accounted for the pure double diffusion for a squared enclosure. The right and left walls have been set as hot and cold sources respectively with no heat transfer from the upper and lower walls. Figure 4.6 shows the obtained isotherm which shows an agreement between the current study and the study that has been done by [110] and [63] at $Ra = 10^4$. The fourth validation that has been investigated by comparing our results with the results taken by [63] for double diffusion at $Ra = 10^5$. Figure 4.7 shows the agreement with our current study results for the temperature distribution across the squared cavity with the same set of walls that has been adopted by the previous references. The fifth validation examined is with the inclusion of the radiation transfer of heat in a squared cavity. Figure 4.8 shows the comparison that has been obtained with the results carried out by [139] for

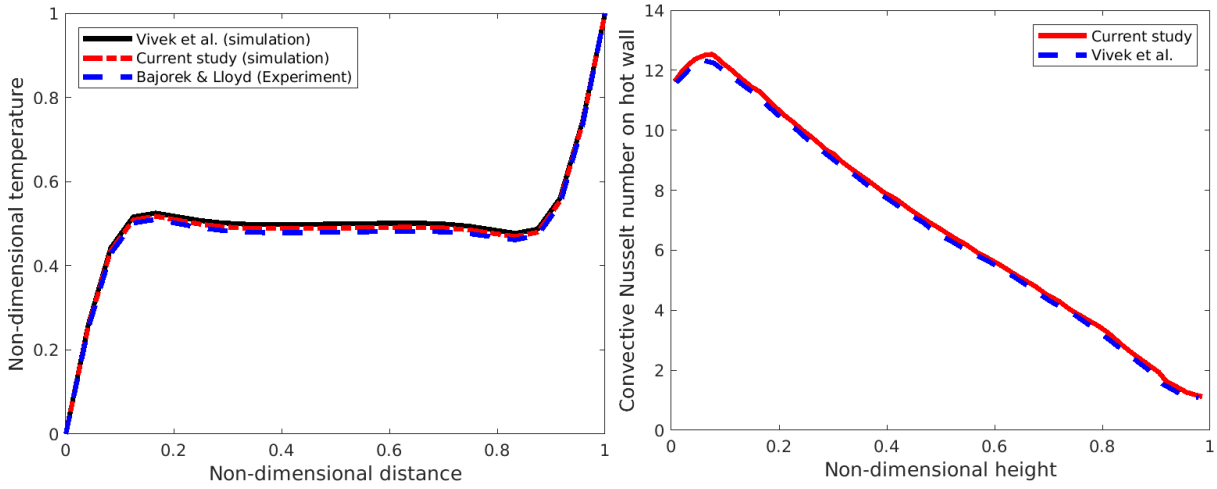

Figure 4.4: A comparison for the cross-section of the dimensionless temperature with Bajorek and Lloyd [130] and Vivek et al. [154] (left) and the convective Nusselt number (right) at $Ra = 3.557 \times 10^5$.

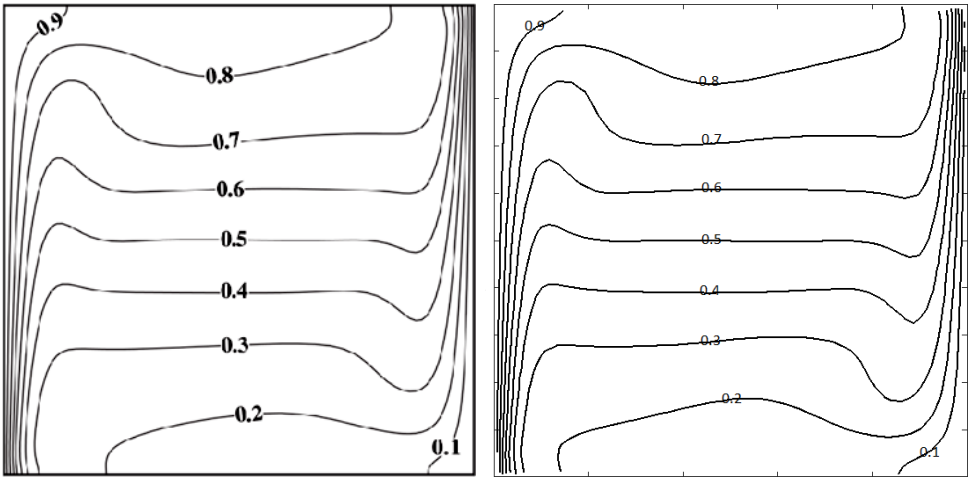

Figure 4.5: A comparison for the temperature isotherms for our results (right) and the results obtained by [76] at $Ra = 10^6$ (left).

accounting radiation at $Ra = 10^4$, $Pl = 1.0$, $\tau = 5$. It is worth mentioning that our approach is valid for low value of τ. In [139], it was reported that at high value of τ, convective heat became dominant and there was no effect for the radiation. We have performed the same values of the pertinent parameters for calculating only the heat convection. Our results matches the results conducted by [139] and shown in Figure 4.8. Our final validation accounts for the effect of radiation-convection. The current results have been compared with cross-sectional results examined by [76] at $Ra = 10^4$ and 10^5 with a fixed τ of 1 and $Pl = 0.1$. Figure 4.9 shows a very good agreement with our results taken for the horizontal cross sectional study for the temperature at the middle of the enclosure.

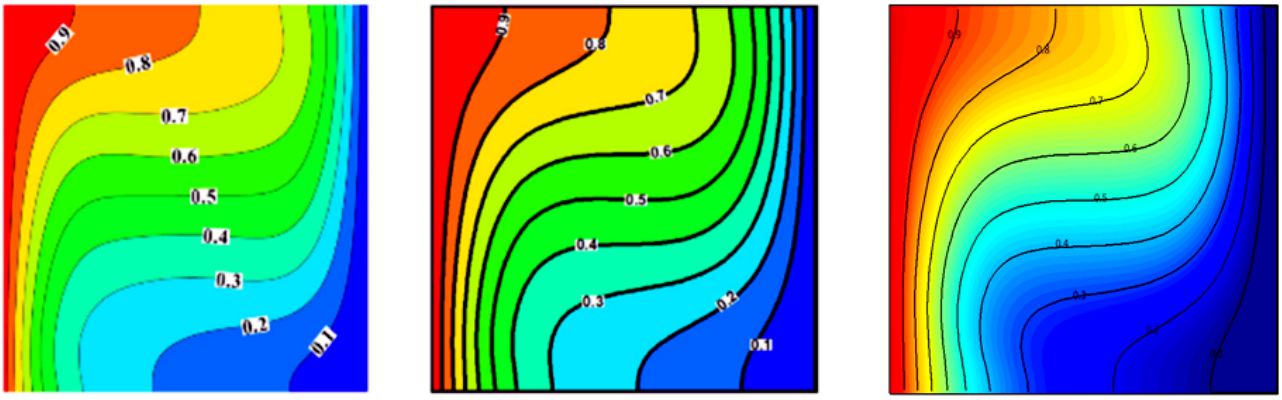

Figure 4.6: A comparison for the temperature isotherms from the obtained results (right), the results obtained by [110] (left) and the results achieved by [63] (middle) at $Ra = 10^4$.

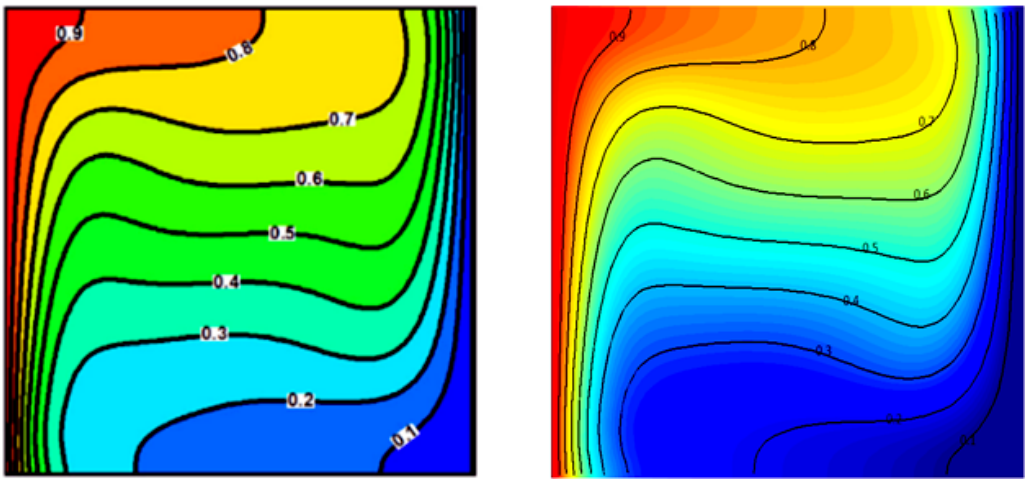

Figure 4.7: A comparison for the temperature isotherms for our results (right) and the results obtained by [63] at $Ra = 10^5$ (left).

4.6.2 Validation of convection-radiation heat transfer with inclination angles

The second part of the validation is taking into account the inclined angle as well as the inclusion of a complex circular heater inside the cavity. Figure 4.10 shows an excellent match with the results obtained by [63] at an angle value of 40° and with $Ra = 10^5$. The inclined left and right walls are the hot and cold walls respectively, while maintaining adiabatic inclined top and bottom walls. Another validation that has been accounted for the results from two inclined angles of 40° and 120° obtained by [75] with $Ra = 10^6$. Figure 4.12 shows a very good match with our convective heat results. One more validation is also taken into consideration by comparing our results with the results carried out by [1] for a squared enclosure with an inclined angle of 60° with $Ra = 10^6$. Figure 4.11 shows close results compared with our obtained results. The final validation considered is a cavity with inclined angle of 30° containing a circular heating source at two values of Ra of 10^5 and 10^6 with a circular heater diameter of 0.1. The inclined left and right walls are kept at cold temperatures while maintaining an inclined adiabatic upper and lower walls. Figure 4.13 shows the convection heat transfer results between the current results and the results accomplished by [114].

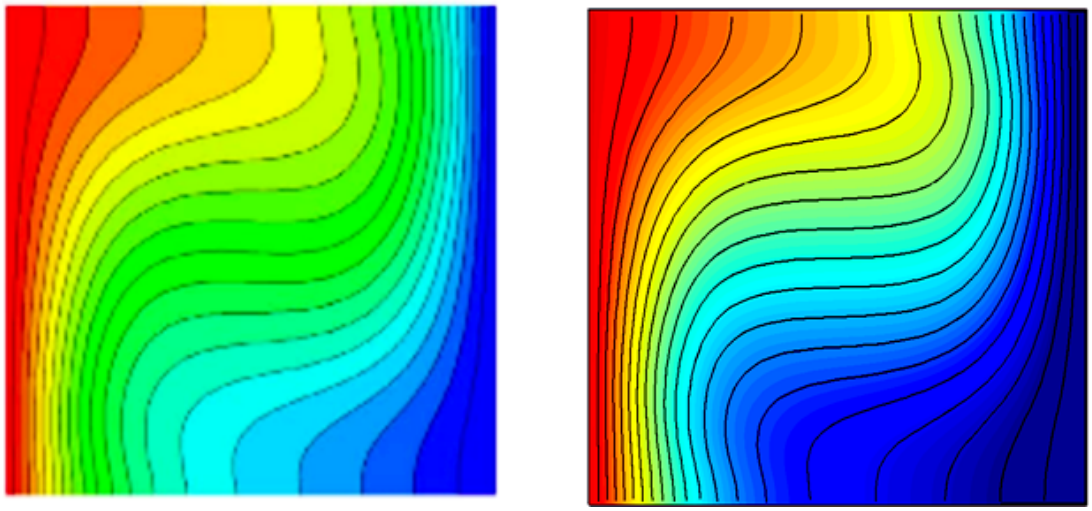

Figure 4.8: A comparison for the temperature isotherms for our results (right) and the results obtained by [139] at $Ra = 10^4$, $Pl = 1.0$, $\tau = 5$ (left).

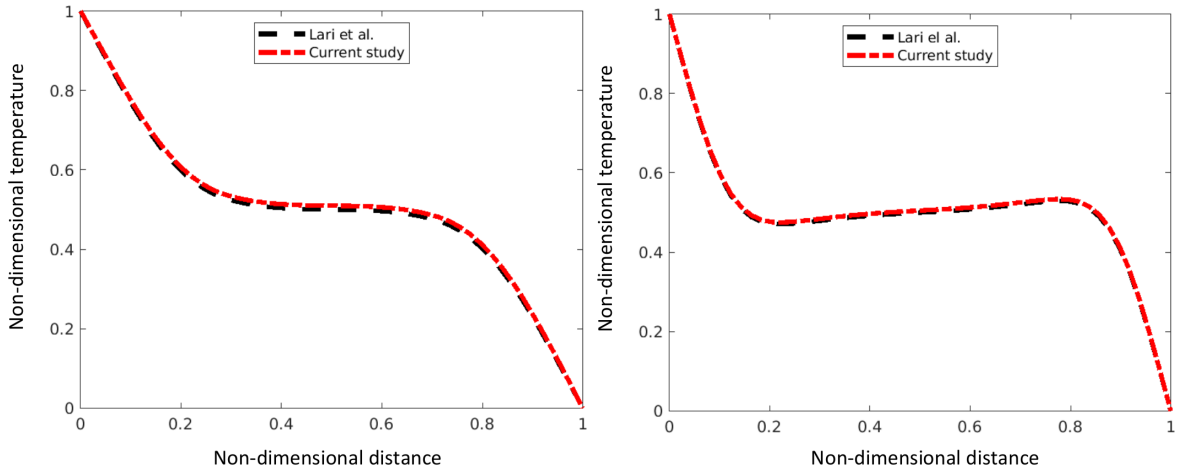

Figure 4.9: A comparison for the cross-section non-dimensional temperature along the non-dimensional x axis in the middle of the squared cavity obtained by [76] and the current study at $Ra = 10^4$ (left) and $Ra = 10^5$ (right) at $Pl = 0.1$ and $\tau = 1$.

4.6.3 Validation of convective-radiative heat transfer in a cylindrical annulus

More complex geometry is considered for validating the natural convection-radiation. Double pipe heat exchanger is taken into our consideration. Figure 4.14 shows the diameter of the inner pipe of the annulus geometry. The L is the space between the inner and the out pipes. The T_H is the hot temperature, T_C is the cold temperature and θ is the angle of rotation that moves in a clockwise direction. The value L/D has been considered according to the previous published work to match their dimensions. The first validation that has been considered in this study is a comparison of our natural convection heat transfer results with experimental data from [73], numerical data from [159] and numerical data from [161] at $Ra = 5 \times 10^5$ and $Pr = 0.7$ with three rotational angles of 0°, 90° and 180°. Figure 4.15 shows a good match between the conducted results and the previous published data. The second validation that has

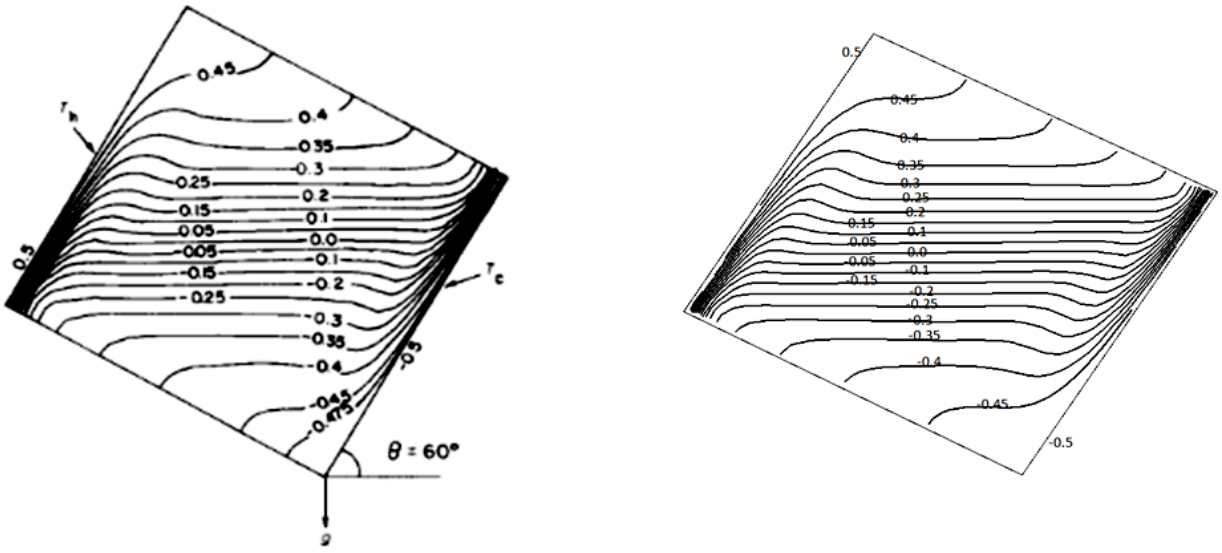

Figure 4.11: A comparison between the obtained natural convective results (right) and the results obtained by [1] (left) for an angle of 60° with $Ra = 10^6$.

been accounted for the results conducted by Jha et al. [59] for the interaction of the natural convection heat with thermal radiation and our conducted results. Figure 4.16 illustrates an acceptable match of results between the current study and the published work by Jha et al. [59] for $Pr = 7$, the temperature difference parameter that appears in the dimensionless Navier-Stokes equation of energy $C_T = 1.5$ and perturbation parameter that determines the effect of their asymptotic expansion $R = 0.1$. Another validation has been done by comparing the current study with the experimental results conducted by [73], simulation done by [134] and simulation accomplished by [159] for values of $Ra = 4.7 \times 10^4$ and $Pr = 0.706$. It can be seen from Figure 4.17 that the temperature plume is in agreement with the mentioned results.

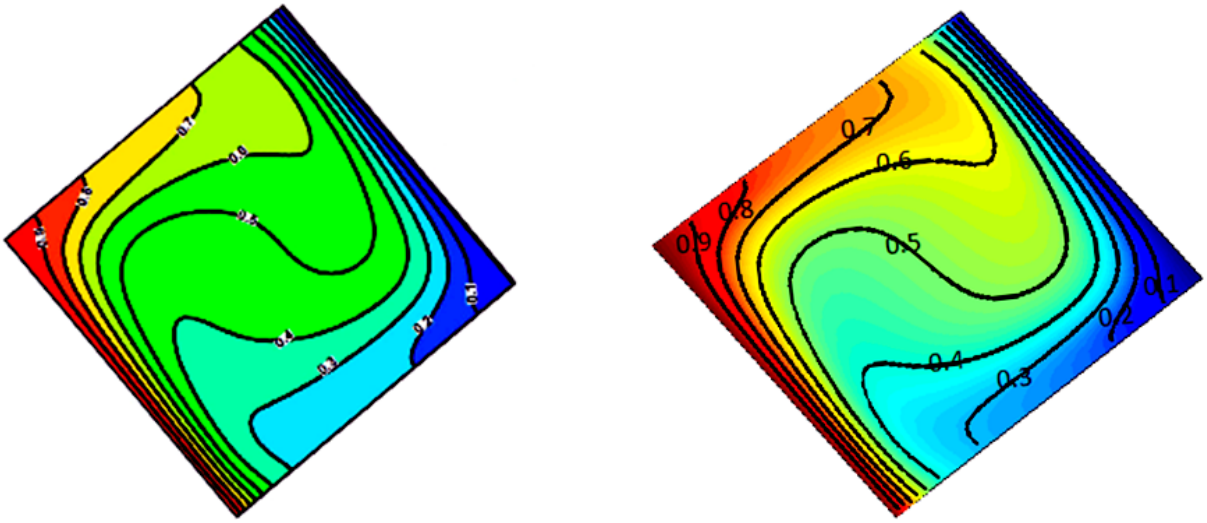

Figure 4.10: A comparison between the obtained natural convection results (right) and the results obtained by [63] (left) for an angle of 40° and with $Ra = 10^5$.

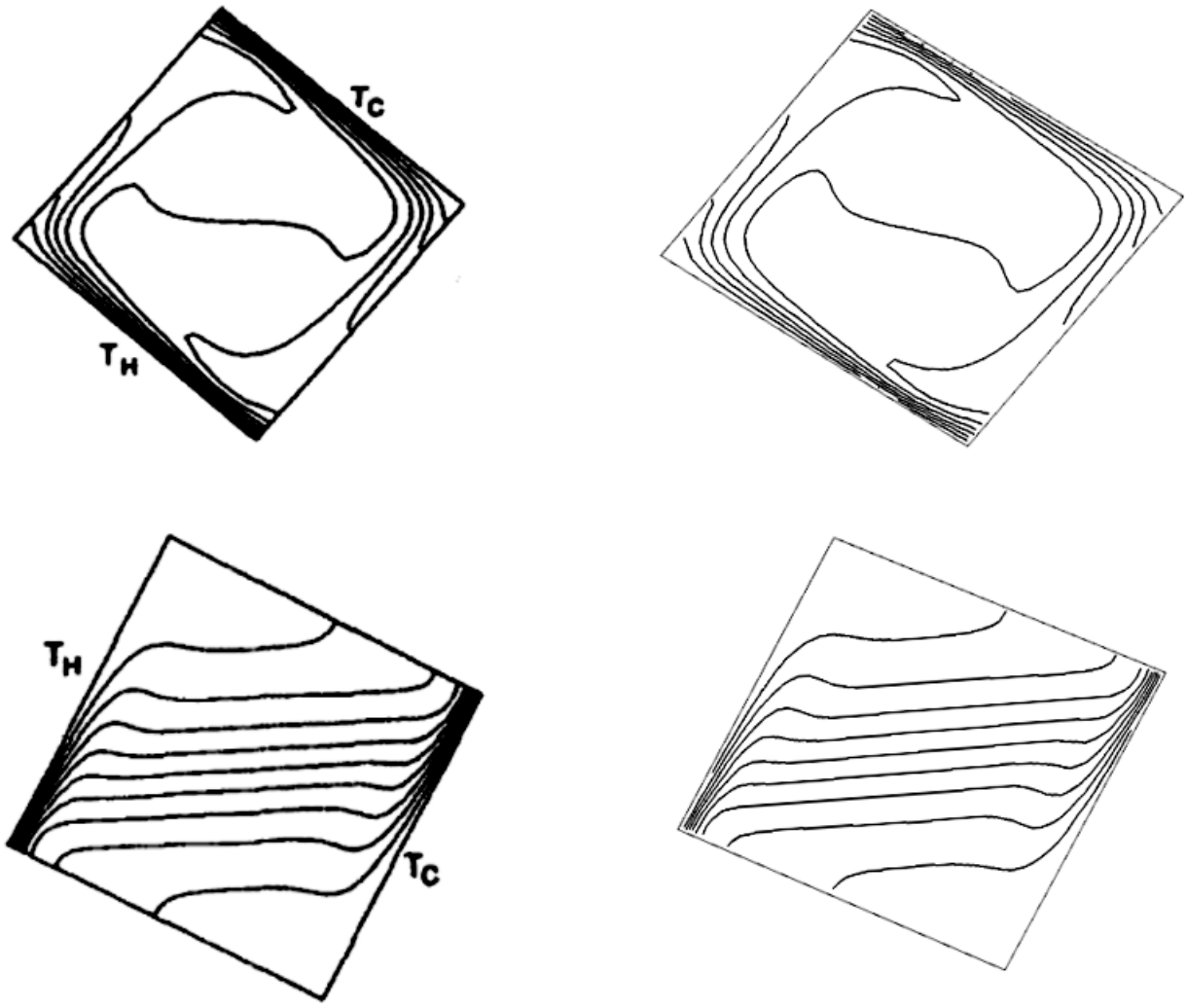

Figure 4.12: A comparison between our natural convection results (right column) and the results obtained by [75] (left column) for an angle of 40° (upper row) and an angle of 120° (lower row) with $Ra = 10^6$.

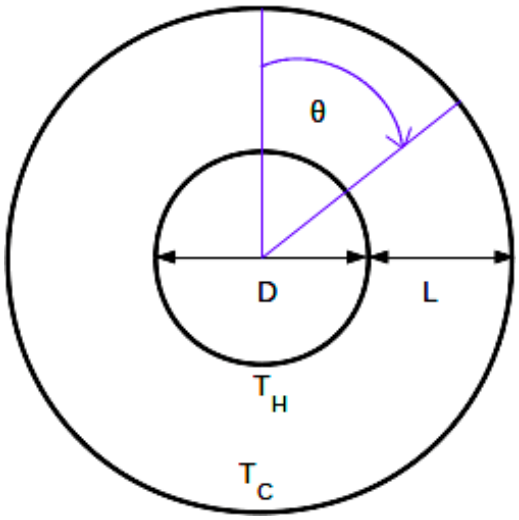

Figure 4.14: Cross-sectional view of the annulus geometry with θ is the angle that moves in a clockwise direction.

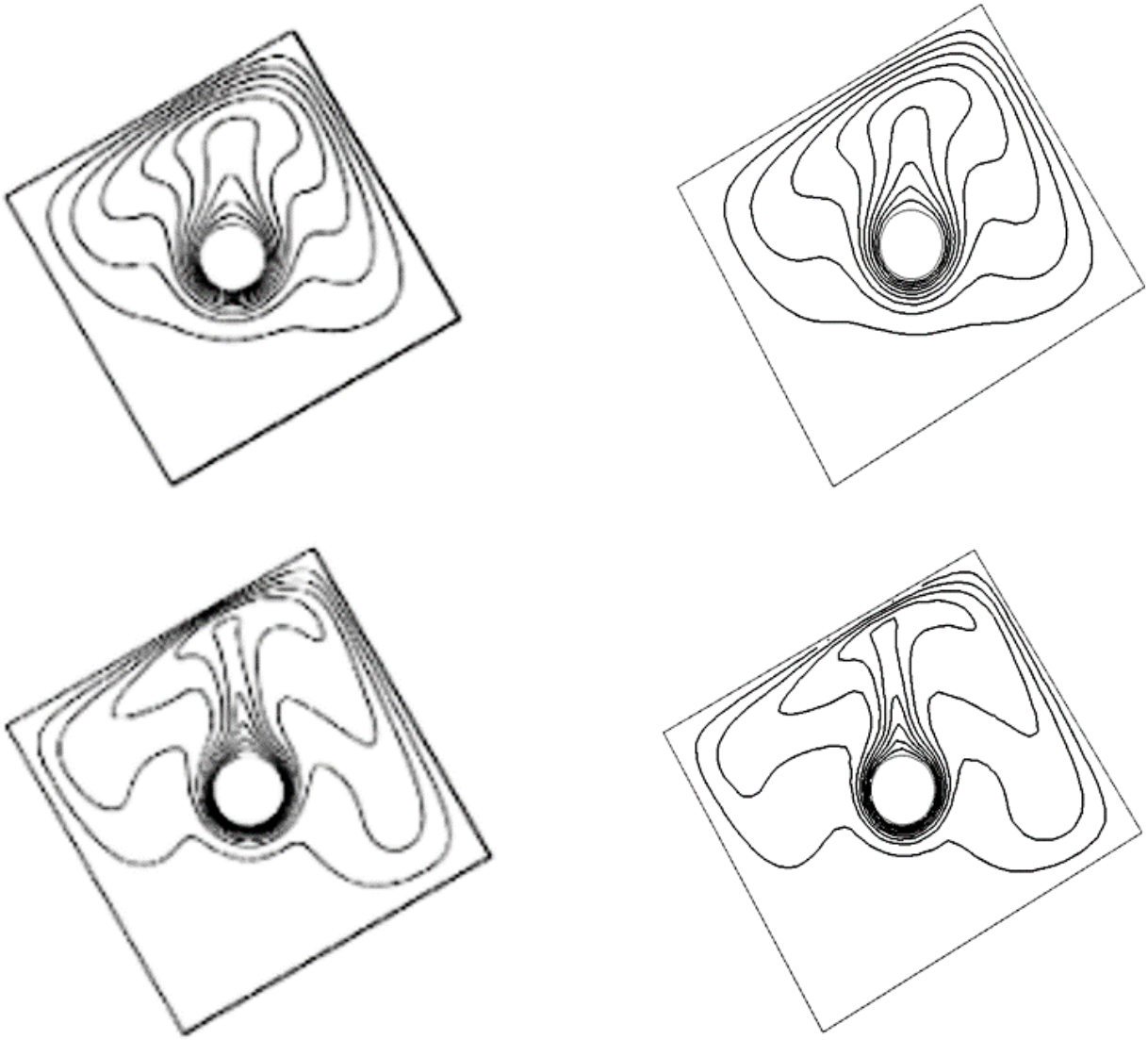

Figure 4.13: A comparison between our natural convection results (right column) and the results obtained by [114] (left column) for an angle of 30° for $Ra = 10^5$ (upper row) and $Ra = 10^6$ lower row with a circular heater diameter of 0.1.

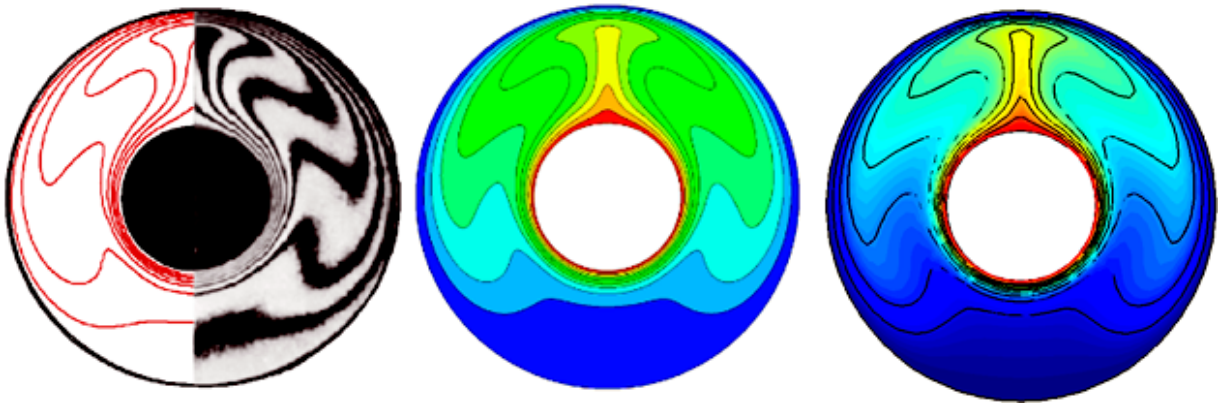

Figure 4.17: Comparison of temperature plume between the current study (right), the published work by [134, 73] (left) and simulation by Yang and Kong [159] (middle) for $Pr = 0.706$ and $Ra = 4.7 \times 10^4$. In the left Figure, the left part is the simulation results carried out by Sheikholeslami et al. [134] and right part is the interferograms from the experimental results of Kuehn and Goldstein [73].

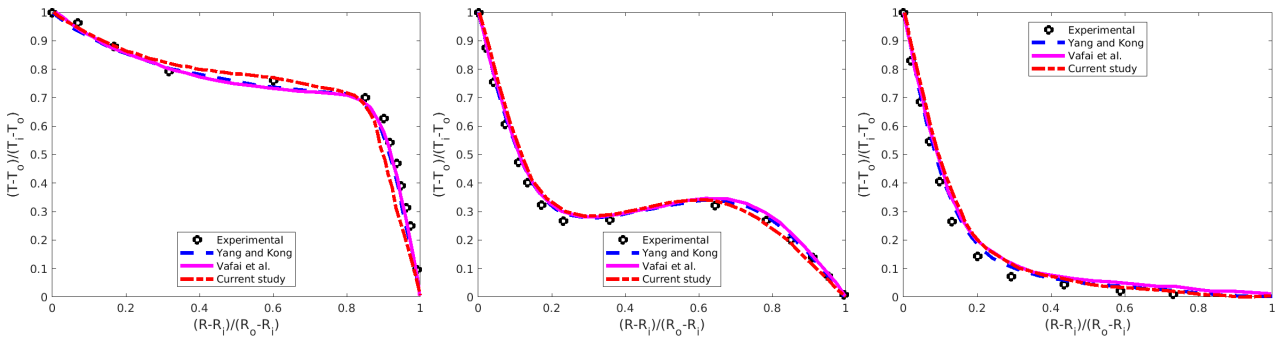

Figure 4.15: Comparison between our results and the published results from Kuehn and Goldstein [73], numerical data from Yang and Kong [159] and simulation study from Vafai et al. [161] at an angle of 0° (left), 90° (middle) and an angle of 180° (right) for values of $Ra = 5 \times 10^5$ and $Pr = 0.7$.

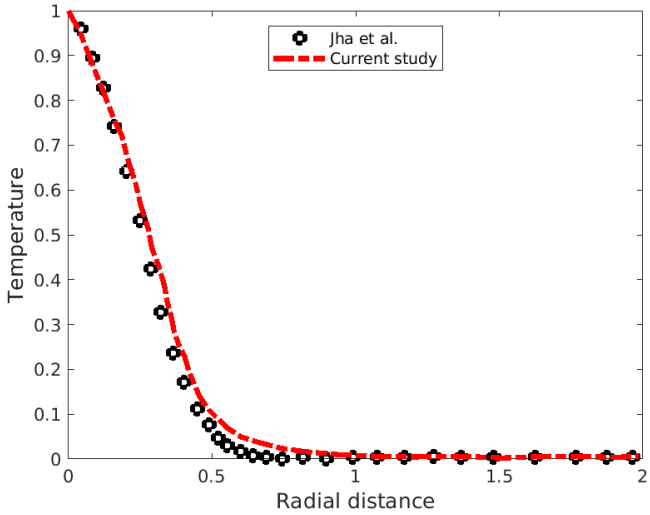

Figure 4.16: Comparison of convection-radiation results between the current study and the published work by Jha et al. [59] for $Pr = 7$, temperature difference parameter $C_T = 1.5$ and perturbation parameter $R = 0.1$.

4.6.4 Obtained results

In all the results presented hereinafter, some variables are kept fixed using our chosen heat transfer coefficients and boundary conditions. The upper and the lower walls of the cavity are adiabatic. The hot wall on the left side is at temperature $\Theta_H = 228$ °C while maintaining the temperature of the cold wall on the right side $\Theta_C = 28$ °C. The Prandtl number $Pr = 0.707$ and $\tau = 0.1$ (as fluid flows inside the cavity is considered air [90]). It is worth noting that the results obtained are for a flow of fully developed and it is not laminar.

4.6.5 Results for squared cavity without internal heater

Different values of Ra, Pl, the inclined angle θ are considered to study the effect of natural convection-radiation inside the cavity. The simulation experiments that are considered at $Ra = 10^4$-10^7 with two different values of $Pl = 0.2$ and 0.5 and three different angles θ of 0°, 30° and 60°. Figure 4.18 shows the temperature contour at a wide range of Ra with $Pl = 0.5$ for the SP_3 approximations and for the considered angles. It can be seen the circulation of flow inside the cavity is affected by the inclined angle. At $\theta = 0°$ and 30°, the flow circulates in a

clockwise direction. However, at $\theta = 60°$, the flow recirculates anti-clockwise. This is due to the buoyancy forces. Although the upper and lower surfaces are adiabatic, it should be noted that the temperature isotherms are not perpendicular to the adiabatic walls owing to the presence of the inclined angle, the radiation and convection heat transfer. The gradients of temperature increase at the top of the cavity as the hot air get less dense (lighter) when it is heated up. However, when the inclined angle increases, the direction of the stagnant position gets affected by the buoyancy forces. It is worth mentioning that the recirculation of the flow covers the entire cavity and concentrated at the center of the cavity despite the value of the angle. As the cavity is inclined, the buoyancy driving force for the natural convection boundary layers will reduce, where the buoyancy term varies with $\cos(\theta)$. This kind of the buoyancy flow has been monitored at $\theta = 0^o$ in [110]. The next step is to investigate the effect of Planck coefficient. Figure 4.19 and Figure 4.20 show the cross-sectional study for temperature at the center of the squared cavity at the three mentioned angles for the considered Rayleigh numbers. At a $Pl = 0.5$, the ratio of radiation to convection heat decreases, although this variation with optical depth remains the same. When the Rayleigh number increases, the effect of radiation decreases dramatically even at a lower value of the Planck coefficient. This indicates that when convection is more intense, the effect of radiation gets smaller.
For the case of $Pl = 0.2$ in which the radiation is more dominant over the conduction, isotherms are high, unlike the pure convection condition where the heat has not reach the cold side, the adiabatic wall condition requires that the conductive heat equals to the radiative heat. If the latter is similar or larger than the former, there will be a temperature gradient near the wall. There are two evident changes to the temperature contour. First, the temperature gradient reduces with the increase values of the Planck coefficient which indicates more heat radiation intensity. Another difference is that the isotherm skewness appears in the middle of the domain towards the hot wall side. In this condition where the conduction heat transfer dominates over the radiation and the radiation has less effect compared with the diffusion heat. This results mean that the effect of heat in case of larger Pl is only due to the adiabatic wall condition. Results show that the temperature layers are thinner than the case of $Ra = 10^4$. As mentioned before, for the Planck coefficient $Pl = 0.5$, the heat transfer acts a little bit same like the pure convection heat transfer as the convection heat becomes dominant. It can be seen that the heat flow decreases along the cold wall and tends to accumulate at the hot wall. The flow with an inclined angle has a dramatic effect on the heat flow behaviour. The results of isotherms show a reduction in the transfer of heat as compared with the results conducted at $\theta = 0°$. The flow of the temperature contour show a reduction of almost 30 % in the heat flow towards the cold direction. Heat is accumulating at the hot wall with reduction in the effect of heat radiation as compared with the results at the horizontal domain (without angle rotation). This unsteady flow is involved of a series of waves circulating around the edges of the cavity and travelling in the same direction as the flow, that is up the heated wall, from left to right across the cavity adjacent to the adiabatic walls. The transition flow is the result of both the natural convection boundary layers and the attached jet/plumes being able to sustain travelling waves. Despite the fact that heat transfer is stable, at an inclination angle of 30° the desolation in the heat plumes is balanced by the expansion in the natural convection boundary layers which lead to the observed transition.

4.6.6 Results for cavity with internal complex heating source

The second part of the study has been considered for a squared cavity with adiabatic upper and lower walls. The left and the right walls are kept at a temperature of 28 °C. A circular

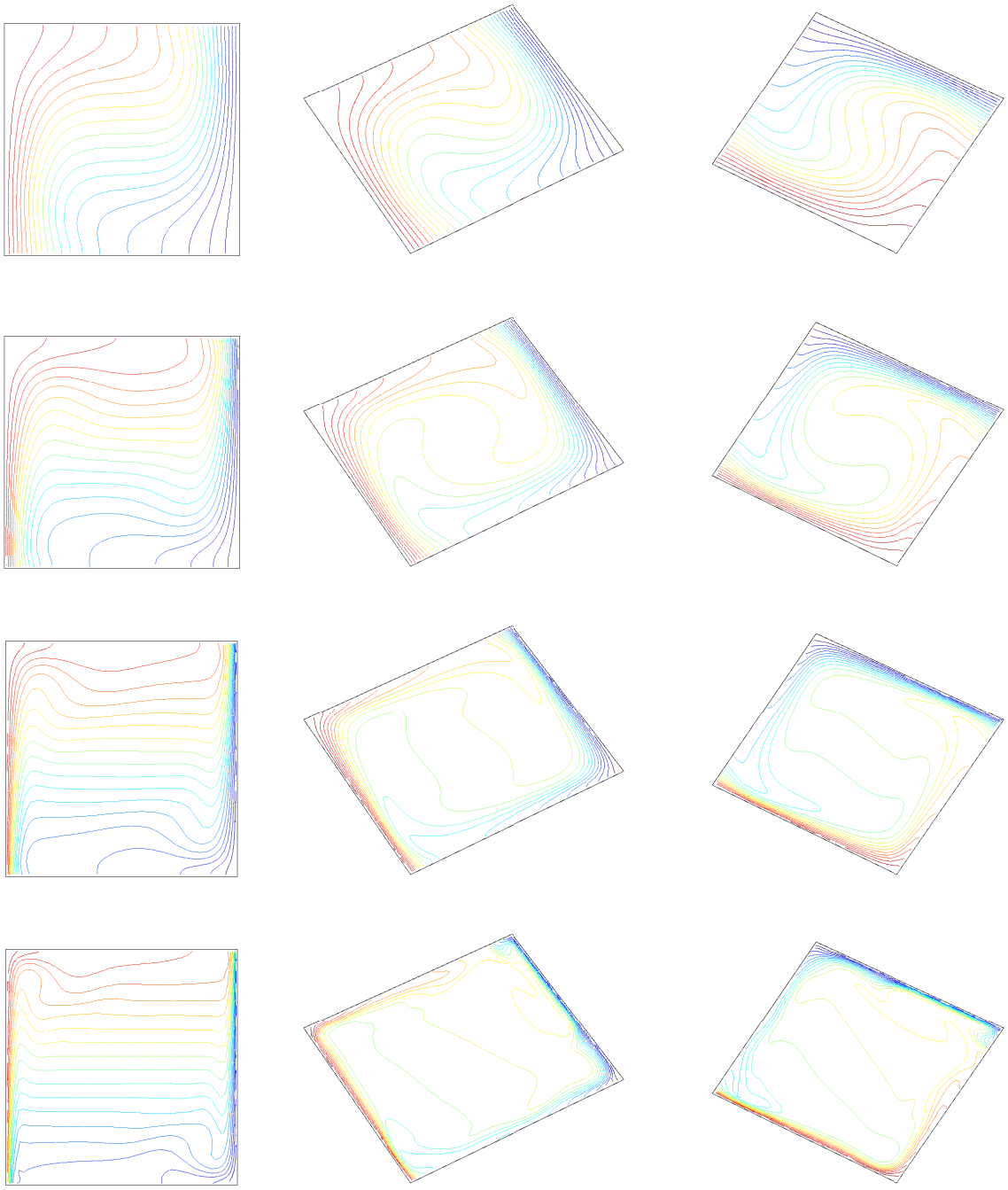

Figure 4.18: Temperature contour for the SP_3 solution at $Ra = 10^4$ (first row), $Ra = 10^5$ (second row), $Ra = 10^6$ (third row) and $Ra = 10^7$ (fourth row) with $Pl = 0.5$ at $\theta = 0°$ (first column), $\theta = 30°$ (second column) and $\theta = 60°$ (third column).

heater is installed at the center of the squared cavity at a temperature of 228 °C. Figure 4.21 shows the SP_3 evolution of the thermal plume at the three mentioned angles. This evolution of the thermal plume can be defined as the interaction between the thermal plume at high temperature from the circular heating element and the thermal plume at lower temperature at the sides of the cavity. It can still be seen that the temperature distribution inside the cavity is affected by the Rayleigh number and the inclined angle. At a dominant heat radiation ($Ra =$

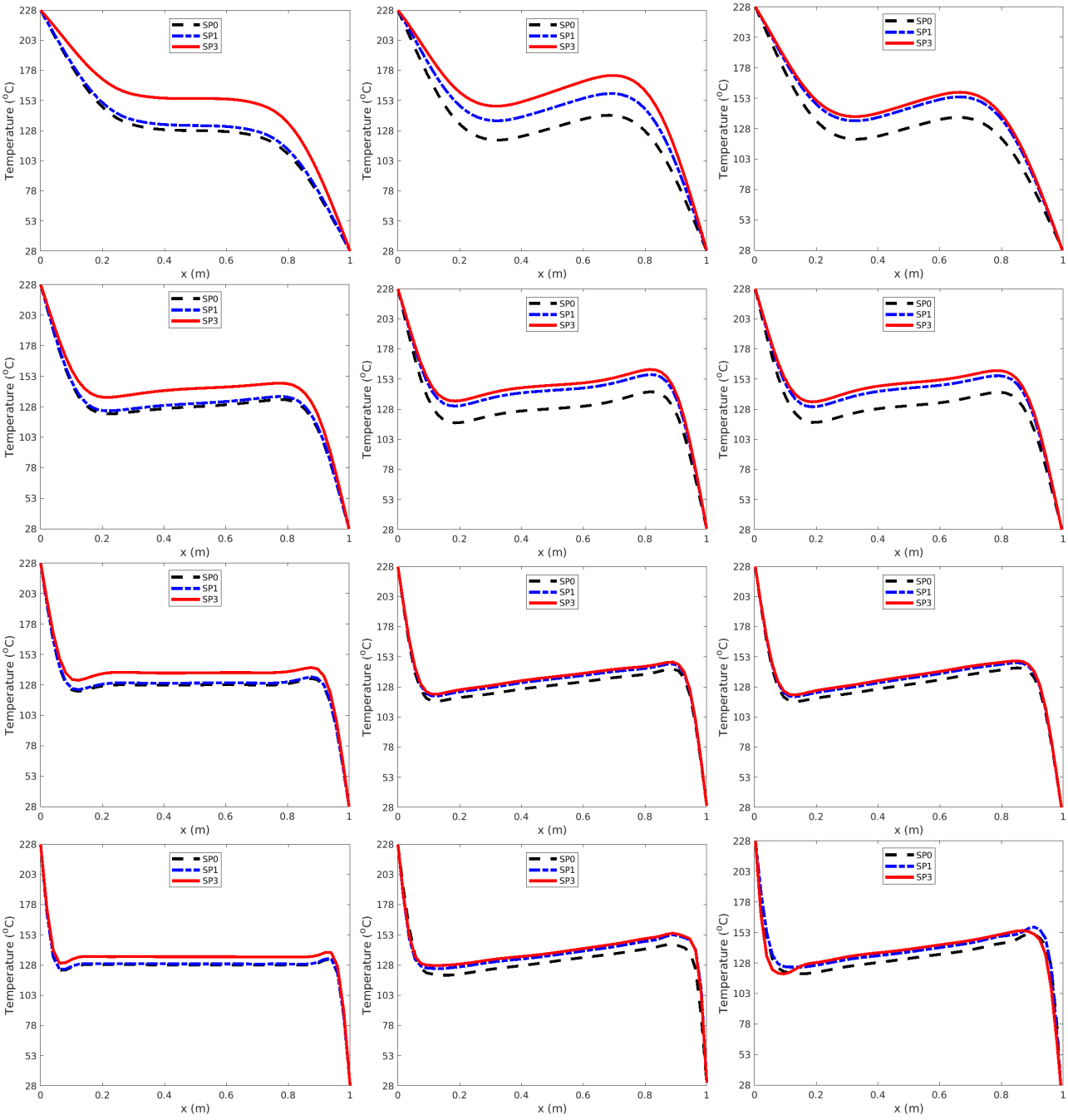

Figure 4.19: Temperature cross-sectional study for the pure convection SP_0 and radiation-convection SP_1 and SP_3 solutions at $Ra = 10^4$ (first row), $Ra = 10^5$ (second row), $Ra = 10^6$ (third row) and $Ra = 10^7$ (fourth row) with $Pl = 0.2$ at $\theta = 0°$ (first column), $\theta = 30°$ (second column) and $\theta = 60°$ (third column).

10^4), thermal plume tends to move upward. The only reason for this behaviour is the presence of the adiabatic wall. However, fluid flow rate increases and it is flowing towards the shortest cold region at higher values of the Rayleigh number. This is due to the fact that the capability of the cold wall to absorb the heat is more than the heat flux flow into the adiabatic upper wall at higher Ra and with the effect of the inclination angles. Since the temperature difference is established across the right side of the cavity, the heat starts to flow towards that direction and accumulates there. Figure 4.22 and Figure 4.23 show the horizontal cross-sectional study

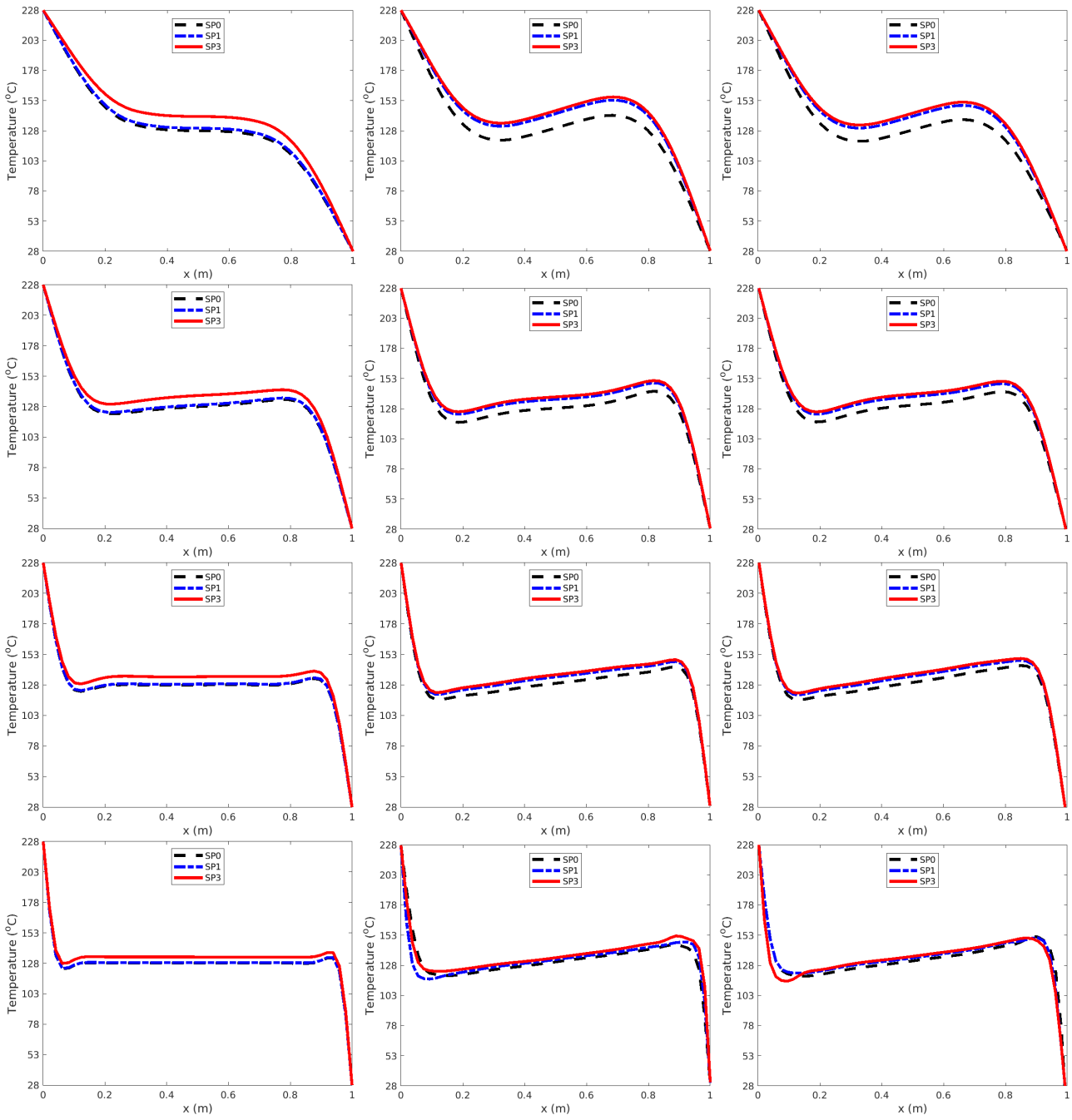

Figure 4.20: Temperature cross-sectional study for the pure convection SP_0 and radiation-convection SP_1 and SP_3 solutions at $Ra = 10^4$ (first row), $Ra = 10^5$ (second row), $Ra = 10^6$ (third row) and $Ra = 10^7$ (fourth row) with $Pl = 0.5$ at $\theta = 0°$ (first column), $\theta = 30°$ (second column) and $\theta = 60°$ (third column).

that has been accounted across the cavity at $y = 0.8$. It can be seen that the effect of radiation is not quite dominant. Different values of the Planck coefficient has no dramatic effect on radiation. This is due to the close distance of the heating source which is located in the middle. Introducing the heating element in the middle part of the cavity caused less heat transfer circulation across the geometry. This indicates that the longer the heat travels, the higher radiation of heat becomes. The effect of the adiabatic walls on the direction of heat is reduced massively with the augmentation of the inclined angle. The complete study has been

Table 4.1: Temperature values in the middle of the geometry without including the circular heater in °C of SP_0, SP_1 and SP_3 at the chosen experimental simulations of $\theta = 0°$.

$Ra = 10^4$					$Ra = 10^5$				
$Pl = 0.2$			$Pl = 0.5$		$Pl = 0.2$			$Pl = 0.5$	
SP_0	SP_1	SP_3	SP_1	SP_3	SP_0	SP_1	SP_3	SP_1	SP_3
128.14	132.38	154.63	130.17	139.89	127.85	130.48	143.27	129.44	137.24
$Ra = 10^6$					$Ra = 10^7$				
$Pl = 0.2$			$Pl = 0.5$		$Pl = 0.2$			$Pl = 0.5$	
SP_0	SP_1	SP_3	SP_1	SP_3	SP_0	SP_1	SP_3	SP_1	SP_3
127.95	129.47	137.82	128.76	134.72	128.54	128.95	134.84	128.93	133.17

summarized in the Tables 4.1 - 4.4. It can be seen from the tables that the inclined cavity with angles of inclination of 30° and 60° is shown to have a considerably different flow effect to that of the non-inclined cavity. The fluid in the diffuse intrusion flows horizontally across the cavity to be entrained by the far wall boundary layer. As the angle of inclination increases the fluid flow pattern changes. This is due to the change in the buoyancy forces in the direction of flow between the hot and the cold walls. The effect of the inclusion of the heating source inside the squared cavity is affected mainly by the inclined angle then by Rayleigh number. At a dominant radiation of the Planck coefficient of 0.2 and the Rayleigh number of 10^4, convection alone captured a temperature of 128.14 °C, while the temperature with the SP_1 was 132.38°C and a value of 154.63°C under the SP_3. From these novel obtained results, it is worth mentioning that the commercial softwares as well as the previous studies based on P_1 approximations failed to give accurate results when studying radiation heat transfer inside industrial applications. The radiation heat transfer has a dramatic effect on heat transfer even at a dominant convection effect of the Rayleigh number of 10^6 and moderate the Planck coefficient of 0.5. The novel developed method is then applied to different inclination angles and with the inclusion of complex heating source inside the cavity. This is done to understand and study the effect of the change in the buoyancy forces. It was shown that as the angle of inclination increases the fluid flow pattern changes. Our results for radiation accounts for the SP_3 are still dominant and can not be underestimated inside the investigated domains. This chapter proved that results obtained from the SP_3 approximations are the most desirable for numerical and industrial purposes with natural heat transfer.

4.7 Concluding remarks

Combined heat transfer of natural convection and radiation in a squared cavity was studied numerically at three different inclined angles. The continuity, momentum and energy equations were solved using the Taylor-Hood finite element approach for the first time. Splitting method is considered to deal with the advection term and Galerkin-characteristics technique is a very good bonus to deal with the pressure surge. To deal with radiation effects which are the dominant mode, the simplified P_N approximations are used and the SP_3 is applied and considered for the first time. After thorough experimental and numerical validations, the robust methods show that it can be taken for granted. The considered medium is air with two upper and lower adiabatic walls. The heat transfer characteristics inside the cavity were obtained at a

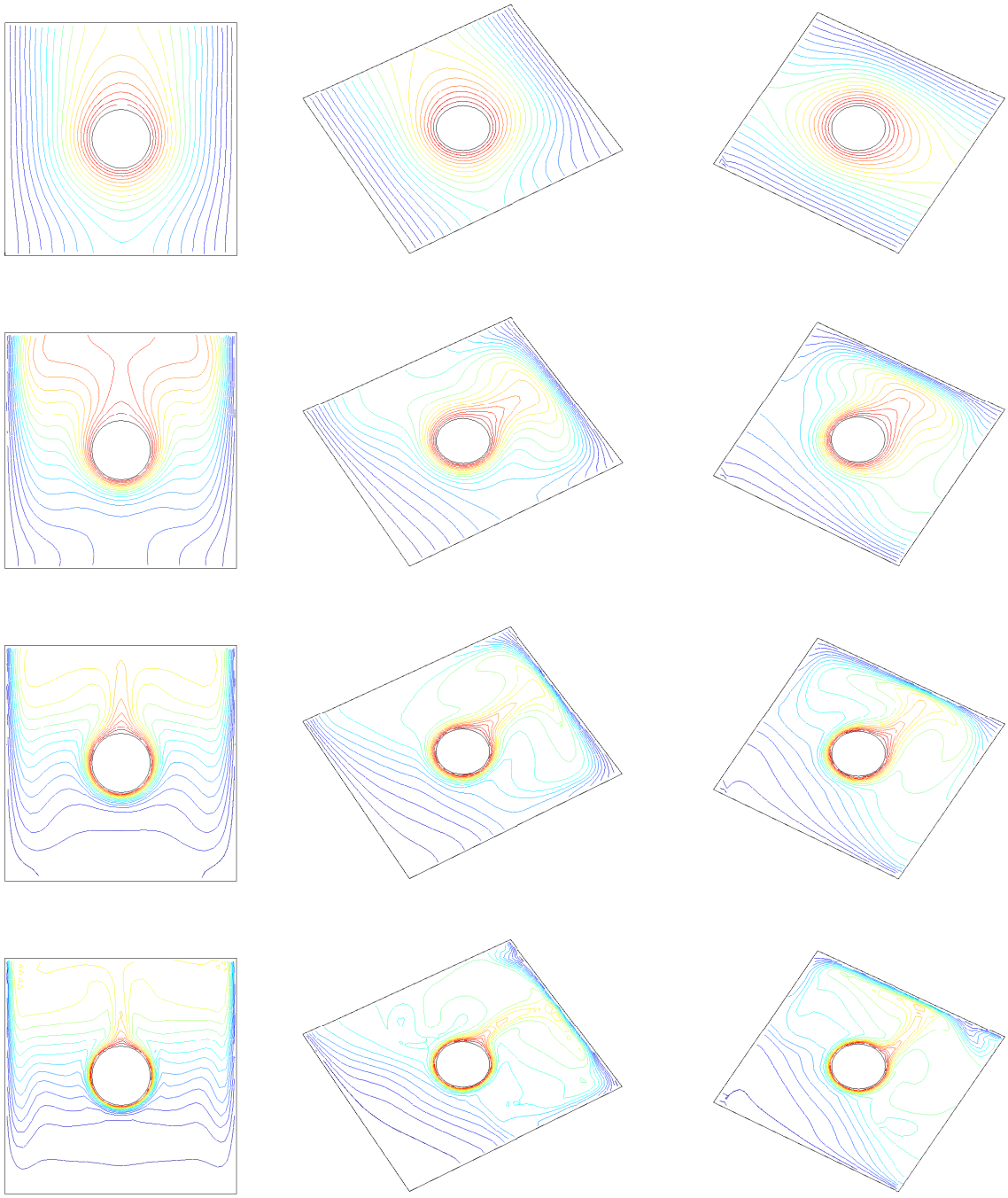

Figure 4.21: Temperature contours for the SP_3 solution at $Ra = 10^4$ (first row), $Ra = 10^5$ (second row), $Ra = 10^6$ (third row) and $Ra = 10^7$ (fourth row) with $Pl = 0.2$ at $\theta = 0°$ (first column), $\theta = 30°$ (second column) and $\theta = 60°$ (third column).

broad range of Rayleigh numbers (10^4-10^7) with optical thickness value of 0.1 and the Planck coefficient values of 0.2 and 0.5. The goal of this study is to apply the novel approaches for the first time to cover the turbulent natural convection-radiation heat transfer that takes places in realistic applications that can serve the industry. The presented study in this chapter is essential as it considered as the cornerstone for real applications like, ovens, microwaves, heat exchangers... etc. To the best of our knowledge, the entire previous studies failed to describe

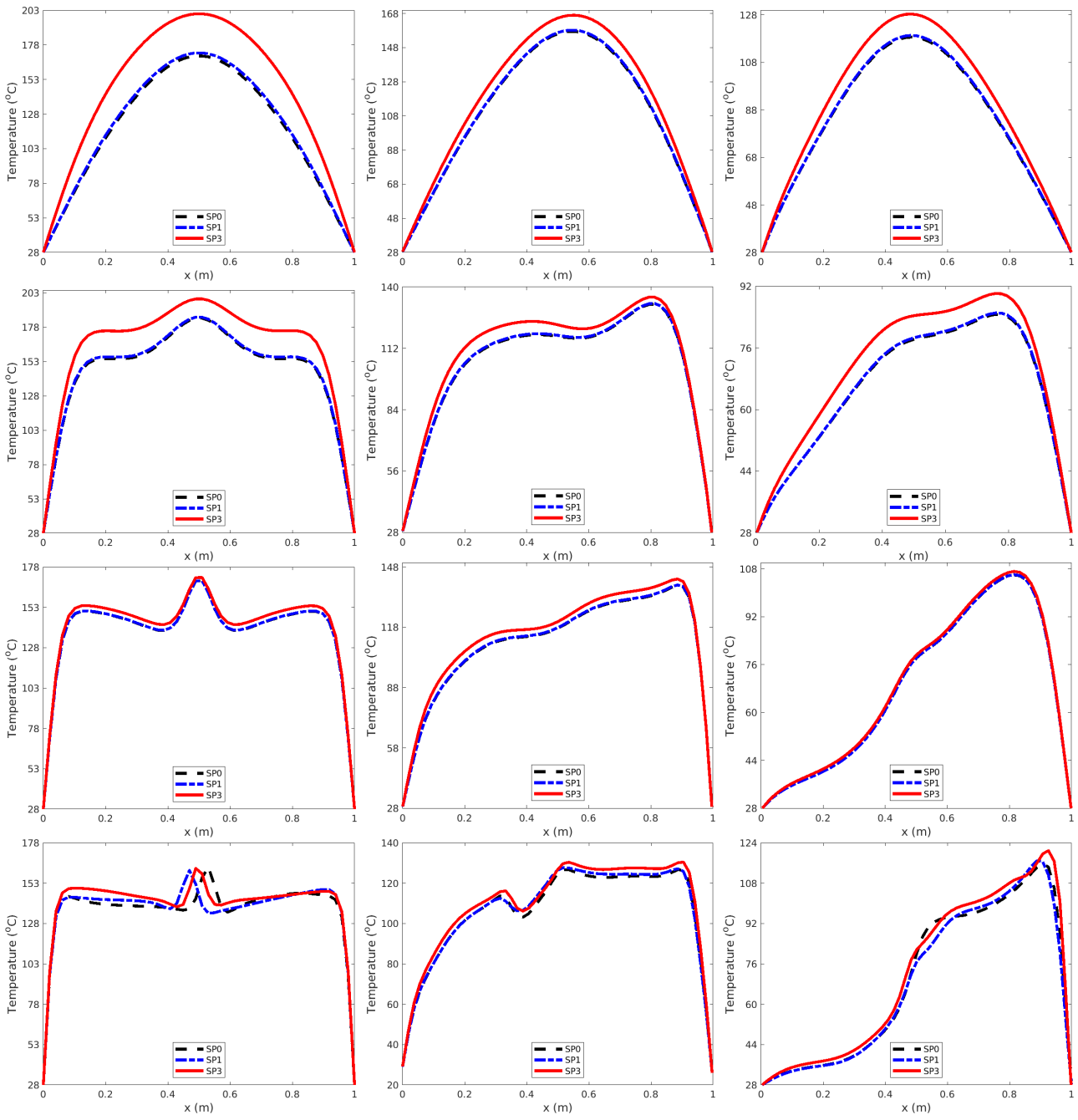

Figure 4.22: Temperature cross-section for the SP_3 solution at $Ra = 10^4$ (first row), $Ra = 10^5$ (second row), $Ra = 10^6$ (third row) and $Ra = 10^7$ (last row) with $Pl = 0.2$ at $\theta = 0°$ (first column), $\theta = 30°$ (second column) and $\theta = 60°$ (third column).

radiation accurately. We believed that the previous studies misfigured the accurate methods that can lead to the accurate results that can simulate part of/whole industrial applications as real and skilful as possible. Our stable solver was able to capture a significant temperature difference under a dominant radiation heat transfer. At a dominant radiation of the Planck coefficient of 0.2 and the Rayleigh number of 10^4, convection alone captured a temperature of 128.14°C, while the temperature with SP_1 was 132.38°C and a value of 154.63°C under the SP_3. From these novel obtained results, it is worth mentioning that results obtained from commercial softwares as well as the previous studies based on P_1 approximations failed to

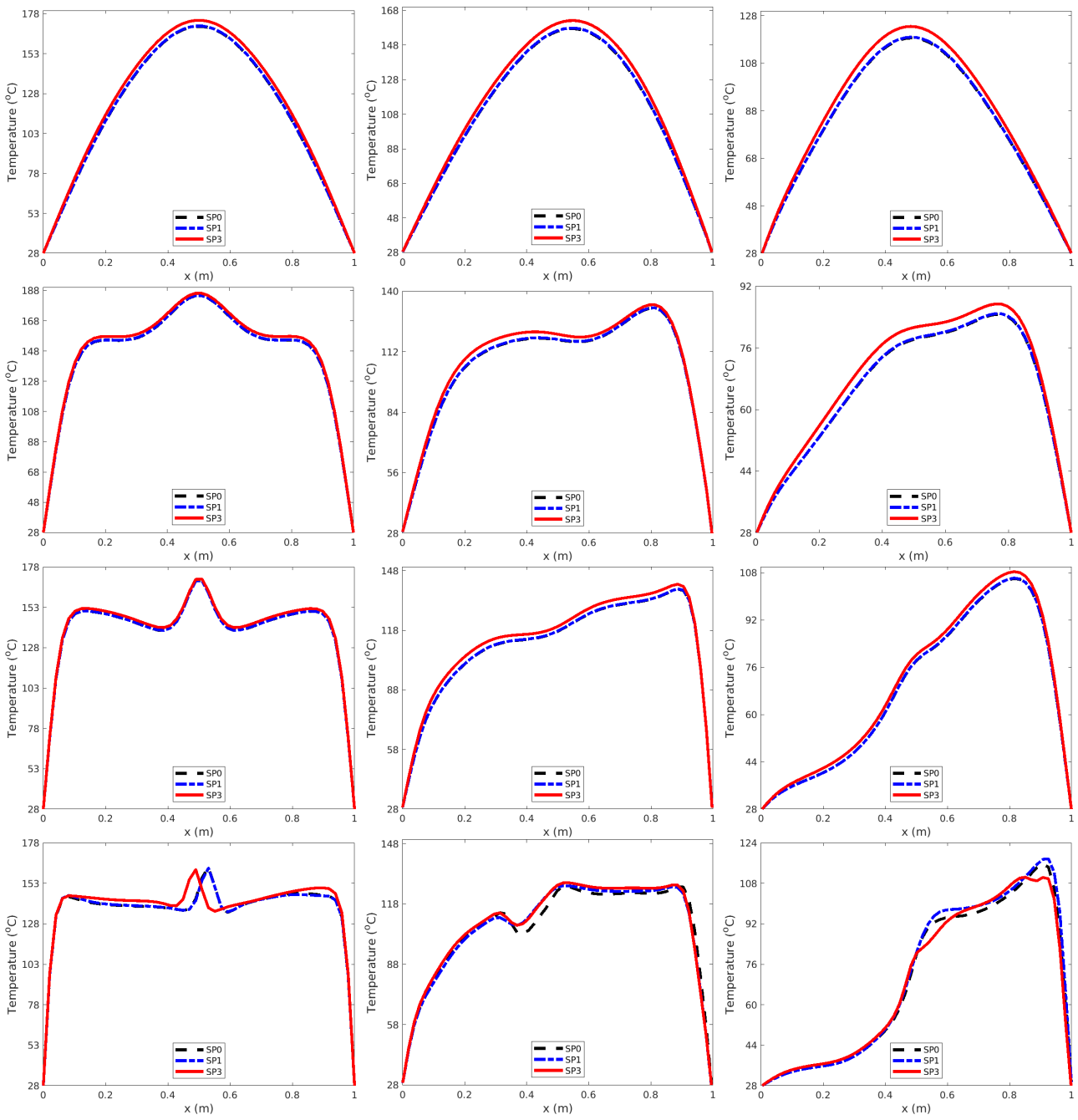

Figure 4.23: Temperature cross-section for the SP_3 solution at $Ra = 10^4$ (first row), $Ra = 10^5$ (second row), $Ra = 10^6$ (third row) and $Ra = 10^7$ (last row) with $Pl = 0.5$ at $\theta = 0°$ (first column), $\theta = 30°$ (second column) and $\theta = 60°$ (third column).

give accurate results when studying radiation heat transfer inside industrial applications. The radiation heat transfer has a dramatic effect on heat transfer even at a dominant convection effect of Rayleigh number of 10^6 and moderate Planck constant of 0.5. This chapter proves that the SP_3 approximations are the most desirable for numerical and industrial purposes with natural heat transfer. It can be seen from the validated novel results that the inclined cavity with angles of inclination of 30° and 60° is shown to have a considerably different flow effect to that of the non-inclined cavity. The fluid in the diffuse intrusion flows horizontally across the cavity to be entrained by the far wall boundary layer. As the angle of inclination increases the

Table 4.2: Temperature values in the middle of the geometry without including the circular heater in °C of SP_0, SP_1 and SP_3 at the chosen experimental simulations of $\theta = 30°$.

$Ra = 10^4$					$Ra = 10^5$				
$Pl = 0.2$			$Pl = 0.5$		$Pl = 0.2$			$Pl = 0.5$	
SP_0	SP_1	SP_3	SP_1	SP_3	SP_0	SP_1	SP_3	SP_1	SP_3
140.67	158.54	173.82	153.16	155.76	128.45	143.97	148.25	136.13	138.12
$Ra = 10^6$					$Ra = 10^7$				
$Pl = 0.2$			$Pl = 0.5$		$Pl = 0.2$			$Pl = 0.5$	
SP_0	SP_1	SP_3	SP_1	SP_3	SP_0	SP_1	SP_3	SP_1	SP_3
130.39	135.64	137.42	135.11	136.88	131.56	136.67	138.66	133.44	135.02

Table 4.3: Temperature values in the middle of the geometry without including the circular heater in °C of SP_0, SP_1 and SP_3 at the chosen experimental simulations of $\theta = 60°$.

$Ra = 10^4$					$Ra = 10^5$				
$Pl = 0.2$			$Pl = 0.5$		$Pl = 0.2$			$Pl = 0.5$	
SP_0	SP_1	SP_3	SP_1	SP_3	SP_0	SP_1	SP_3	SP_1	SP_3
128.73	146.14	149.71	140.06	142.65	130.92	145.52	150.36	138.05	140.16
$Ra = 10^6$					$Ra = 10^7$				
$Pl = 0.2$			$Pl = 0.5$		$Pl = 0.2$			$Pl = 0.5$	
SP_0	SP_1	SP_3	SP_1	SP_3	SP_0	SP_1	SP_3	SP_1	SP_3
130	135.89	137.74	135.22	137.07	131.69	137.01	139.27	134.2	135.51

Table 4.4: Temperature values in the middle of the geometry with the inclusion the circular heater in °C of SP_0, SP_1 and SP_3 at the chosen experimental simulations of $\theta = 0°$.

$Ra = 10^4$					$Ra = 10^5$				
$Pl = 0.2$			$Pl = 0.5$		$Pl = 0.2$			$Pl = 0.5$	
SP_0	SP_1	SP_3	SP_1	SP_3	SP_0	SP_1	SP_3	SP_1	SP_3
169.97	172.19	200.44	170.27	173.84	184.46	185.27	198.54	184.6	186.16
Ra $= 10^6$					Ra $= 10^7$				
$Pl = 0.2$			$Pl = 0.5$		$Pl = 0.2$			$Pl = 0.5$	
SP_0	SP_1	SP_3	SP_1	SP_3	SP_0	SP_1	SP_3	SP_1	SP_3
169.27	169.42	171.39	169.36	170.37	162.95	160.87	162.13	162.33	161.42

fluid flow pattern changes. This is due to the change in the buoyancy forces in the direction of flow between the hot and the cold walls. The effect of the inclusion of the heating source inside the squared cavity is affected mainly by the inclined angle then by the Rayleigh number.

Chapter 5

Simplified P_N models for forced convection-radiation heat transfer

The present chapter is dedicated to the modelling of the heat flow inside two types of furnaces, direct fired furnace and furnace with regenerative burners. The stabilized Taylor-Hood finite element approximation from the previous chapter using triangular mesh will be extended and applied for the resolution of the 2D Navier-Stokes equations for solving radiation and the forced convection heat transfer. The Boussinesq approximation for modelling the change in density is considered. The simplified P_N approximations are carried out for the radiative transfer which is coupled with convection. The Galerkin-characteristics method is accounted for the dominant advection. The developed models are tested and results are presented under the operation of different burners. Comparisons between simulations without radiation and with radiation are discussed. The main goal of the chapter is to provide such an alternative novel method for simulating heat flow that occurs inside industrial furnaces. The chapter focuses on getting acceptable validated results while minimizing the computational time. For the first time, the simplified P_N approximations are accounted for the simulation of heat flow inside the furnaces with different operating scenarios.

5.1 Modelling forced convection-radiation

It is known that the property of incompressibility is a feature of the fluid dynamics. The flow is said to be incompressible if it is incapable of the reduction in volume by pressure. The gases are mostly considered as compressible flows. For low Mach number around 0.3, they can be also be treated as incompressible [30]. This non-dimensional number quantifies the relation between a characteristic velocity u of the flow and the velocity of the sound c by:

$$M = \frac{u}{c}.$$

The Mach number is named after physicist and philosopher Ernst Mach (1836-1916). Since the velocity of the sound is 340 m/s in the air, then the conditions of incompressibility is well respected up to a fluid velocity of 100 m/s. In this work, the values for the flow velocity that are chosen are compatible with the velocity of the flame inside industrial furnaces [120, 14]. Therefore, some assumptions and simplifications are made. Another important non-dimensional number that quantifies the properties of a particular flow is the Reynolds number given by

$$Re = \frac{Lu}{\wp},$$

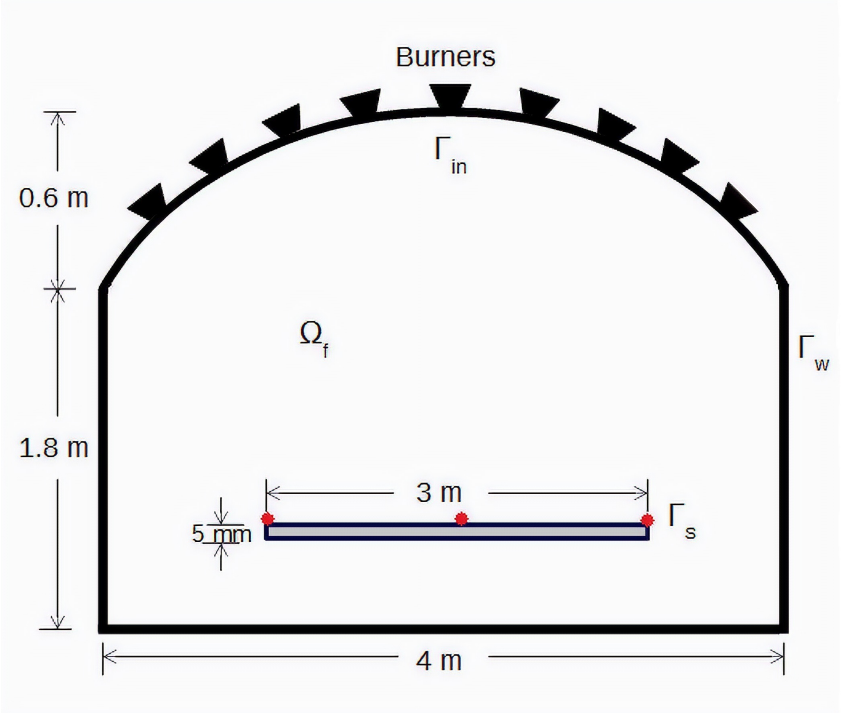

Figure 5.1: Illustration of a cross-sectional view of the considered furnace containing multiple burners and a structure.

where L is a characteristic length scale, u is the flow velocity and $\wp$ is the kinematic viscosity of the respective flow. It gives a measure of the ratio of inertial forces to viscous forces and, consequently it quantifies the relative importance of these two types of forces for given flow conditions. The Reynolds numbers is frequently used to characterize different flow regimes, such as laminar ($Re \leq 2300$), transition ($2300 < Re < 4000$) or turbulent flow ($Re \geq 4000$): laminar flow occurs at low Reynolds numbers, where viscous forces are dominant, and is characterized by smooth, constant fluid motion, while turbulent flow occurs at high Reynolds numbers and is dominated by inertial forces, which tend to produce random eddies, vortices and other flow fluctuations. The Reynolds number is named after Osborne Reynolds (1842-1912), who proposed it in 1883. In most of the heating and manufacturing applications, maintaining a uniform temperature distribution over the surface of the enclosure inside the furnace is required for the product quality [148]. Therefore, moderate values of the Reynolds number inside the furnace are required to adjust the heat flow vortices. A special attention is needed in the study of the effect of vortices inside the furnace because of their big effect on the heat flow stabilization [66]. The vortex takes place when the pressure gradient is large enough to create heat flow recirculation along the furnace axis.

5.2 Equations for convection-radiation problems

Figure 5.1 represents a schematic of the geometry for the furnace studied in this work which consists of two-dimensional cross-sectional view (with vertical burners) containing a flat structure. The domain is initially at the room temperature $\Theta'_C = 300$ K. The burners blow fire at a temperature of $\Theta'_H = 1800$ K. Thickness of the heated structure sheet is very thin about 5 mm. The following scales have been produced to formulate a dimensionless form of the governing

equations:

$$\mathbf{x} = \frac{\mathbf{x}'}{D'}, \qquad t = \frac{t'}{t_{ref}}, \qquad \mathbf{u} = \frac{\mathbf{u}'}{u_{ref}}, \qquad p = \frac{p'}{\rho' u_{ref}^2}, \qquad \wp' = \frac{\varsigma'}{\rho'}, \qquad I = \frac{I'}{I_{ref}},$$
$$\Theta = \frac{\Theta' - \Theta'_C}{\Theta'_H - \Theta'_C}, \qquad g = \frac{D' g'}{u_{ref}^2}, \qquad \beta = \beta' \Theta'_H, \qquad D = \frac{D'}{D_{ref}}, \qquad \kappa = \frac{\kappa'}{\kappa_{ref}}.$$

The kinematic viscosity is $\wp'$, ς the dynamic viscosity and D' is the structure thickness. The non-dimensional numbers are defined as

$$\tau = \kappa_\infty L_\infty, \qquad Pr = \frac{\nu'}{\alpha'}, \qquad Re = \frac{D' u_\infty}{\nu'}, \qquad Pl = \frac{\epsilon'}{D' \ \sigma'_B \ \Theta'^3_H},$$

where τ is the optical depth, L_∞ is the length parameter, ϵ' thermal diffusivity, Re the Reynolds number, Pr the Prandtl number, Pl is the Planck constant. Substituting the dimensionless variables in the governing equations (4.1)-(4.4), we get

$$\begin{aligned} \nabla \cdot \mathbf{u} &= 0, \\ \frac{D\mathbf{u}}{Dt} + \nabla p - \frac{1}{Re}\nabla^2 \mathbf{u} &= \Theta \mathbf{e}, \\ \frac{D\Theta}{Dt} - \frac{1}{PrRe}\nabla^2 \Theta &= -\frac{1}{PrRe}\nabla \cdot \mathbf{q}_R, \end{aligned} \tag{5.1}$$

where $\mathbf{e} = (0,1)^T$ is the unit vector associated with the gravitational force. The radiative transfer equation (4.6) can be rewritten in dimensionless as

$$\tau\omega \cdot \nabla I + \kappa I = \kappa B(\Theta). \tag{5.2}$$

The governing equations (5.1) and (5.2) are solved in a computational domain Ω with smooth boundary $\partial\Omega = \Gamma_{\mathrm{w}} \cup \Gamma_{\mathrm{in}} \cup \Gamma_{\mathrm{s}}$ as shown in Figure 5.1, and subject to the following boundary conditions

$$\begin{aligned} \mathbf{u}(t, \hat{\mathbf{x}}) &= \mathbf{0}, && \forall\, \hat{\mathbf{x}} \in \Gamma_{\mathrm{w}}, \\ \mathbf{u}(t, \hat{\mathbf{x}}) &= u_\infty, && \forall\, \hat{\mathbf{x}} \in \Gamma_{\mathrm{in}}, \end{aligned}$$

for the flow velocity, and

$$\begin{aligned} \Theta(t, \hat{\mathbf{x}}) &= \Theta_C, && \forall\, \hat{\mathbf{x}} \in \Gamma_{\mathrm{w}}, \\ \Theta(t, \hat{\mathbf{x}}) &= \Theta_H, && \forall\, \hat{\mathbf{x}} \in \Gamma_{\mathrm{in}}, \\ \mathbf{n}(\hat{\mathbf{x}}) \cdot \nabla\Theta(t, \hat{\mathbf{x}}) &= 0, && \forall\, \hat{\mathbf{x}} \in \Gamma_{\mathrm{s}}, \end{aligned} \tag{5.3}$$

for the temperature. Here, $\mathbf{n}(\hat{\mathbf{x}})$ denotes the outer unit normal with respect to $\partial\Omega$. For the radiative transfer, the boundary conditions are for emitting and reflecting walls

$$\begin{aligned} I(\hat{\mathbf{x}}) &= B(\Theta_C), && \forall\, \hat{\mathbf{x}} \in \hat{\Gamma}_{\mathrm{w}}, \\ I(\hat{\mathbf{x}}) &= B(\Theta_H), && \forall\, \hat{\mathbf{x}} \in \hat{\Gamma}_{\mathrm{in}}, \\ \mathbf{n}(\hat{\mathbf{x}}) \cdot \nabla I(\hat{\mathbf{x}}) &= 0, && \forall\, \hat{\mathbf{x}} \in \hat{\Gamma}_{\mathrm{s}}, \end{aligned} \tag{5.4}$$

where the boundary regions are defined as

$$\hat{\Gamma}_i = \left\{ \hat{\mathbf{x}} \in \Gamma_i : \qquad \omega \cdot \mathbf{n}(\hat{\mathbf{x}}) < 0 \right\}, \qquad i = w, in, s.$$

It is important to mention that other boundary conditions for the radiation flow can also be introduced in our formulation without main conceptual changes.

Table 5.1: SP_1 horizontal cross sectional results for one burner with CPU time in minutes.

	# of elements	# of nodes for temperature & velocity	# of nodes for pressure	Error in temperature	Error in velocity v	Error in pressure	CPU times
Mesh A	12351	25133	6391	0.0961	0.2593	0.2034	2
Mesh B	24898	50442	12772	0.0778	0.1195	0.0861	5
Mesh C	**49411**	**99693**	**25141**	**0.0154**	**0.0646**	**0.0451**	**14**
Mesh D	99112	199504	50196	0.0103	0.0293	0.0202	35
Reference	247534	497122	124794	——	——	——	116

5.3 Numerical results for direct fired furnace

In this section, in order to validate the results, two steps are considered. Since no study for direct fired Convective Glass Melting furnace (CGM) has been investigated. We have taken into account two of the configurations that has been examined by [37] using four vertical burners inside a walking-beam type reheat furnace domain for the temperature of the billet inside the furnace. The only difference is that we have chosen a triangular mesh for the current validation while they have chosen a quadrilateral mesh. The billets travel a distance of 3.8 m along the furnace. The separation between the burners axis is 1 m and the burner closest to the right wall is 0.65 m from it. In order to avoid billets overheating, given due to the location of the flames directly over the billets, the back wall supporting the burners was located 0.36 m away from the last billet position. The rectangular furnace had an internal width of 4.15 m and an internal height of 0.7 m. The mean ambient pressure and temperature are 74.7 kPa and 300 K, respectively. The burners blow fire to a temperature of above 1100 K for the purpose of heating steel structures at time t = 10 s. Two points for two cases C1 and C2 have been monitored a long the billet as it travels through the furnace. In case of C1 and C2, the location of the burners are on the back wall opposite to direction of the billet movement. The difference between the cases C1 and C2 is that the latter geometry is 20 % shorter. The distance between the burners is 1 m and the fourth burner is 0.65 m from the right wall. A full schematic of the geometry as well as the temperature isotherms are provided in [37]. Figure 5.2 shows a great match between the conducted results and the results obtained by [37] for the temperature profile in the considered cases of C1 and C2 versus billet position.
The second validation that has been accounted for is mesh convergence for the SP_1 under the operation of a single burner attached to the middle position of the roof curvature of the domain at time $t = 10$ s. The heat transfer characteristics values for the SP_1 are taken into account for the mesh convergence with an optical depth τ of 1 and the Planck coefficient of $Pl = 0.5$. Very fine mesh density is taken as a reference mesh for the calculation of errors with CPU time. In this study, two values of the Reynolds number are considered of $Re =$ 500 and 1000, the Prandtl number is $Pr = 0.72$. Table 5.1 illustrates the validation of the results represented by the mesh convergence and Figure 5.3 shows the mesh convergence for a horizontal cross-sectional study taken for the heat flow temperature, pressure and velocity at the wall height $y = 1.8$ m. Comparing the results taken from the mesh convergence, Mesh C is taken into account for the study of operations under one, three, five, seven and nine burners as it has a considerable percentage errors and CPU time among the rest. Results show that the radiative heat transfer is dominant and it does have an effect on the distribution of heat even at time $t = 10$ s. The second part of the study has been accounted for the convection-radiation heat transfer inside the domain using the SP_0, SP_1 and SP_3 models at $t = 30$ s. When the

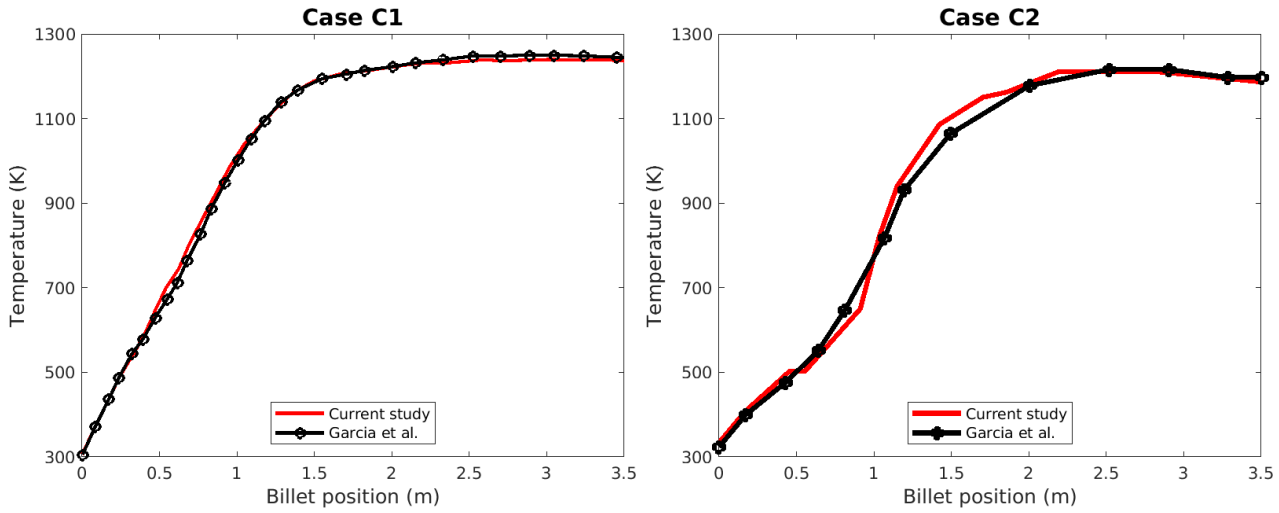

Figure 5.2: Validation between the current study and Garcia et al. [37] for temperature profile vs billet position for the cases C1 (left) and C2 (right).

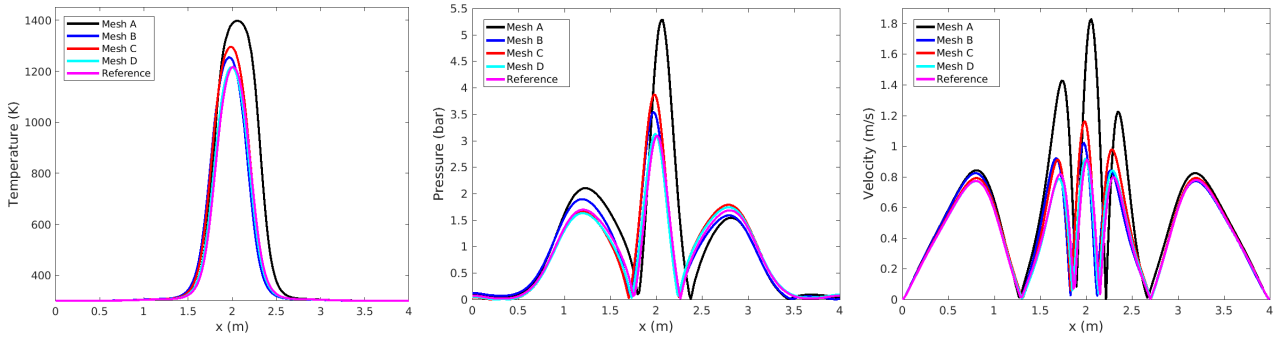

Figure 5.3: Horizontal cross-sectional study for temperature (left column), pressure (middle column) and velocity (right column) at time $t = 10$ s for the considered meshes.

burners are firing, convection-radiation heat transfer plays an important role in the distribution of temperature inside the domain. Heat flow inside the furnace begins with the radiation and forced convection heat transfer generating from the burners. Figure 5.4 shows the unsteady state condition of the temperature distribution under the operation of single burner, three, five, seven and nine burners using the SP_0 positioned at the left column, SP_1 located in the middle column and SP_3 lies on the right column at time $t = 10$ s.

During the operation of the burners across the geometry of the furnace, vertices appear. Figure 5.5 shows the vortices generated by the effect of the temperature and velocity at the same mentioned conditions. The forced convection-radiation heat transfer is the result of the interaction between the fixed fluid inside the domain which is at room temperature and the moving flow of fire. The movement of the heat flow is very interesting. It promotes us to study the influence of heat for different arrangements and applications. Due to the high temperature inside the furnace, heat radiation is the dominant mode and it depends on the number and position of burners, dimensions of the domain and the operation conditions. In radiation, energy is carried by the electromagnetic waves (no molecules) emitted by the fire. It is a volumetric phenomenon, which is emitted randomly in the form of photons in all possible directions. Since the furnace is initially at room temperature, absorption of heat inside the furnace is greater than emission of heat. Convection occurs as the hot fluid inside the furnace absorbs the heat within the layers of it. When the gas gets heated up, its molecules are carried away and scattered causing that the mass of the gas becomes less dense. The warm layer of the gas tends

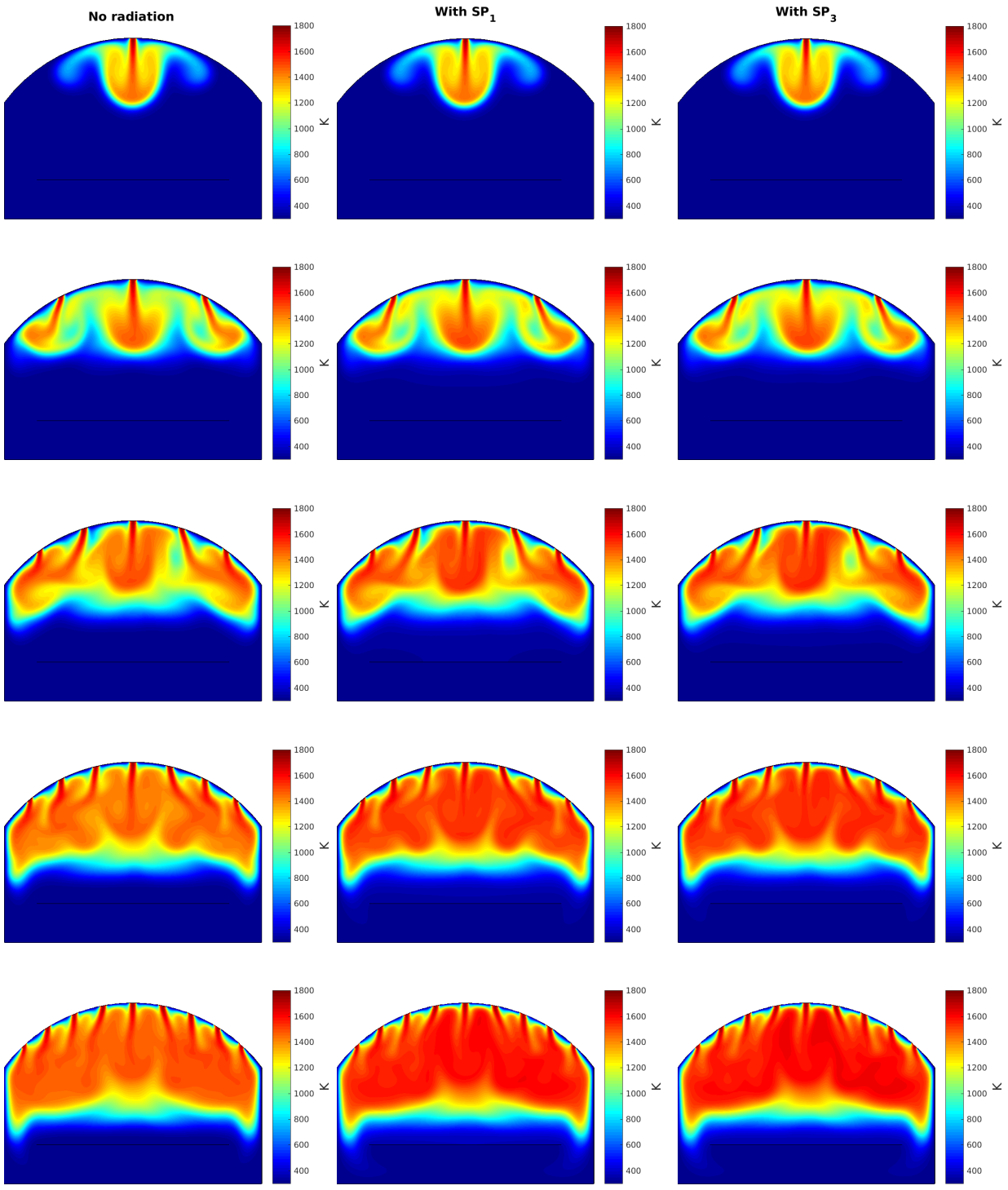

Figure 5.4: Temperature distribution under the operation of single burner (first row), three burners (second row), five burners (third row), seven burners (fourth row) and nine burners (last row) with no radiation (left), SP_1 (middle) and SP_3 (right) at $Pl = 0.5$, $\tau = 1$ and $t = 10$ s.

to float vertically and horizontally, while the colder layer (heavier) falls down due to gravity. Through this process, the molecules of the hot layers transfer heat continuously toward the volumes of the colder layers. The third part that has been carried out is taking into account

the cross-sectional study at $y = 1.8$, 1.2 and 0.7 m under the operation of the mentioned burners and time. Figure 5.6 shows the temperature behaviour effects using different simulation experiments.
Results show that the temperature inside the furnace is higher with the SP_1 and SP_3. The reason behind these results are that when radiation (SP_1 and SP_3) are taken into account, temperature difference between the air inside the furnace and heat flow becomes larger which makes the flow tends to move upward close to the roof curvature of the furnace. It is worth mentioning that the study is a fire dynamics application, hence Planck coefficient value has been kept constant with a value of 0.5 (under 1) [25]. The drawback of the heat radiation flow is that it generates stronger vortices which cause a non-uniform temperature distribution across the geometry of the furnace as well as the surface of the structure. This kind of behaviour is expected inside the furnace and it is compatible with the heat flow behaviour obtained in [46]. Another reason behind this disposal is the Reynolds number. The Reynolds number generates flow vortices, eddies and wakes which make the flow unpredictable during the transfer of heat from the hot layers to the colder layers. The inertial forces dominate considerably which result in large chaotic flow. Thus, two values of the Reynolds number here has been chosen that are equal to 500 and 1000 to reduce vortices effect. It can be seen from Figure 5.4 and Figure 5.5 that the flow tends to move downward. However, at a further time, the flow starts circulating and tends to float upward. To examine the temperature distributions on the structure sheet, three main finite element nodes are considered. The first node located on the left upper corner of the structure with coordinates (0.5, 0.605) m, the second node is located on the right upper corner of the structure with cordinates (2, 0.605) m and the third and last node is located on the middle upper surface of the structure with coordinates (3.5, 0.605) m. Figure 5.1 illustrates the chosen nodes for the study in red colour. At time $t = 30$ s in which the heat flow reaches the structure, the temperature of the chosen nodes on the upper surface of the structure has been monitored with time. Figure 5.7 shows the evolution of temperature at time $t = 30$ s at the left node under the operation of single burner, three, five, seven and nine burners. Results show that the heat is greater with radiative heat transfer. However, it is noticeable that the heat has more unsteady flow. This behaviour creates a higher temperature fluctuations over the structure surface as more and faster vortices occur.
It can be noticeably seen under the operation of five, seven and nine burners. Larger vortices increases with the increase in heat which can be seen that unsteady flow conducted from the SP_3 is slightly greater than the unsteady flow evaluated from the SP_1. The temperature of the right node on the upper surface of the structure is the second node that has been monitored with time. Figure 5.7 shows the evolution of the temperature with time t = 30 s at the right node under the operation of single burner, three, five, seven and nine burners. Unsteady state results show that higher unsteady flow and vortices take place on the right side of the furnace which lead to a higher temperature fluctuation particularly under the operation of five, seven and nine burners. The temperature behaviour with time for the middle node is illustrated in Figure 5.7 and has a minimum unsteady flow and the heat flow accumulates at the sides of the structure leaving the center of the furnace. Figure 5.7 represents the evolution of temperature with time $t = 30$ s at the middle node under the operation of different simulation experiments. This behaviour is due to higher temperature difference that draws the flow towards the sides of structure as the temperature under the structure is the minimum. It can be seen that radiation heat transfer has a dramatic influence under the operation the various burners and it depends very much on the radiative heat transfer. This effect increases dramatically with time. However, with the operations of nine burners, the heat tends to fill the furnace which makes the amount heat reflected on the structure sheet is higher than the one with the operation of

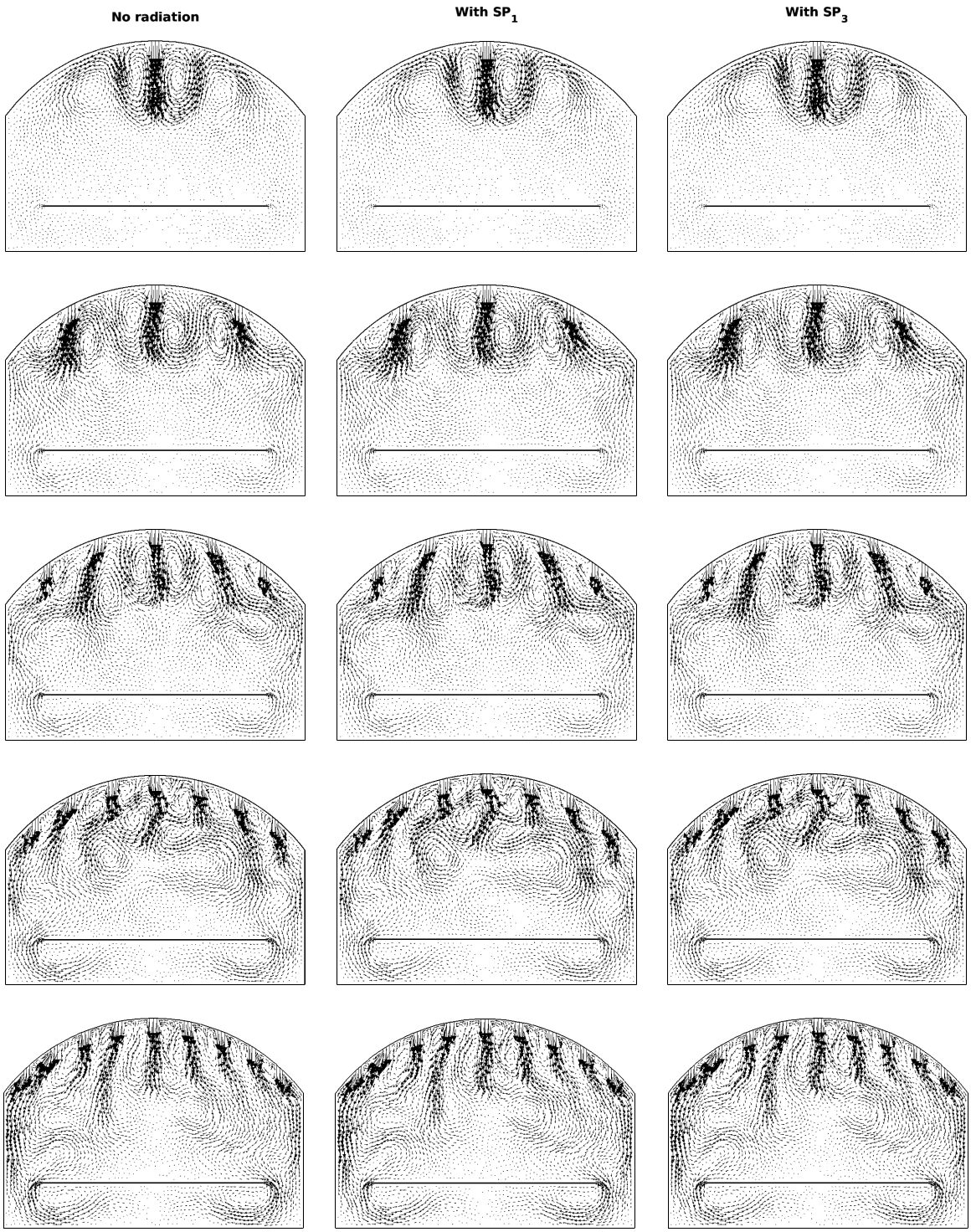

Figure 5.5: Velocity flow under the operation of single burner (first row), three burners (second row), five burners (third row), seven burners (fourth row) and nine burners (last row) without radiation (left), SP_1 (middle) and SP_3 (right) at $Pl = 0.5$, $\tau = 1$ and $t = 10$ s.

the other different number of burners where the vast majority of the amount of heat rate is absorbed by the fluid inside the furnace creating higher temperature change. A maximum temperature difference can be shown between the SP_0 and SP_3 on the middle, left and right nodes specially under the operation of nine burners. Results show that the temperature on the sides of the furnace is not equal. This is due to the fact that the unsteady convection-radiation

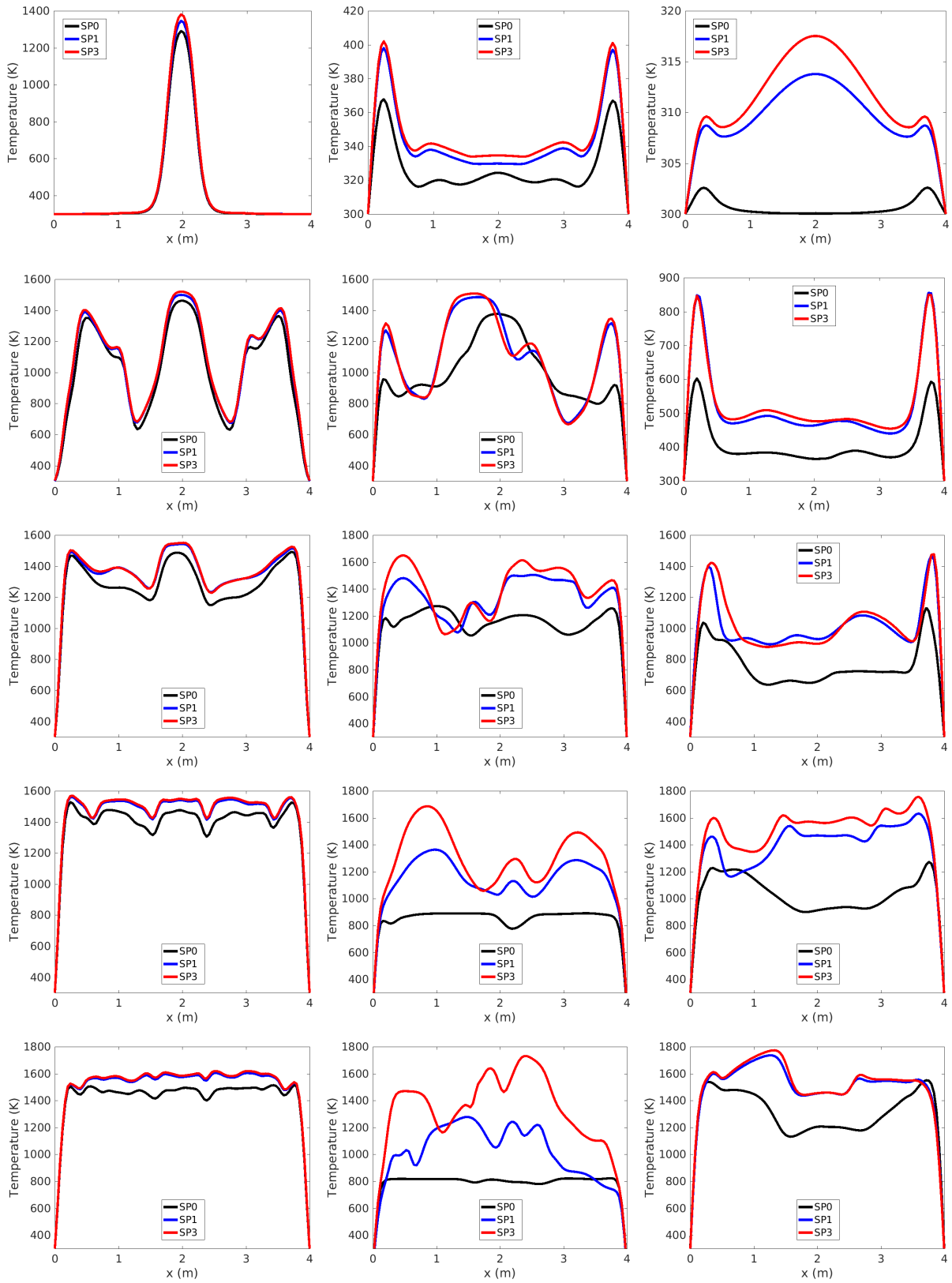

Figure 5.6: Temperature cross-section along x direction at $y = 1.8$ m (left column), $y = 1.2$ m (middle column) and on the surface of the structure along the furnace (right column) under the operation of 1 (first row), 3 (second row), 5 (third row), 7 (fourth row) and nine (fifth row) burners at $t = 30$ s and $Re = 500$.

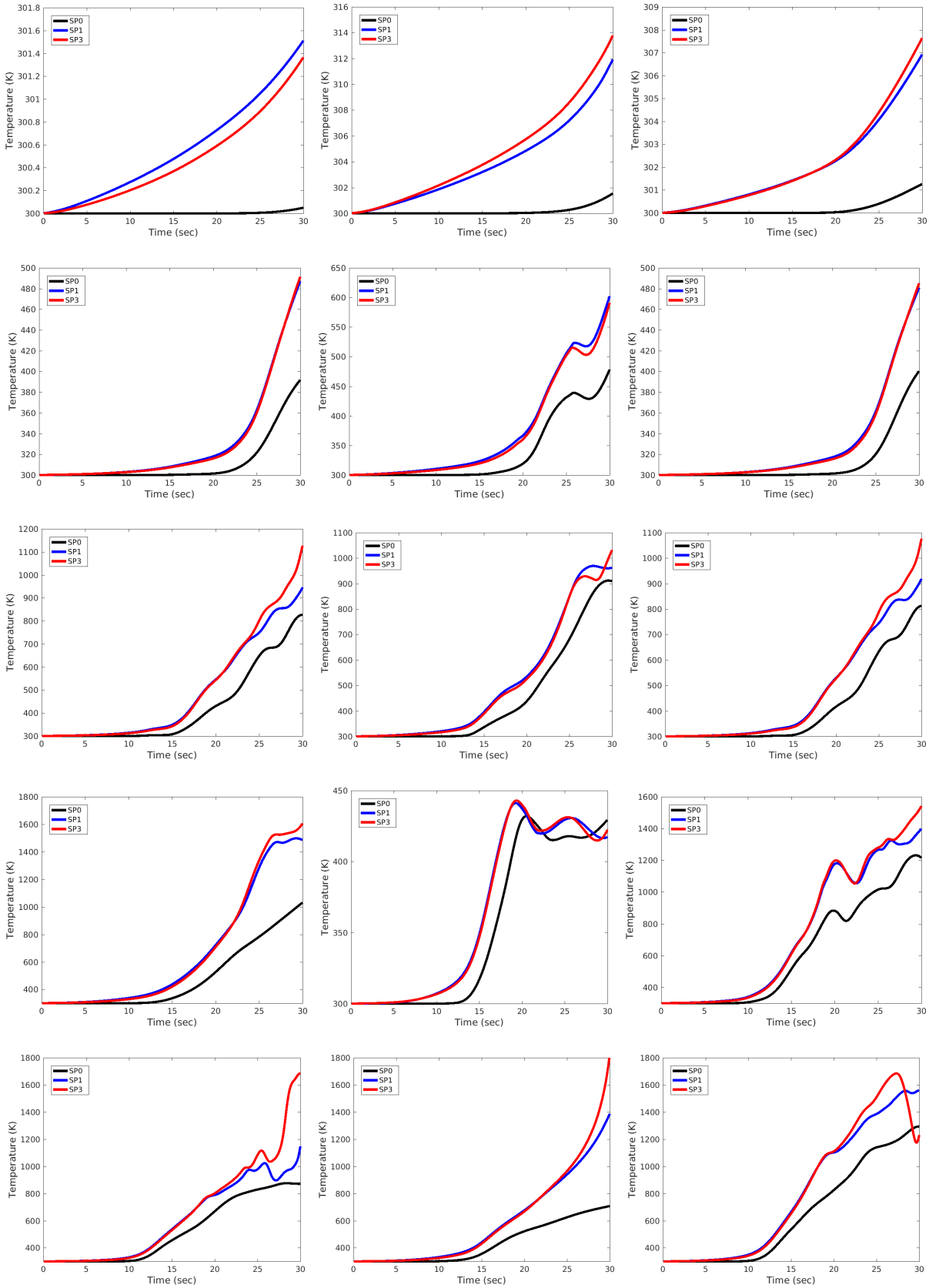

Figure 5.7: Temperature evolution for the structure left node (left column), middle node (middle column) and right node (right column) under the operation of single burner (first row), three burners (second row), five burners (third row), seven burners (fourth row) and nine burners (fifth row) at $Re = 500$.

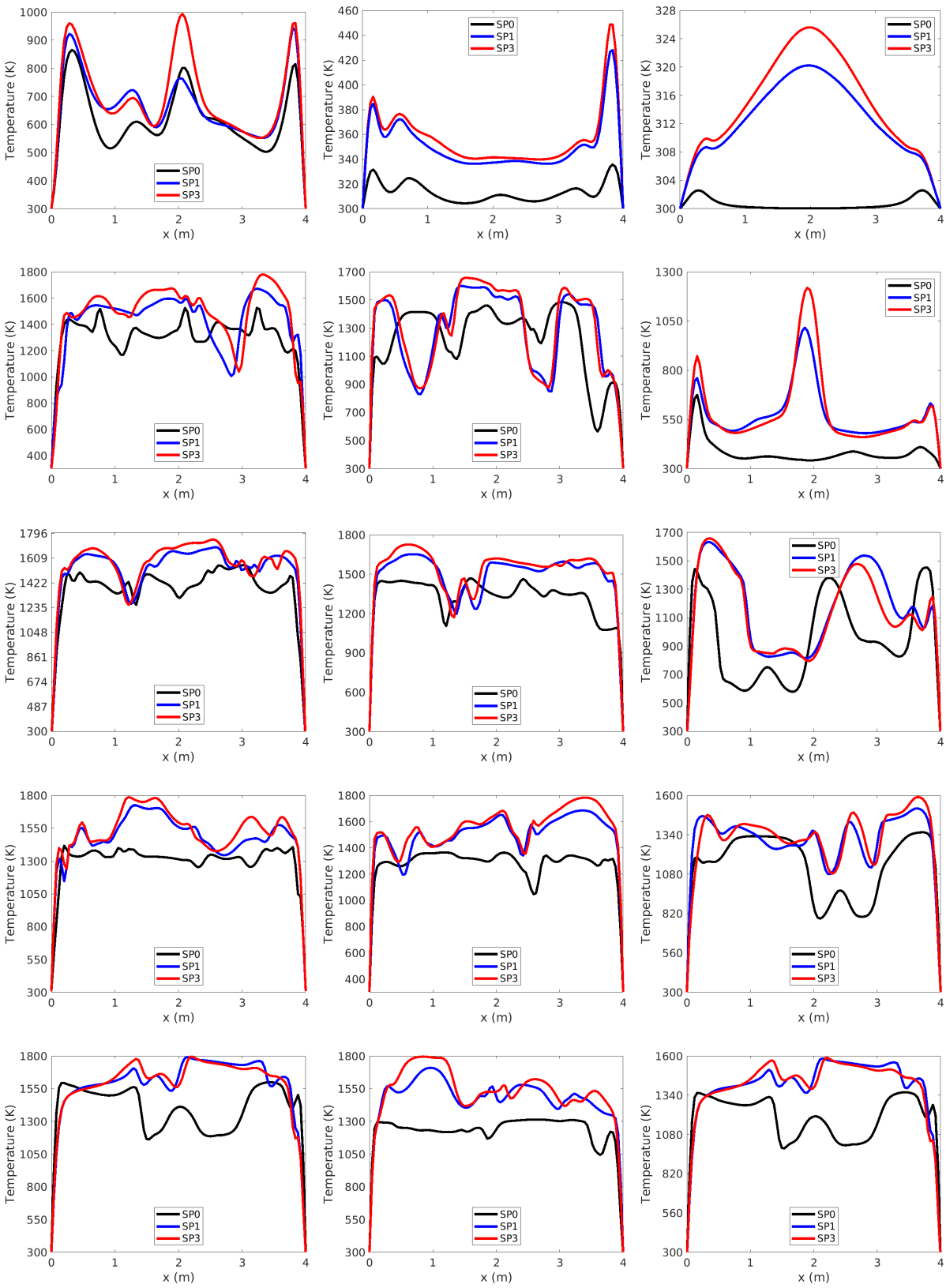

Figure 5.8: Temperature cross-section along x direction at $y = 1.8$ m (left column), $y = 1.2$ m (middle column) and on the surface of the structure along the furnace (right column) under the operation of 1 (first row), 3 (second row), 5 (third row), 7 (fourth row) and nine (fifth row) burners at $t = 30$ s and $Re = 1000$.

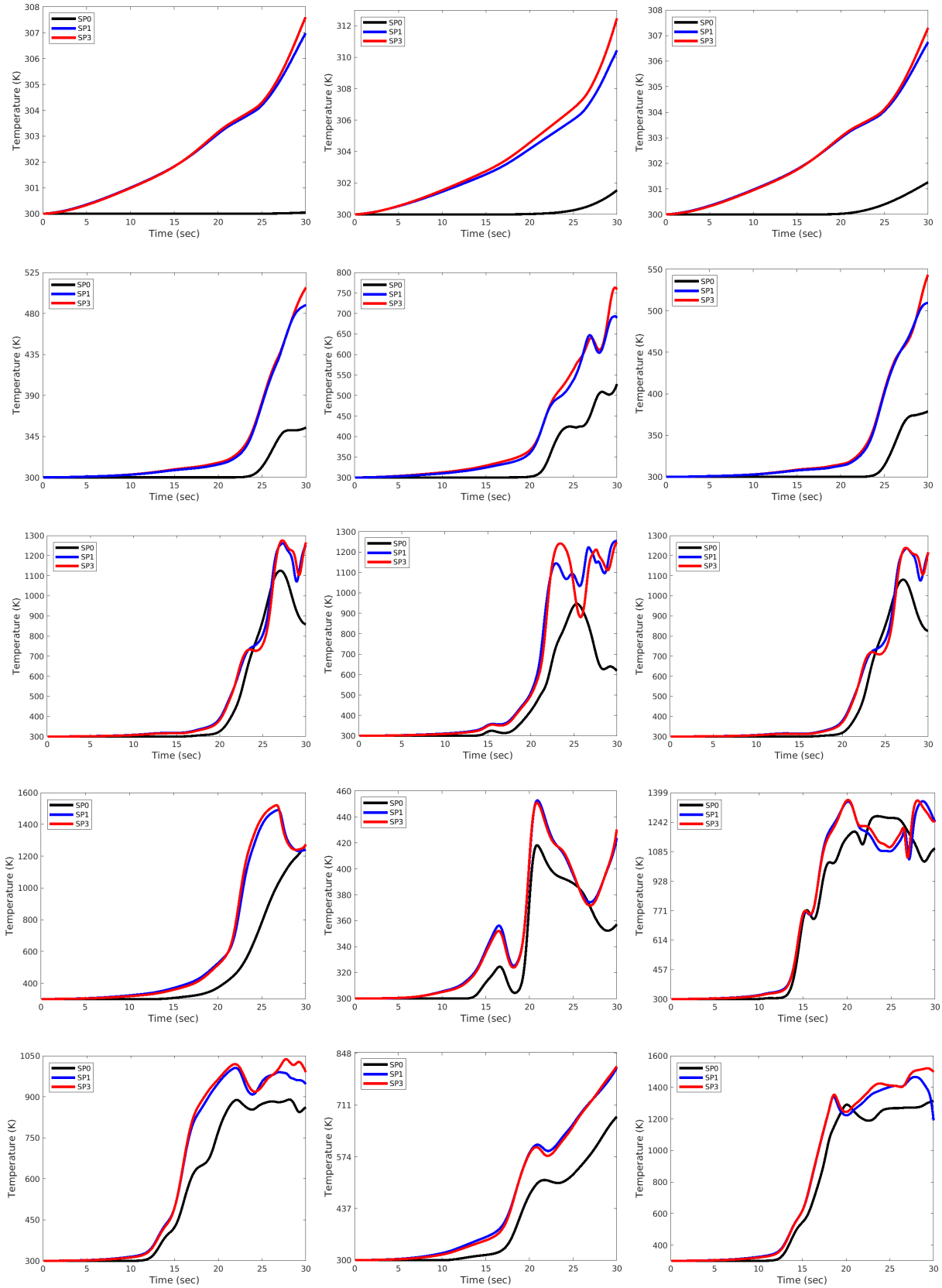

Figure 5.9: Temperature evolution for the structure left node (left column), middle node (middle column) and right node (right column) utilizing single burner (first row), three burners (second row), five burners (third row), seven burners (fourth row) and nine burners (fifth row) at $Re = 1000$.

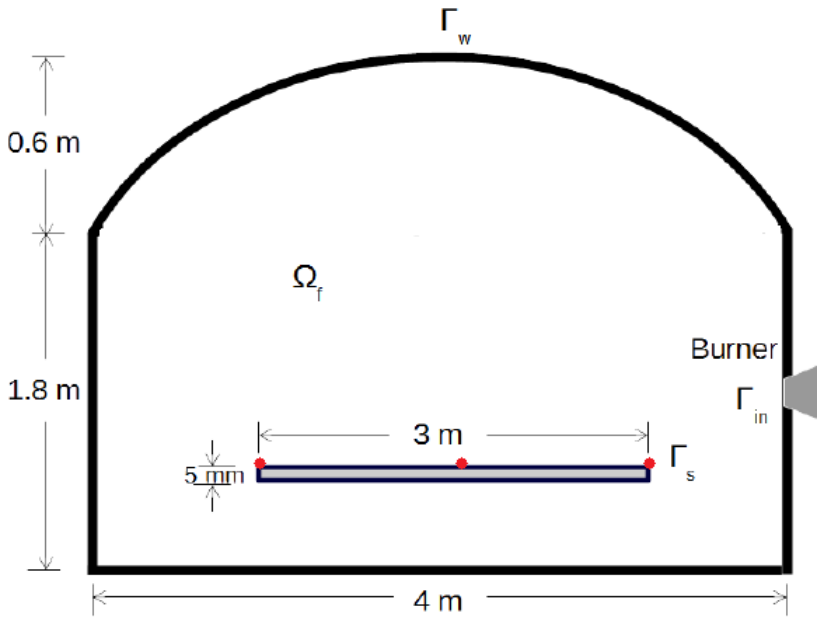

Figure 5.10: Cross-section view of the furnace with regenerative burners.

heat draws the unstable heat flow towards the sides at the chosen time. The effect of higher value of the Reynolds number as far as heat transfer is concerned, is that an additional mechanism of heat transfer in the azimuthal and radial directions becomes available and higher. This is commonly termed "eddy transport" and is intense, providing much better transfer of energy across the flow at a given position than in lower value of Re. Another difference worth noting is the extent of the thermal entrance region in which the transverse temperature distribution becomes fully developed. This region is relatively short in operation with 7 and 9 burners (precisely because of the intense turbulent transverse transport of energy), whereas it tends to be long under the operation of 1 and 3 burners. Figure 5.8 shows the temperature distribution across three horizontal regions inside the furnace domain. Compared with the results obtained, the flow contains eddying motions of all sizes, and a large part of the mechanical energy in the flow goes into the formation of these eddies which eventually dissipate their energy as heat. It can also be seen from Figure 5.9 is that the heat increases for the chosen nodes compared with the results of the temperature growth per time obtained at $Re = 500$ in Figure 5.7.

5.4 Operation under regenerative furnaces

Tremendous opportunities for improvement of process efficiency and product quality is desirable by the industry through better control of the furnaces [108]. Keeping a stable glass temperature decreases defects such as cords, seeds, and other inclusions. Glass temperature control allows for controlling the forming operations [112]. Most glass furnaces use simple, single-loop control of the firing rate based on the temperature of the refractory in the furnace crown. The first step in any control design is modelling. The accuracy and robustness of a control system is entirely dependent on the quality of the underlying mathematical model of the process and its environment. Modelling means describing a physical element or system using mathematical equations. These equations can be used to predict how a system will behave in response to any feasible set of inputs, and thus a controller can be designed to provide a series of control signals which will result in the system producing the desired outputs or at least a set of outputs that

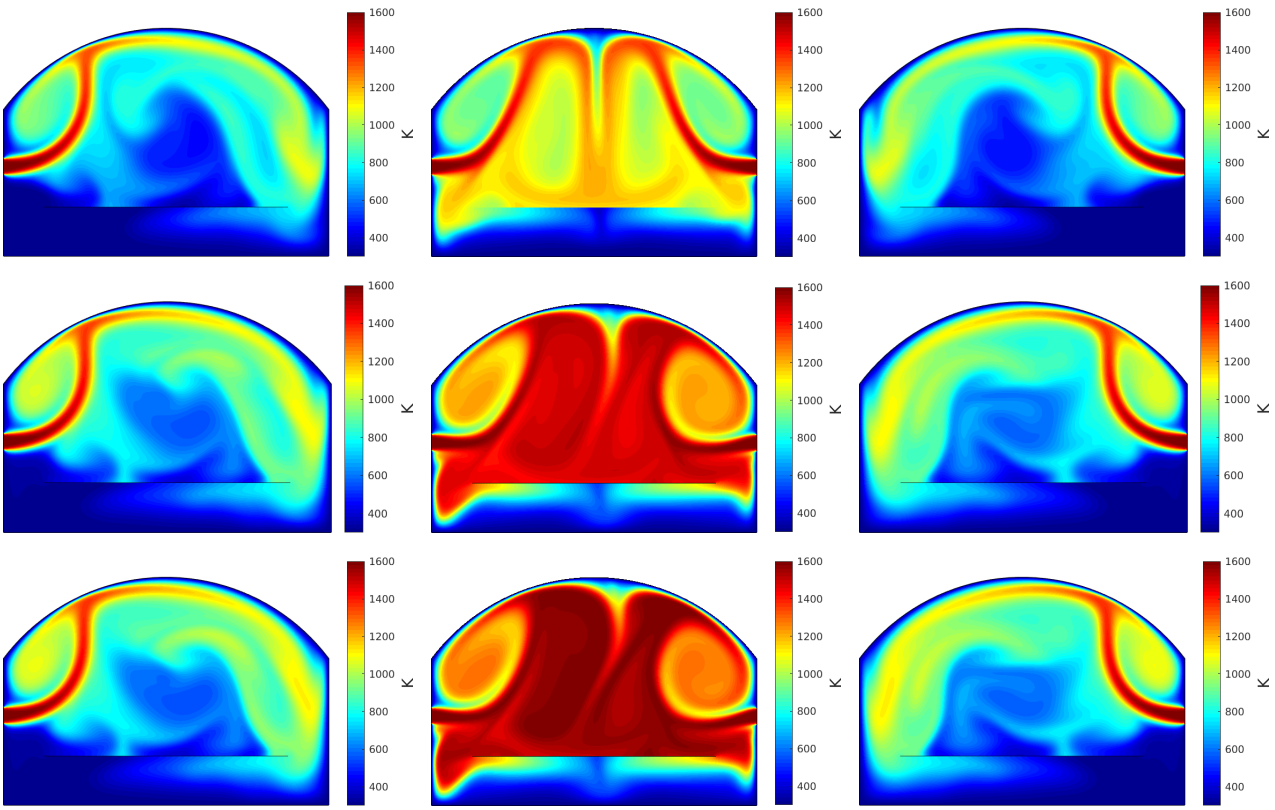

Figure 5.11: Distribution of temperature under the operation of the left burner, the right burner and both using the SP_0 (upper row), SP_1 (middle row) and SP_3 (lower row) at $Pl = 0.5$, $\tau = 0.75$ and $t = 30$ s.

is acceptably close to the desired set. The furnace considered in this study is similar to the CGM furnace. The only difference is that the burners are located on the side walls of the furnace. Figure 5.10 represents a schematic of the geometry of the furnace studied in this work which consists of two-dimensional cross-section heat flow. Same procedure done for the furnace with vertical burners are considered here.

In this section, results for the convection-radiation heat transfer inside the furnace are obtained using the SP_0 (no radiation), SP_1 and SP_3 models at $Re = 700$, $Pr = 0.72$, $Pl = 0.5$ while the value of $\tau = 0.75$ and 1 [25]. Since a glass furnace operates at high temperatures (above 1500 K), the primary mode of heat transfer from the flame to the glass is radiation. The energy is absorbed and re-radiated from the floor refractory and from the glass itself, and is internally reflected from the air/glass interface. Thus, the energy impinging on the surface of the mold is not all absorbed at the surface, once the batch materials have melted and become translucent/transparent. This phenomenon is considered in the model by including an Opacity Factor (OF) [162]. The opacity factor can be adjusted for each furnace and type of inclusion by adjusting the value of τ. The opacity factor was determined by trial and error to make the temperature gradients in the melt agree with estimates of those found in the prototype furnace. Opacity is the amount of radiation absorbed by a semi clear solid, liquid, or gas. The OF is an approximation and can be adjusted for each furnace and type of glass. Figure 5.11 shows the unsteady state condition of the temperature distribution utilizing single burner attached to the left and single burner attached to the right and operation of both at time interval $t = 30$ s. It can be seen that radiation effect is dominant specially under the operation of both

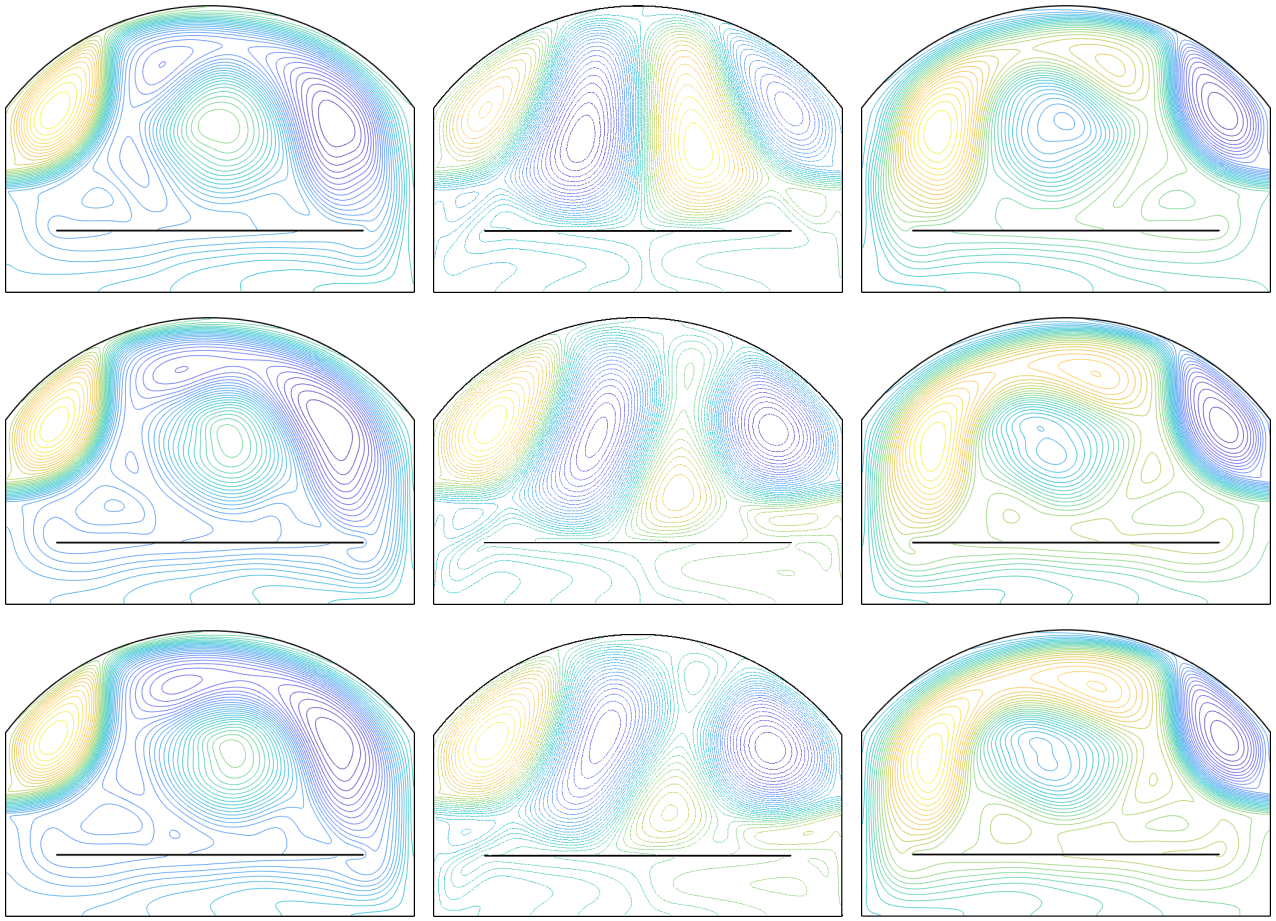

Figure 5.12: Heat flow distribution under the operation of the left burner, the right burner and both using the SP_0 (upper row), SP_1 (middle row) and SP_3 (lower row) at $Pl = 0.5$, $\tau = 0.75$ and $t = 30$ s.

burners. This is due to the fact that radiation heat fills the entire furnace chamber while convection heat transfer tends to float. Figure 5.12 shows the distribution of the heat flow under different operations of the burners. Since the temperature inside the furnace is very high, heat radiation is the dominant mode and it depends very much on number and position of the burners, dimensions of the furnace and the heat transfer coefficients of Pl and τ.
It can be clearly seen that the operation of the regenerative burners cause a flashover. Flashover is defined as the sudden involvement of a furnace in flames from floor to ceiling caused by thermal radiation feedback [145]. Thermal radiation feedback is the energy of the fire being radiated back to the contents of the furnace from the walls, floor, and ceiling. This simply means that flashover depends mainly on the temperature. It requires that the fires energy be radiated back to the contents to produce a rapid rise in temperature and simultaneous ignition. Flashover indicates that the heat flow has grown to the fully developed stage. On exposure to radiative (or convective) heat, the surface temperature of the enclosure (glass sheet) will increase, eventually to reach a steady-state (equilibrium) value. This can be estimated on the basis of simple heat transfer calculations, assuming the material to be inert. Figure 5.15 shows the temperature behaviour for the chosen nodes shown in Figure 5.10 using the SP_0, SP_1 and SP_3 models when using $\tau = 0.75$. The next study is to try to predict the thermal behaviour over the entire glass sheet. Figure 5.13 shows the temperature, velocity and pressure over the inclusion at $\tau = 1$. In Figure 5.15, results show that temperature over the glass sheet

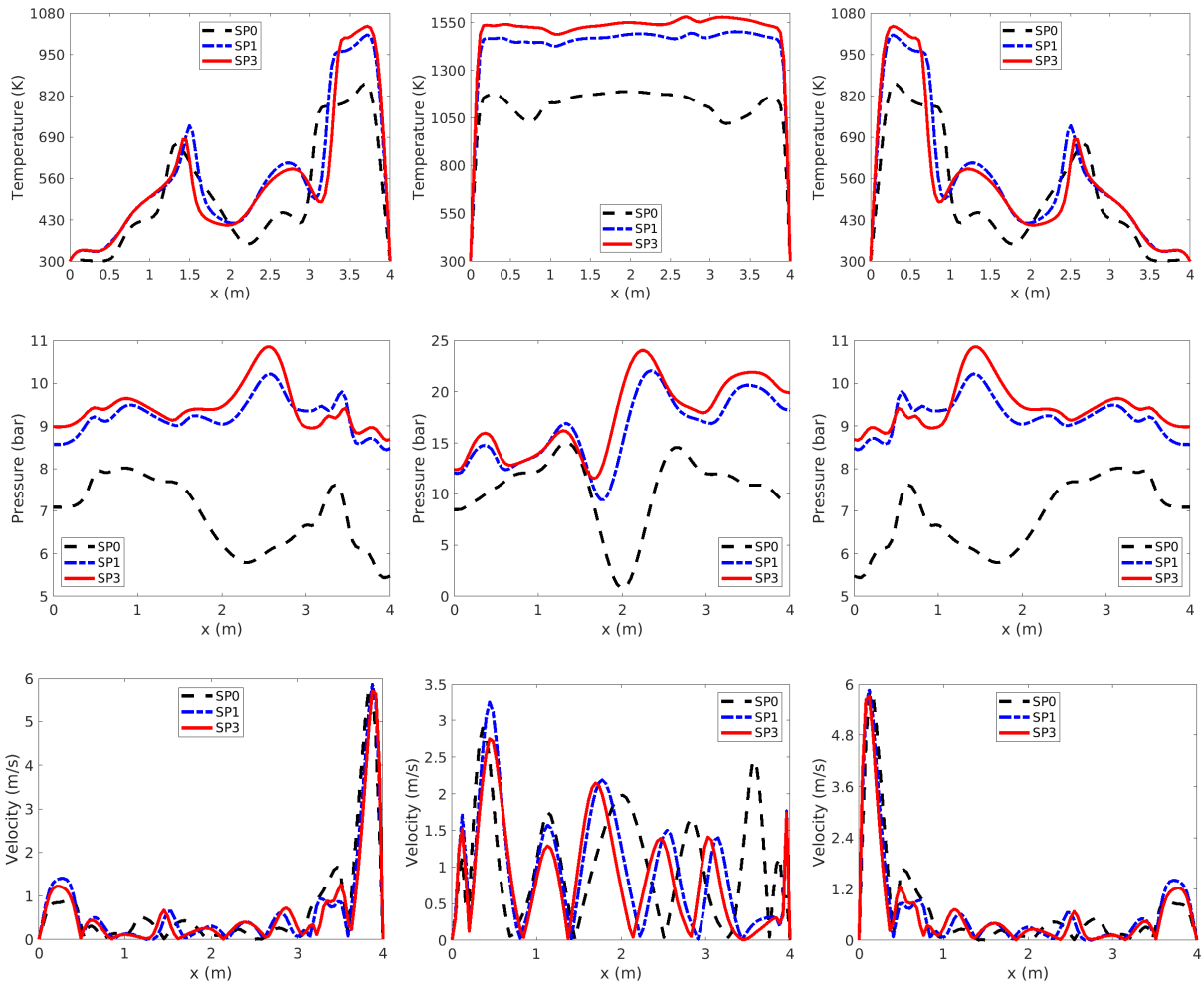

Figure 5.13: Temperature, pressure and velocity profiles along x direction over the surface of the structure (at $y = 0.605$ m) under the operation of the left burner (left column), the operation of both burners (middle column) and the operation of the right burner (right column) for temperature (upper row), pressure (middle row) and velocity (lower row) at $Pl = 0.5$, $\tau = 0.75$ and $t = 30$ s.

is higher with the SP_1 and SP_3 under the operation of single burner (on the left wall or on the right wall). The reason behind this result is that when radiation (SP_1 and SP_3) is taken into account, more heat is generated from the heat flow on the surface of the structure and it is higher than when using SP_0. However, the operation under dual burners shows that heat radiation is dominant on both sides of the glass sheet. This is due to the fact that the furnace is filled with heat in such away that radiation is dominant and tends to move towards the lower temperature area located under the glass sheet leaving the middle of the furnace geometry. Less heat transfer effect has been shown with lower effect of opacity factor with a value of $\tau = 1$. Figures 5.14 and 5.16 show the effect of τ on the heat transfer across the geometry. It can be seen that with higher value of τ, radiation transfer becomes less dominant. However, with $\tau = 0.75$, a noticeable effect between the SP_1 and SP_3 can be recognized. Results show that the SP_3 describes better radiation effect when the radiation is dominant.

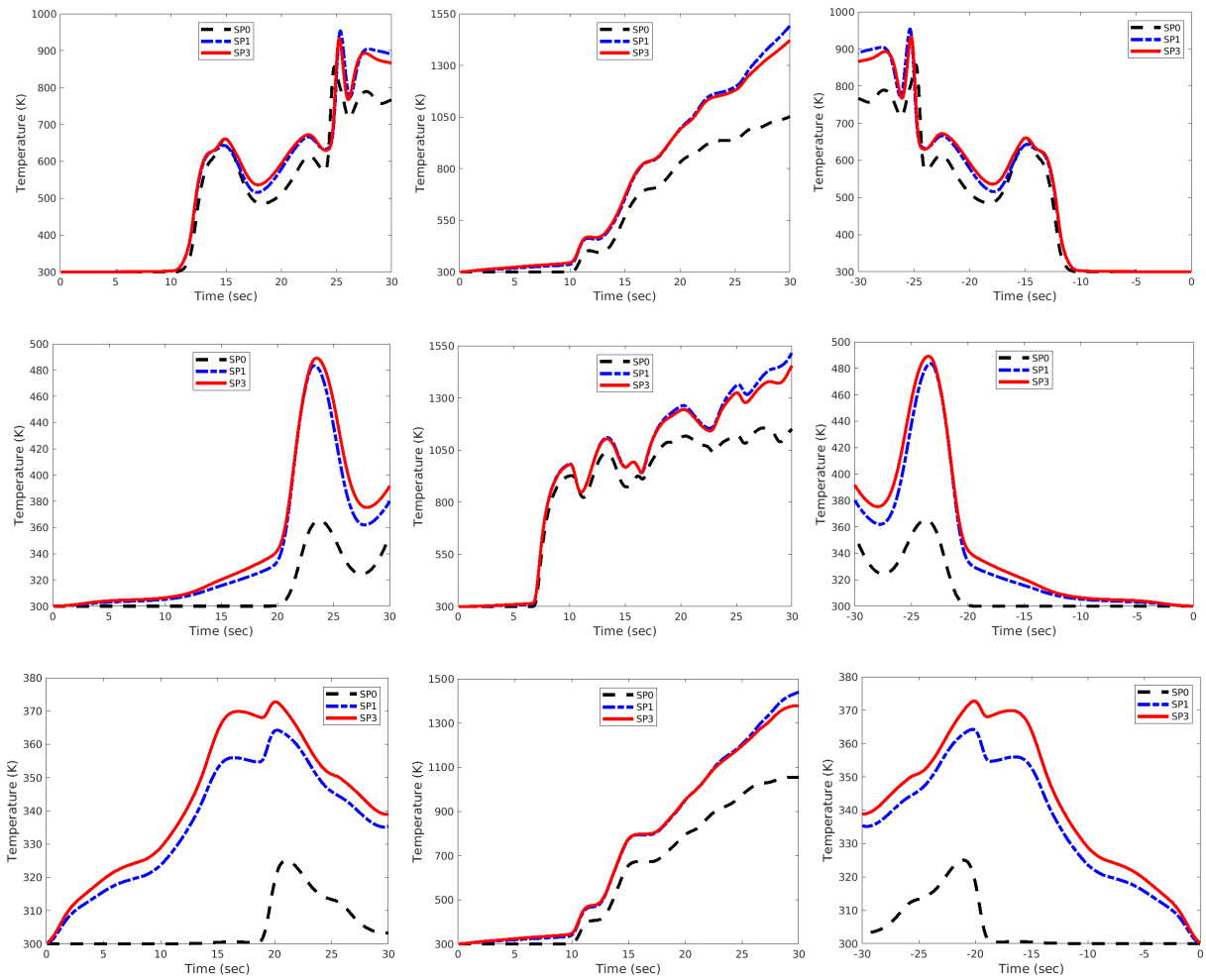

Figure 5.14: Temperature behaviour with time for the glass left node (upper row), right node (lower row) and middle node (middle row) under the operation of left burner (left column), right burner (right column) and both burners (middle column) at $Pl = 0.5$, $\tau = 1$ and $t = 30$ s.

5.5 Concluding remarks

In the present chapter, forced convection-radiation heat flow was studied inside the investigated furnaces for the first time numerically using a stabilized mixed finite element formulation for the incompressible Navier-Stokes equations with the simplified P_N approximations for dealing with radiation. The simplified P_N approximations are considered and the SP_3 is applied to the investigated furnaces for the first time. The proposed approach solves the set of equations inside the investigated furnaces in order to get a stabilized and satisfactory results. As discussed in chapter 4, the developed splitting method is considered to deal with the dominant advection term and the adopted Galerkin-characteristics technique is used to deal with the pressure surge. Numerical validations are performed and the results show that the proposed study can generate the accurate numerical solutions for the unsteady heat flow. The novel developed solver is performed over two types of furnaces: convective glass melting furnace with vertical burners and furnace with horizontal regenerative burners. The heat transfer characteristics inside the furnaces were obtained at two values of the Reynolds number of 500 and 1000 in case of the glass melting furnace and two values of the optical thickness of 0.75 and 1.0 are considered for

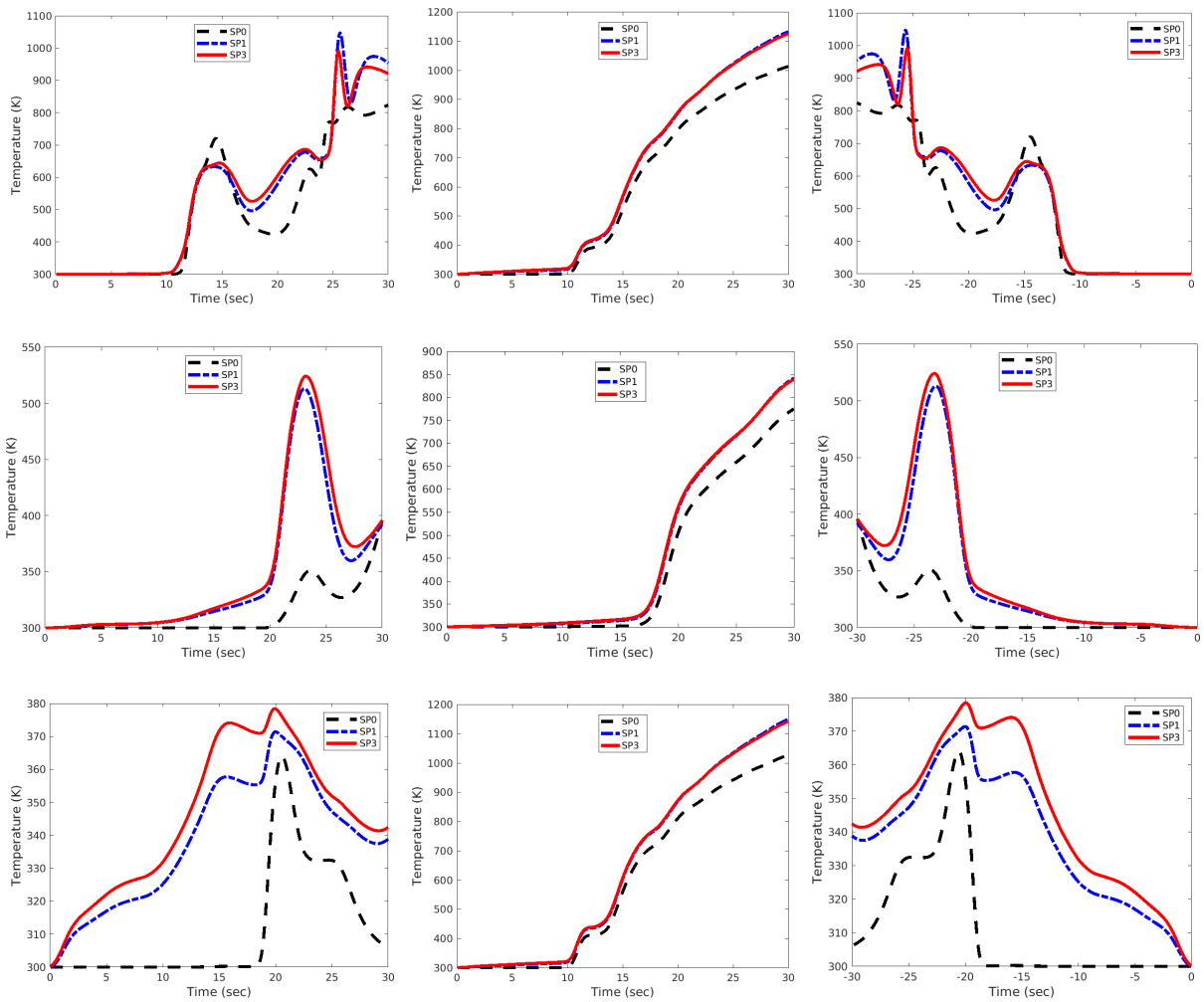

Figure 5.15: Temperature behaviour with time for the glass left node (upper row), right node (lower row) and middle node (middle row) under the operation of left burner (left column), right burner (right column) and both burners (middle column) at $Pl = 0.5$, $\tau = 0.75$ and $t = 30$ s.

the furnace with regenerative burners. Five different operations are carried out to investigate the heat flow inside the glass melting furnace and three different operations are taken into account for the the furnace with regenerative burners. All operations are done at the Planck coefficient of 0.5. The novel obtained results show a maximum temperature difference of 200 K between the SP_1 and the SP_3 and a temperature difference of 500 K between no radiation and the SP_3 under a dominant radiation effect of the Planck coefficient of 0.5 and optical depth of 0.75 over the surface of the inclusion. The novel validated results clearly show that the commercial softwares as well as the previous developed methods based on P_1 approximation failed to capture the accurate temperature distribution inside furnaces. The novel developed method proved that the SP_3 approximation is the only accurate solution that can serve the industrial furnaces for different thermal scenarios. The developed method showed that it is reliable over different values of different heat transfer coefficients and under various operations. From the industrial point of view, the novel technique is highly recommended to: (i) control the desired temperature distribution over the structure surface (ii) reduce the vortices generation since different operations are considered with different heat transfer coefficients (iii) choose the

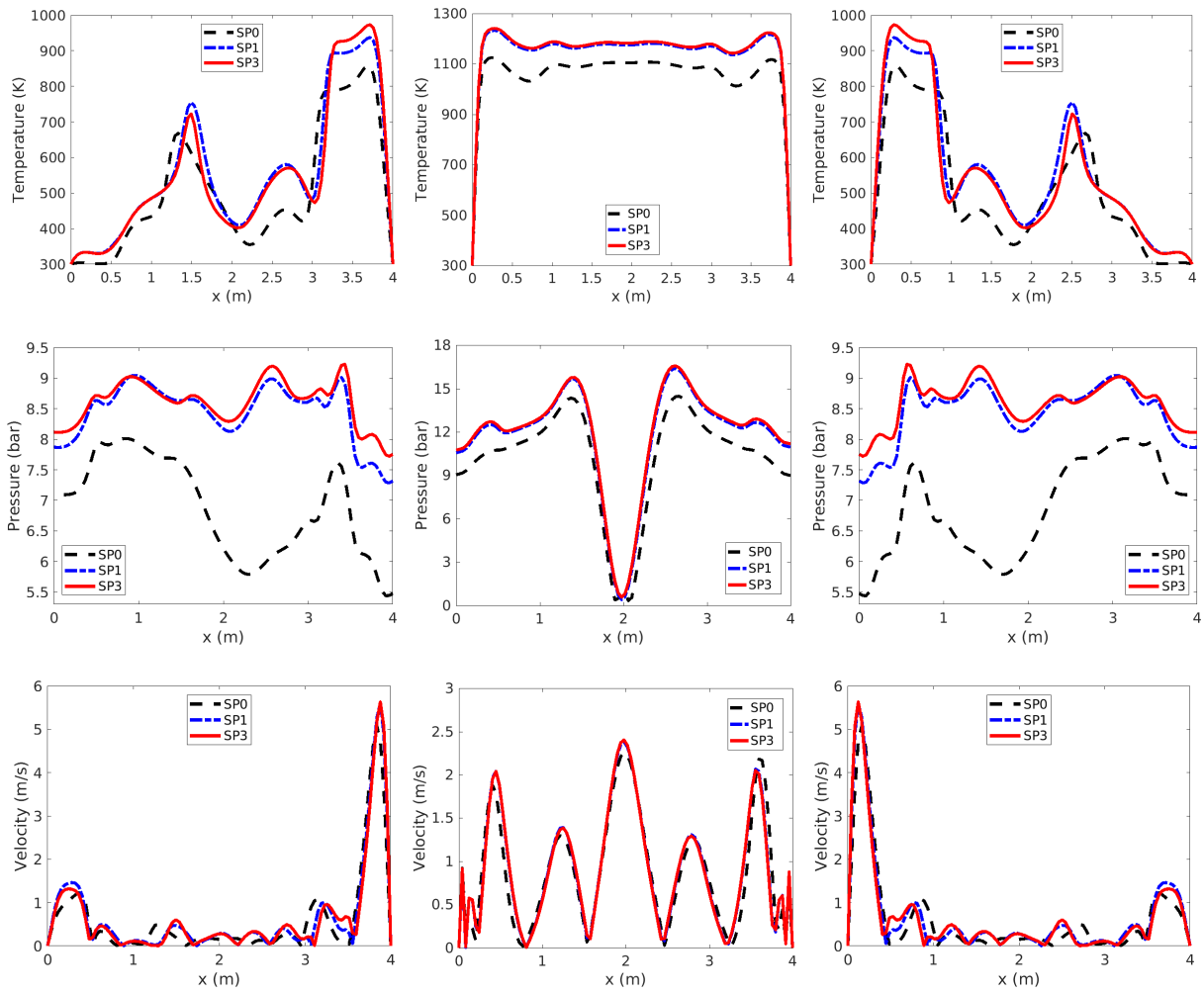

Figure 5.16: Temperature, pressure and velocity profiles along x direction over the surface of the structure all the way to the furnace walls (at $y = 0.605$ m) under the operation of the left burner (left column), the operation of both burners (middle column) and the operation of the right burner (right column) for temperature (upper row), pressure (middle row) and velocity (lower row) at $Pl = 0.5$, $\tau = 1$ and $t = 30$ s.

required furnace dimensions (iv) increase furnace life time (v) reduce the fuel consumption by controlling the operations time.

Chapter 6

Conclusions and future work

6.1 Conclusions

The original contribution of this thesis is the development of an efficient method which is able to simulate complex flow problems inside thermal engineering applications including radiation. Such simulation involves heat flow, unsteady heat transfer containing convection and thermal radiation all in multi-component formulations. The techniques used in this thesis are the mixed finite element method and the Navier-Stokes equations. This method is shown as an attractive way to solve heat flow and heat transfer inside different thermal engineering chambers and it can be applied for a variety of geometries and boundary conditions. All the necessary methods and models required to simulate and study heat transfer (radiation and convection) and its applications are reviewed thoroughly in chapter 1. The previous studies promote us to find motivations, novelties and choose the best strategy that can help us get the best possible results. It has been proven by the previous studies that finite element method is the best when it comes to simulate heat flow. Previous studies struggled with dominant convection term. Previous studies failed to accurately capture the effect of radiation heat transfer inside realistic applications. The motivation for us is then to overcome these challenges and propose a novel technique and validate it by applying it on realistic applications. Based on that, major research objectives were set out to determine the importance and the effect of radiation heat that takes place in both natural and forced transfer.
The novel developed method is needed to study the interaction between convection and radiation and to test, understand and adjust it based on the chosen engineering applications. The plan was set by choosing the Taylor-Hood finite element method due to the presence of the non-thermodynamic variable (pressure) in the Navier-Stokes equations. Linear triangular elements were chosen for the pressure and quadratic elements were selected for the velocity, radiation and temperature to deal with any simple or complex geometry. Our developed Galerkin-characteristics approach is used and tested for different values of the Reynolds number. The SP_N approximations are adopted to deal with the effect of radiation and for the first time ever, it has been adopted and applied to our different thermal scenarios and applications. We started in chapter 2 by reviewing the full discretization procedures coupled with the discrete ordinates method which is often used for the spatio-angular discretization of the radiative transfer equation. To improve the efficiency of the solver, instead of using a single standard iterative method, variety of iterative methods were performed and a comparison among all was done. It was shown that the BICGSTAB method gives the most desirable results, with smooth convergence and less CPU, and memory requirements. In chapter 2, we investigated and set our goals in terms of building and implementing the required solver, algorithms and

methods to carry out with this research. In chapter 3, a complete SP_N derivations have been obtained as the results from chapter 2 showed that simplified approximations give favourable results compared with the full radiative transfer equation with less computational time. The outcomes from this chapter are the governing equations and the boundary conditions that are adopted for radiative transfer.
The second part of the thesis consisted in developing numerical methods for modelling the unsteady heat flow under different simulation experiments. Standard finite element method normally exhibits overall spurious oscillations in convection-dominated problems, especially in the vicinity of sharp gradients. The Galerkin-characteristics are more advanced methods in the stabilization context which were proposed in chapter 4. We have explained in chapter 4 a stabilized finite element method for the transient incompressible Navier-Stokes equations for solving natural convection-radiation in squared cavities with and without complex heaters and inclined angles. The preliminary results have been obtained and validated thoroughly and extensively against those from the literature. Our obtained results were the most acceptable compared with the experimental data available from the literature. After validating our technique, we carried out in our novel research and applications adopted. Our novel applications and results were accomplished under different thermal and engineering scenarios. First, we chose a squared domain and applied our novel SP_N approximations on it. We compared and adjust the effect of radiation heat transfer by adjusting the value of the Planck coefficient. Then we regulate the effect of convection heat transfer by regulating the values of Rayleigh number. The medium inside the cavity were chosen as air.
Our stable solver was able to capture a significant temperature difference under a dominant radiation heat transfer. At a dominant radiation of the Planck coefficient of 0.2 and Rayleigh number of 10^4, convection alone captured a temperature of 128.14 °C, while the temperature with SP_1 was 132.38°C and a value of 154.63°C under the SP_3. From these novel obtained results, it is worth mentioning that reults obtained from commercial softwares as well as the previous studies based on P_1 approximations failed to give an accurate description when studying radiation heat transfer inside industrial applications. The radiation heat transfer has a dramatic effect on heat transfer even at a dominant convection effect of Rayleigh number of 10^6 and moderate Planck coefficient of 0.5. The novel developed method is then applied to different inclination angles and with the inclusion of complex heating source inside the cavity. This is done to understand and study the effect of the change in the buoyancy forces. It was shown that as the angle of inclination increases the fluid flow pattern changes. The novel achieved results of the SP_3 still dominant and can not be underestimated. This chapter proved that the SP_3 approximations are the most desirable for numerical and industrial purposes with natural heat transfer.
In chapter 5, the motivation of using these advanced methods comes from the need of extending the created solver in order to deal with highly convection-dominated flows that may occur in the furnaces. The core of the proposed approach was to keep the previous implementation of the stable velocity-pressure formulation and to extend it by taking into account the change in pressure and the convection terms in the equations. Results for the unsteady Navier-Stokes equations obtained via the new modified scheme have been compared and analyzed with the results provided from the literature. The operations chosen show that the method is stable. The performance and the efficiency of the overall new scheme have been demonstrated using five different burner operations for the convective glass melting furnace and for three operations of furnace with regenerative burners. The motivation of using such models comes from the necessity of solving highly unsteady flow problems, for instance the temperature coming out from the burners into the furnace chamber could reach 1800 K. Again, the stabilized finite

element approach for solving the SP_N equations proposed in chapter 2 and chapter 3 were used and applied for the resolution of the set of equations. Most importantly, we concluded from the numerical experiments that a chosen model should introduce the minimum amount of complexity while capturing the essence of the relevant physics. An improved version of this model appropriate for simulation of different operations was also introduced and adopted in this work. However, the question of which suitable operation must be used to simulate accurately heat flow in the furnace chamber requires certain attention. Our main objective remained on understanding and implementing these models to open the choice to the user to decide which method one must use regarding the application in hand. We explained briefly that each method offers the accuracy of the results with respect to the computational costs and the required computing time. Finally, the performance and the efficiency of the overall models were demonstrated using the mentioned operations as benchmark with results validations. Our novel method were applied to our novel industrial furnaces under different engineering scenarios. We carried out first by testing our Galerkin-characteristics method by adjusting the Reynolds number within the industrials values. It was shown that our developed method is stable and can deal with different values of the Reynolds number. The novel obtained results show a higher and dominant temperature distribution over the inclusion with the SP_3 approximations. The SP_3 approximations enabled us to understand the heat flow behaviour inside different locations and under the operations of different burners and for the first time inside a glass melting furnace.
The second part of the study was to investigate our novel developed approach by applying it on an industrial furnace with regenerative burners. Since the burners are located on the walls of the furnace, heat transfers to the structure is solely from radiation. This study promotes us to investigate the effect of the radiation heat characteristics namely, the Planck coefficient and optical depth. The novel obtained results show that radiation is dominant even when reducing the effect of radiation with higher values of the Planck coefficient and optical depth. The novel SP_3 obtained results showed a higher temperature difference on the surface of the structure of 10 K than the SP_1 and 20 K higher than SP_0. This is another evidence that commercial softwares as well as studies based on P_1 approximation will not be able to serve the industry and that are incapable of simulating heat flow accurately for forced heat transfer.
As mentioned in the results sections of chapter 4 and chapter 5, thermal radiation exchange plays an important role on the overall efficiency, the quality of the heated structure (glass or ingots) and the production rates since it is the dominant mode of heat transfer in most furnaces. We showed that the proposed SP_N approximations for modelling such multi material heat flow allows a simple and accurate resolution. Full description, details and examples about this method are discussed in this thesis. One important feature of the proposed approach is that the SP_3 are performed for the first time on unprecedented applications considered which are needed for solving the transient heat transfer and heat flow inside the furnaces. The engineering applications are completely suited with this approach without additional efforts.
The focus in this work is on a new concept for numerical methods to estimate the temperature distributions at the same time in the furnace and with the inclusion under specified furnace geometry, thermal schedule, parts loading design, initial operation conditions, and performance requirements. It is then to develop the SP_N approximations for solving radiative transfer. The importance of this study is due also to the fact that the model created has been proved to be applicable to very large variety of natural and forced heat transfer applications, as it depends mainly on the geometry and on the operating conditions. The created model can be used for complex application of every dimension and powered under any thermal conditions. The spherical harmonic P_3 offered the possibility to improve the obtained accuracy of the solution

by capturing the transport effects while still preserving the features that makes the diffusion solver attractive.

6.2 Scope of future works

Several recommendations arose from the results that are carried out in this study. For future development areas, three main goals must be considered:

- Reduce the computational costs.
- Increase discretization flexibility.
- Enhancement of the mathematical and physical methods.

Due to the time constraints, additional work was not possible to be carried out and although valuable results were obtained. It is deemed to be preferable if more in-depth understanding of heat transfer/heat flow behaviour is to be obtained. Based on the results obtained, there are different areas where we think it can be good opportunities for future investigation and study. Some are:

- Our work was limited to the SP_3 approximations for radiative transfer. Further approximations can be considered for dealing with radiation heat transfer.
- The study was focused on 2D natural-convection radiation heat transfer. Mass transfer is another possible study to consider with the extension of 3D Taylor-Hood finite element approach.
- The research was done using the Galerkin-characteristics technique to deal with the presence of the advection term that can cause node-to-node oscillations. Our approach however, is valid for laminar flow conditions. Another approach that can be used for higher values of the Reynolds number with different other engineering applications.
- The focus was limited to convection and radiation. Conduction can be considered for the future work along with coupling heat flow with the structure in order to calculate the deformation of the inclusion.
- Our study focused on adjusting a uniform temperature distribution across the entire furnaces. This is done by choosing different operation conditions. The effect of flow swirling (heat flow angle) on the distribution of the heat flow is another interesting idea that can be applied to focus the heat on a particular area.
- Capturing the melting points of structures (phase change) inside the furnace is another interesting study that can be investigated.
- The proposed study managed very well in understanding the behaviour of the heat flow. Thermoforming applications are another type of study that can be an extension to the current results in both 2D and 3D.
- Effect of fuel:air on both the furnace geometry and emissivity is another continuation of the investigation that can be carried out.

Bibliography

[1] S. Acharya. Natural convection in an inclined enclosure containing internal energy sources and cooled from below. *International Journal of Heat & Fluid Flow*, 6:113–121, 1985.

[2] M. L. Adams and E. W. Larsen. Fast iterative methods for discrete-ordinates particle transport calculations. *Progress in Nuclear Energy*, 40:3–159, 2002.

[3] R. E. Alcouffe. Diffusion synthetic acceleration methods for diamond-differenced discrete-ordinates equations. *Nuclear Science and Engineering*, 64:344–355, 2017.

[4] E. Altschuler, P. Marino, and A. Pignotti. Numerical models of reheating gas furnaces in the steel industry. In *Proceedings of the Fourth ISHMT/ASME Heat and Mass Transfer Conference*, 2000.

[5] A. El Kahoui andM. Malek, N. Izem, S. Mohamed, and M. seaid. Partition of unity finite element analysis of nonlinear transient diffusion problems using p-version refinement. *Computer Modeling in Engineering and Sciences*, 124(1):61–78, 2020.

[6] S. F. Ashby, P. N. Brown, M. R. Dorr, and A. C. Hindmarsh. A linear algebric analysis of diffusion synthetic acceleration for the boltzmann transport equations. *SIAM Journal on Numerical Analysis*, 32:128–178, 1995.

[7] G. Barakos, E. Mitsoulis, and D. Assimacopoulo. Natural convection flow in a square cavity revisited: laminar and turbulent models with wall functions. *International Journal of Numerical Methods in Fluids*, 18:695–719, 1994.

[8] P. Barr. The development, verification and application of a steady-state thermal model for the pusher-type reheat furnace. *Metallurgical and Materials Transactions B*, 26:851–869, 1995.

[9] M. Bercovier and O. Pironneau. Error estimates for finite element solution of the stokes problem in the primitive variables. *Numerische Mathematik*, 33:211–224, 1979.

[10] M. N. Borjini, C. Mbow, and M. Daguenet. Numerical analysis of the effect of radiation on laminar steady natural convection in a two-dimensional participating medium between two horizontal confocal elliptical cylinders. *Numerical Heat Transfer Part A*, 35:467–494, 1999.

[11] H. Bouali, A. Mezrhab, and H. Bouzidi. Radiation-natural convection heat transfer in an inclined rectangular enclosure. *International Journal of Thermal Science*, 45:553–566, 2006.

[12] P. S. Brantley and E. Larsen. The simplified P_3 approximation. *Nuclear Science and Engineering*, 134:1, 2000.

[13] P. N. Brown. A linear algebric development of diffusion synthetic acceleration for three-dimensional transport equations. *SIAM Journal on Numerical Analysis*, 32:179–214, 1995.

[14] C. Cardona, A. Amell, and H. Burbano. Laminar burning velocity of natural gas/syngas-air mixture. *Dyna*, 180:136–143, 2013.

[15] S. Chandrasekhar. Radiative transfer. *Dover*, 1960.

[16] K. S. Chapman, S. Ramadhyani, and R. Viskantra. Modeling and parametric studies of heat transfer in a direct-fired continuous reheating furnace. *Metallurgical Transactions B*, 22B:513–521, 1991.

[17] R. Collin. A flexible mathematical model for the simulation of reheating furnace performance. In *Proceeding of Conference for Hot Working*, 1968.

[18] J. Cui. Finite pointset methods on the sphere and their application in physical geodesty. PhD thesis, *University of Kaiserslautern*, 1995.

[19] B. Davison. Neutron transport theory. In *Oxford University Press*, 1958.

[20] E. J. Dean and R. Glowinski. On some finite elements methods for numerical simulation of incompressible viscous flow. *M. D. Gunzburger and R. A. Nicolaides, editors, Incompressible computational fluid dynamics, Cambridge University Press, Cambridge*, 1993.

[21] J. F. Doglas. An introduction to dimensional analysis for engineers. *Pitman. vii*, 1969.

[22] L . A. Dombrovsky, J. H. Randrianalisoa, W. Lipinski, and V. Timchenko. Simplified approaches to radiative transfer simulations in laser-induced hyperthermia of superficial tumors. In *Proceedings of the 7^{th} international symposium on Radiative Transfer*, 2013.

[23] T. F. Douglas and J. Russell. Numerical methods for convection dominated diffusion problems based on combining the method of characteristics with finite elements or finite difference. *SIAM Journal on Numerical Analysis*, 19:871–885, 1982.

[24] A. Draoui, F. Allard, and C. Beghein. Numerical analysis of heat transfer by natural convection and radiation in participating fluids enclosed in square cavities. *Numerical Heat Transfer, Part A*, 20:253–261, 1991.

[25] D. Drysdale. An introduction to fire dynamics. *John Wiley & Sons, second Edition*, 1999.

[26] M. C. Duluc, S. Xin, and P. Le Quéré. Transient natural convection and conjugate transients around a line heat source. *International Journal of Heat and Mass Transfer*, 46:341–354, 2003.

[27] M. El-Amrani and M. Seaid. Finite element P_1 solution of unsteady thermal flow past a circular cylinder with radiation. *International Journal of Computer Mathematics*, pages 1–16, 2006.

[28] R. Fedkiw, T. Aslam, B. Merriman, and S. Osher. A non-oscillatory eulerian approach to interfaces in multimaterial flows (the ghost fluid method). *Journal of Computational Physics*, 152:457, 1999.

[29] C. A. Felippa. Partitioned analysis for coupled mechanical systems. *Engineering Computations*, 5:123–133, 1988.

[30] J. H. Ferziger and M. Peric. Computational methods for fluid dynamics (2nd edition). *Springer-Verlag*, 1999.

[31] F. Fitzgerald and A. T. Sheridan. Heating of a slab in a furnace. *Journal of Iron and Steel Institute*, 208, 1970.

[32] W. A. Fiveland. The selection of discrete ordinate quadrature sets for anisotropic scattering. *American Society of Mechanical Engineers Heat Transfer Division Fundimental Radiation Heat Transfer*, 160:89–96, 1991.

[33] T. Fusegi and B. Farouk. Laminar and turbulent natural convection-radiation interactions in a square enclosure filled with a non-gray gas. *Numerical Heat Transfer Part A*, 15:303–322, 1989.

[34] T. Fusegi, J. M. Hyun, K. Kuwaharas, and B. Farouk. A numerical study of three-dimensional natural convection in a differentially heated cubical enclosure. *International Journal of Heat and Mass Transfer*, 34:1543–1557, 1991.

[35] T. Fusegi, K. Ishii, B. Farouk, and K. Kuwahara. Natural convection-radiation interaction in a cube filled with a non-gray gas. In *Advanced Computational Methods in Heat Transfer Vol 1: Heat Conduction, Convection and Radiation, Proceedings of the First International Conference*, pages 157–168, 1990.

[36] T. Fusegi, K. Ishii, B. Farouk, and K. Kuwahara. Three-dimensional study of convection-radiation interactions in a cubical enclosure field with a non-gray gas. In *Proceedings of the Ninth International Heat Transfer Conference*, pages 421–426, 1990.

[37] A. M. Garcia, A. F. Colorado, J. F. Obando, C. E. Arrieta, and A. A. Amell. Effect of the burner position on an austenitizing process in a walking-beamtype reheating furnace. *Applied Thermal Engineering*, 153:633–645, 2019.

[38] E. Gelbard. Simplified spherical harmonic equations and their use in shielding problems. In *Technical Report WAPD-T-1182 Bettis Atomic Power Laboratory*, 1961.

[39] S. I. Gerasinwv, S. Yu. Efroimovich, M.D. Klimovitskii, and V.N. Khloponin. Stastical modelling of heating of metal in conveyor furnaces taking into account heating-atmosphere temperature profile. *Steel in the USSR*, 14:461–462, 1984.

[40] S. Giani and M. Seaid. hp-adaptive discontinuous Galerkin methods for simplified P_N approximations of frequency-dependent radiative transfer. *Computer Methods in Applied Mechanics and Engineering*, 301:52–79, 2016.

[41] S. Glasstone and P. J. Dolan. The effects of nuclear weapons. *United States Department of Defense and United States Department of Energy*, 1977.

[42] G. H. Golub and C. F. Van Loan. Matrix computations. *The Johns Hopkins University Press, Third Edition*, 1996.

[43] T. Gotz. Coupling heat conduction and radiative transfer. *Journal of Quantitative Spectroscopy and Radiative Transfer*, 72:57–73, 2002.

[44] A. Greenbaum. Iterative methods for solving linear systems. *Society for Industrial and Applied Mathematics Philadelphia*, 1997.

[45] M. Gupta, K. Bumtariya, H. Shukla, P. Patel, and Z. Khan. Methods for evaluation of radiation view factor: a review. *Materials Today: Proceedings*, 4:1236–1243, 2017.

[46] E. Hachem, T. Kloczko, H. Digonnet, and T. Coupez. Stabilized finite element solution to handle complex heat and fluid flows in industrial furnace the using immersed volume method. *International Journal for Numerical Methods in Fluids*, 68:99–121, 2012.

[47] C. Han and S. Baek. The effects of radiation on natural convection in a rectangular enclosure divided by two partitions. *Numerical Heat Transfer, Part A*, 37:249–270, 2000.

[48] J. Harish. Computational Modelling of Heat Transfer In Reheat Furnaces. *M.S. Thesis, Dept. of Mechanical Engineering, Indian Institute of Science*, 2000.

[49] J. Harish and P. Dutta. Heat transfer analysis of pusher type reheat furnace. *Ironmaking Steelmaking*, 32:151–158, 2005.

[50] H. C. Hottel and E. S. Cohen. Radiant heal exchange in gas-filled enclosure. *Journal of American Institute of Chemical Engineers*, 4:3, 1958.

[51] G. Houzeaux and R. Codina. An overlapping Dirichlet/Robin domain decomposition method. *Journal of Computational and Applied Mathematics*, 158(2):243–276, 2003.

[52] S. S. Hsieh and S. S. Yang. Transient three-dimensional natural convection in a rectangular enclosure. *International Journal of Heat and Mass Transfer*, 39:13–26, 1996.

[53] U. K. Ibrahim, R. M. Salleh, and W. Zhou. Radiation heat transfer analysis in high emissivity baking oven using network representation method. *APCBEE Procedia*, 3:11–16, 2012.

[54] F. P. Incropera. Introduction to heat transfer. *John Willey & Sons, New York*, 1985.

[55] D. C. Ipsen. Units, dimensions, and dimensionless numbers. *McGraw-Hill*, 1960.

[56] T. Ishii, C. Zhang, and S. Sugiyama. Numerical modeling of an industrial aluminium melting furnace. *Journal of Energy Resources Technology*, 120:276–284, 1998.

[57] Y. Jaluria. Natural convection heat and mass transfer. *Pergamon Ress, Oxford*, 1980.

[58] J. H. Jeans. The equation of radiative transfer of energy. *Monthly Notices Royal Astronomical Society*, 78:28–36, 1917.

[59] B. Jha, I. Yabo, and J-E. Lin. Transient natural convection in an annulus with thermal radiation. *Applied Mathematics*, 8:1351–1366, 2017.

[60] C. Johnson. Numerical solution of partial differential equations by the finite element method. *Cambridge University Press: Cambridge-Lund*, 1987.

[61] M. Kaltenbacher. Computational Acoustics. *Springer, Cham*, 2018.

[62] V. Karlovice. A collection of papers. In 9^{th} *International Seminar Mathematical Modeling of Furnace Design and Operation*, 2007.

[63] G. Kefayati. Double-diffusive natural convection and entropy generation of bingham fluid in an inclined cavity. *International Journal Heat and Mass Transfer*, 116:762–812, 2018.

[64] C. T. Kelly. Iterative methods for linear and nonlinear equations. *Society for Industrial and Applied Mathematics Philadelphia*, 1995.

[65] A. J. Khalifa and S. E. Abdullah. Buoyancy driven convection in undivided and partially divided enclosures. *Energy Conservation and Management*, 40:717–727, 1999.

[66] K. Khalil. Flow, mixing and heat transfer in furnaces: the science & applications of heat and mass transfer reports, reviews & computer programs. *Pergamon Press*, 2014.

[67] M. Kim. A heat transfer model for the analysis of transient heating of the slab in a direct-fired walking beam type reheat furnace. *International Journal of Heat and Mass Transfer*, 50:3740–3748, 2007.

[68] A. Klar, J. Lang, and M. Seaid. Adaptive solution of SP_N-approximations to radiative heat transfer in glass. *International Journal of Thermal Sciences*, 44:1013–1023, 2005.

[69] H. Kohno and T. Tanahashi. Finite element simulation of single crystal growth process using GSMAC method. *Journal of Computational and Applied Mathematics*, 149:359–371, 2002.

[70] V. Kourganoff. Basic methods in transfer problems. *Dover Publications*, 1963.

[71] C. K. Krishnaprakas and K. B. Narayana. Interaction of radiation with natural convection. *Journal of Thermophysics*, 13:387–390, 1999.

[72] V. A. Krivandie and B. L. Markov. Metallurgical Furnaces. *Mir Publishers*, 1980.

[73] T. H. Kuehn and R. J. Goldstein. An experimental and theoretical study of natural convection in the annulus between horizontal concentric cylinders. *Journal of Fluid Mechanics*, 74:695–719, 1976.

[74] P. Kumar and V. Eswaran. The effect of radiation on natural convection in slanted cavities of angle $\gamma = 45^o$ and 60^o. *International Journal of Thermal Science*, 67:96–106, 2013.

[75] R. A. Kuyper, TH. H. Van Der Meer, and C. J. Hoogendoorn. Numerical study of laminar and turbulent natural convection in an inclined square cavity. *International Journal of Heat and Mass transfer*, 36:2899–2911, 1993.

[76] K. Lari, M. Baneshi, S. Gandjalikhan Nassab, and S. Maruyama. Combined heat transfer of radiation and natural convection in a square cavity containing participating gases. *International Journal of Heat and Mass Transfer*, 54:5087–5099, 2011.

[77] E. Larsen, J. E. Morel, and J. M. McGhee. Asymptotic derivation of the multigroup P_1 and simplified P_N equations with anisotropic scattering. *Nuclear Science and Engineering*, 123:328, 1996.

[78] E. Larsen, G. Pomraning, and V. C. Badham. Asymptotic analysis of radiative transfer problems. *Journal of Quantitative Spectroscopy and Radiative Transfer*, 29:285–310, 1983.

[79] E. Larsen, G. Thommes, A. Klar, M. Seaid, and T. Gotz. Simplified P_N approximations to the equations of radiative heat transfer and applications. *Journal of Computational Physics*, 183:652–675, 2002.

[80] E. W. Larsen and J. E. Morel. Asymptotic solutions of numerical transport problems in optically thick, diffusive regimes II. *Journal of Computational Physics*, 83:212–236, 1989.

[81] E. W. Larsen, J. E. Morel, and W. F. Miller. Asymptotic solutions of numerical transport problems in optically thick, diffusive regimes. *Journal of Computational Physics*, 69:283–324, 1987.

[82] G. Lauriat. Combined radiation-convection in gray fluids enclosed in vertical cavities. *International Journal of Heat and Mass Transfer*, 104:609–615, 1982.

[83] G. Lauriat. Numerical study of the interaction of natural convection with radiation in nongray gases in a narrow vertical cavity. *International Journal of Heat and Mass Transfer*, pages 153–158, 1982.

[84] C. Lei and J. C. Patterson. A direct three-dimensional simulation of radiation-induced natural convection in a shallow wedge. *International Journal of Heat and Mass Transfer*, 46:1183–1197, 2001.

[85] C. Lei and J. C. Patterson. Natural convection in a reservoir sidearm subject to solar radiation: A two-dimensional simulation. *Numerical Heat Transfer, Part A*, 42:13–32, 2002.

[86] M. Leporini, F. Corvaro, B. Marchetti, F. Polonara, and M. Benucci. Experimental and numerical investigation of natural convection in tilted square cavity filled with air. *Experimental Thermal and Fluid Science*, 99:572–583, 2018.

[87] E. E. Lewis and W. F. Miller. Computational methods of Neutron transport. *Jon Wiley & Sons*, 1984.

[88] X. Li and P. Durbetaki. Advanced computational methods in heat transfer vol. 2: Natural and forced convection, proceedings of the first international conference. In *Transient natural convection boundary layer induced by radiant heating*, pages 135–146, 1990.

[89] Z. Li, P. V. Barr, and J.K. Brimacombe. Computer simulation of the slab reheating furnace. *Can. Metall. Quarterly*, 27:187–196, 1988.

[90] K. Liou. An Introduction to Atmospheric Radiation. *International Geophysics*, 2002.

[91] S. K. Mahapatra, S. Sen, and A. Sarkar. Interaction of surface radiation and variable property natural convection in a differentially heated square cavity-a finite element analysis. *International Journal of Numerical Methods in Heat & Fluid Flow*, 9:423–443, 1999.

[92] M. Malek, N. Izem, S. Mohamed, and M. seaid. Numerical solution of rosseland model for transient thermal radiation in non-grey optically thick media using enriched basis functions. *Mathematics and Computers in Simulation*, 180:258–275, 2020.

[93] M. Malek, N. Izem, S. Mohamed, M. Seaid, and O. Laghrouche. A partition of unity finite element method for three-dimensional transient diffusion problems with sharp gradients. *Journal of Computational Physics*, 396:702–717, 2019.

[94] M. Malek, N. Izem, and M. seaid. A three-dimensional enriched finite element method for nonlinear transient heat transfer in functionally graded materials. *International Journal of Heat and Mass Transfer*, 155:119804, 2020.

[95] M. Malek, N. Izem, M. seaid, S. Mohamed, and M. Wakrim. A partition of unity finite element method for nonlinear transient diffusion problems in heterogeneous materials. *Computational and Applied Mathematics*, 38(2):31, 2019.

[96] P. Marino. Proceedings of the fifth european conference on industrial furnaces and boilers. In *Numerical Modeling of Steel Tube Reheating in Walking Beam Furnaces*, 2000.

[97] R. McClarren. Theoretical aspects of the simplified pn equations. *Transport Theory and Statistical Physics*, 39(2-4):73–109, 2011.

[98] D. Mihalas and B. S. Mihalas. Foundations of radiation hydrodynamics. *Oxford University Press, New York*, 1983.

[99] S. Mikhailenko, M. Sheremet, and A. Mohamad. Convective-radiative heat transfer in a rotating square cavity with a local heat-generating source. *International Journal of Mechanical Sciences*, 142–143:530–540, 2018.

[100] A. F. Mills. Heat Transfer second edition. *Prentice Hall, Euglewood Cliffs, New Jersey.*

[101] A. N. Minaev, S. I. Reshetnyak, and I. G. Butenko. Heat transfer in walking beam furnaces. *Steel in the USSR*, 13:417–418, 1983.

[102] M. Modest. Further development of the elliptic pde formulation of the p-n approximation and its marshak boundary conditions. *Numerical Heat Transfer, Part B: Fundamentals*, 62(2-3):181–202, 2012.

[103] M. Modest. Radiative Heat Transfer. *Academic Press*, 2013.

[104] M. Modest and J. Yang. Elliptic pde formulation and boundary conditions of the spherical harmonics method of arbitrary order for general three-dimensional geometries. *Journal of Quantitative Spectroscopy and Radiative Transfer*, 109:1641–1666, 2008.

[105] M. Mohamed, M. Seaid, J. Trevelyan, and O. Laghrouche. Time-independent hybrid enrichment for finite element solution of transient conduction-radiation in diffusive grey media. *Journal of Computational Physics*, 251:81–101, 2013.

[106] S. Mohamed, M. seaid, and A. Bouhamidi. Iterative solvers for generalised finite element solution of boundaryvalue problems. *Numerical Linear Algebra with Applications*, 25(6):e2205, 2018.

[107] S. Mohamed, M. Seaid, J. Trevelyan, and O. Laghrouche. An enriched finite element model with q-refinement for radiative boundary layers in glass cooling. *Journal of Computational Physics*, 258:718–737, 2014.

[108] H. A. Morris. Advanced modeling for small glass furnaces. Master's thesis, *West Virginia University, Department of Mechanical Engineering*, 2007.

[109] R. L. Murray. Nuclear reactor physics. *Prentice Hall*, 1957.

[110] M. Nia and S. Nassab. Thermohydrodynamic characteristics of combined double-diffusive radiation convection heat transfer in a cavity. *Comptes Rendus Mecanique*, 347:406–422, 2019.

[111] A.O. Nieckele, M.F. Naccache, and M.S.P. Gomes. Numerical modeling of an industrial aluminium melting furnace. *Journal of Energy Resources Technology*, 126:72–81, 2004.

[112] U.S. Department of Energy. Check burner air to fuel ratios, process heat tip sheet 2. `www.oit.doe.gov`. Jumo.

[113] A. C. Palmer. Dimensional analysis and intelligent experimentation. *Hackensack, NJ: World Scientific. x*, 2008.

[114] H. K. Park, M. Y. Ha, H. S. Yoon, Y. G. Park, and C. Son. A numerical study on natural convection in an inclined square enclousure with a circular cylinder. *International Journal of Heat and Mass transfer*, 66:295–314, 2013.

[115] S. V. Patankar and D. B. Spalding. Seminar of the international center for heat and mass transfer. In *Simultaneous prediction of flow patterns and radiation for three-dimensional flames*, 1973.

[116] C. S. Peskin. The immersed boundary method. *Acta Numerica*, 11:1–39, 2002.

[117] O. Pironneau. On the transport-diffusion algorithm and its applications to the Navier-Stokes equations. *Numerical Mathematics*, 38:309–332, 1982.

[118] J. Pitaranta. On the spatial differencing of the discrete ordinate Neutron transport equation. *SIAM Journal on Numerical Analysis*, 15:859–869, 1980.

[119] J. Pitaranta and L. R. Scott. Error estimates for the combined spatial and angular approximations of the transport equation for slab geometry. *SIAM Journal on Numerical Analysis*, 20:922–950, 1983.

[120] L. Pizzuti, C. A. Martins, L. R. dos Santos, and D. R. S. Guerra. Laminar burning velocity of methane/air mixtures and flame propagation speed close to the chamber wall. *Energy procedia*, 120:126–133, 2017.

[121] G. Pomraning. Initial and boundary conditions for equilibrium diffusion theory. *Journal of Quantuantitative Spectroscopy and Radiative Transfer*, 36:69, 1986.

[122] G. C. Pomraning. Asympototic and variational derivations of simplified P_N equations. *Annals of Nuclear Energy*, 20 (9):623–637, 1993.

[123] J. Principe and R. A. Codina. A numerical approximation of the thermal coupling of fluids and solids. *International Journal for Numerical Method in Fluids*, 59:1181–1201, 2009.

[124] J. Pudykiewicz and A. Staniforth. Some properties and comparative performance of the semi-lagrangian method of robert in the solution of advection-diffusion equation. *Atmosphere Ocean*, 22:283–308, 1984.

[125] N. Ramesh and S. P. Venkateshan. Effect of surface radiation on natural convection in a square enclosure. *Journal of Thermophysics and Heat Transfer*, 13:299–301, 1999.

[126] H. Rarnaruthy, S. Ratnadhvani, and R. Viskanta. Proceedings with the 3^{rd} ASME/JSME thermal engineering joint conference. In *Modeling of heat transfer in directly-fired batch reheating furnace*, pages 205–215, 1991.

[127] A. C. Ratzel and J. R. Howell. Two-dimensional energy transfer in radiatively participating media with conduction by the P_N approximation. In *Proceedings of the Seventh International Heat Transfer Conference*, pages 535–540, 1982.

[128] J. Raycraft, M. D. Kelleher, H. Q. Yang, and K. T. Yang. Fire spread in a three-dimensional pressure vessel with radiation exchange and wall heat loss. *Mathematical Computational Modeling*, 14:795–800, 1990.

[129] D. Rixen and P. Gosselet. Domain decomposition methods applied to challenging engineering problems. In *16^{th} International Conference on Domain Decomposition Method*, pages 12–15, 2005.

[130] J. Lloyd S. Barjorek. Experimental investigations of natural convection in partitioned enclousures. *ASME Journal of Heat Transfer*, 104:527–532, 1982.

[131] Y. Saad and M. H. Schultz. GMRES: a generalized minimal residual algorithm for solving nonsymmetric linear systems. *SIAM Journal on Scientific and Statistical Computing*, 7:856–869, 1986.

[132] M. Seaid and A. Klar. Efficient preconditioning of linear systems arising from the discretization of radiative transfer equation. In *Challenges in Scientific Computing-CISC 2002*, pages 211–236. Springer, 2003.

[133] M. Seaid, A. Klar, and R. Pinnau. Numerical solvers for radiation and conduction in high temperature gas flows. *Journal on Flow Turbulence and Combustion*, 75:173–190, 2005.

[134] M. Sheikholeslami, M. Gorji-Bandpy, D. Ganji, and S. Soleimani. Effect of a magnetic field on natural convection in an inclined half-annulus enclosure filled with cuwater nanofluid using cvfem. *Advanced Power Technology*, 24(6):980–991, 2013.

[135] G. Song, T. Bjorge, J. Holen, and B.F. Magnussen. Simulation of fluid flow and gaseous radiation heat transfer in a natural gas-fired furnace. *International Journal of Numerical Methods for Heat and Fluid Flow*, 7:169–182, 1997.

[136] N. Sukumar, N. Moës, B. Moran, and T. Belytschko. Extended finite element method for three-dimensional crack modeling. *International Journal for Numerical Methods in Engineering*, 48:1549–1570, 2000.

[137] R. Suliman, O. Oxtoby, A. Malan, and S. Kok. Develop of a partisioned finite volume-finite element fluid-structure interaction scheme for strongly-coupled problems. In 10^{th} *World Congress on Computational Mechanics*, 2012.

[138] R. Suliman, O. Oxtoby, A. Malan, and S. Kok. A matrix free, partitioned solution of fluid-structure interaction problems using finite volume and finite element methods. *International Journal for Numerical Methods in Fluids*, 68:1031–1052, 2012.

[139] Y. Sun, X. Zhang, and J. Howell. Assessment of different radiative transfer equation solvers for combined natural convection and radiation heat transfer problems. *Journal of Quantitative Spectroscopy and Radiative Transfer*, 194:31–46, 2017.

[140] T. Szirtes and P. Rozsa. Applied dimensional analysis and modeling. *Elsevier / Butterworth-Heinemann*, 2 edition, 2007.

[141] Z. Tan and J. Howel. Combined radiation and natural convection in a two-dimensional participating square medium. *International Journal of Thermal Science*, 34:785–793, 1991.

[142] E. S. Taylor. Dimensional Analysis For Engineering. In Oxford: Oxford University Press, 1974.

[143] I. Teleaga and M. Seaid. Simplified radiative models for low-mach number reactive flows. *Applied Mathematical Modelling*, 32(6):971–991, 2008.

[144] C. Temperton and A. Staniforth. An efficient two-time-level semi-lagrangian semi-implicit intergration scheme. *Quartely Journal of Royal Meteorological Society*, 113:1025–1039, 1987.

[145] P. H. Thomas. Testing products and materials for their contribution to flashover in rooms. *Fire and Materials*, 5:103–111, 1981.

[146] G. Thommes. Radiative heat transfer equations for glass cooling problems: Analysis and numerics. PhD thesis, *Technische Universitat Darmstadt*, 2002.

[147] D. I. Tomasevic and E. W. Larsen. The simplified P_2 approximation. *Nuclear Science and Engineering*, 122:309–325, 1996.

[148] W. Trinks, M. Mawhinney, R. Shannon, R. Reed, and J. Garvey. Industrial furnaces. *John Wiley & Sons*, 2004.

[149] R. J. Tucker and R. Lorton. Mathematical modelling of load-recuperative gas-fired furnaces. In *First UK National Heat Transfer Conference, Institutions of Chemical Engineers, Symposium Series*, 1984.

[150] H. A. van der Vorst. BI-CGSTAB: a fast and smoothly converging variant of BI-CG for the solution of nonsymmetric linear systems. *SIAM Journal on Scientific and Statistical Computing*, 13:631–644, 1992.

[151] K. Velusamy, T. Sundararajan, and K. Seetharamu. Interaction effects between surface radiation and turbulent natural convection in square and rectangular enclosures. *Journal of Heat Transfer*, 123:1062–1070, 2001.

[152] M. Venturino and P.A. Rubini. Coupled fluid flow and heat transfer analysis of steel reheat furnaces. In 3^{rd} *European Conference on Industrial Furnaces and Boilers*, 1995.

[153] R. Verfürth. Error estimates for a mixed finite element approximation of the stokes equation. *RAIRO Numerical Analysis*, 18:175–182, 1984.

[154] V. Vivek, A. Sharma, and C. Balaji. Interaction effects between laminar natural convection and surface radiation in tilted square and shallow enclousures. *International Journal of Thermal Science*, 60:70–84, 2012.

[155] P. Wainwright. Thermal effects of radiation from cellular telephones. *Physics in Medicine & Biology*, 45:8, 2000.

[156] J. Wang, M. Yang, and Y. Zhang. Onset of double-diffusive convection in horizontal cavity with soret and dufour effects. *International Journal of Heat and Mass Transfer*, 78:1023–1031, 2014.

[157] J. Yang and M. Modest. High-order p-n approximation for radiative transfer in arbitrary geometries. *Journal of Quantitative Spectroscopy and Radiative Transfer*, 104(2):217–227, 2007.

[158] K. T. Yang. Numerical modeling of natural convection-radiation interaction in enclosures. In *Proceedings of the Eighth International Heat Transfer Conference*, pages 131–140, 1986.

[159] X. Yang and S. C. Kong. Numerical study of natural convection in a horizontal concentric annulus using smoothed particle hydrodynamics. *Engineering Analysis with Boundary Elements*, 102:11–20, 2019.

[160] A. Yäcel and S. Acharya. Combined natural convection and radiation in partitioned enclosures. In *Proceedings of the Ninth International Heat Transfer Conference*, pages 445–450, 1990.

[161] X. Yuan, F. Tavakkoli, and K. Vafai. Analysis of natural convection in horizontal concentric annuli of varying inner shape. *Numerical Heat Transfer*, 68:1155–1174, 2015.

[162] S. Zwart and S. McMillan. Astrophysical Recipes. *IOP Publishing Ltd*, 2018.